NASA Contractor Report 165923

NASA-CR-165923
19830011443

Subsonic Balance and Pressure Investigation of a 60-Degree Delta Wing With Leading-Edge Devices

Stephen A. Tingas
Dhanvada M. Rao

MAY 1982
NCCI-46

National Aeronautics and Space Administration
Langley Research Center
Hampton, Virginia 23665

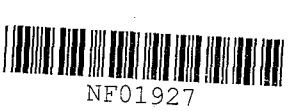

TABLE OF CONTENTS

LIST OF TABLES

LIST OF FIGURES

Page

Page

Page

Page

Page

LIST OF SYMBOLS

A	area, cm^2
AR	aspect ratio
a	length of pressure panel along leading edge, cm
b	span, cm
BW	basic wing
C_A	axial force coefficient, Axial force/$q_\infty S_{ref}$
C_{A_o}	axial force coefficient at $\alpha = 0^o$, Axial force/$q_\infty S_{ref}$
C_D	drag coefficient, Drag/$q_\infty S_{ref}$
C_{D_o}	drag coefficient at $\alpha = 0^o$, Drag/$q_\infty S_{ref}$
C_{D_i}	induced drag coefficient, Induced drag/$q_\infty S_{ref}$
C_L	lift coefficient, Lift/$q_\infty S_{ref}$
C_l	rolling moment coefficient, Rolling moment/$q_\infty S_{ref} b$
C_m	pitching moment coefficient, Pitching moment/$q_\infty S_{ref} \bar{c}$
C_{m_1}	pitching moment coefficient about original moment reference center indicated in figure 2, Pitching moment/$q_\infty S_{ref} \bar{c}$
C_N	normal force coefficient, Normal force/$q_\infty S_{ref}$
C_{N_o}	normal force coefficient at $\alpha = 0^o$, Normal force/$q_\infty S_{ref}$
C_p	static pressure coefficient, $(p - p_\infty)/q_\infty$
C_S	suction force coefficient, Suction force/$q_\infty S_{ref}$
C_T	leading-edge thrust coefficient, Thrust/$q_\infty S_{ref}$
C_X	flap thrust parameter, $/m^2$
c_r	root chord, cm
$\bar{c}$	mean geometric chord, cm
cg	center of gravity

D	drag, N
e	spanwise efficiency factor
ext.	extension perpendicular to leading edge, cm
F	fence
K	induced drag parameter, 1/e
L	lift, N
L.E.	leading edge
ℓ	semispan leading-edge length, cm
PD	percent drag reduction
p	static pressure, N/m^2
p_∞	free-stream static pressure, N/m^2
q_∞	free-stream dynamic pressure, N/m^2
S	planform area, cm^2
SC	slot contour
SF	suction force, N
SLEE	sharp leading-edge extension
STA	spanwise pressure station
S'	chordwise slot in vortex flap
T.E.	trailing edge
V_∞	free-stream velocity, m/sec
VF	leading-edge vortex flap
VG	pylon vortex generator
VLM-SA	Vortex Lattice Method with Suction Analogy code
X	chordwise distance from wing leading edge, cm
X'	distance from vortex flap apex along wing leading edge, cm

x	chordwise distance from wing apex, cm
Y'	perpendicular distance from wing leading edge, cm
y	spanwise distance from plane of symmetry, cm
z	vertical distance from chordline, cm
α	angle of attack, deg
α_D	departure angle of attack, deg
δ	vortex flap deflection angle, deg
Λ	leading-edge sweep angle, deg
η	spanwise coordinate in fraction of semispan

Subscripts

avg	average
cm	center of moments
des	local design point
front	frontal
LE	leading edge
loc	local
min	minimum
ref	reference
sep	leading-edge separation
tot	total

INTRODUCTION

Modern aircraft designed for supersonic flight are often fitted with thin, highly swept delta wings to take advantage of reduced supersonic wave drag. At high subsonic speeds, where good maneuverability and high accelerations are desirable, thin delta wings provide added advantages. These include high drag divergence Mach number and high-g maneuverability due to increased lift generated by stable leading-edge vortices. These vortices, which result from leading-edge flow separation, and subsequent flow reattachment on the upper surface produce the added advantage of sustained performance capability at high angles of attack. However, the large induced drag penalty characteristic of delta wings in high-lift flight limits the aircraft's maneuver capability at high subsonic and transonic speeds. This increase in the induced drag is due to early leading-edge flow separation, which causes a total loss of the leading-edge suction associated with attached flow around a blunt leading edge. Consequently, excess engine thrust must be used to counteract the drag increase, reducing the acceleration capability of the aircraft. In addition to the drag penalty, the spread of vortex origin from the tip to the apex of the wing with increasing angle of attack produces severe longitudinal instability in the mid-α range, as the center of vortex lift moves ahead of the wing center of gravity (ref. 1).

One method of alleviating the induced drag and stability problems associated with highly swept delta wings is through leading-edge flow

control to delay the onset of leading-edge flow separation. Attached flow at a blunt leading edge allows for partial recovery of leading-edge suction, providing a reduction in drag and alleviation of the longitudinal instability resulting from leading-edge vortices. The use of a cambered leading edge has been one method of maintaining attached flow to higher angles of attack. However, severe drag penalties at supersonic cruise speeds and the added weight and mechanical complexity involved with the use of a variable camber leading edge make this method less desirable. Leading-edge devices such as flaps and slats have also been used for the purpose of maintaining attached flow; however, they have not been overly successful on highly swept wings (ref. 1). Fixed leading-edge devices such as pylon vortex generators, fences, and chordwise slots (notches) have previously been used for alleviation of stability problems of highly swept wings. However, recent research has shown that these devices also have potential for drag reduction by maintaining attached flow to higher angles of attack and, thus, seem to be a practical solution to the induced drag problem (ref. 2).

An alternative to the conventional approach of drag reduction through attached flow is accomplished through the use of leading-edge vortex flaps and sharp leading-edge extensions (SLEE) (refs. 1, 2, 3, and 4). These devices utilize the natural tendency toward separation by forcing vortex formation and using the resulting suction forces for drag reduction. The downward-deflected vortex flap generates a coiled vortex whose suction force acts directly on the forward face of the flap, producing thrust and lift force components. The sharp leading-edge

extension makes use of the same type of induced vortex; however, by keeping the vortex directly ahead of the leading edge, the suction effect produces strictly a thrust component and, thus, a reduction in drag. The flow mechanisms of the vortex flap and sharp leading-edge extension are shown below:

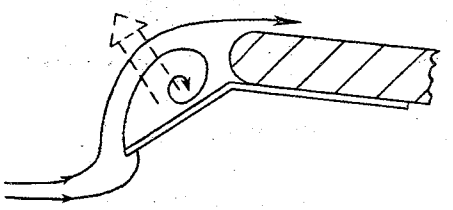

Leading-edge vortex flap

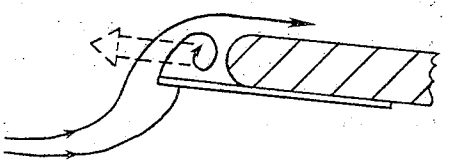

Sharp leading-edge extension

Sketch A

This report presents the results of a wind-tunnel investigation undertaken to examine the potential for further drag reduction through refined versions of devices such as fences, chordwise slots, pylon vortex generators, leading-edge vortex flaps, and sharp leading-edge extensions. Since previous research had established the effectiveness of these devices, the present investigation was primarily concerned with modifications to overcome their limitations. Methods of reducing the low-angle-of-attack drag penalty while maintaining the effectiveness of the devices at higher angles of attack were studied. Results of previous research (ref. 5) were used to design and test certain device combinations which were believed to have drag-reduction capabilities beyond

those of the individual devices. In addition, several novel configurations were included to determine the feasibility of concepts such as the use of pylon vortex generators as carriers of slender external stores (such as air-to-air missiles) and leading-edge vortex flaps for roll augmentation and as "drag" devices for landing purposes.

Use of commercial products or names of manufacturers in this report does not constitute official endorsement of such products or manufacturers, either expressed or implied, by the National Aeronautics and Space Administration.

BACKGROUND

This section presents a brief discussion of the basic flow mechanisms of the devices and results of previous research which led to the present investigation.

Chordwise Slots

Typical high-angle-of-attack performance improvements through the use of chordwise slots cut into swept leading edges are presented in reference 5. The slot flow mechanism results from the high velocity jet sheet emanating from the slot due to the natural flow of air from the lower to the upper wing surface (sketch B). It is believed that the

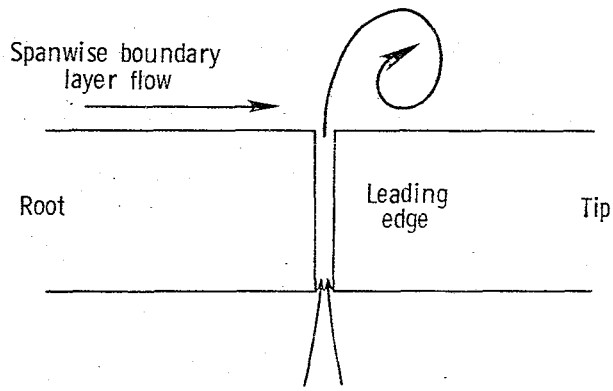

Sketch B

vortex shed from the outboard edge of the slot acts to obstruct the spanwise boundary layer flow on the upper surface, reducing boundary layer buildup and, thus, separation tendencies near the wing tip. In addition, the sense of rotation of the slot vortex opposes that of the

primary vortex, thereby hindering its inboard movement and growth. It is this "compartmentation" effect of the chordwise slot which prompted its use in combination with the vortex flaps and sharp leading-edge extension in the present investigation. The principal concern, however, was alleviation of a sudden loss of slot effectiveness at the higher angles of attack and a low-α drag penalty arising from pressure drag on the vertical face and friction on the internal wetted area of the slot. Through internal contouring of the device, an attempt was made to reduce this low-α drag and maintain slot effectiveness to higher α. In an attempt at further performance improvements, a very limited study of the effects of slot depth and width was also included.

Fences

The use of fences on delta wings has traditionally been as a fix for longitudinal instability. Previous research, however, has shown these devices to be effective in the role of drag reducers at high angles of attack, aiding in the alleviation of severe lift-dependent drag penalties. Typical performance improvements with single and multiple fences similar to those presently tested are given in reference 5.

Fence flow mechanisms are described in detail in reference 6 and briefly summarized here. First, the fence forces the swept wing upper surface isobars, normally parallel to the leading edge, to be unswept locally, reducing suction peaks and pressure gradients outboard, with opposite effects inboard. Subsequently, outboard stall and loss of

leading-edge suction are delayed. The adverse effects inboard are of minor concern due to lower prevailing upwash. The fence also acts as an obstruction to the spanwise boundary layer flow on the upper wing surface, further delaying the onset of separation near the tip. However, a loss of effectiveness is observed at high α, possibly due to an accumulation of viscous fluid on the inboard side of the device. It was believed that the flow through an adjacent inboard slot would "blow off" this viscous accumulation (sketch C) and was, thus, tested here.

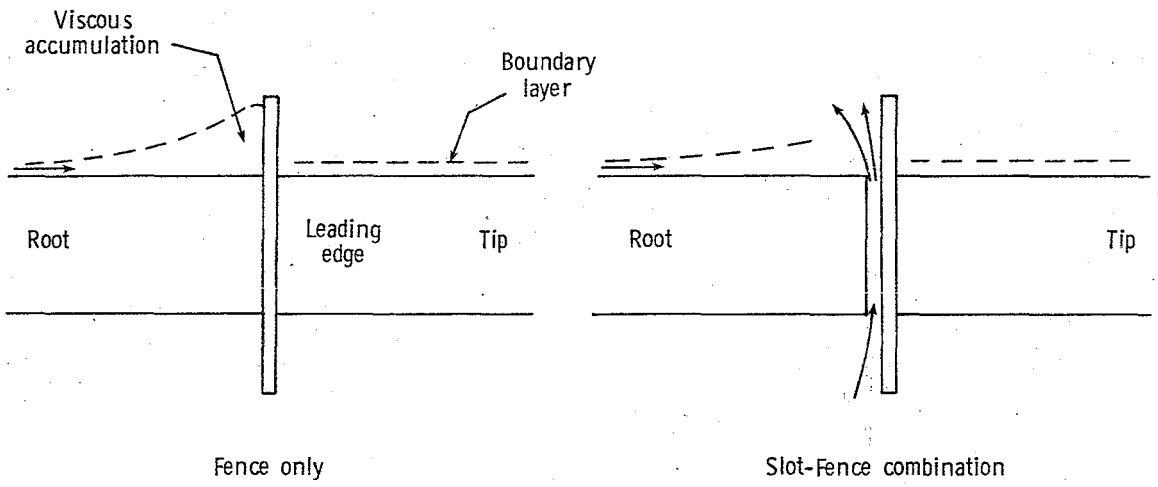

Sketch C

Finally, the fence impedes the inboard movement and growth of the primary vortex, allowing for the formation of a second, undisturbed leading-edge vortex inboard, with both acting primarily on the wing leading edge. For this reason, fences were also selected in the

present investigation for use in combination with the vortex flaps and sharp leading-edge extension.

Pylon Vortex Generators

The pylon vortex generator relies on the formation of a vortex originating at its swept-forward upper edge as a result of the effective angle of attack of the device relative to the wing leading-edge cross-flow. Except at the lowest angles of attack, this vortex travels over the wing upper surface and rotates in a sense so as to act as a barrier to the spanwise boundary layer flow, while at the same time inducing a downwash velocity outboard, with a subsequent delay in outboard stall (sketch D). In addition, the rotating motion of the vortex promotes a

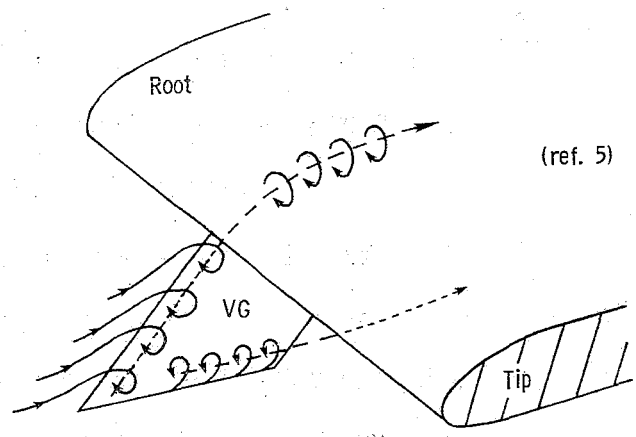

Sketch D

certain degree of boundary layer energization through turbulent mixing of viscous boundary layer fluid with high-momentum fluid from the

external stream. Again, the result is increased resistance to separation (ref. 7). However, a drag penalty is paid at low angles of attack since the leading-edge cross-flow is not yet of sufficient magnitude to cause vortex formation. The present investigation attempts to reduce the vortex generator low-α drag through systematic size reductions (basically, lower and aft edge removal), with minimal sacrifice of high-α performance. The constant 30° forward sweep and 10° toe-in angle of these devices were optimum values selected on the basis of previous research (ref. 5). In addition, the characteristic pylon shape of the vortex generators suggested their possible use also as carriers of slender external stores (such as air-to-air missiles); therefore, the effect of a simulated missile attached to the lower edge of a vortex generator on its aerodynamic effectiveness was investigated.

Leading-Edge Vortex Flaps

Results of previous tests on leading-edge vortex flaps and detailed descriptions of their aerodynamic mechanisms are presented in references 1 and 3. In essence, the vortex flap relies on the prevailing upwash ahead of the wing leading edge to force separation and formation of a coiled vortex whose suction effect acts on the flap, producing aerodynamic thrust and lift components (see sketch A in INTRODUCTION). By maintaining this sweep-stabilized vortex on the flap along its entire spanwise extent, with the flow reattachment position ideally at the wing-flap junction (knee), attached flow is maintained on the wing upper surface. Flow entrainment and increasing upwash, however, cause

the flap vortex to grow and migrate onto the wing surface with increasing angle of attack and outboard distance. In an attempt to maintain the ideal flow condition along the entire flap span, an inverse tapered flap was selected in the present investigation for comparison with a constant chord flap, under the assumption that increasing chord outboard could better accommodate the conical flap vortex. Segmented flaps of various planform shapes (constant chord, parabolic, and inverse tapered) were also included to further assist in this matter through the formation of a distinct vortex on each segment, each acting primarily on the flap surface. The use of fences and chordwise slots in combination with the vortex flaps was based on their compartmentation effect, again with the segmentation of the primary vortex into two smaller, undisturbed vortices (sketch E). The ability of the vortex flap to modify the wing

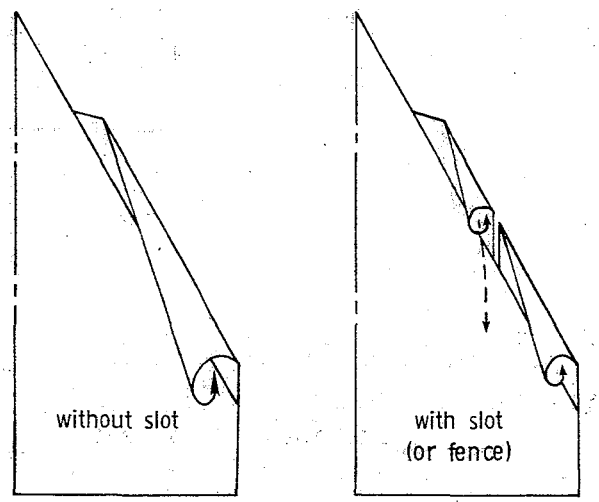

Sketch E

spanwise lift distribution suggested that sizable rolling moments might be obtained by means of asymmetric flap deflections at high angles of attack, when other control surfaces are degraded by flow separation. This concept was tested along with the possibility of adapting vortex flaps for aerodynamic braking at landing through appropriate control of vortex suction forces (sketch F).

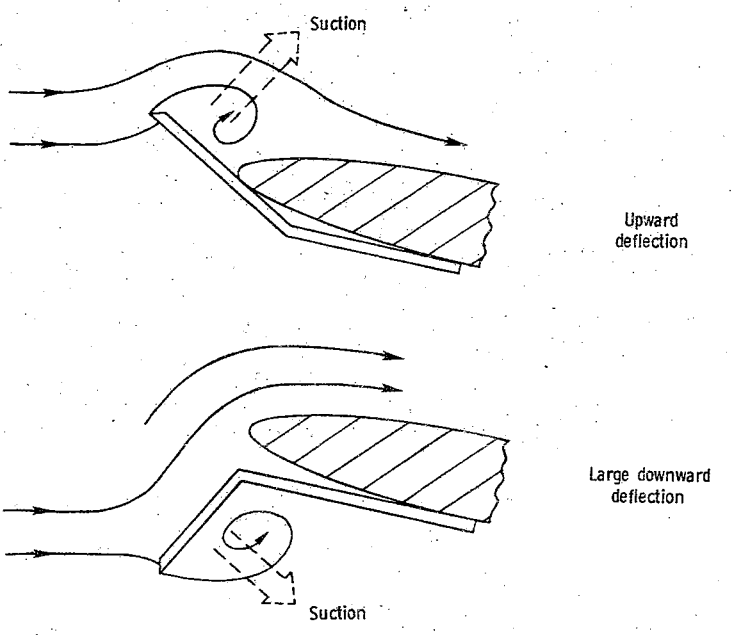

Sketch F

Sharp Leading-Edge Extension

Results of preliminary research on a sharp leading-edge extension are given in reference 5. This device, operating on the same principle of forced separation as the vortex flap, derives its drag-reduction capabilities from a tightly coiled vortex maintained ahead of a blunt

leading edge, utilizing its suction effect to obtain a thrust force (ref. 8). Ideally, flow reattachment occurs just aft of the wing leading-edge curvature (see sketch A in INTRODUCTION). However, a downstream expansion of the vortex core due to flow entrainment leads to eventual migration of the reattachment point onto the wing upper surface with increasing angle of attack and outboard distance. The resulting upper surface separated flow and associated drag increase act to partially nullify the thrust derived from the suction effect of the device. The compartmentation effect of fences and chordwise slots located at various positions along the SLEE was utilized in the present investigation for the purpose of delaying this growth of the leading-edge vortex. In addition, tests were performed to determine the optimum SLEE extension producing the ideal vortex size and position just described.

RESEARCH MODEL AND LEADING-EDGE DEVICES

The following is a description of the research model and leading-edge devices used in the investigation. Actual photographs of the sting-mounted model and selected devices appear in figure 1.

60-Deg Delta Wing Model

Figure 2 shows a drawing of the wooden, 60-deg cropped delta wing model used in the investigation. The flat-plate wing has semi-elliptic leading edges (ellipse ratio of 26.7 percent) with uniform leading-edge radius of 0.231 cm.

The right-hand wing panel was equipped with six chordwise rows of static pressure orifices around the leading edge at approximately the 20, 33, 45, 57, 70, and 82 percent semispan positions. Each station consisted of four orifices on the upper surface, four on the lower surface, and one near the leading edge. Thirteen additional orifices were provided along the span at the leading edge (X = 0) and one on the wing upper surface near the trailing edge. The pressure orifices were fed by 0.10 cm outside diameter metal tubing, which was protected by a removable metal base plate on the lower surface of the wing. The orifice locations are given in Table I.

The research model also had six 5.08 cm long chordwise slots on either leading edge at approximately the 25, 37.5, 50, 62.5, 75, and 87.5 percent semispan positions. The slots were meant for holding the leading-edge devices but also used as "devices" themselves, being sealed when not in use.

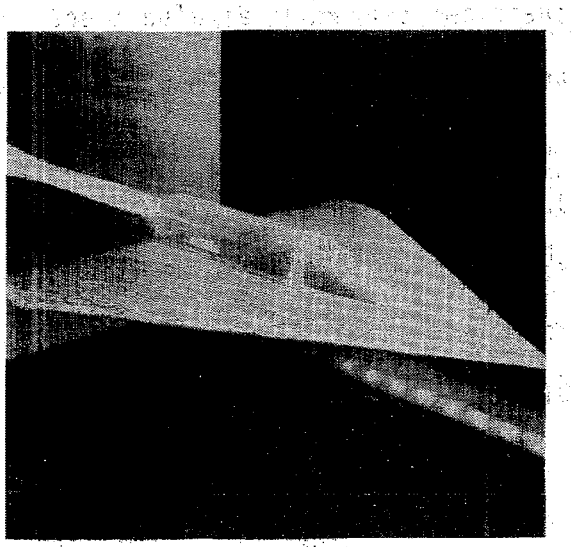

(a) Basic wing.

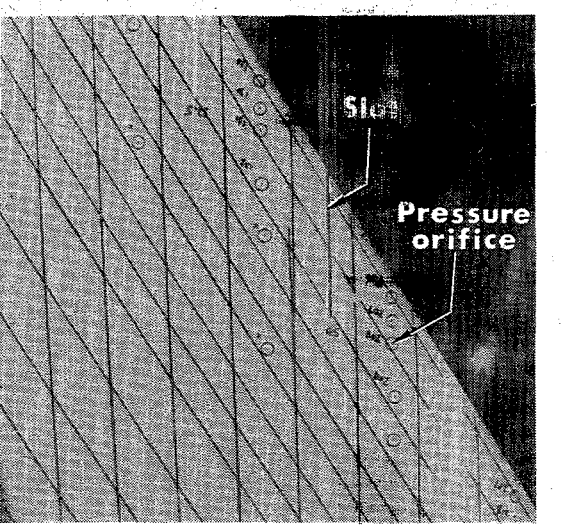

(b) Open slot.

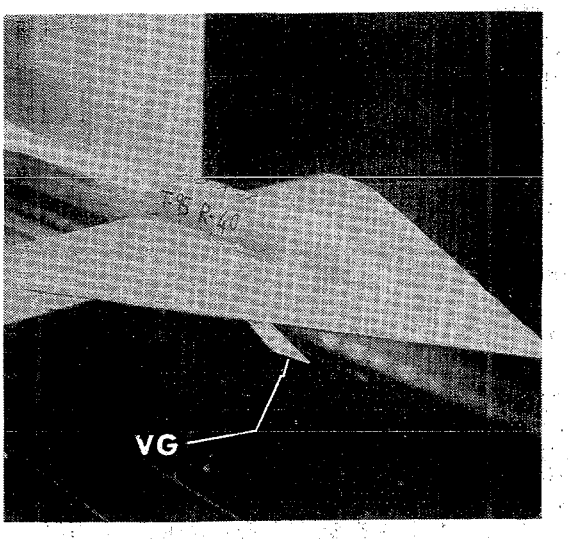

(c) Vortex generator.

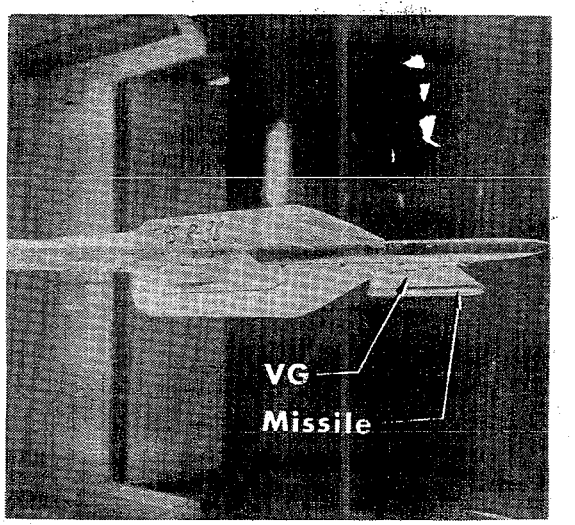

(d) Vortex generator w/missile.

Figure 1.- Photographs of research model and leading-edge devices.

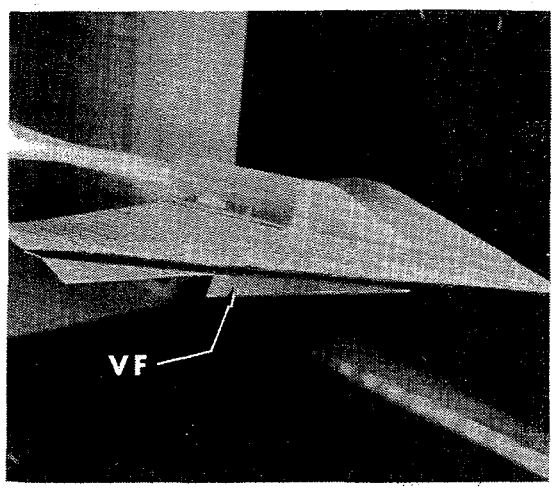

(e) Down-deflected leading-edge vortex flap.

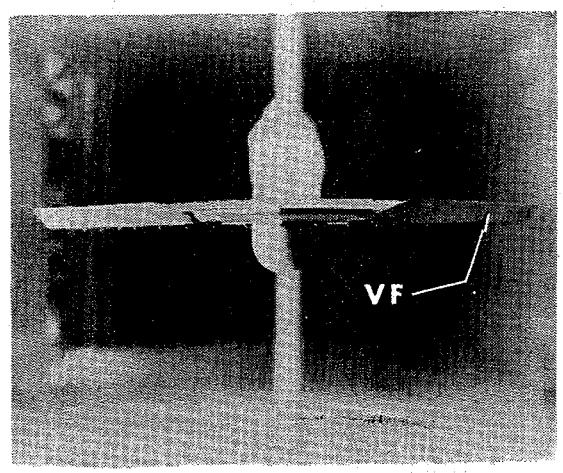

(f) Up-deflected leading-edge vortex flap.

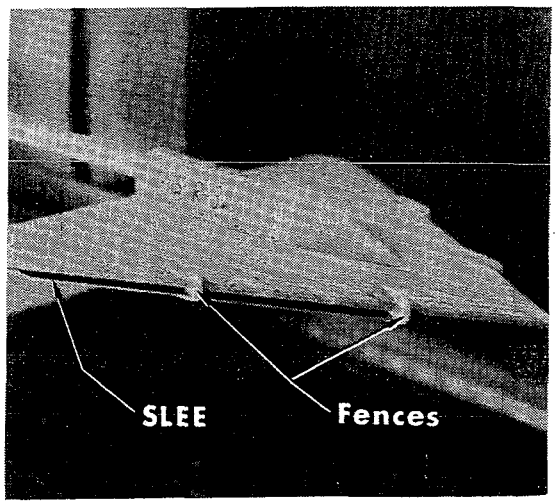

(g) SLEE w/fences.

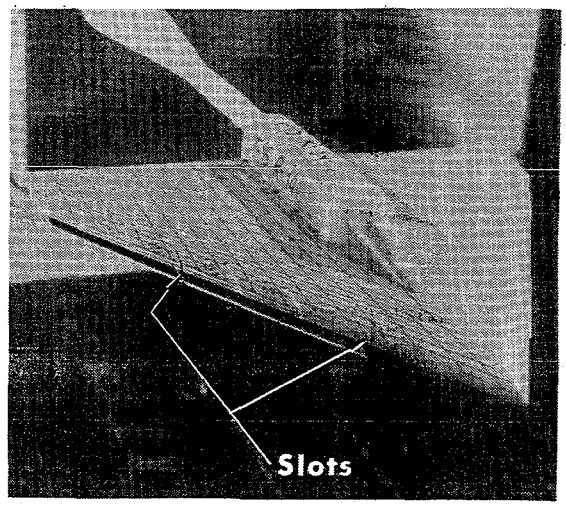

(h) SLEE w/slots.

Figure 1.- Concluded.

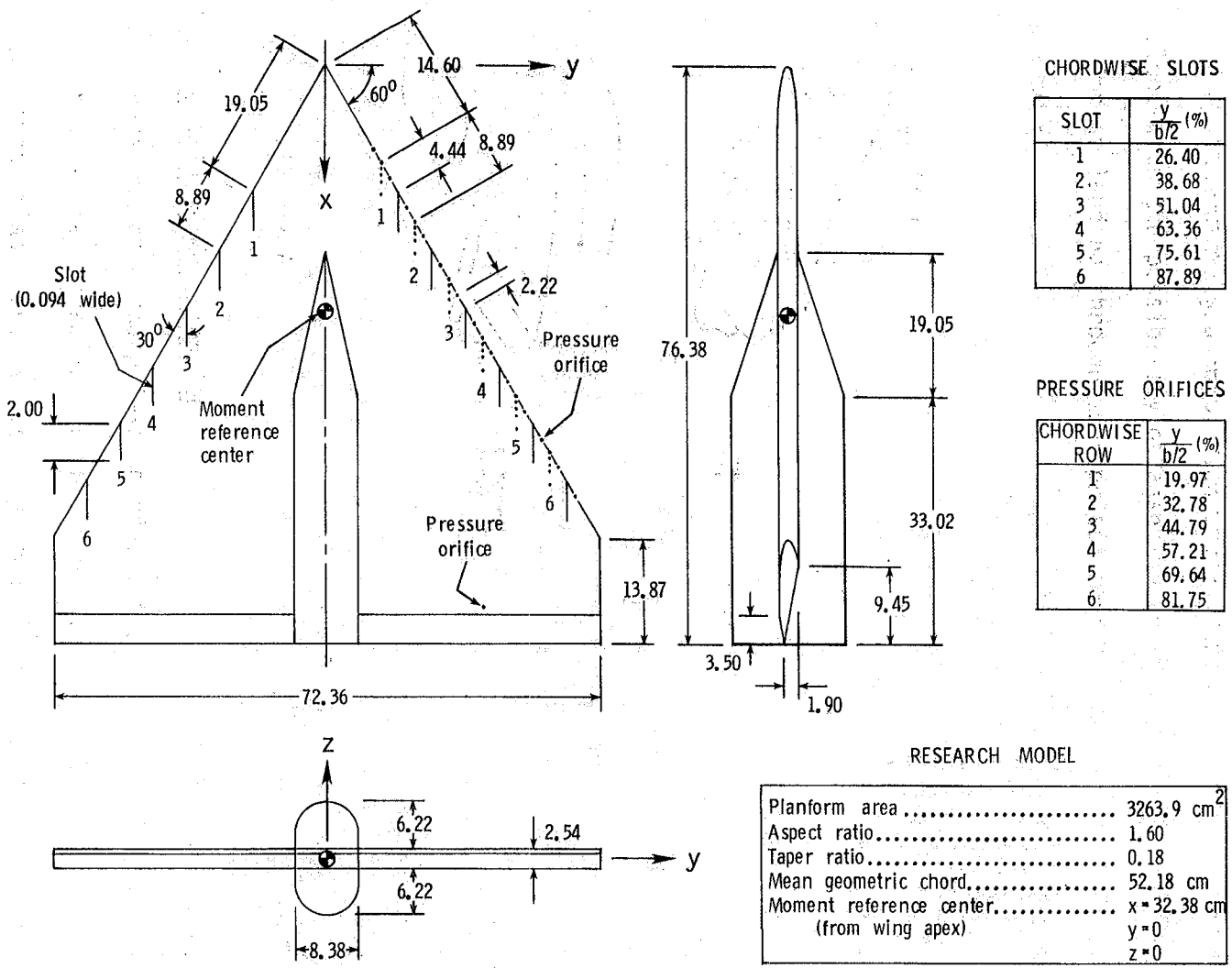

CHORDWISE SLOTS

SLOT	$\frac{y}{b/2}$ (%)
1	26.40
2	38.68
3	51.04
4	63.36
5	75.61
6	87.89

PRESSURE ORIFICES

CHORDWISE ROW	$\frac{y}{b/2}$ (%)
1	19.97
2	32.78
3	44.79
4	57.21
5	69.64
6	81.75

RESEARCH MODEL

Planform area	3263.9 cm^2
Aspect ratio	1.60
Taper ratio	0.18
Mean geometric chord	52.18 cm
Moment reference center (from wing apex)	x = 32.38 cm y = 0 z = 0

Figure 2.- Drawing of 60-deg delta wing research model. Dimensions in centimeters.

TABLE I.- PRESSURE ORIFICE LOCATIONS

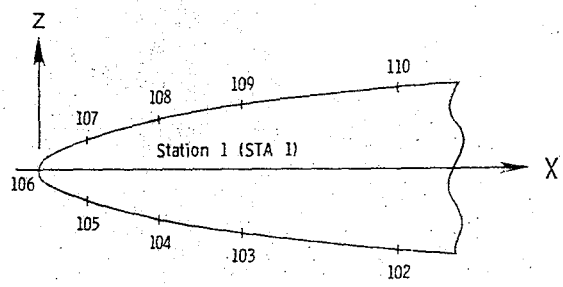

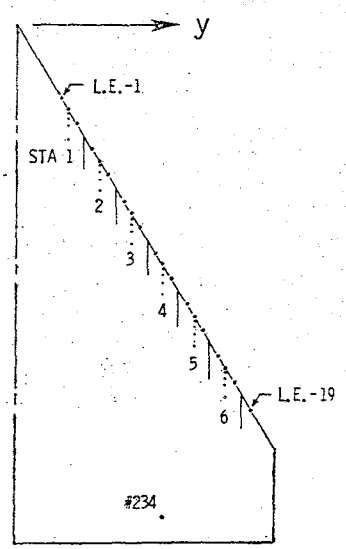

ORIFICE NUMBER	X(cm)	y(cm)	z(cm)	DESCRIPTION
101	0	6.03	0	L.E.-1
102	4.07	7.29	-0.96	Bottom STA 1
103	2.38	↓	-0.77	↓
104	1.41		-0.61	
105	0.51		-0.37	
106	0		-0.02	L.E.-2, STA 1
107	0.57		0.36	Top STA 1
108	1.46		0.61	↓
109	2.45		0.78	
110	4.34	↓	0.98	↓
111	0	8.38	0	L.E.-3
* 112	0	10.69	0	L.E.-4
113	3.94	11.95	-0.97	Bottom STA 2
114	2.44	↓	-0.79	↓
115	1.52		-0.62	
116	0.69		-0.41	
117	0		-0.05	L.E.-5, STA 2
118	0.56	11.94	0.44	Top STA 2

TABLE I.- Continued.

ORIFICE NUMBER	X(cm)	y(cm)	z(cm)	DESCRIPTION
119	1.57	↓	0.64	↓
120	2.55		0.78	
* 121	4.44		0.96	
122	0	12.88	0	L.E.-6
123	0	15.06	0	L.E.-7
124	4.02	16.28	-0.99	Bottom STA 3
125	2.56	↓	-0.82	↓
126	1.48		-0.64	
127	0.56		-0.40	
128	0		-0.04	L.E.-8, STA 3
129	0.67	16.32	0.42	Top STA 3
130	1.64	↓	0.67	↓
131	2.40		0.80	
132	4.28		1.01	
133	0	17.28	0	L.E.-9
* 134	0	19.54	0	L.E.-10
201	3.94	20.77	-1.00	Bottom STA 4
202	2.50	↓	-0.82	↓
203	1.50		-0.66	
204	0.61		-0.42	
205	0		-0.14	L.E.-11, STA 4
206	0.78	20.84	0.47	Top STA 4
* 207	1.58	↓	0.67	↓
208	2.42		0.81	
209	4.32		1.01	
210	0	21.77	0	L.E.-12
211	0	23.99	0	L.E.-13
212	4.26	25.27	-1.01	Bottom STA 5
213	2.48	↓	-0.82	↓
214	1.47		-0.64	
215	0.59		-0.40	
216	0		0	L.E.-14, STA 5
217	0.69	25.35	0.45	Top STA 5
218	1.62	↓	0.68	↓
219	2.53		0.82	
220	4.08		1.00	
221	0	26.21	0	L.E.-15
222	0	28.44	0	L.E.-16

TABLE I. - Concluded.

ORIFICE NUMBER	X(cm)	y(cm)	z(cm)	DESCRIPTION
223	4.23	29.69	-1.00	Bottom STA 6
224	2.36	↓	-0.80	↓
225	1.38	↓	-0.61	↓
226	0.51	↓	-0.38	↓
227	0	↓	0.04	L.E.-17 STA 6
228	0.55	29.79	0.39	Top STA 6
229	1.43	↓	0.65	↓
230	2.43	↓	0.81	↓
231	4.28	↓	1.01	↓
232	0		0	L.E.-18
233	0	32.85	0	L.E.-19
234	36.07	20.84	1.25	Upper Surface

*malfunction suspected.

The balance (NASA-LRC model 846) used for force and moment measurements was a six-component internally mounted strain-gage balance with maximum allowable loads as follows (accurate to within 0.5 percent of these values):

Component	Load
Normal	3113.6 N
Axial	378.1 N
Side	1334.4 N
Pitch	197.8 N-m
Roll	36.2 N-m
Yaw	84.8 N-m

The balance was located on the upper surface of the wing and shielded by a fuselage-like aluminum housing to prevent wind interference.

The two scani-valves used for pressure readings were equipped with 3.45 N/cm^2 pressure transducers, accurate to within 0.017 N/cm^2, and were located on the lower surface of the wing. They were also covered by an aluminum housing identical to the balance housing.

An accelerometer, located inside the upper nose cone of the wing, was used to measure angle of attack. It was a pendulum-type strain-gage unit, accurate to within 0.2^{o}.

Slot Contours (SC)

Details of the internal slot contours of the open slots are shown in figure 3. With the exception of SC-4, the slot contours were made from 0.079 cm thick aluminum stock and were inserted directly into the

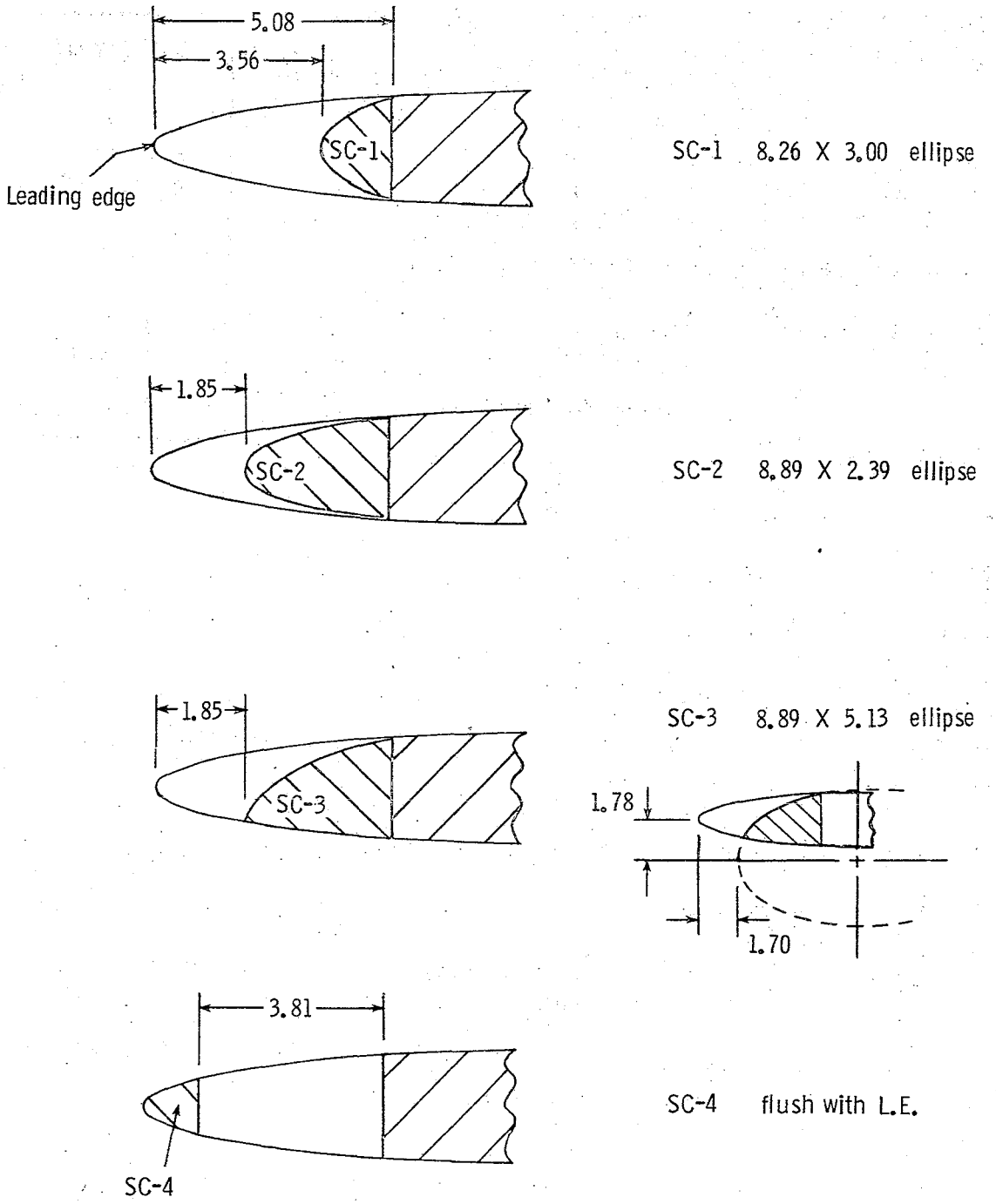

Figure 3.- Drawing of slot contours tested. Ellipse dimensions given are length of major and minor axes. Dimensions in centimeters.

chordwise slots. SC-4 was made by forcing 0.159 cm thick balsa wood into the slots and sanding it flush with the leading edge.

Fences (F)

The fences used in the investigation are shown in figure 4. They were constructed from 0.079 cm thick flat-plate aluminum and were also held in position by the chordwise slots.

Pylon Vortex Generators (VG)

The geometry and dimensions of the pylon vortex generators tested are given in figure 5. These flat-plate devices were constructed of 0.079 cm thick aluminum and were reinforced by an additional thickness of 0.159 cm on the outboard side to prevent bending under air loads. An additional vortex generator, with aft extension of the lower edge as a possible external store-carrier (fig. 6), was tested with and without a 1.27 cm diameter wooden dowel simulating a sidewinder missile scaled from the F-4D aircraft. The vortex generators were held in position by the chordwise slots.

Leading-Edge Vortex Flaps (VF)

Undeflected plan views of the vortex flaps, along with their corresponding planform areas, are shown in figure 7. The figure also indicates the deflection angles and the semispan coverage and position of each flap test configuration. The flaps were bent from 0.159 cm thick aluminum and had sharp tapered edges to induce vortex formation. For mounting, they were bolted directly onto the lower surface of the wing.

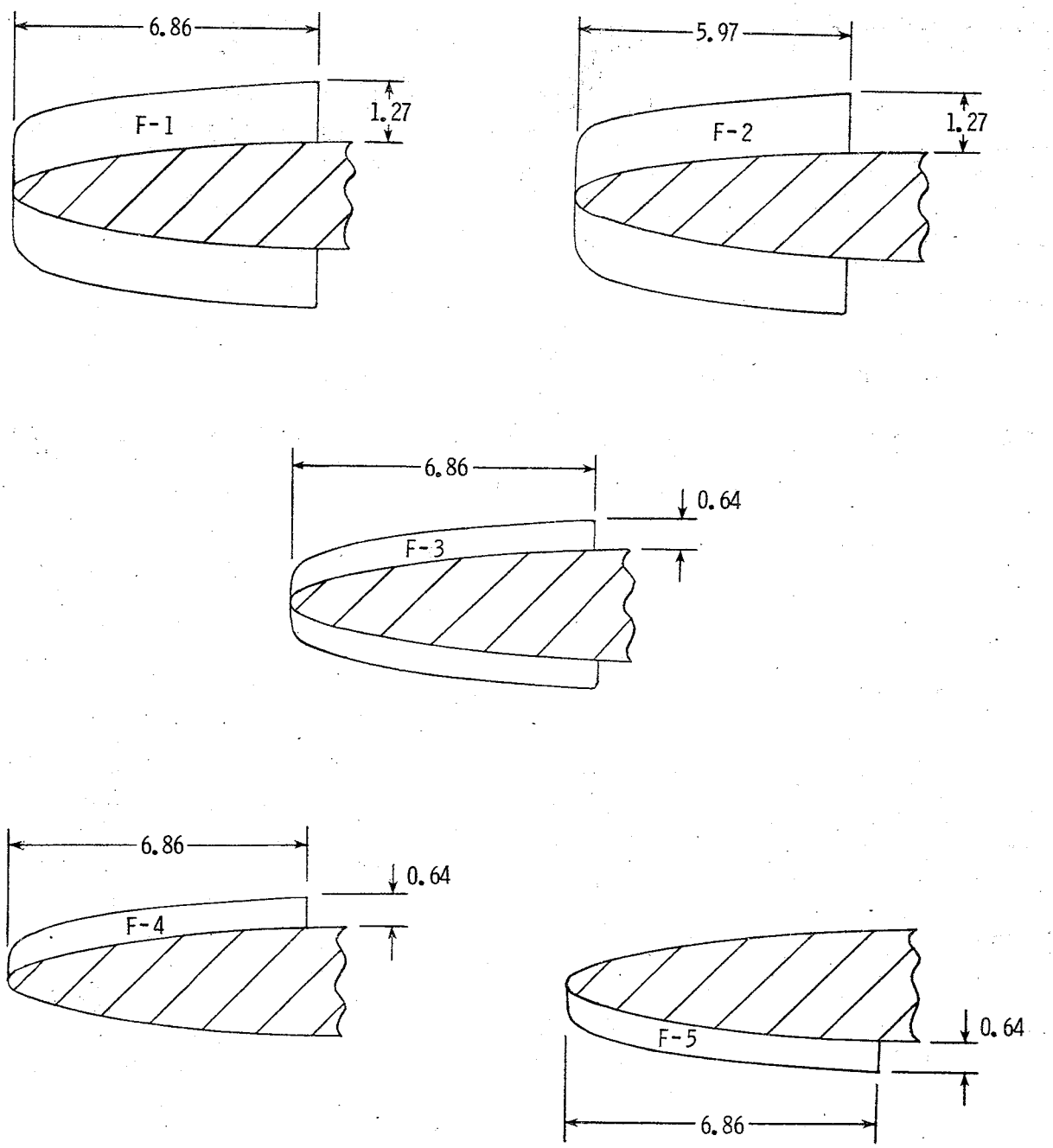

Figure 4.- Drawing of fences tested. Dimensions in centimeters.

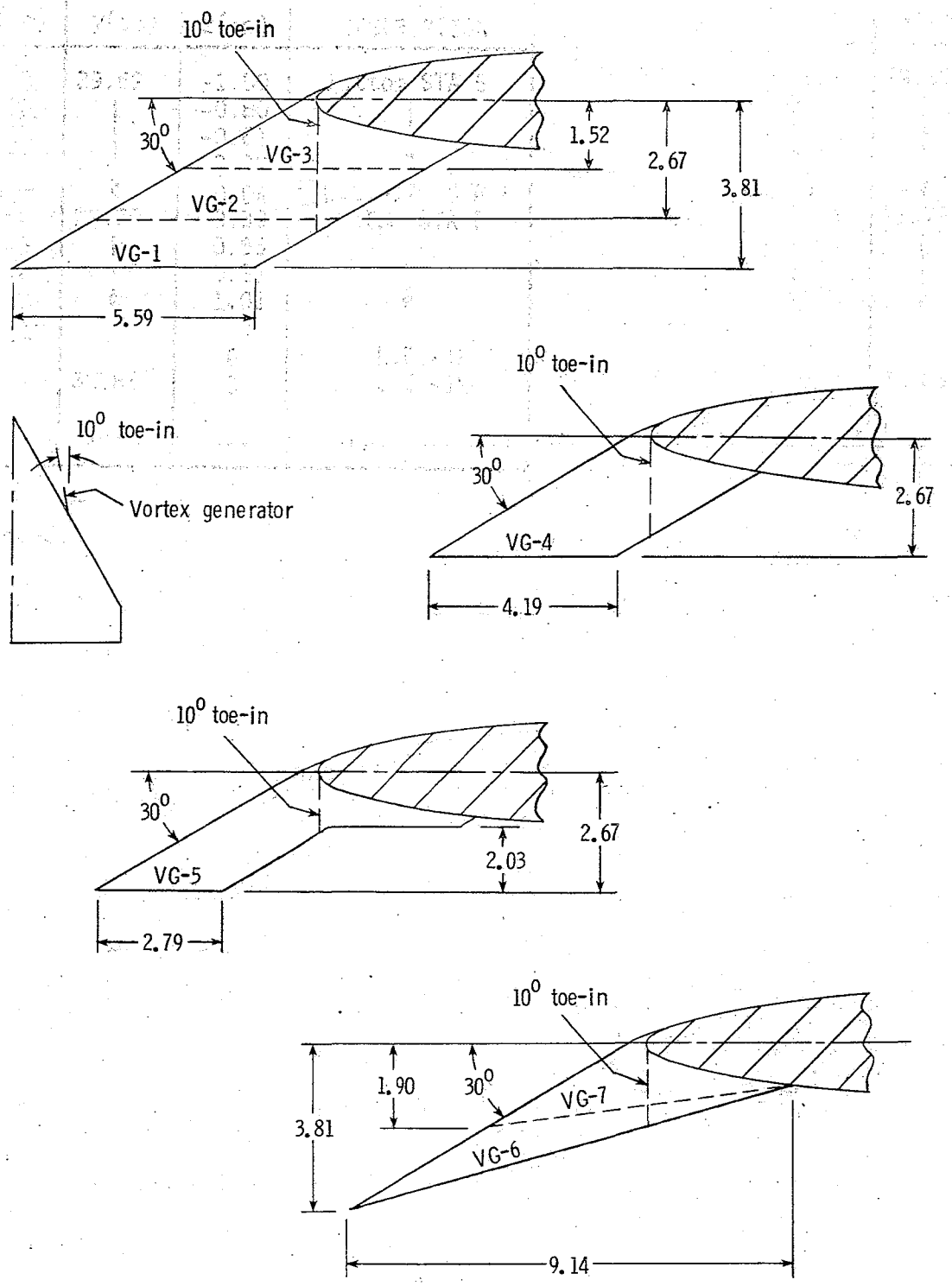

Figure 5.- Drawing of pylon vortex generators tested. Dimensions in centimeters.

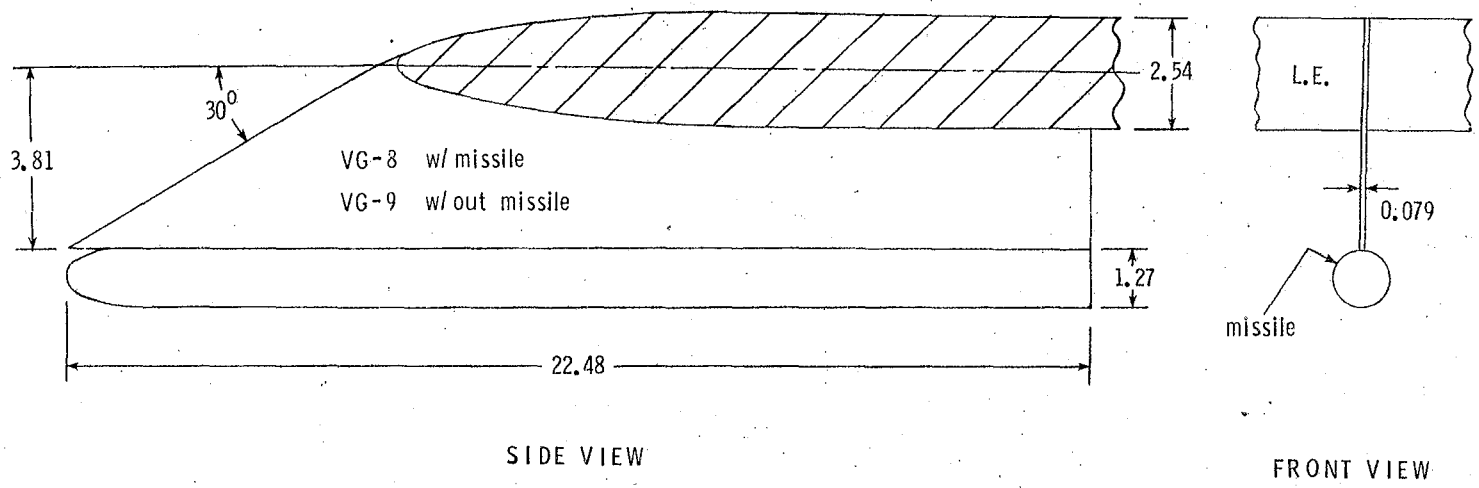

Figure 6.- Drawing of pylon vortex generator with missile tested. Dimensions in centimeters.

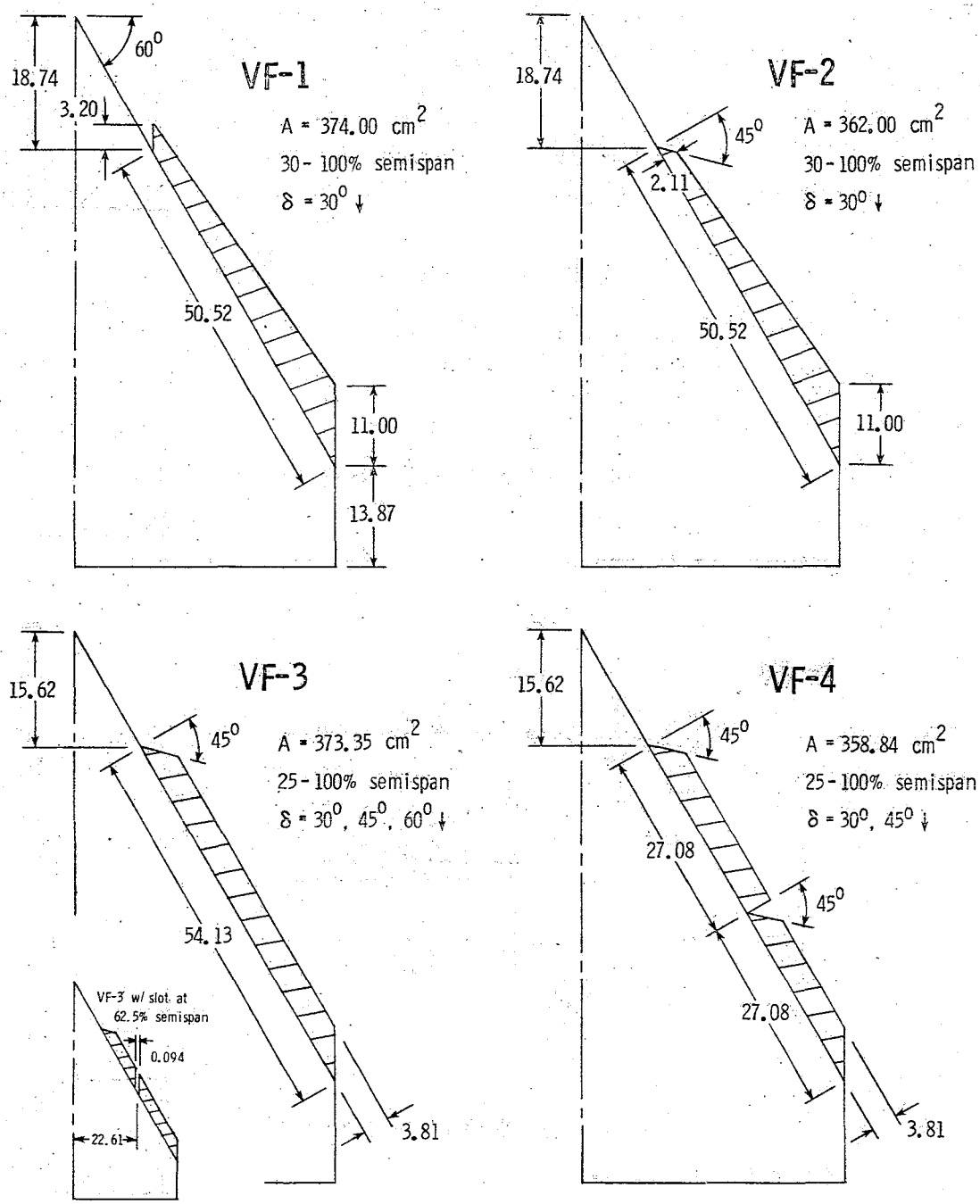

Figure 7.- Drawing of leading-edge vortex flaps tested. Planform areas given are for undeflected case and include both right and left flaps. Dimensions in centimeters.

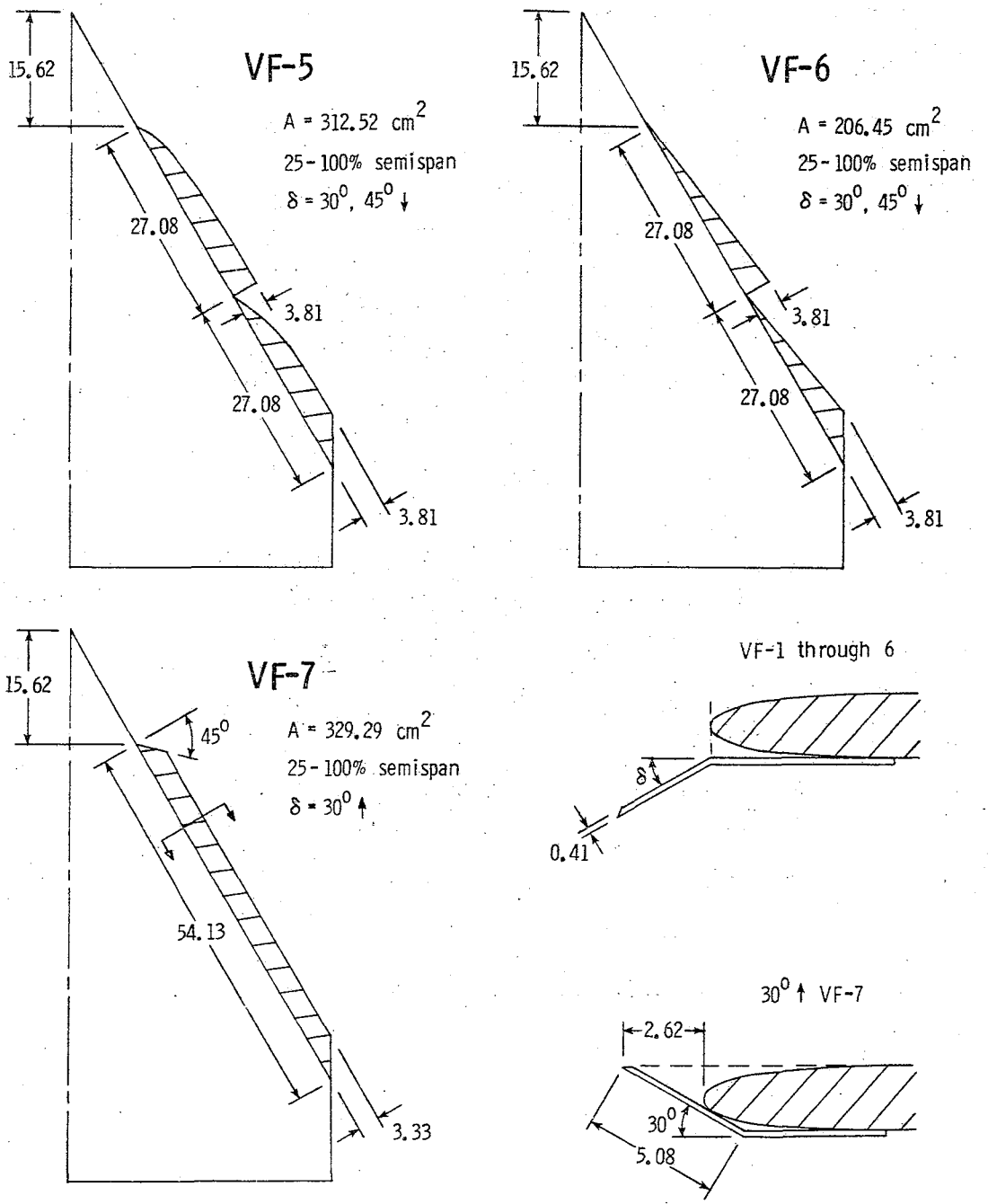

Figure 7.- Continued.

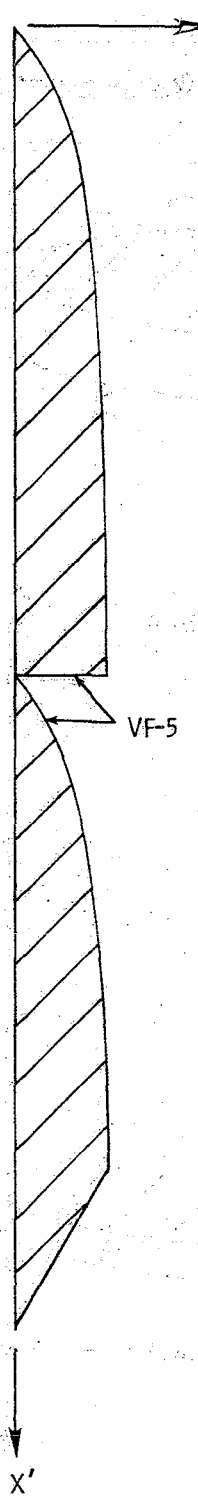

VF-5

Flap Coordinates

X'	Y'
0.00	0.00
0.94	0.79
2.92	1.85
7.29	3.00
13.26	3.50
18.90	3.68
27.08	3.81
27.08	0.00
28.45	1.07
31.27	2.76
36.83	3.30
44.45	3.73
47.70	3.81
54.15	0.00

Figure 7.- Concluded.

Sharp Leading-Edge Extension (SLEE)

The sharp leading-edge extension tested appears in figure 8. The SLEE had a variable extension ranging from 0 to 0.76 cm measured perpendicular to the wing leading edge. This 0.101 cm thick aluminum device had a sharp leading edge and was bolted directly onto the lower surface of the wing.

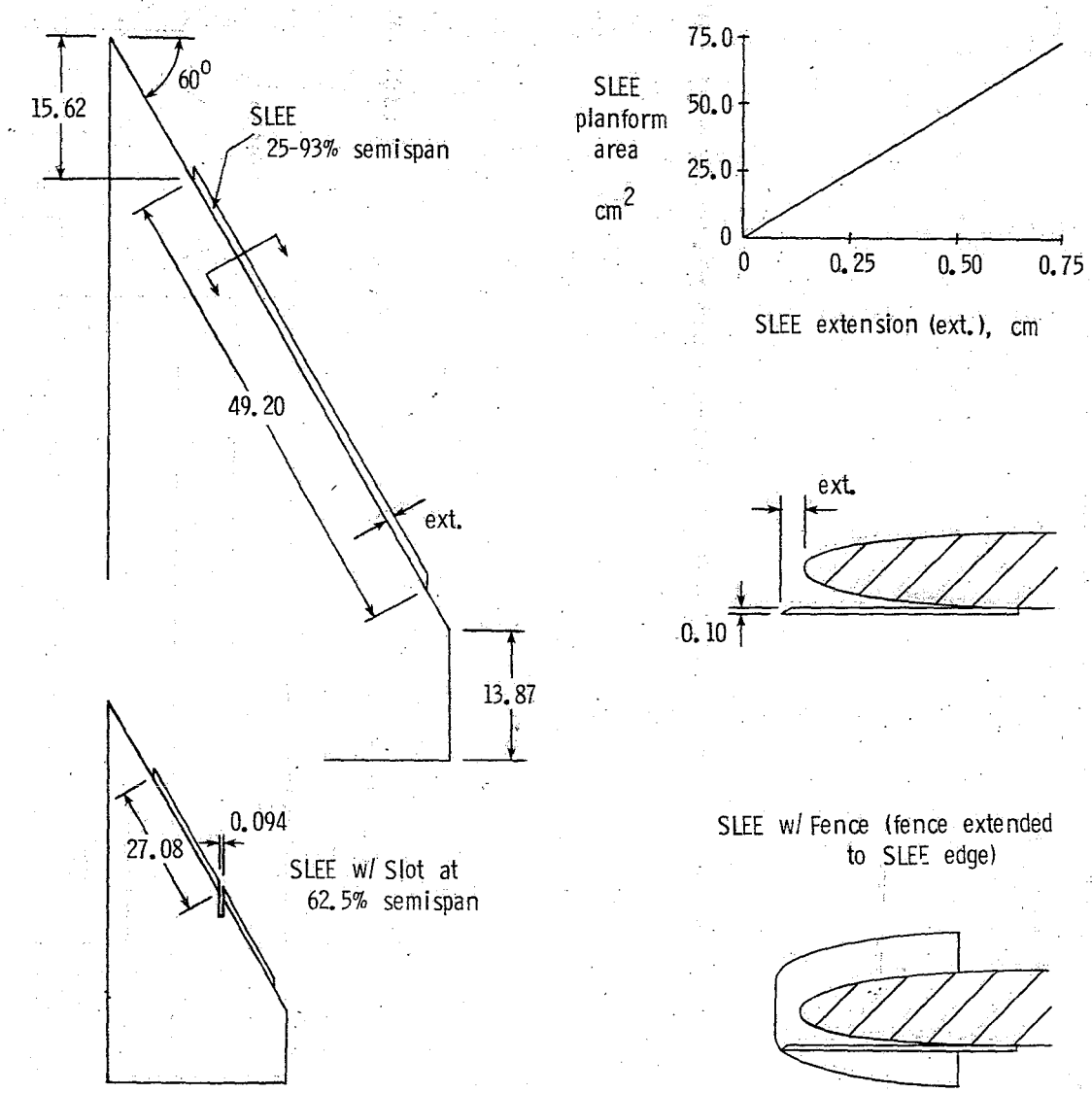

Figure 8.- Drawing of sharp leading-edge extension tested. Planform area includes both right and left SLEE. Dimensions in centimeters.

WIND-TUNNEL FACILITY

The study was conducted in NASA-Langley Research Center's 7- by 10-foot high-speed tunnel. This is a continuous-flow, closed-circuit, subsonic-transonic atmospheric wind tunnel which operates at ambient atmospheric conditions.

The drive system consists of a motor generator system which powers a 10.5 megawatt fan motor. The fan motor drives an 18-blade, 9.14 m diameter fan at a maximum speed of 485 rpm, producing a maximum test section Mach number of approximately 0.94.

The test section of the tunnel is 2.01 m high and 2.92 m wide, with a usable length of 3.30 m.

The model support system used in the test is referred to as the standard angle-of-attack sting. It consists of a vertical strut with a variable pitch angle sting support system with a range of approximately -1^{o} to 23^{o}. In addition to the pitch mode, the standard sting also has a translation mode which allows the model to be translated vertically from floor to ceiling, keeping it near the center of the test section throughout the angle-of-attack range. Reference 9 contains a detailed description of the tunnel facility.

The data acquisition, display, and control system for the 7- by 10-foot high-speed tunnel is controlled by a dedicated on-site computer. The system includes a Xerox Sigma 3 computer, a data acquisition unit, a line printer, and a Tektronix 4014 graphics terminal. Reference 10 contains a detailed description of the data reduction capabilities of the system.

EXPERIMENTAL PROGRAM

The present investigation was performed at nominal Mach and Reynolds numbers of 0.16 and 2.0×10^6 (based on a mean geometric chord of 52.18 cm), respectively. Force, moment, and surface static pressure data were taken at angles of attack ranging from -1^o to 23^o. A summary of the test is presented in Table II. The run number(s) corresponding to each test configuration is the key to locating the test data presented in reference 11.

Surface flow visualization using a fluorescent tuft technique was included in the investigation to aid in interpretation of balance and pressure data. This technique involved the use of 0.02 mm diameter mini-tufts made of a nylon monofilament material treated with a fluorescent dye. Approximately 300 mini-tufts of 3.8 cm average length were mounted on the upper surface of the right-hand wing panel and, in some cases, on the leading-edge devices, using a mixture of three parts Duco cement and one part lacquer thinner. The tufts were illuminated by ultraviolet strobe and photographed through windows in the top and side of the test section at various angles of attack during a test run. This mini-tuft technique had been shown in previous testing of this model (ref. 5) to have a negligible effect on the flow field and, thus, could be performed simultaneously with force and pressure tests.

In comparison with the model used in the investigation of reference 5, the present model was basically identical with a few minor exceptions. The most obvious was a reduced fuselage housing in order to

TABLE II.- TEST SUMMARY

	DEVICE(S)	SEMISPAN POSITION (%) 25	30	50	62.5	75	93	100	RUN NUMBER
	Basic Wing								3, 56
Slots	Open Slots (no contour)	●		●		●			4
	SC-1 (short semi-elliptic)				●				47
	SC-1 "	●		●		●			36
	SC-2 (long semi-elliptic)	●		●		●			7
	SC-3 (quarter-elliptic)	●		●		●			8
	SC-4 (flush with L.E.)	●		●		●			9
	Double Slot Width (0.18 cm) w/ SC-1				●				48
Slot/Fence combinations	F-3 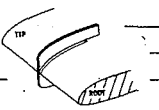				●				53
	SC-1, F-3				●				49, 50
	SC-1, F-4				●				51
	SC-1, F-5				●				52
Vortex generators	VG-1 (baseline)			●					40
	VG-1 "	●		●					54
	VG-1 "	●		●		●			55
	VG-2 (leading-edge length reduction)			●					43
	VG-3 "			●					46
	VG-4 (chord reduction)			●					41
	VG-5 "			●					44
	VG-6 (variable chord)			●					42
	VG-7 "			●					45
	VG-8 (extended chord w/ missile)			●					38
	VG-9 (extended chord w/ out missile)			●					39
Leading-edge vortex flaps	30^0 ↓ VF-1 (full length, inverse tapered)		●					●	10
	30^0 ↓ VF-2 " (tapered apex)		●					●	12
	30^0 ↓ VF-3 (full length, constant chord)	●						●	11
	45^0 ↓ VF-3 "	●						●	31
	60^0 ↓ VF-3 "	●						●	16
	30^0 ↓ VF-4 (segmented, constant chord)	●						●	14
	45^0 ↓ VF-4 "	●						●	15
	30^0 ↓ VF-5 (segmented, parabolic)	●						●	17
	45^0 ↓ VF-5 "	●						●	18, 19
	30^0 ↓ VF-6 (segmented, inverse tapered)	●						●	22
	45^0 ↓ VF-6 "	●						●	23
	30^0 ↓ VF-3, SC-1	SC ●						●	29
	30^0 ↓ VF-3, F-1	F ●						●	30
	30^0 ↓ VF-3, Slot (0.094 cm) in flap (S)	●			S			●	37
	30^0 ↓ on left, 45^0 ↓ on right VF-6	●						●	57
	30^0 ↑ VF-7 (full length, constant chord)	●						●	21
Sharp leading-edge extensions	0.71 cm ext. SLEE, F-2	F ●					●		24
	0.48 cm ext. SLEE, F-2	F ●					●		25
	0.23 cm ext. SLEE, F-2	F ●					●		26
	0.00 cm ext. SLEE, F-2	F ●					●		27
	0.48 cm ext. SLEE, SC-1	SC ●					●		28
	0.48 cm ext. SLEE, SC-1	SC ●			SC		●		34, 35
	0.48 cm ext. SLEE, F-2, SC-1	F ●			SC		●		33
	0.48 cm ext. SLEE, F-2	F ●			F		●		32

minimize its influence on the leading-edge flow development of the basic delta wing. The accompanying reduction in profile drag acted to better show up the effect of the leading-edge devices on reduction of the lift-dependent drag. Indeed, the size of the housing was reduced to a minimum compatible with the requirement to contain the balance adaptor and scanning-valves.

In an effort towards economizing wind-tunnel time per configuration, several pressure orifices on the original research model (ref. 5 investigation) were omitted in the present investigation. The effect of eliminating the four most aft pressure orifices (two each on the upper and lower surfaces at each of the six spanwise leading-edge pressure stations of the original research model) on the accuracy of leading-edge thrust calculations by pressure integration was checked and found to be within 5 percent of the value obtained with all the original orifices in use within the α range of interest. This was considered acceptable since the present investigation was mainly concerned with relative, rather than absolute, levels of leading-edge thrust. In addition, all except one of the original upper surface orifices near the trailing edge were eliminated. However, 13 additional orifices were added along the wing leading-edge interjacent existing orifices in an attempt to better define the movement of leading-edge separation in the spanwise direction. It was estimated that, in this manner, the test duration per run was reduced by approximately 20 percent without sacrificing the prime objective of the study.

DATA REDUCTION

Forces and moments sensed by a wind-tunnel balance must be corrected for external interferences unrealistic of actual flight. Calibration of the wind-tunnel test section in reference 9 shows a constant streamwise static pressure distribution at the test Mach number and, thus, no correction was needed for longitudinal buoyancy effect. Jet boundary corrections were applied to angle of attack to account for the vertical velocity induced on the model by the test section walls (ref. 12). To account for initial balance loads due to model weight, wind-off weight tare measurements were taken at various balance attitudes and used in the reduction of balance data (ref. 10). Balance axial force measurements were also corrected to eliminate housing pressure drag using chamber (base) pressure measurements. Reference 13 was used to calculate solid and wake blockage corrections due to the presence of the model and wake in the test section. Since the angle of attack was measured by means of an accelerometer located inside the model, no correction for sting bending due to aerodynamic loading was required.

Once all necessary corrections had been applied to the balance data, the final results were expressed in terms of force, moment, and pressure coefficients. Force and moment coefficients were computed based on the basic wing (devices off) planform area. This is quite legitimate since any addition of planform area from a device is an essential part of that particular concept. Lift and drag coefficients

(C_L and C_D, respectively) are oriented along the conventional wind axis coordinate system, with the axial and normal force coefficients (C_A and C_N, respectively) along the body axis system (sketch G).

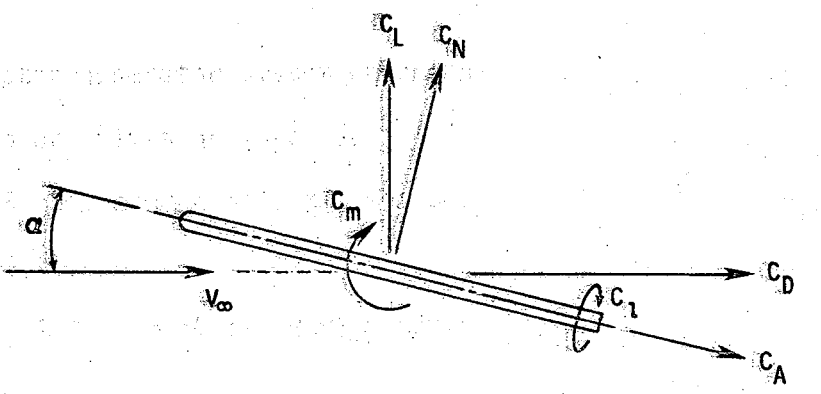

Sketch G

Moment coefficients refer to the body axes. Pitching moment coefficients have been modified from those reported in reference 11 by moving the moment center further aft using the equation

$$C_m = C_{m_1} + \frac{\Delta x_{cm}}{c_r} C_N, \qquad \frac{\Delta x_{cm}}{c_r} = 0.05 \text{ for SLEE and vortex flaps}$$
$$= 0.165 \text{ for other devices}$$

where C_{m_1} is computed about the original moment reference center (see fig. 2). Defining equations for force, moment, and pressure coefficients used in the analysis are given in the SYMBOLS section.

The effectiveness of the devices under consideration depends crucially on leading-edge flow control, which in turn is best observed

through improvements in the leading-edge thrust characteristics. The method of integration of the measured static pressures around the wing leading edge to obtain the local leading-edge thrust is described with the aid of the following sketch:

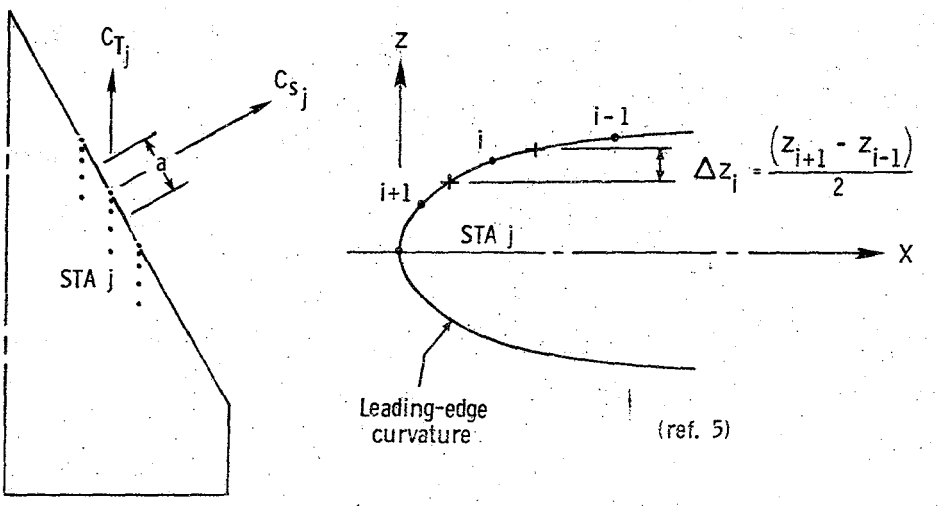

Sketch H

The suction force developed at the jth spanwise pressure station is defined as

$$SF_j = \sum_{i=1}^{m} (p_{ij} - p_\infty) a \, \Delta z_{ij}$$

where i denotes a specific orifice at the jth station and a is the length and Δz_{ij} the height of the vertical i-jth pressure panel. Assuming a constant suction force per unit length of the span (ref. 14),

$$SF_{j_{avg}} = \frac{SF_j}{a}$$

the total suction force contributed by the jth pressure station is

$$SF_{j_{loc}} = (2\ell)\frac{SF_j}{a}$$

where 2ℓ is the total leading-edge length of the wing. Using the definition of the pressure coefficient,

$$C_{p_{ij}} = \frac{p_{ij} - p_\infty}{q_\infty}$$

and nondimensionalizing using the reference force ($q_\infty S_{ref}$) yields the suction force coefficient

$$C_{S_{loc}} = \frac{SF_{j_{loc}}}{q_\infty S_{ref}}$$

$$= (2\ell) \sum_{i=1}^{m} \frac{C_{p_{ij}} \Delta z_{ij}}{S_{ref}}$$

Taking the thrust component of the suction force gives the local leading-edge thrust coefficient

$$C_{T_{loc}} = \sum_{i=1}^{m} \frac{(2\ell)C_{p_{ij}} \Delta z_{ij} \cos \Lambda}{S_{ref}}$$

Averaging the sum of the local thrust contributions and noting that $(2\ell) \cos \Lambda = b$, the total leading-edge thrust coefficient becomes

$$C_{T_{tot}} = \frac{1}{n} \sum_{j=1}^{n} \left(\sum_{i=1}^{m} \frac{bC_{p_{ij}} \Delta z_{ij}}{S_{ref}} \right)$$

PRESENTATION OF DATA

The force, moment, and static pressure graphs used in support of discussion of results are briefly summarized in this section.

Forces in the body axis coordinate system (C_A and C_N) were the main parameters used for the initial performance assessment of each device. Since the investigation was mainly concerned with drag reduction through leading-edge flow control, axial force was particularly well-suited for this purpose since it provides a sensitive and direct indication of leading-edge thrust. For demonstration of longitudinal stability effects, the pitching-moment data were transformed to a reference position different from that prevailing during the tests (see DATA REDUCTION). This new reference center was chosen so as to give approximately neutral stability at low angles of attack for a closer approximation to the condition expected to prevail on an actual aircraft. Lift-to-drag and drag polar (C_D vs C_L) curves, conventionally used for description of the aerodynamic characteristics from a performance point of view, were given secondary importance in the assessment of the devices. An advantage of using the lift-to-drag parameter is elimination of planform area effects in case of devices such as the vortex flaps and sharp leading-edge extension. Since the basic intent of this investigation was alleviation of induced drag penalties, the effect of each device on the induced drag of the wing was reflected in plots of an induced drag parameter, K. Details on the calculation of this parameter are given in the Basic Wing section of RESULTS AND

DISCUSSION. Additional force plots such as C_L, C_D, and C_l as functions of α were also included in support of discussion. It should be noted, however, that the overall force data are representative of the wind-tunnel model rather than of any actual aircraft. Therefore, emphasis should be on the relative rather than the absolute magnitudes of forces and moments and also on the leading-edge static pressure measurements.

Leading-edge pressure data were basically used as an aid in interpretation of trends in the balance data and also in assessing a device's ability to favorably modify the leading-edge flow field. Graphs of leading-edge static pressure $\left(C_{p_{LE}}\right)$ and integrated thrust $\left(C_{T_{loc}}\right)$ as functions of α, at specific spanwise locations, were useful in detection of local leading-edge separation and determination of the leading-edge suction effectiveness of a device throughout the angle-of-attack range. These figures were also used to plot a boundary between separated and attached flow and, thus, follow the inboard progression of leading-edge separation. These same parameters $\left(C_{p_{LE}}\right.$ and $\left.C_{T_{loc}}\right)$ plotted against spanwise position, at specific angles of attack, also depicted the effectiveness of a device along the entire span. Static pressure variations around the leading edge (at the six chordwise rows of pressure orifices) provided added insight into the specific flow patterns existing at the leading edge and also reflected the relative thrust and normal force contributions from various positions on the leading-edge curvature. For comparison, basic wing (devices off) data appear as a dashed line on selected balance and pressure data plots.

RESULTS AND DISCUSSION

60-Deg Delta Wing

The basic 60-deg delta wing (devices off) served as the baseline configuration throughout the investigation for comparison and performance assessment of the various leading-edge devices. Force and moment data obtained for this basic wing configuration are presented graphically in figure 9. The negative normal force and positive pitching moment at $\alpha = 0^{o}$ are attributed to the negative camber effect of an asymmetrically bevelled wing trailing-edge region (see fig. 2), which simulated an up-deflected trailing-edge flap.

Below $\alpha \simeq 8^{o}$, the delta wing is under the influence of fully attached flow with 100 percent leading-edge suction, as evidenced by the close agreement of the axial and normal force curves (corrected for zero-lift forces) with potential flow theory (vortex lattice method with suction analogy code (VLM-SA); ref. 15) in figure 9. At approximately $\alpha = 9^{o}$, referred to as the departure angle of attack (α_D), flow separation occurs at the streamwise tip, and the subsequent vortex formation spreads toward the wing apex with increasing α. The low pressure produced locally on the wing upper surface by the high rotational velocities within the vortex generates additional lift, which can be noted in the departure of the C_N curve from the initially linear theoretical 100 percent suction curve. However, there is an accompanying reduction in leading-edge suction. The deviation of the C_A curve from the parabolic theoretical potential flow curve at approximately 9^{o} is

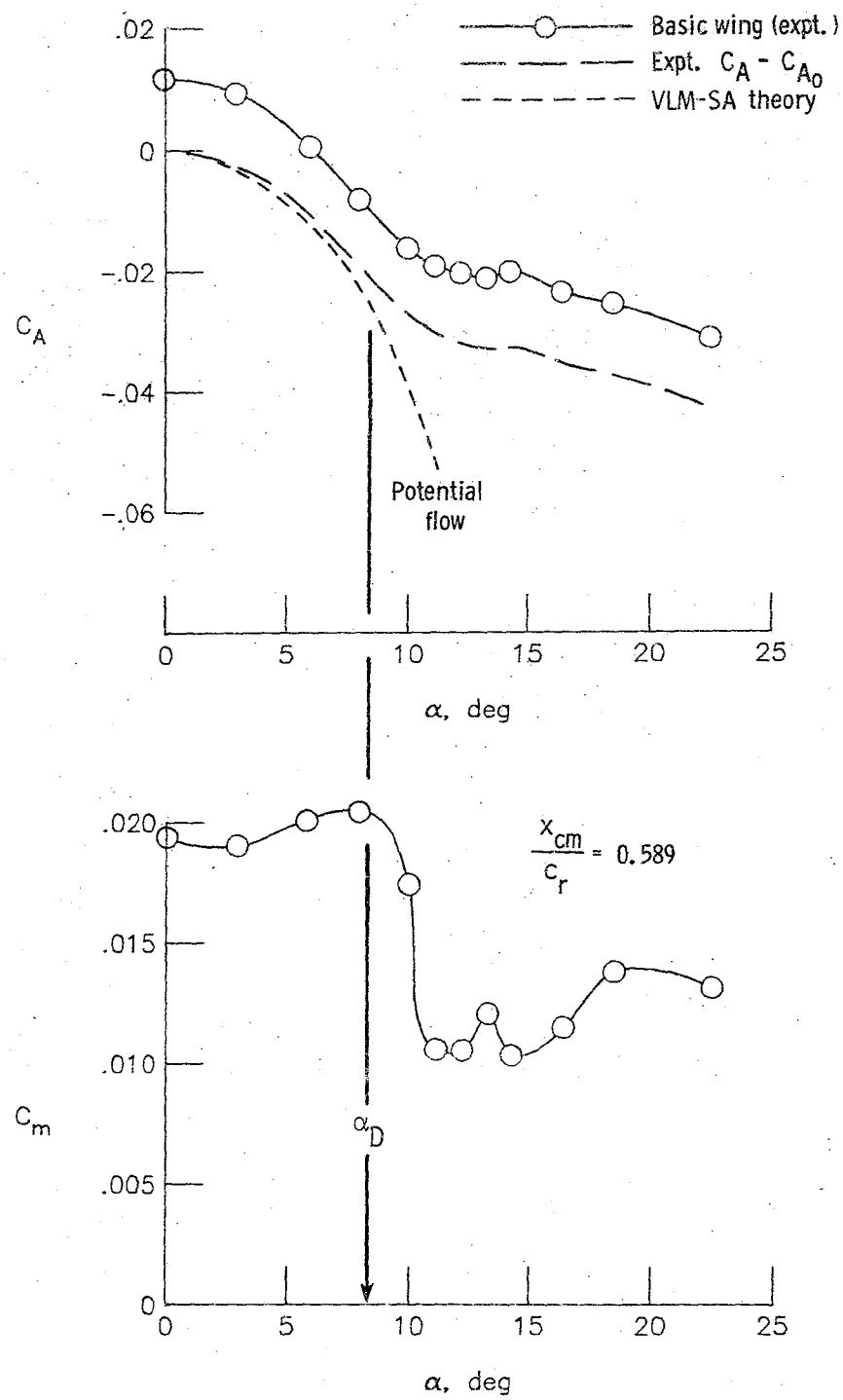

Figure 9.- Basic wing force and moment characteristics.

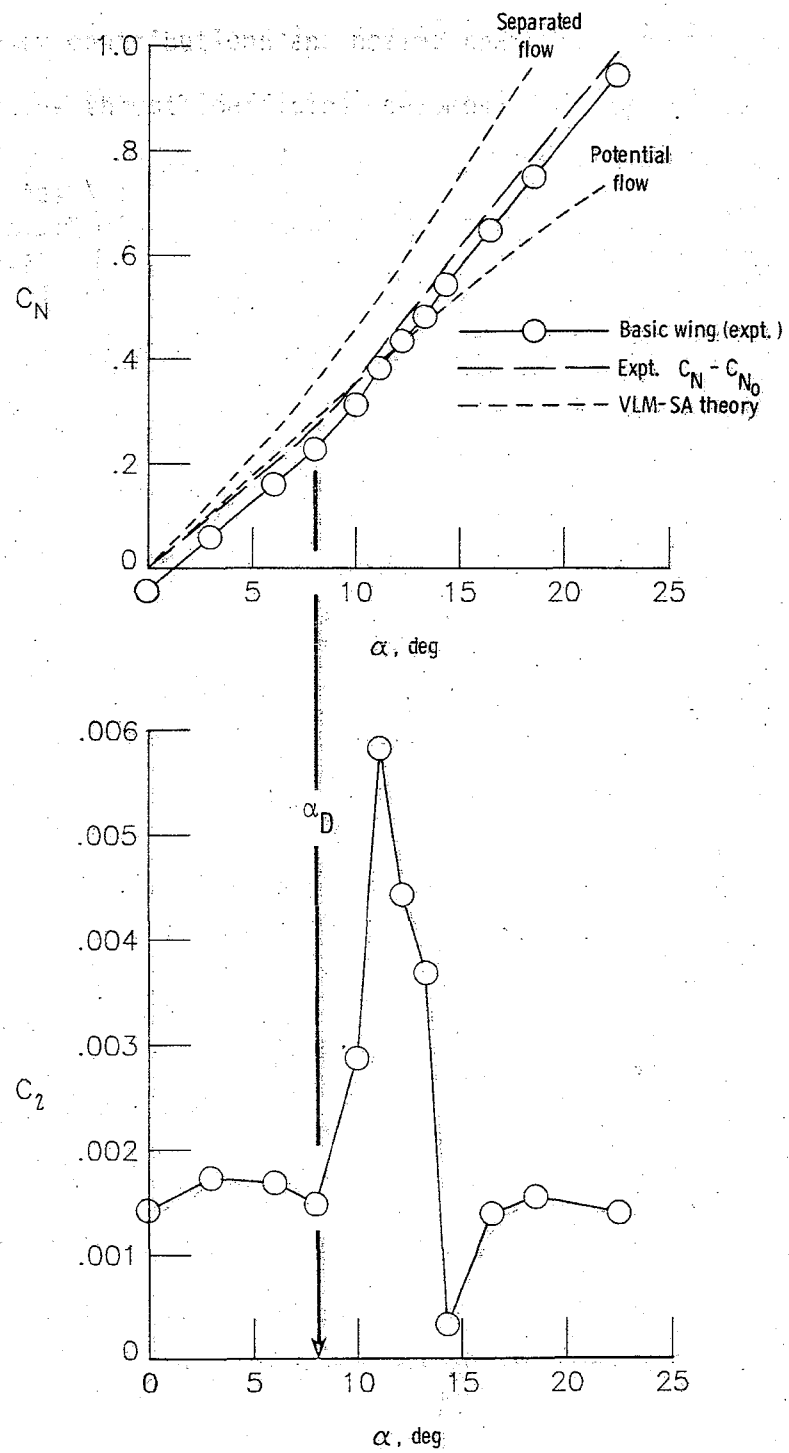

Figure 9.- Concluded.

characteristic of this gradual loss of leading-edge suction. This trade-off between leading-edge suction and vortex-induced normal force is the basis for the Polhamus suction analogy theory (ref. 15) used in this paper for comparison with experimental data. In addition, the aft position of the primary vortex at $\alpha = 9^{o}$ locates the center of vortex lift aft of the wing moment reference center (approximately at the cg), resulting in a strong pitch-down, as reflected by the sharp downturn of the C_m curve (fig. 9). Although not presented here, it is important to note that the maximum lift-to-drag ratio for the basic wing is attained at approximately $\alpha = 8^{o}$. This implies that the additional vortex lift is insufficient to compensate for the loss of leading-edge thrust (drag increase) following the onset of separation.

The inboard spread of leading-edge separation is shown in figure 10 to occur very rapidly with increasing α. Plots of leading-edge pressure as a function of angle of attack at selected spanwise positions indicate a buildup of leading-edge suction (negative C_p) with increasing α up to the local onset of separation, followed by a sharp collapse of suction at all but the inboard-most station. Plots of this type lead to the angle for local onset of separation as a function of spanwise position, shown in the same figure. The locus of data points, which is effectively a boundary between separated and attached flow, indicates a movement of leading-edge separation from approximately the 90 to the 30 percent semispan position within only 3^{o} α increment (viz., 11^{o} to 14^{o}). The corresponding pressure distributions around the leading edge are presented in figure 11. At $\alpha = 10^{o}$, attached flow,

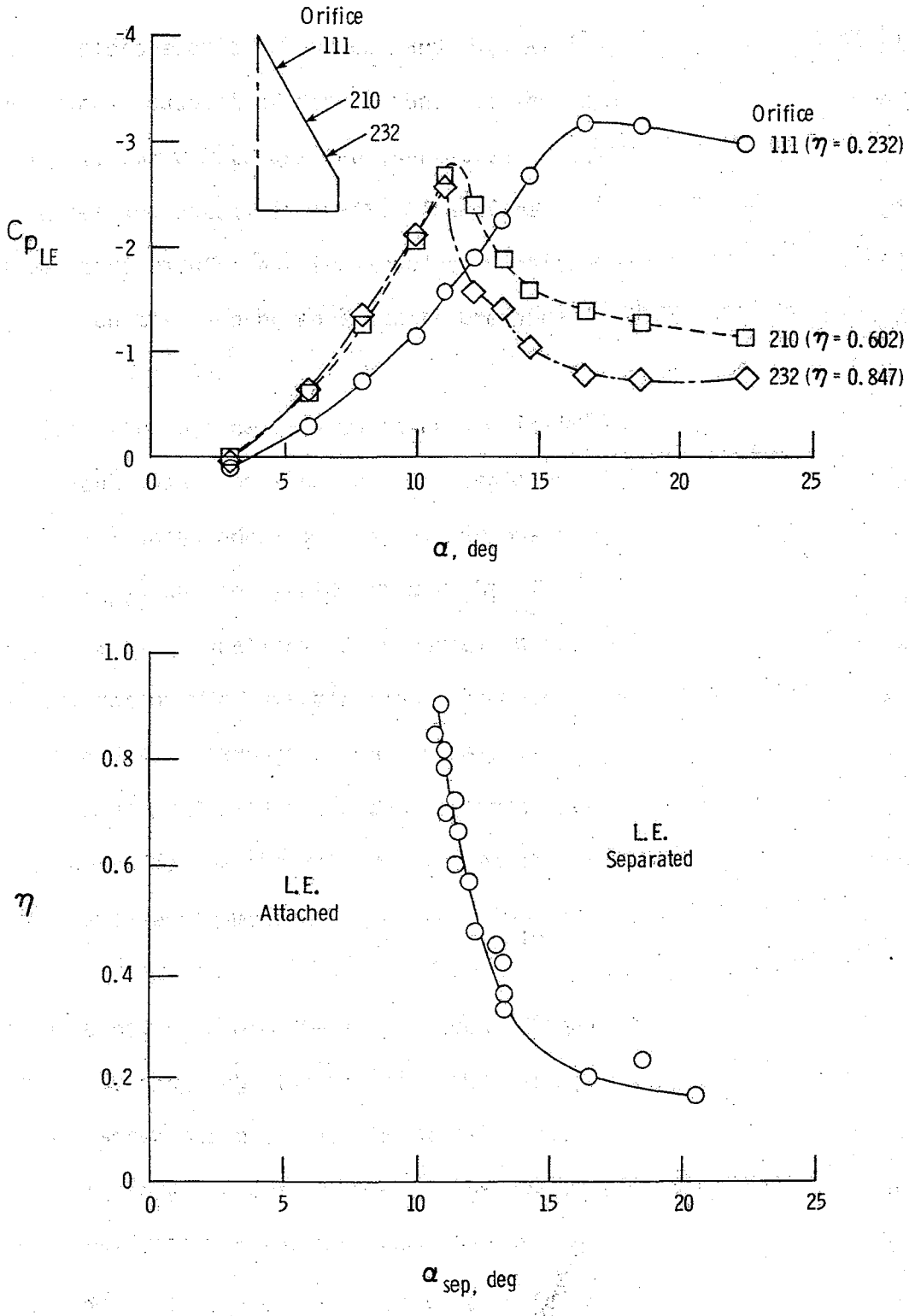

Figure 10.- Basic wing leading-edge static pressure variations and $C_{p_{LE}}$ derived separation boundary.

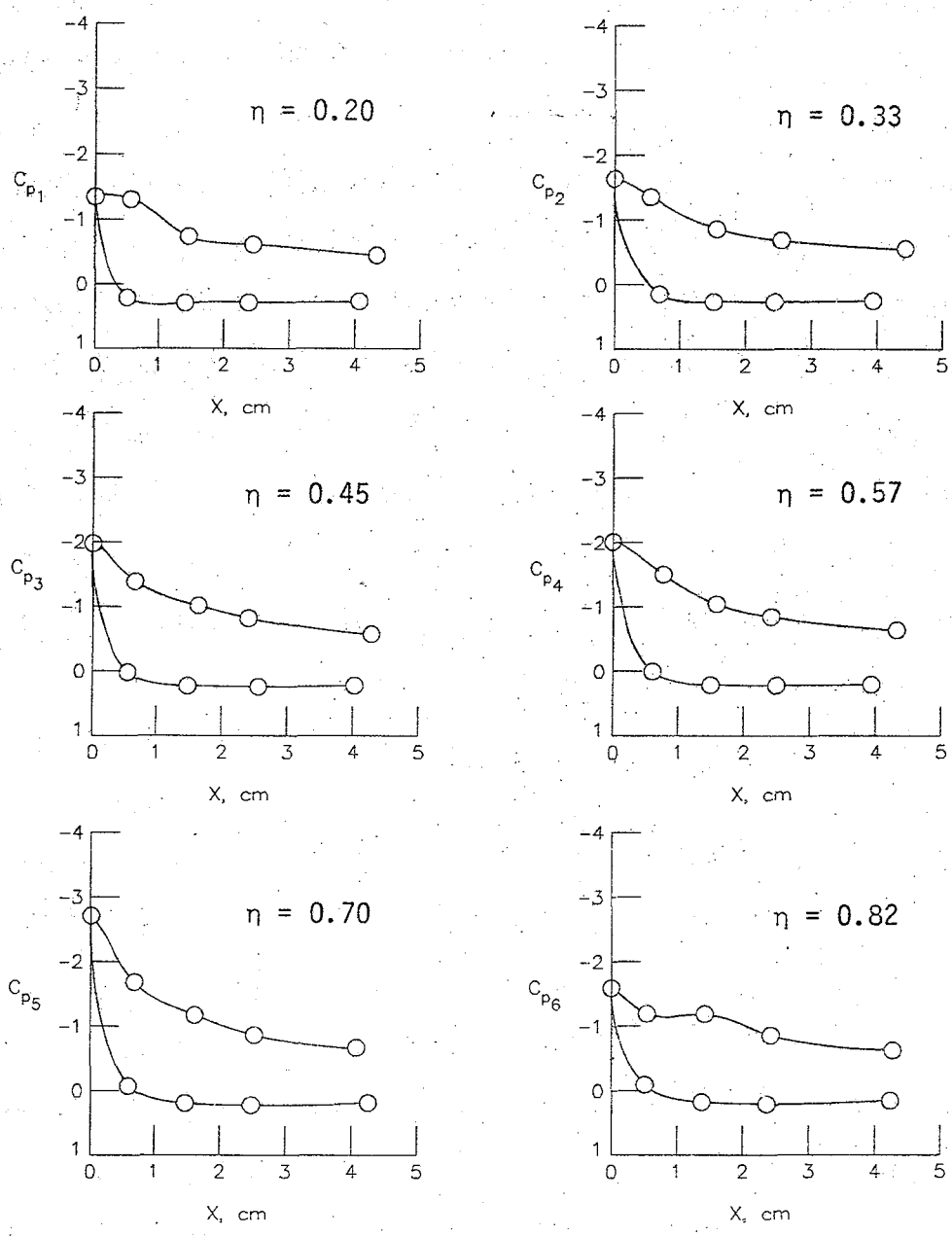

(a) $\alpha = 10^{o}$.

Figure 11.- Static pressure distributions around the basic wing leading edge.

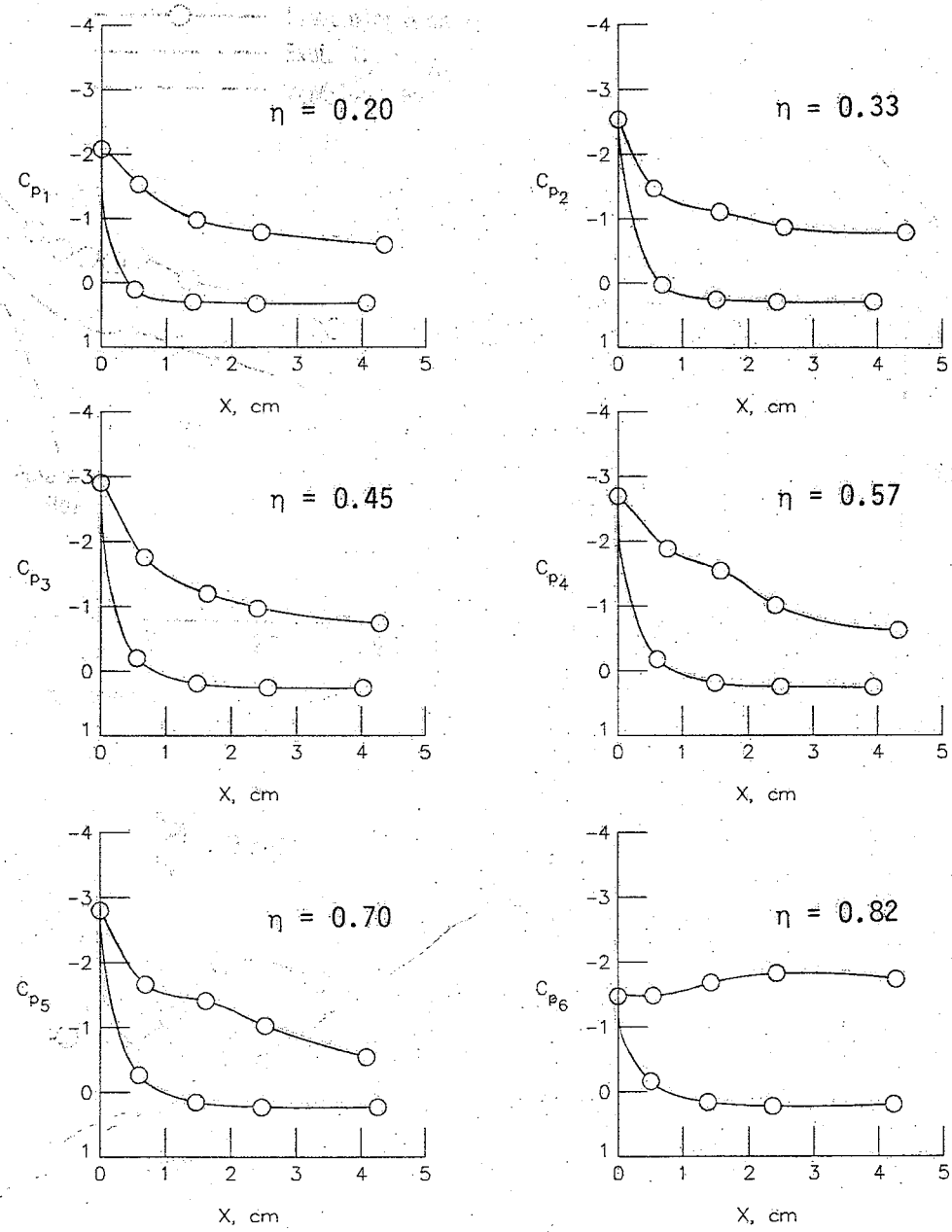

(b) $\alpha = 12^{o}$.

Figure 11.- Continued.

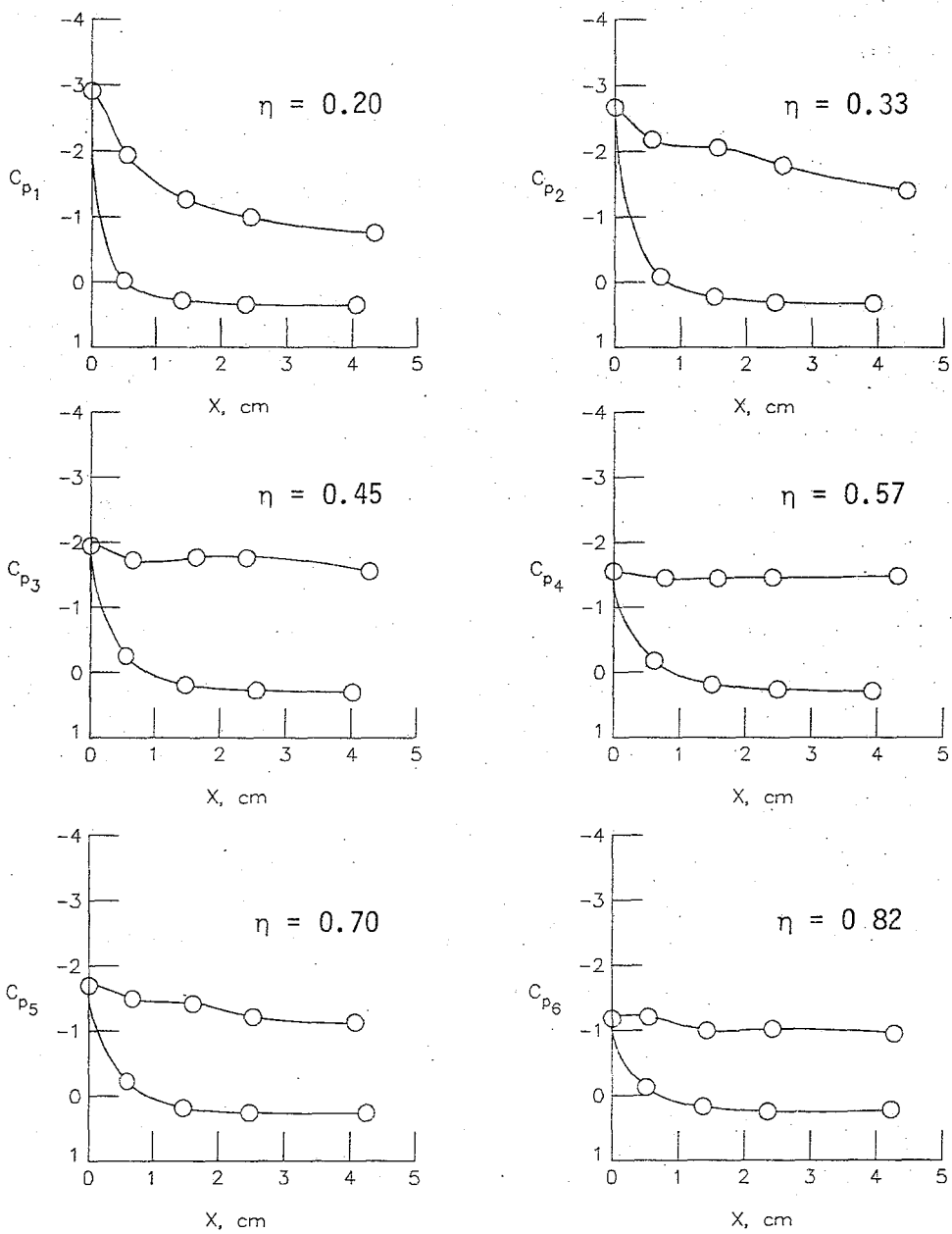

(c) $\alpha = 14^{o}$.

Figure 11.- Concluded.

characterized by a local suction peak near the leading edge, due to flow acceleration, and subsequent pressure recovery on the upper surface, persists at each spanwise station considered. Flow visualization indicates separation has begun near the tip but apparently has not traversed far enough to be detected. At $\alpha = 12^{0}$, local separation is indicated at $\eta = 0.82$ (STA 6) by the constant pressure, stagnated flow region on the upper surface. The leading-edge flow remains attached inboard. An increase in α to 14^{0} shows the rapid inboard movement of separation, as its apex now appears to lie between $\eta = 0.33$ (STA 2) and $\eta = 0.45$ (STA 3).

The rapid inboard spread of leading-edge separation induces an erratic wing rolling moment behavior between 9^{0} and 15^{0} α, as shown in figure 9. This so-called "wing rock," characteristic of all highly swept wings, results from asymmetrical spanwise movement of separation along the two leading edges. In addition, the forward movement of the primary vortex leads to pitch-up at approximately 11^{0} α, as the center of vortex lift moves ahead of the wing moment reference center.

The axial force reversal at $\alpha \simeq 11^{0}$ is best explained through inspection of spanwise leading-edge thrust distributions in figure 12. At low angles of attack, axial force improvement with increasing α is attributed to local thrust gains all along the span. Increasing thrust values toward the tip are due to increasing upwash outboard, resulting in higher local effective angles of attack and, consequently, greater flow accelerations and suction forces around the leading edge. In the mid-α range (11^{0}-14^{0}), however, a balance between thrust loss at the

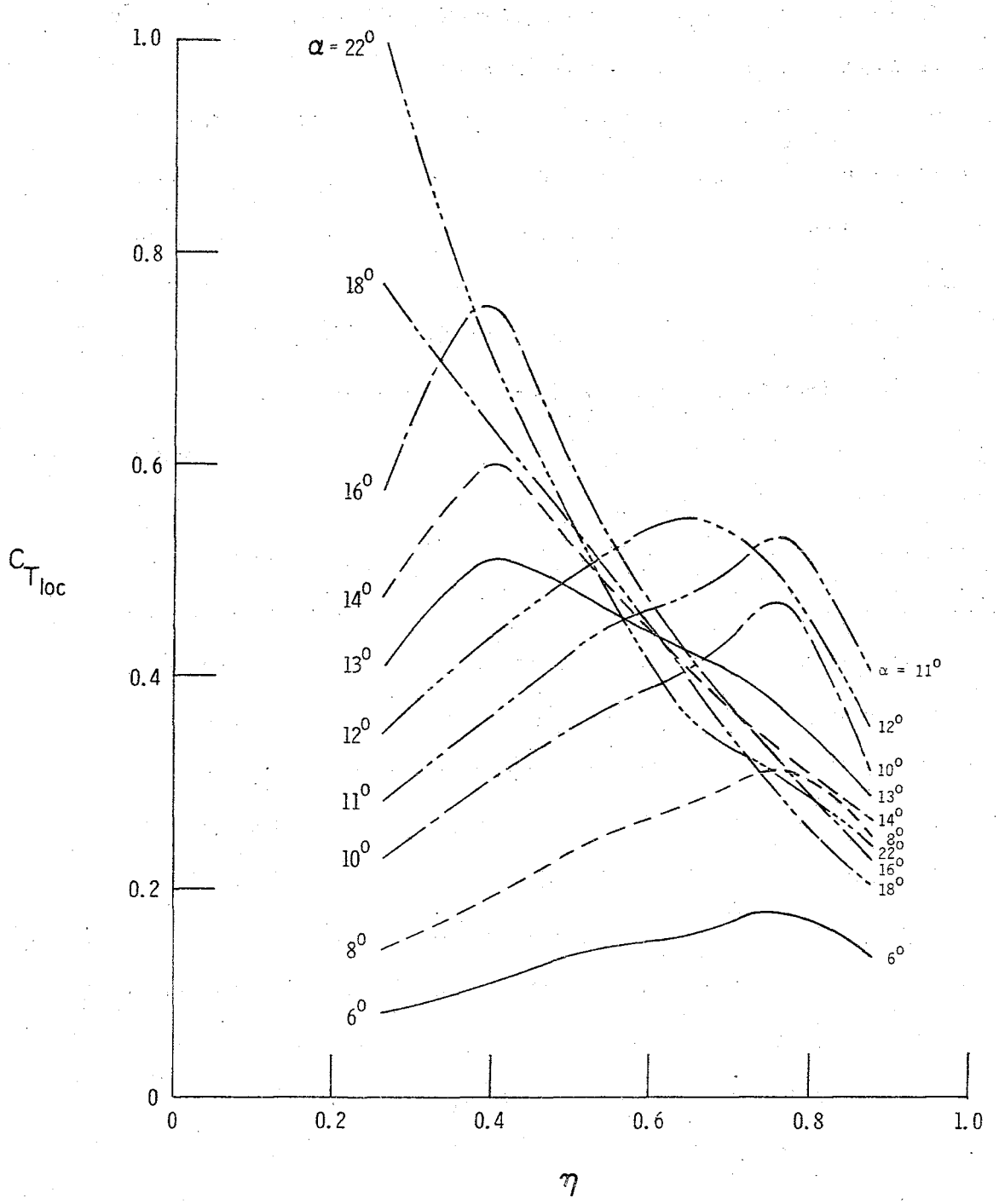

Figure 12.- Basic wing spanwise leading-edge thrust distributions. Symbols omitted for clarity.

outboard stations, due to local leading-edge separation, and continued thrust gains inboard account for the relative insensitivity of the C_A curve to angle of attack. Above $\alpha = 14^o$, additional thrust gains inboard with relatively minor further losses outboard account for the C_A recovery. These same leading-edge thrust data are plotted versus angle of attack in figure 13. Here, local thrust is compared with balance axial force measurements corrected for profile drag $\left(C_A - C_{A_o}\right)$, which should represent strictly leading-edge effects and, thus, an approximate average leading-edge thrust. The close agreement between the local thrust and balance data prior to separation adds credibility to the pressure integrations. Again, as in figure 12, the axial force recovery at high α is shown to result from continued thrust gains at the inboard stations as the outboard stations settle at a constant value below the balance-derived average. Note that in the mid-α range (10^o to 13^o), the balance data consistently fall below the integrated thrust values. The balance is, thus, sensing a source of drag other than that accountable from loss of suction, possibly from trailing-edge separation or interference from the housings.

At high angles of attack, the rate of inboard spread of separation diminishes, as reflected by the leveling off of the separation boundary in figure 10. Continued axial force improvement is observed up to the highest angles tested. Previous research has shown that further increases in angle of attack would eventually lead to vortex burst, spreading rapidly toward the wing apex with an accompanying loss of leading-edge suction and pitch-up.

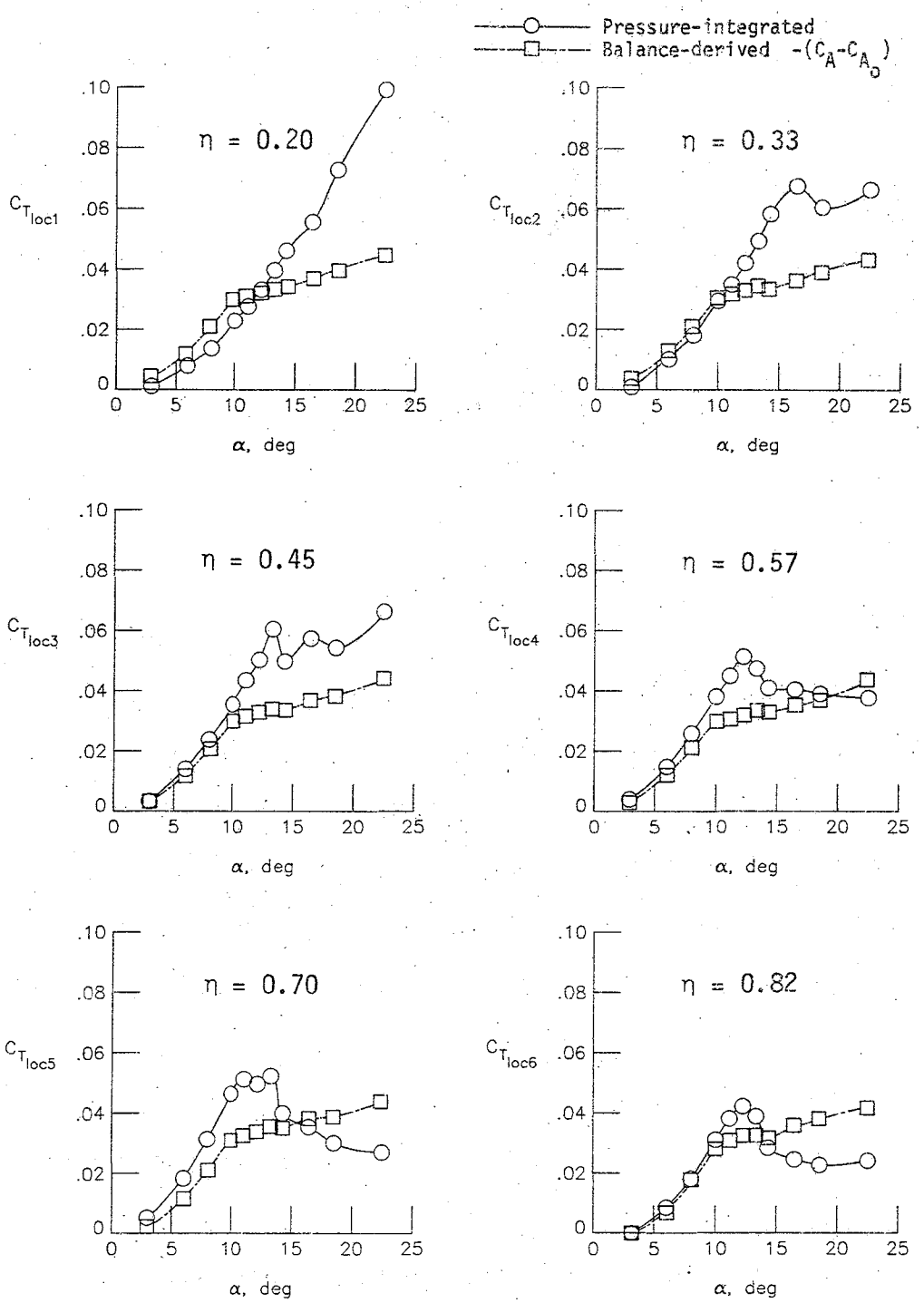

Figure 13.- Basic wing leading-edge thrust characteristics.

It was previously stated that severe induced drag penalties are characteristic of delta wings at high lift. In order to see the effect of leading-edge separation on the total induced drag of the wing, a plot of the induced drag factor K, where

$$K = \frac{C_D - C_{D_{min}}}{C_L^2}(\pi AR) = \frac{1}{e}$$

is presented in figure 14. This formula is derived from the equation for minimum induced drag,

$$C_D = C_{D_{min}} + \frac{C_L^2 K}{\pi AR}$$

where $K = 1$ corresponds to fully attached flow and $K > 1$ to partial leading-edge separation. Very low angles of attack were ignored since low lift and drag coefficients result in sporadic K values. Figure 14 depicts attached flow at low α, followed by a rapid increase in induced drag as leading-edge separation spreads inboard with its accompanying loss of leading-edge suction. The reduction in the rate of spread of leading-edge separation near the wing apex results in a reduction in slope of the induced drag curve at approximately $\alpha = 14^{o}$. In the case of an actual aircraft, induced drag would continue to increase at approximately the mid-α rate since decreasing leading-edge radius toward the tip cannot retain the degree of residual suction of the uniform radius leading edge of the present research model.

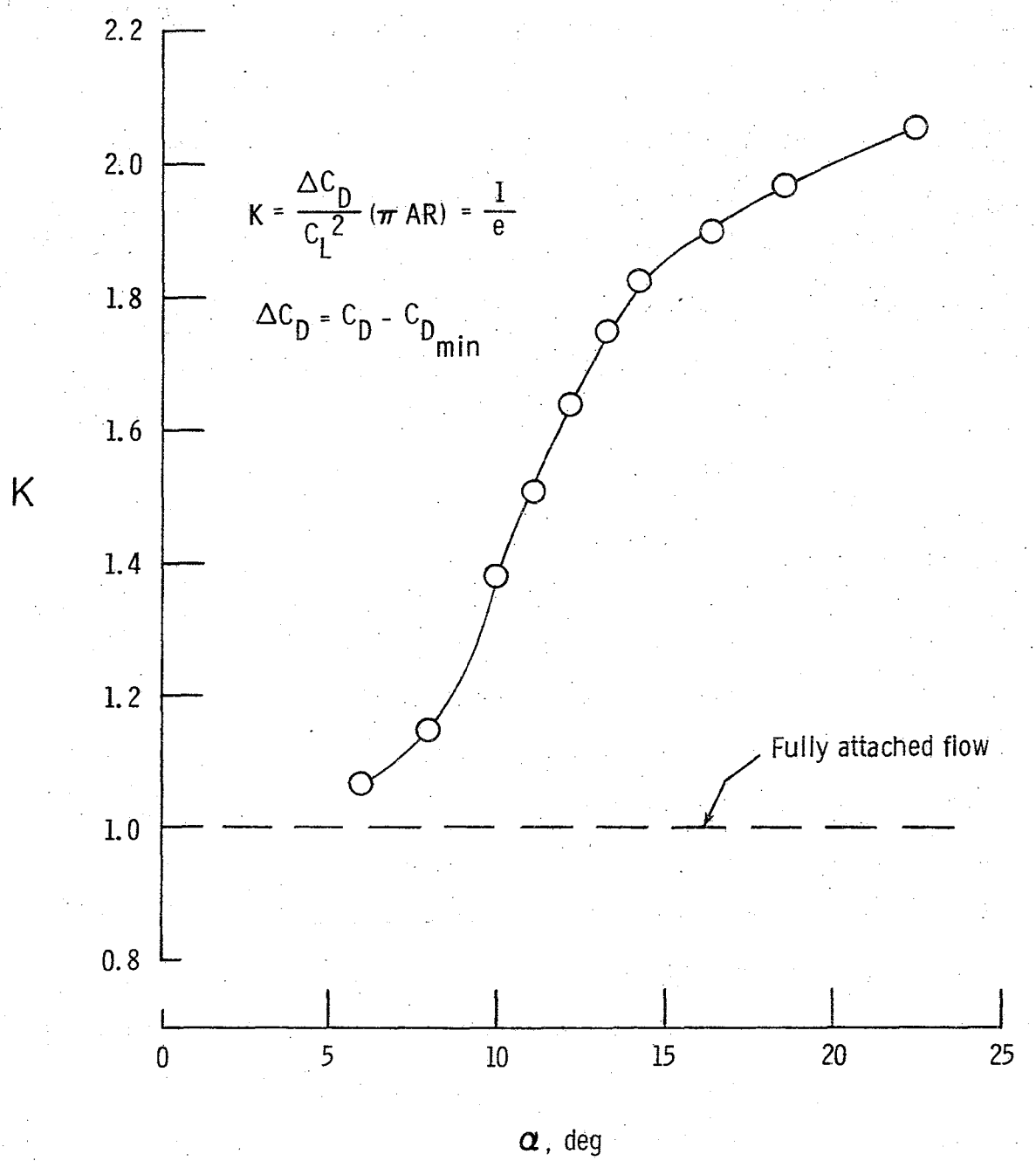

Figure 14.- Basic wing induced drag characteristics.

A comparison of test data with theory is presented in figure 15 in the form of a drag polar corrected for zero-lift drag $\left(C_{D_i} = C_D - C_{D_o}\right)$. Experimental values are compared with theory for zero and full (100 percent) leading-edge suction. At low angles of attack, where fully attached flow prevails, 100 percent leading-edge suction is realized. At approximately $\alpha = 9^o$ $(C_L \simeq 0.25)$, deviation of the experimental values from the theoretical 100 percent suction curve signifies the onset of leading-edge separation. The loss of suction continues with increasing lift and eventually settles along a constant percent suction curve, indicating residual leading-edge suction characteristic of blunt leading edges.

The major contribution to the integrated local leading-edge thrust is developed by those orifices near the wing leading edge (see DATA REDUCTION). This suggests the possibility that a single leading-edge pressure orifice might suffice for a chordwise series of orifices around the leading edge for leading-edge thrust determination on wind-tunnel models. If so, it would result in significant savings in model construction costs and wind-tunnel test time. Figure 16 presents staggered plots of $C_{p_{LE}}$ versus $C_{T_{loc}}$ at the six spanwise pressure stations of the research model. The linearity of the curves is interpreted as attached flow and the departure from linearity as the local onset of separation. This indicates that $C_{T_{loc}}$ can be calculated from $C_{p_{LE}}$ only in the attached flow regime. No systematic relationship between $C_{p_{LE}}$ and $C_{T_{loc}}$ is apparent following the onset of local separation

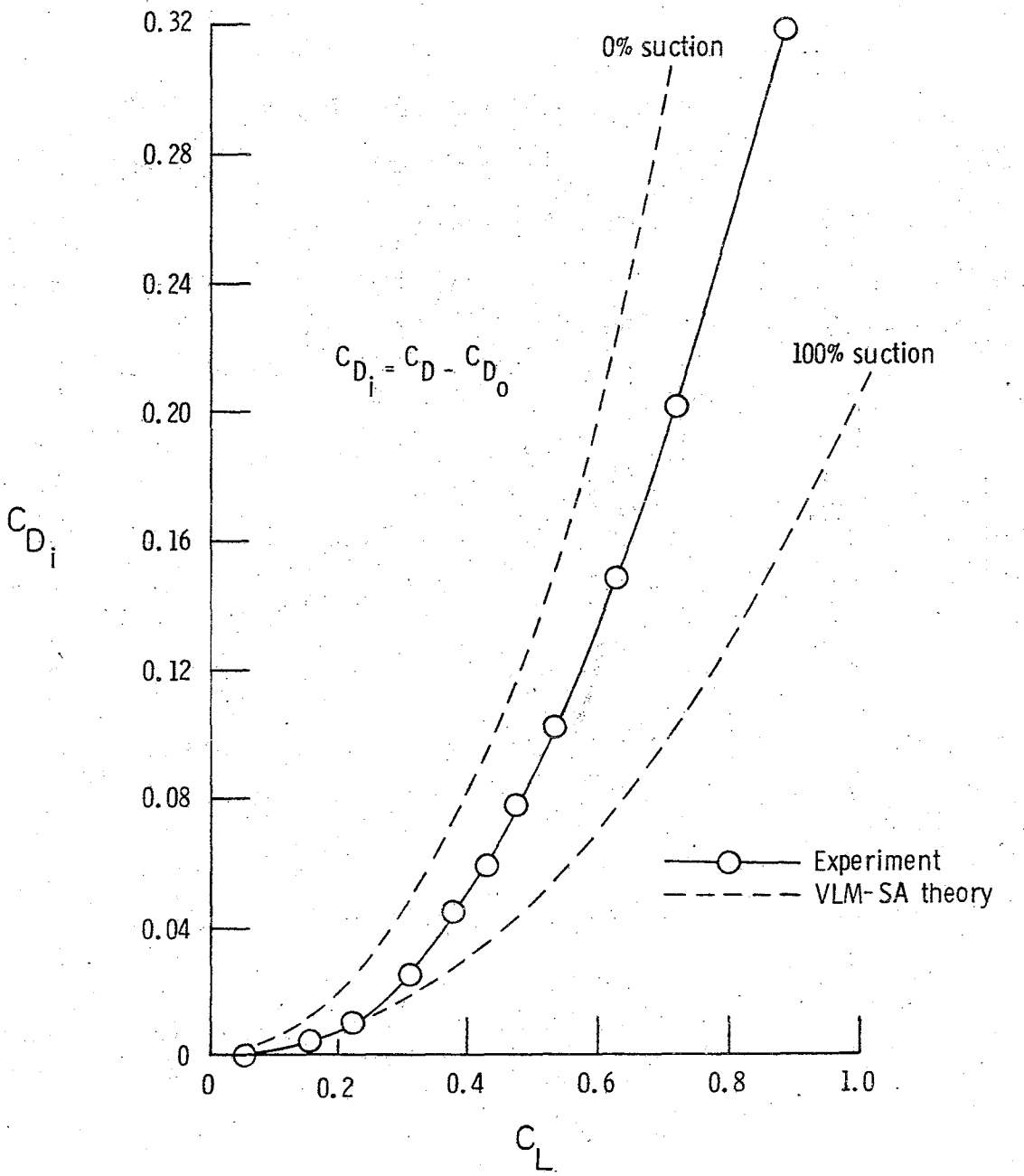

Figure 15.- Comparison of basic wing experimental data with VLM-SA theory.

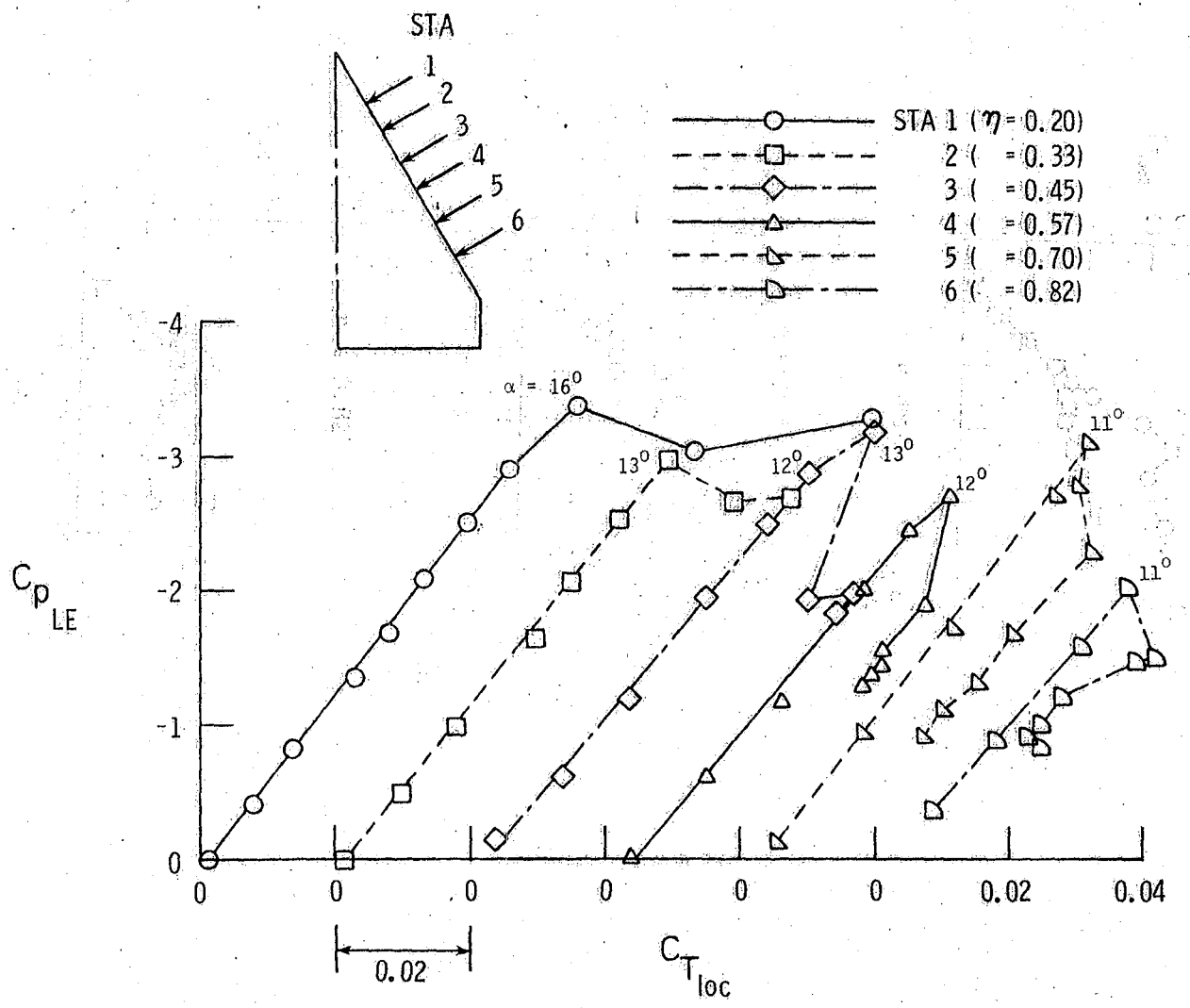

Figure 16.- Basic wing leading-edge static pressure-thrust relationship.

due to the significantly altered C_p distribution around the leading edge. Further discussion on this type of plotting will be presented in conjunction with each leading-edge device.

Chordwise Slots

Single and multiple chordwise slots cut into swept leading edges produce performance improvements as reported in reference 5. For reference purposes, basic configurations of one and three chordwise slots per leading edge were retested in the present investigation.

The results with a single slot were used to illustrate the effects of the device on the wing leading-edge flow pattern and overall performance. To investigate the possibility of further performance improvements, the slot was modified with an internal contour (SC-1), which will be discussed later. Figure 17 presents results of force and moment measurements on a configuration utilizing a single slot at $\eta = 0.625$. The C_A curve shows the expected low-α drag penalty discussed previously (BACKGROUND section). However, the slot acts to delay the onset of separation and vortex lift, as indicated by the slight loss of normal force in the mid-α range. The result is enhanced leading-edge suction and, thus, C_A improvement beyond 11° α. However, a sudden loss of slot effectiveness at high α is indicated by the convergence of the slot and basic wing curves, beginning at approximately $\alpha = 17^\circ$. Longitudinal stability effects of a single slot (C_m curve in fig. 17) can be noted as a slight moderation of the initial pitch-down, as well as a delay of pitch-up to approximately 12° α. From a performance standpoint, a penalty in maximum L/D value occurs, but a substantial improvement is obtained at mid α as a result of the drag reduction.

Static pressure distributions around the leading edge at adjacent stations on either side of the slot, in figure 18 ($\alpha = 16^\circ$), illustrate

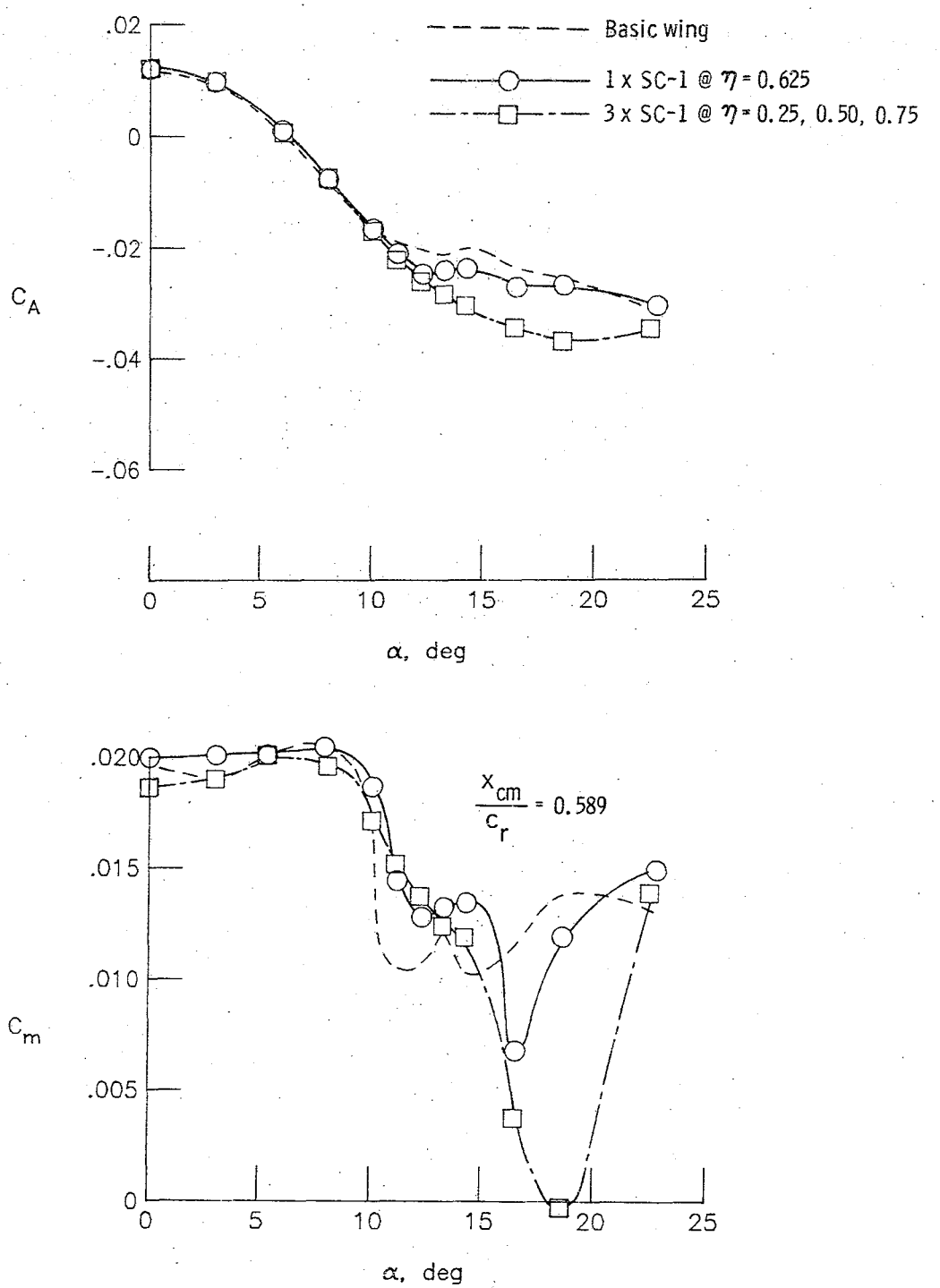

Figure 17.- Force and moment characteristics of single and multiple chordwise slot configurations.

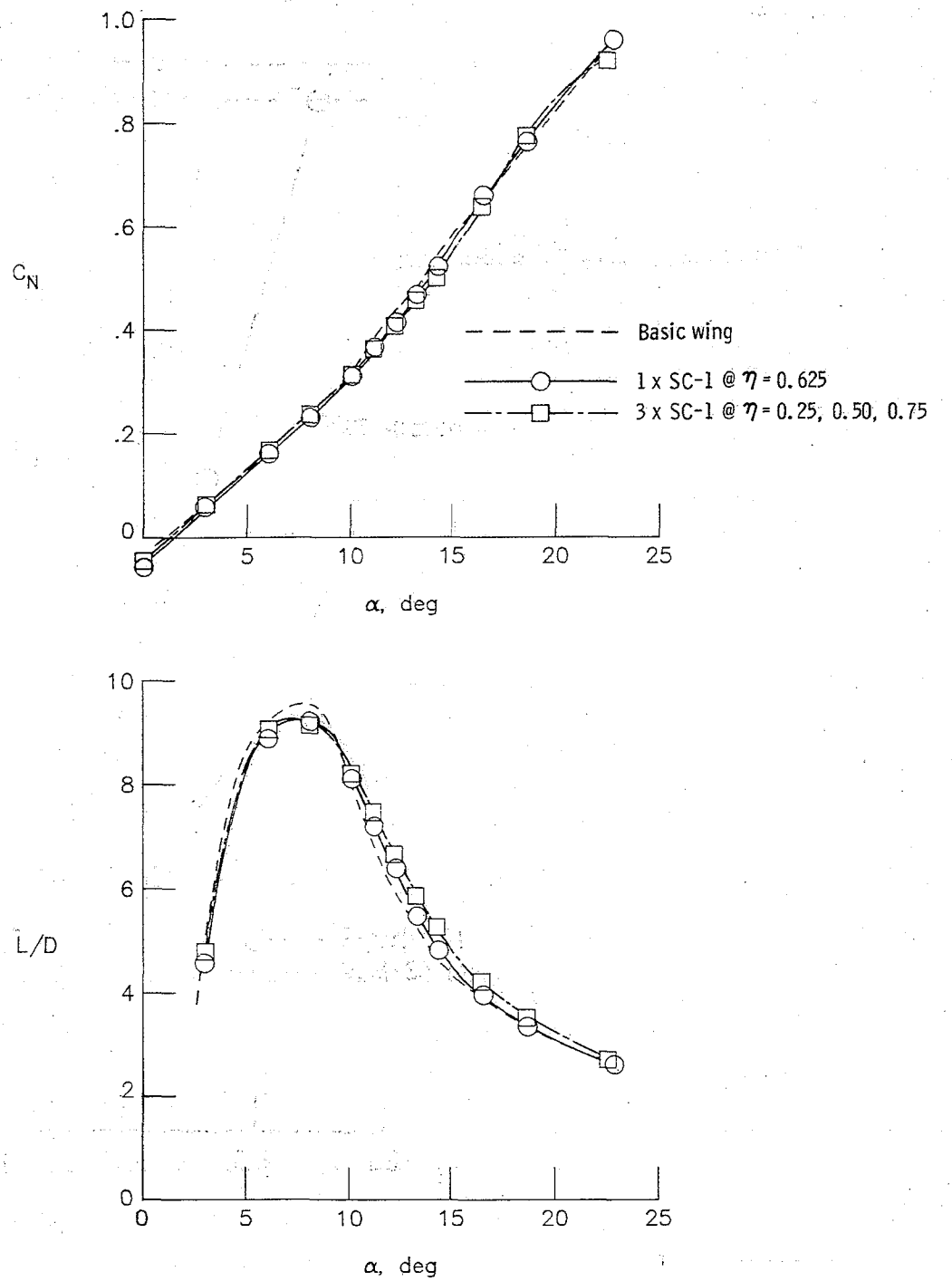

Figure 17.- Concluded.

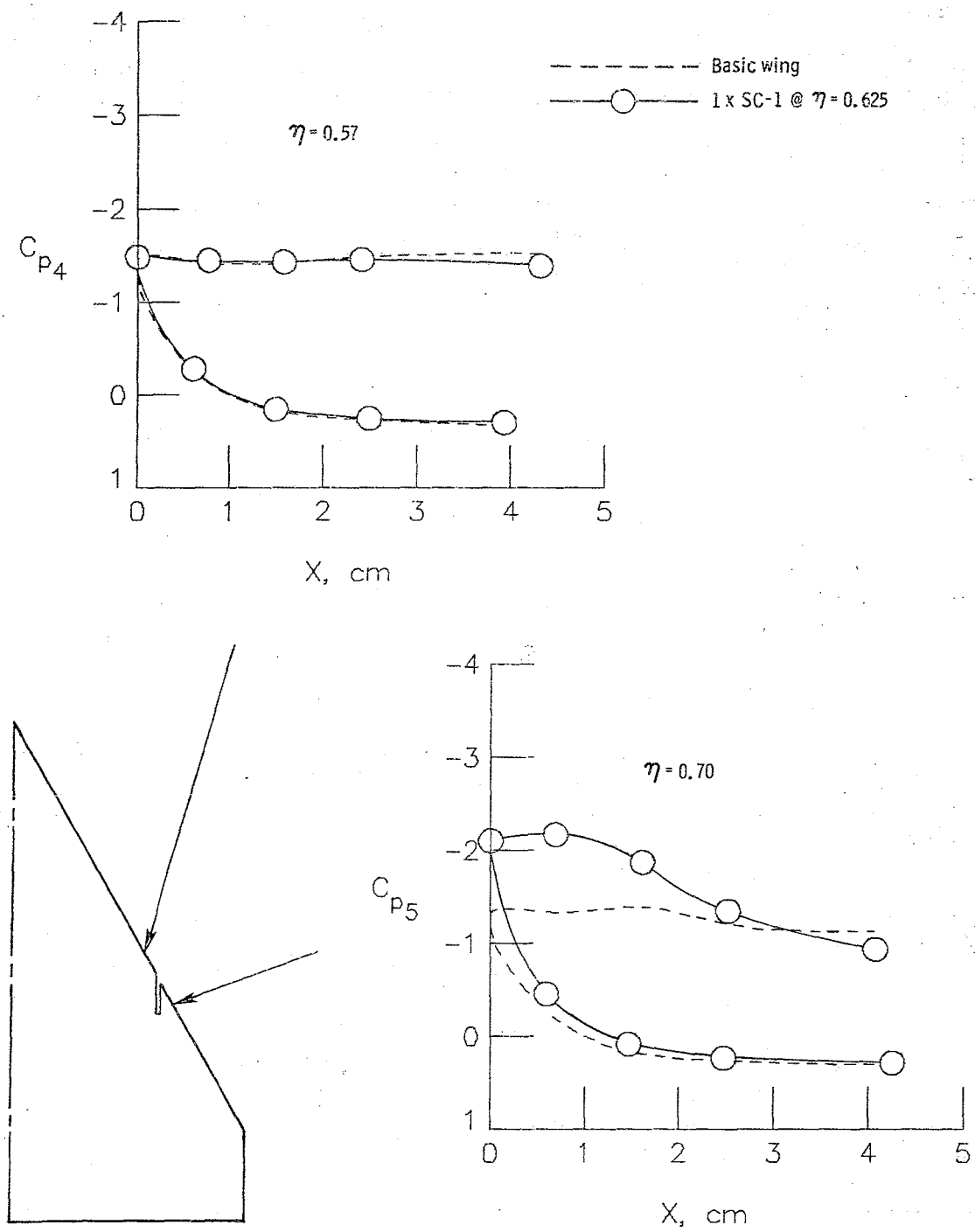

Figure 18.- Local static pressure effects of the chordwise slot at $\alpha = 16^{0}$.

the effects in the vicinity of the device. While little influence is detected inboard, the slot compartmentation effect (see BACKGROUND section) acts to retain attached flow at the leading edge on the outboard side, where the basic wing is stalled. The resulting effects on leading-edge suction are depicted in figure 19, where sizable increases in negative leading-edge pressure (leading-edge suction) are indicated on the outboard side beyond 13^{o} α. The spanwise variation of $C_{p_{LE}}$ at $\alpha = 16^{o}$, in figure 20, reflects these basic trends on either side of the slot.

While the local leading-edge flow field seems to have been favorably modified by the slot, an overall performance improvement depends on the device's ability to increase the total leading-edge thrust. Figure 21 presents local thrust variations with angle of attack. The local onset of separation at the two pressure stations outboard of the single slot (STA's 5 and 6) has been delayed by approximately 1^{o} α, resulting in large thrust improvements beyond $\alpha \simeq 11^{o}$. The loss of axial force at high α, discussed previously, is shown to start at the outboard stations as the local thrust and basic wing data converge. This is believed to result from a breakdown of attached flow on the upper wing surface, which begins at the tip in view of the higher prevailing upwash. The compartmentation effect of the slot is, thus, lost and the primary vortex allowed to spread inboard. The inboard effect of the slot results in a minor penalty in local thrust between 14^{o} and 20^{o} α. However, this unfavorable effect is highly localized, as

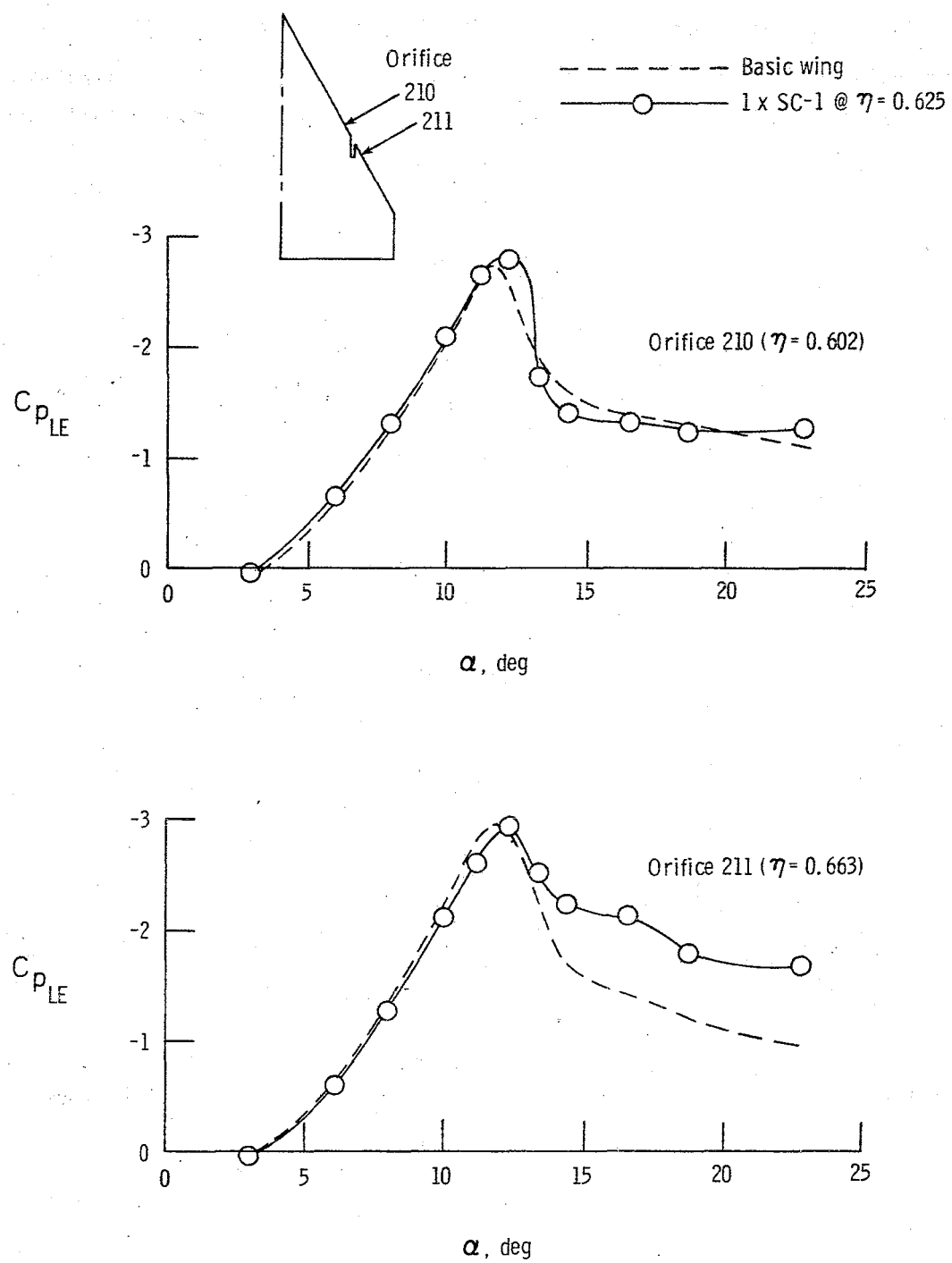

Figure 19.- Local suction effects of the chordwise slot.

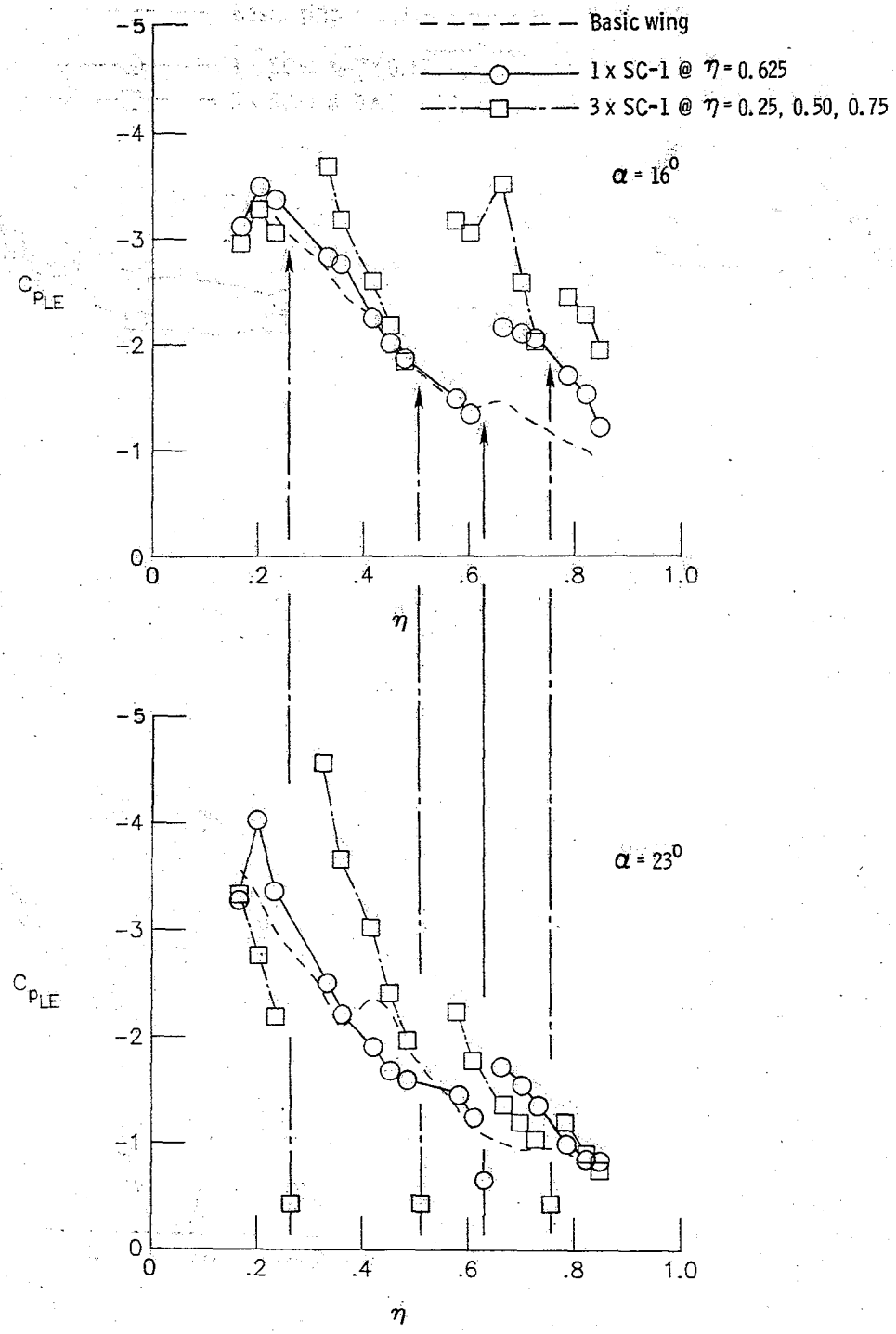

Figure 20.- Spanwise leading-edge static pressure distributions for single and multiple chordwise slot configurations.

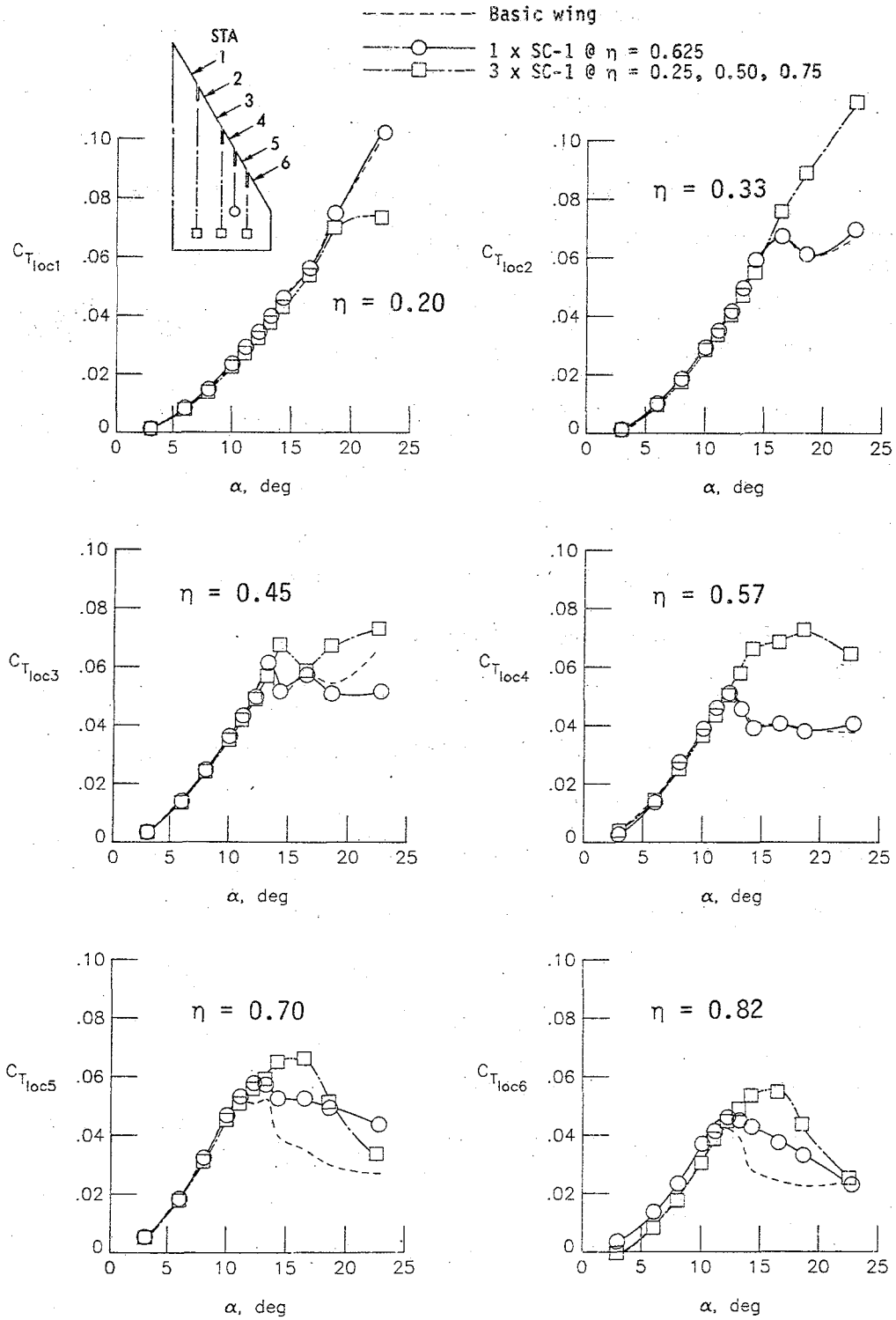

Figure 21.- Effects of single and multiple chordwise slots on leading-edge thrust.

stations inboard of $\eta = 0.57$ remain unaffected. The favorable outboard effect is more widespread.

A multiple slot configuration was tested in an attempt to spread the slot benefit over a larger portion of the span and to delay, or eliminate, the loss of effectiveness at high α. The slots were located at the 25, 50, and 75 percent semispan positions and were again internally contoured with SC-1. The result was further delays in local onset of separation and significantly higher local thrust values in the mid- and high-α range at all but the most inboard pressure station (fig. 21). Apparently, the favorable influence of the "upstream" slot acts to nullify the adverse inboard effect of a single slot, resulting in thrust enhancement along a large portion of the span. The lack of a slot inboard of STA 1 leads to early separation and loss of thrust near the apex. Comparison of spanwise leading-edge pressure variations at $\alpha = 16^{0}$, in figure 20, also reflects suction improvements outboard of $\eta = 0.25$ with multiple slots. Based on these results, it is believed that several slots located along the leading edge have the ability to redirect the spanwise boundary layer flow in the chordwise direction before it builds up in magnitude. Again, however, loss of effectiveness begins near the tip, as the corresponding $C_{P_{LE}}$ data at $\alpha = 22^{0}$ (fig. 20) converge to the basic wing curve. For a ready assessment of the leading-edge effects of multiple slots, the following table presents a comparison of total leading-edge thrust values for single and multiple slot configurations:

	$\alpha = 14^{o}$		$\alpha = 18^{o}$		$\alpha = 22^{o}$	
	$C_{T_{tot}}$	Percent over BW	$C_{T_{tot}}$	Percent over BW	$C_{T_{tot}}$	Percent over BW
Basic Wing (BW)	0.0439	-	0.0466	-	0.0534	-
1 x SC-1	.0486	10.7	.0512	9.9	.0555	3.9
3 x SC-1	.0584	33.0	.0656	40.8	.0645	20.8

These data indicate that high-α thrust improvements of over 40 percent (relative to the basic wing) are obtained with a triple slot configuration.

Figure 17 compares force data for single and multiple chordwise slot configurations. The C_A curve indicates that multiple slots provide a substantial drag advantage beyond 12^{o} α with a more gradual C_A reversal which is delayed from 12^{o} to 19^{o} α. Multiple slots also produce a smoother C_m curve, delaying pitch-up to 19^{o} α. The additional loss of lift beyond 12^{o} α with the use of multiple slots is attributed to the retention of attached flow (and, therefore, loss of vortex-induced lift) over a greater portion of the leading edge. Maximum lift-to-drag is unchanged from the single slot case, but additional improvements are indicated beyond 10^{o} α before the final convergence to the basic wing data at higher α.

The ability of chordwise slots to delay the local onset of separation is reflected by the extension of the linear portions of the $C_{p_{LE}}$ versus $C_{T_{loc}}$ curves in figure 22. Delays of up to 2^{o} α are indicated just outboard of each slot in the triple slot configuration. The extension of the curves along their initial slope suggests that attached

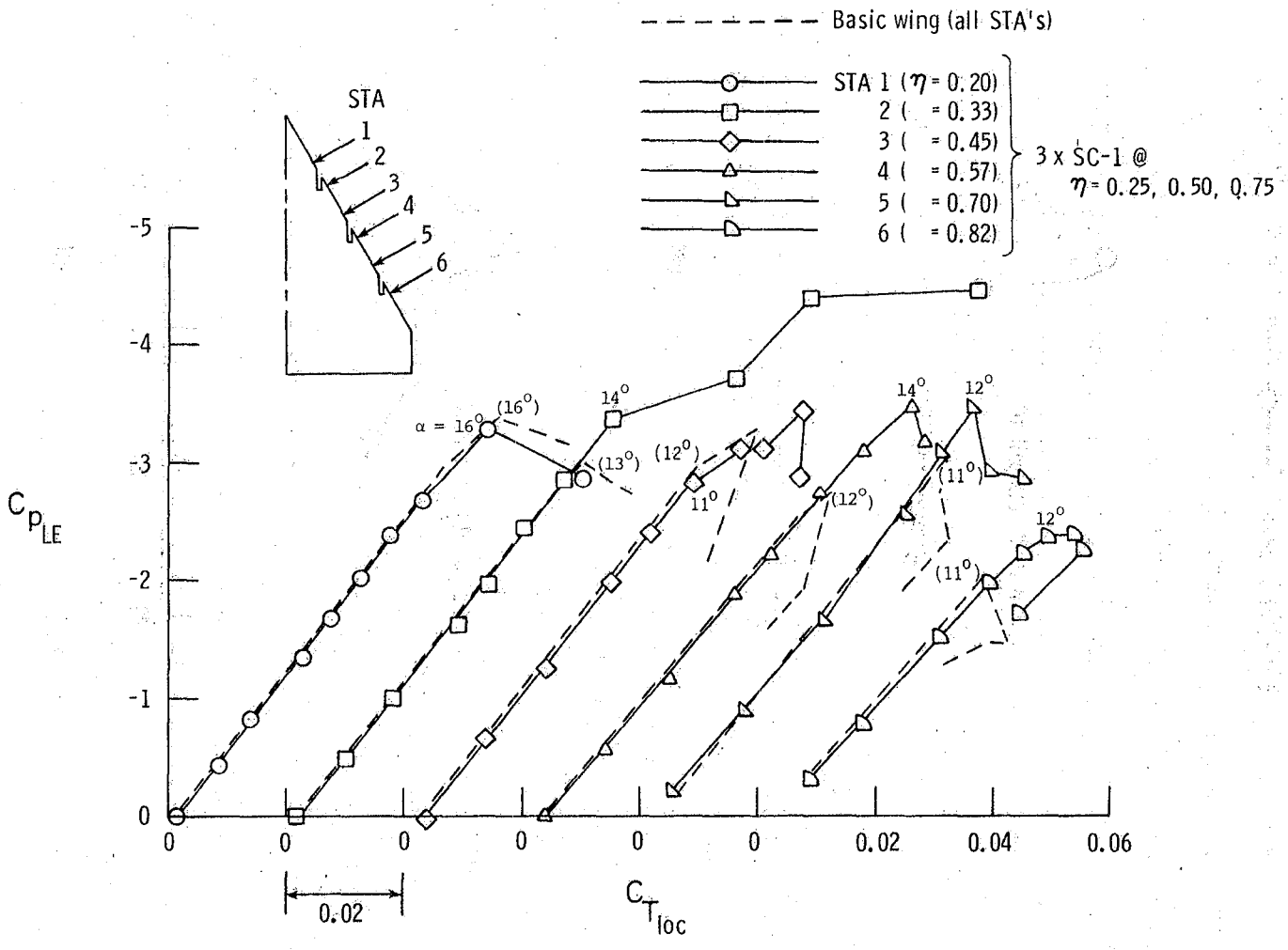

Figure 22.- Effect of multiple chordwise slots on leading-edge static pressure-thrust relationship. Selected high-α data points have been omitted for clarity. Angles in parentheses refer to basic wing data (see fig. 16).

flow has been extended to higher α without modifying the local effective upwash. This suggests that the slot action is more due to compartmentation rather than to any vortex mechanism.

As mentioned in the BACKGROUND section, the object of internal contouring of the chordwise slots was to reduce the low-α drag penalty while improving the high-α performance. The low-α drag effects will be discussed first. The following table compares zero-α drag measurements on a triple slot configuration utilizing the various slot contour shapes tested (fig. 3):

Device	C_{D_o}	Percent over BW
Basic wing	0.01261	-
3 x open slots	.01318	4.52
3 x SC-1	.01321	4.76
3 x SC-2	.01293	2.54
3 x SC-3	.01296	2.78
3 x SC-4	.01307	3.65

Comparison of open (uncontoured) slots with those making use of SC-1 shows relatively insignificant effects of contouring on low-α drag. Therefore, stagnation pressure on the back face of the slot appears not to be the primary cause of the low-α drag penalty. This is not surprising considering the relatively small area of this vertical face.

Two additional contour shapes tested, SC-2 and SC-3, effectively reduced the depth of the slots. Zero-α drag measurements for configurations utilizing these contour shapes indicate a reduction of almost 50 percent of the drag penalty associated with the slots, with a

relatively minor difference between the two. Since these contours differ only in shape, and not length, these data further support the conclusion that pressure on the vertical face at the end of the slot is not the primary source of low-α drag penalty. Comparison of zero-α drag for SC-1 and SC-2, which differ in length but have basically the same contour shape, suggests that slot depth is the determining factor for low-α drag. The reduction in drag penalty with SC-2 and SC-3, therefore, results from reduced friction drag acting on the slot side surfaces.

Comparisons of overall performance for the slot configurations just described appear in figure 23. Axial force shows a slight suction advantage beyond 12^{o} α and delayed loss of effectiveness with the use of SC-1 relative to the shorter slots utilizing SC-2 and SC-3. Minor differences exist between SC-2 and SC-3. Since a slight high-α suction advantage is realized with the use of SC-1 relative to the uncontoured slots, high-α performance may be somewhat dependent on the shape of the back face of the slots. However, slot depth is again the primary factor determining high-α performance. Improved performance with increasing slot depth is explained as follows: Since the postulated slot flow mechanism is partially that of a "fluid fence," increasing slot depth is analogous to increase in the chordwise length of a fence. Results of previous research (ref. 5) indicate that increasing fence length results in improved high-α drag performance and delayed loss of effectiveness, the same trends observed here.

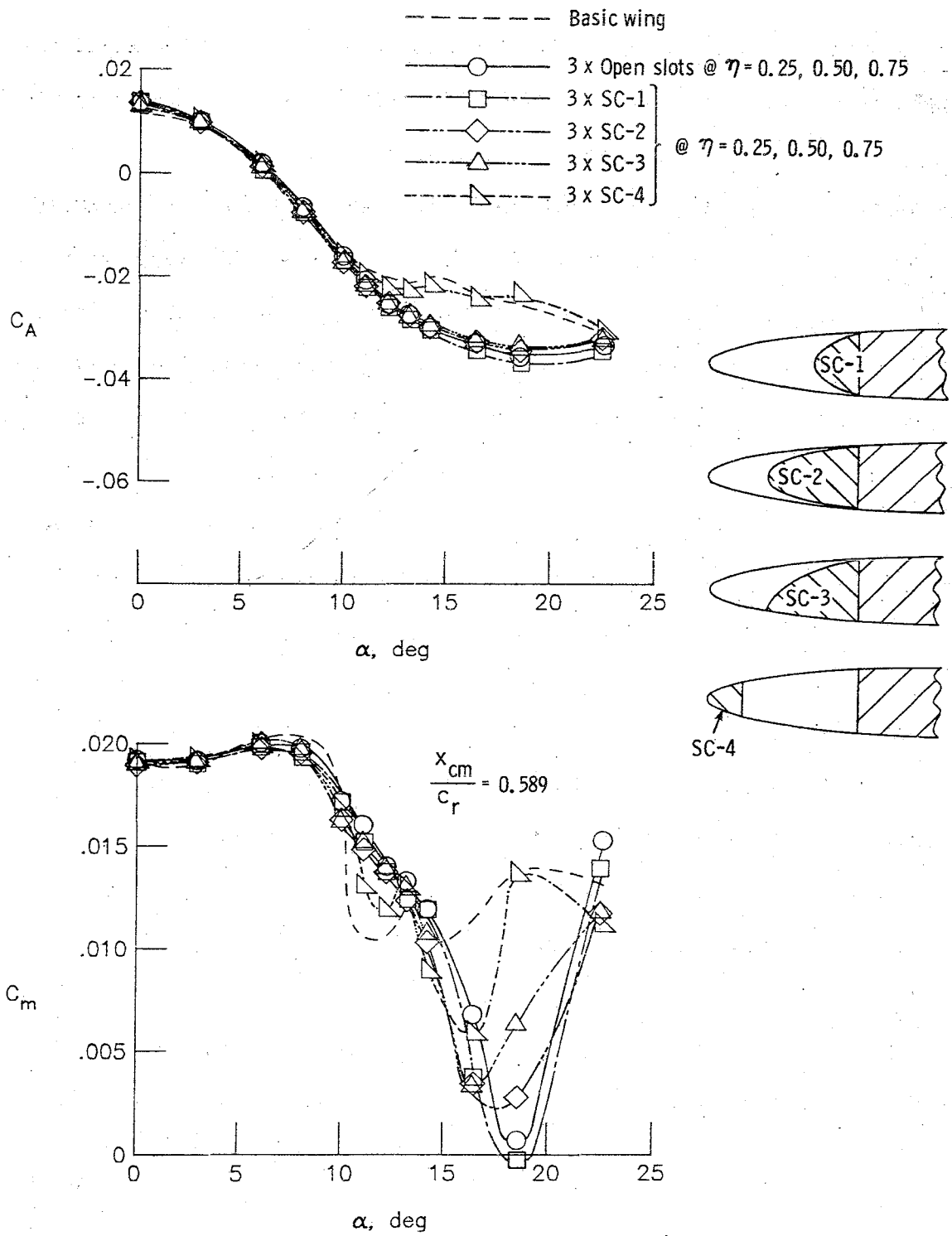

Figure 23.- Effects of internal contouring on chordwise slot performance.

Slot depth is also of prime importance to the longitudinal stability of the configuration. The most notable effect is accelerated high-α pitch-up with reduction in slot depth (fig. 23). Effects of slot depth and contouring on normal force and rolling moment are negligible.

An additional slot contour, SC-4, was tested in an attempt to reduce the low-α drag penalty by contouring the forward portion of the slot, as shown in figure 3. However, static pressure data indicate that the contour may have obstructed the flow through the slot, resulting in practically a nonexistent effect on drag performance (fig. 23). In addition, longitudinal stability is severely degraded, with accentuated pitch-up and pitch-down throughout the angle-of-attack range. Parameters such as normal force and lift-to-drag ratio, not presented, also agree closely with basic wing data, indicating that a slot starting behind the leading edge is ineffective.

Slot width was investigated as another parameter through which further performance improvements might be realized. Comparison of slots with widths of 0.25 and 0.50 percent of the semispan showed, however, that this is not a significant sizing consideration within the range tested.

In summary, the chordwise slot device possesses drag-reduction potential in addition to its ability to improve the longitudinal stability characteristics of the delta wing. Multiple slots spaced along the span produce further performance improvements by bringing more of the leading edge under attached flow and by eliminating the adverse effects inboard of a single slot. The slot effectiveness is primarily

through compartmentation of the leading edge to remove the 3-D effect which causes earlier separation on swept leading edges, rather than from any vortex action. The low-α drag penalty associated with this device results from friction acting on the side surfaces inside the slot; the pressure drag on the vertical face at the end of the slot is of secondary importance. Likewise, high-α performance is primarily dependent on slot depth rather than the shape (contour) of the back face. Increasing slot depth produces progressively higher low-α drag penalty but improved high-α performance.

Fences

As noted in the BACKGROUND section, fences have previously been used on highly swept leading edges primarily for improving longitudinal stability characteristics. The C_m curve in figure 24 shows that addition of a single F-3 fence at $\eta = 0.625$ improves the linearity of the pitch curve, with reduced pitch-down at $\alpha = 8^o$ and generally a more stable configuration throughout the angle-of-attack range. The C_A curve in figure 24 shows that fences also have drag-reduction capability at mid and high α, although some drag penalty at low α is incurred due to friction drag on the fence. The advantage of the device is first seen as a slight delay in the onset of separation to $\alpha \simeq 10^o$. Beyond approximately 11^o α, a significant suction advantage is indicated with the fence, with no sign of loss of effectiveness to the highest angles tested. The reduction in C_N relative to the basic wing at angles of attack greater than at separation onset also indicates delayed separation and vortex formation with the fence attached. This is further supported by static pressure distributions around the leading edge on either side of the fence (fig. 25). Inboard of the device, the flow remains stalled at $\alpha = 16^o$. However, outboard, where leading-edge separation has clearly occurred on the basic wing (as evidenced by nearly uniform upper surface pressures), attached flow is maintained by the fence. As shown by the C_l curve in figure 24, by delaying separation, the fence also reduces the severity of the wing rock characteristic of this delta planform.

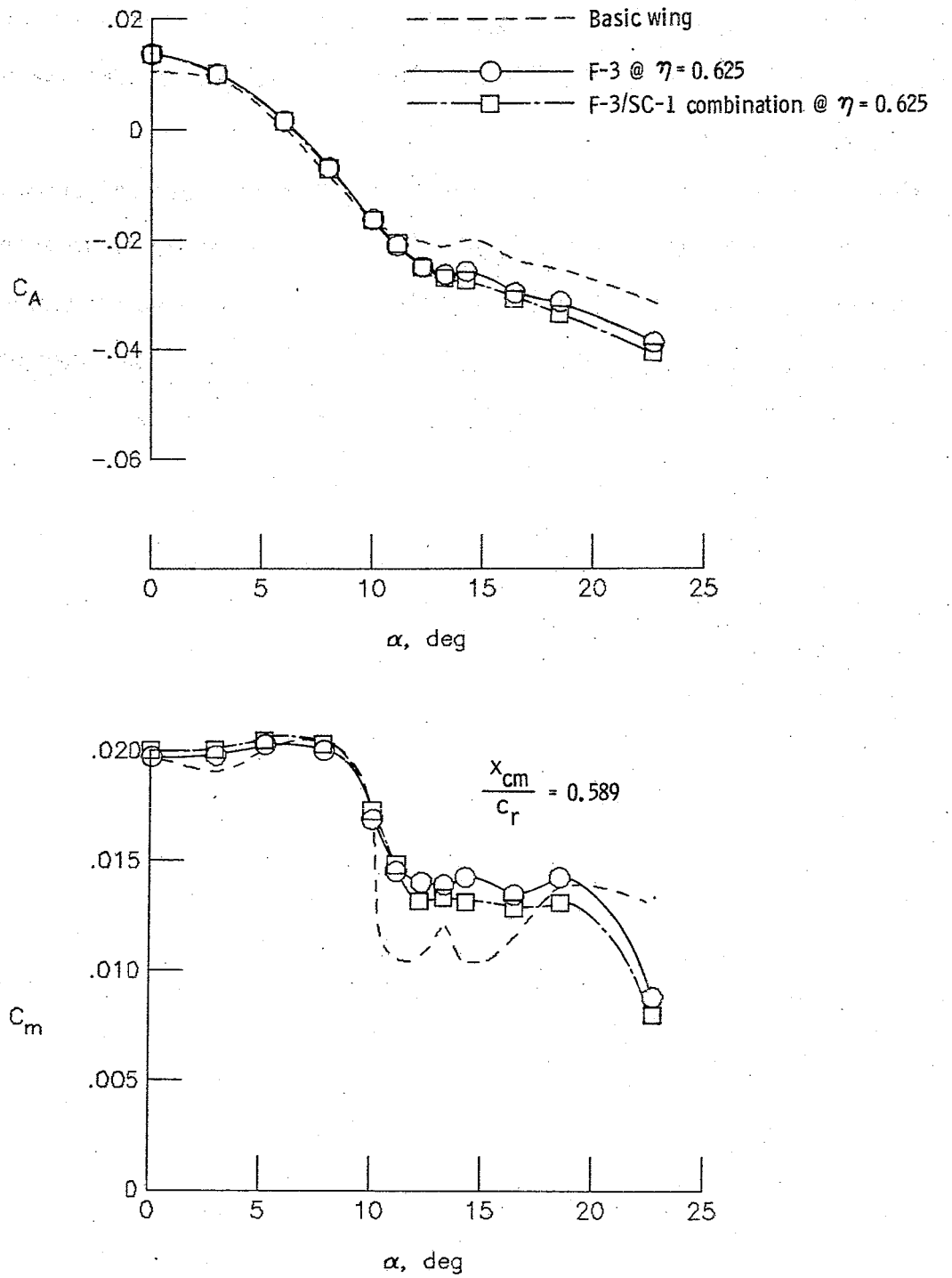

Figure 24.- Force and moment characteristics of single fence and slot-fence configurations.

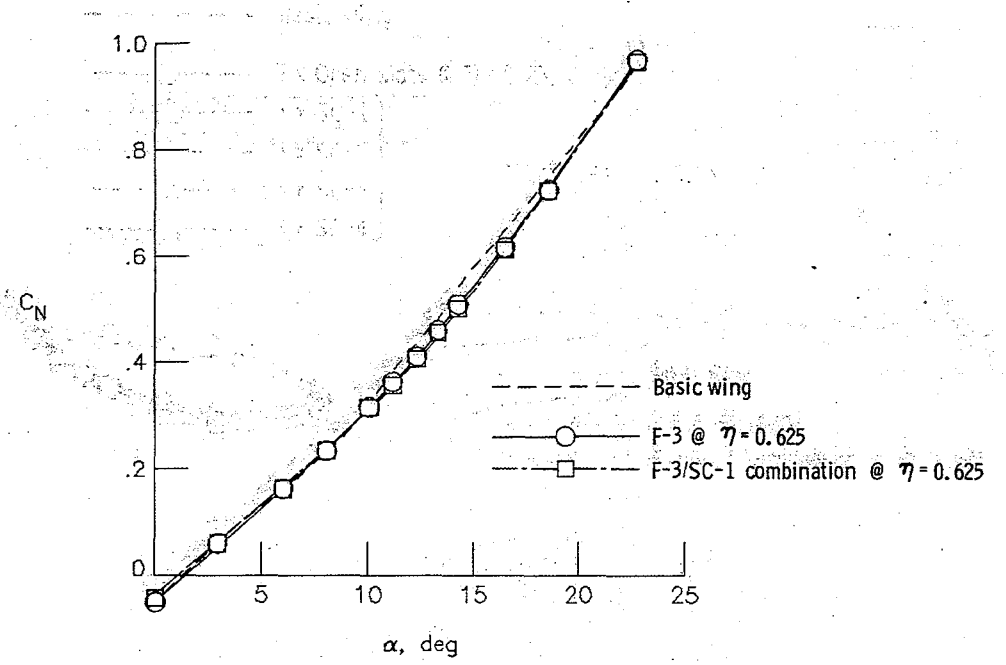

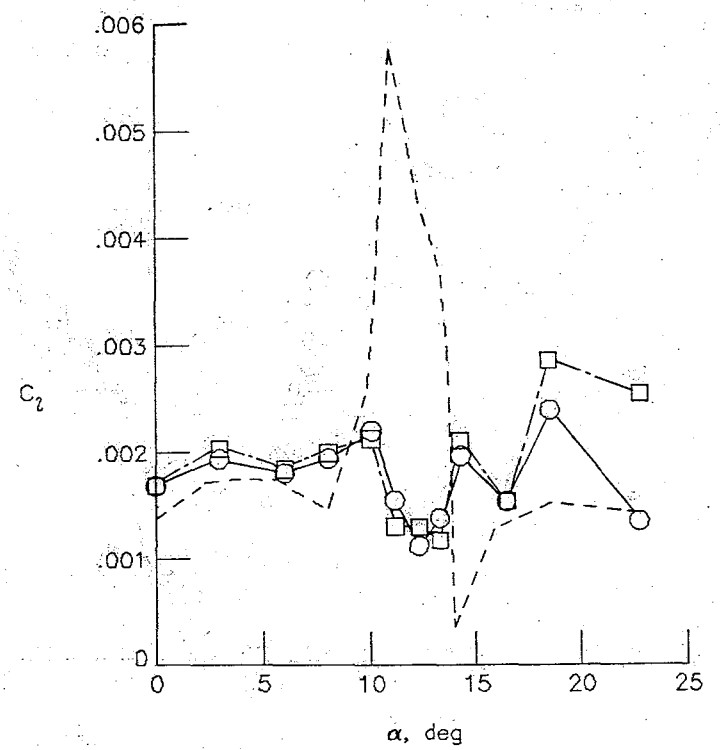

Figure 24.- Concluded.

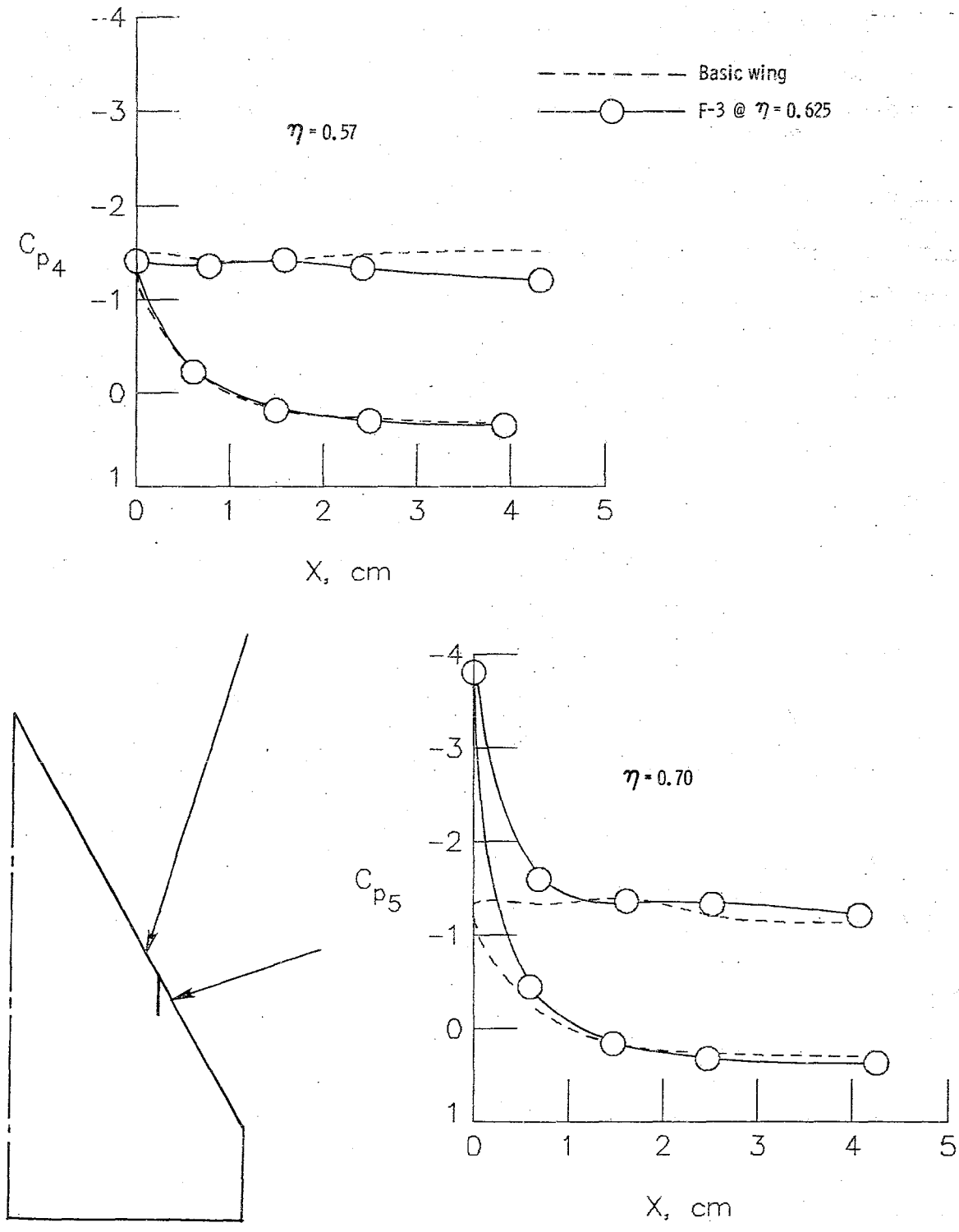

Figure 25.- Local static pressure effects of the fence at $\alpha = 16^{o}$.

The separation boundary in figure 26 shows the effect of the F-3 fence on the inboard movement of leading-edge separation. The compartmentation effect of the device (see BACKGROUND section) is seen to delay the onset of separation on its outboard side by approximately 3^{o} α. This reduction in the rate of inboard movement of separation accounts for the elimination of severe pitch-up, as the forward movement of the center of vortex lift is also delayed. This effect also diminishes the asymmetry in the spanwise lift distribution, responsible for the erratic rolling moment behavior of the basic wing.

Local leading-edge thrust variations with a single F-3 fence at $\eta = 0.625$ are presented in figure 27. At low α, where the basic wing flow remains attached, the fence has no influence on the leading-edge flow conditions. However, beyond the local onset of separation for the basic wing, substantial thrust improvements are evident outboard of the device due to the delay in local stall and subsequent retention of leading-edge suction. This effect can be attributed to the unsweeping of the upper surface isobars in the vicinity of the fence, as sketched below:

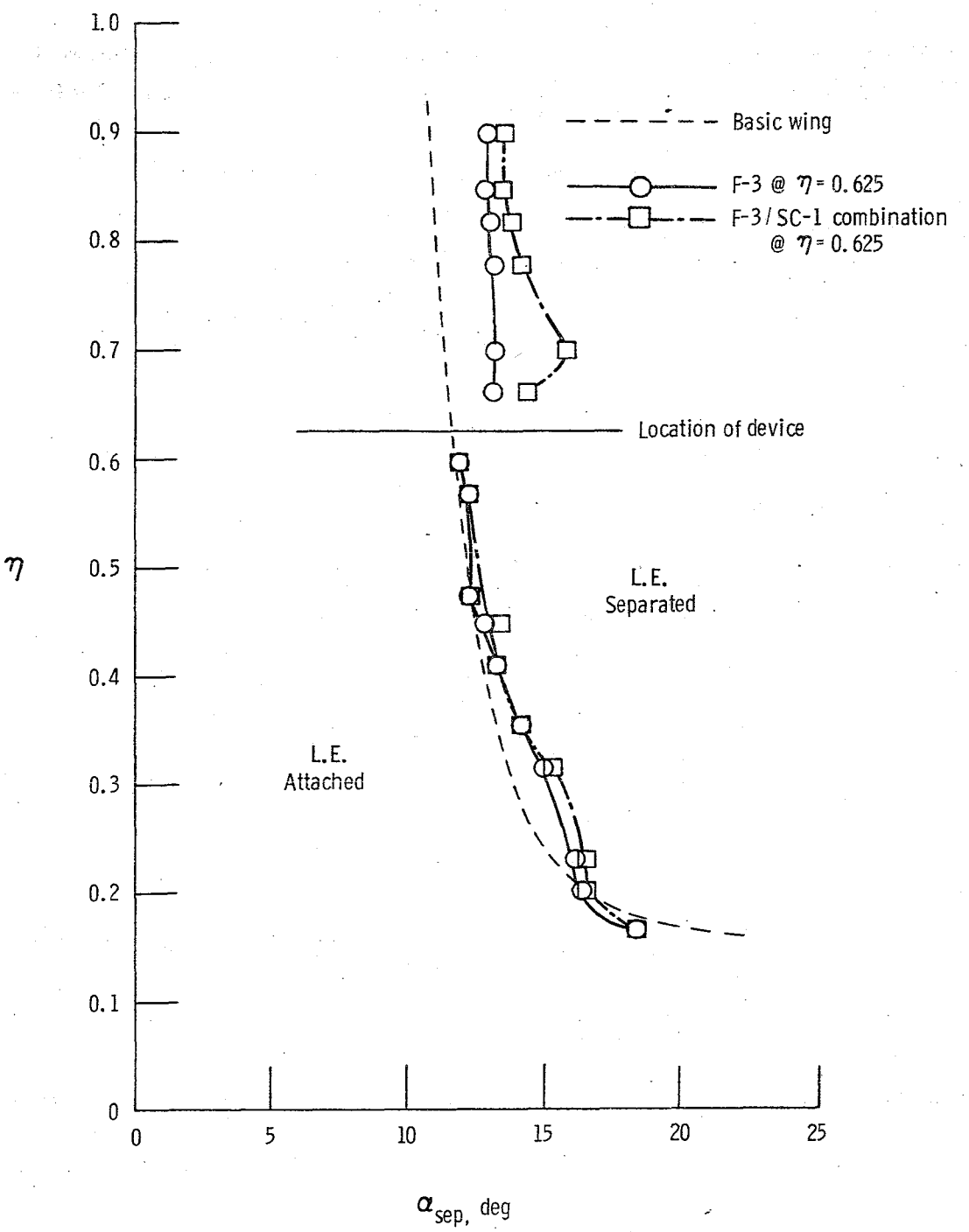

Figure 26.- Effects of the fence and slot-fence combination on leading-edge separation ($C_{p_{LE}}$ derived).

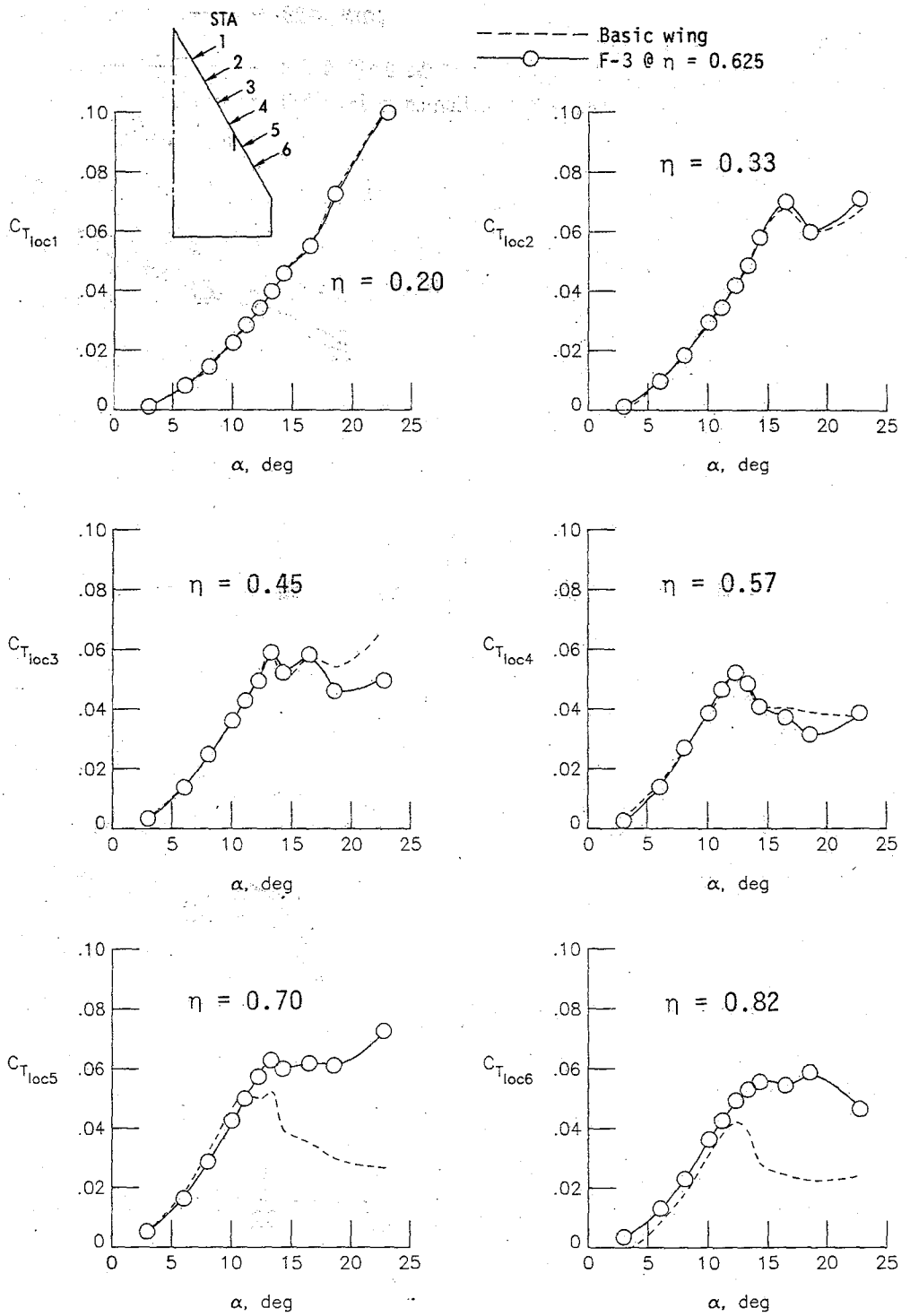

Figure 27.- Effects of the fence on leading-edge thrust.

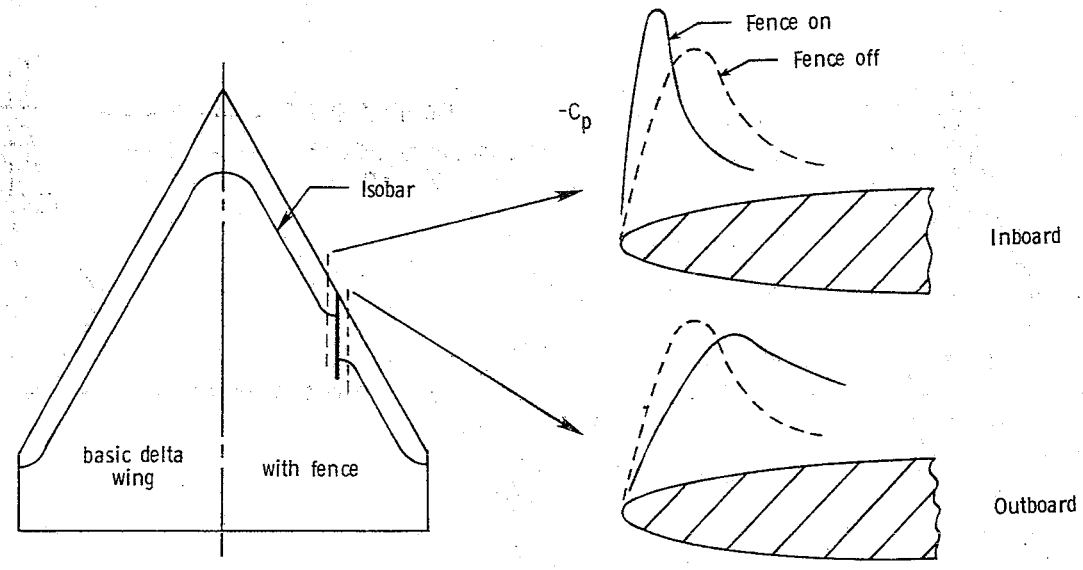

Sketch I

On the outboard side of the fence, suction peaks are reduced and occur further aft of the leading edge. This reduces the tendency toward separation by providing a more gradual pressure recovery on the upper surface. The opposite effects inboard facilitate earlier separation and loss of thrust. However, this adverse effect is only localized, as little influence of the fence is evident further inboard.

The effect of a single fence on the induced drag of the basic wing is shown in figure 28. At low α, before leading-edge separation has spread to the fence location, the indicated increase in K results from the friction drag on the fence. Beyond 10° α, however, the fence provides an induced drag reduction by delaying leading-edge separation and

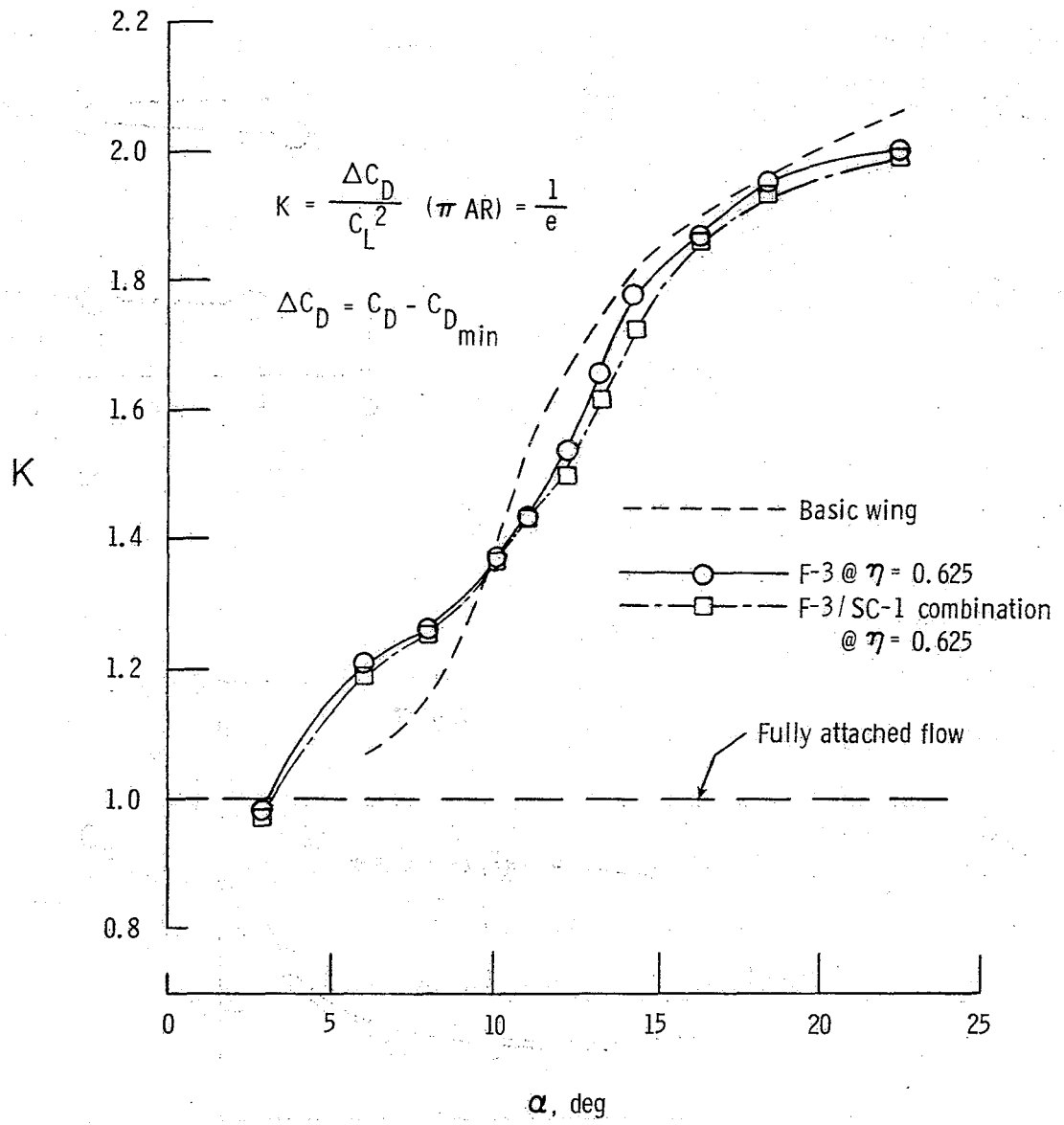

Figure 28.- Induced drag characteristics of single fence and slot-fence configurations.

loss of suction. This benefit is visible up to the highest angles tested, although the maximum relative improvement occurs between 11^{o} and 13^{o} α.

Figure 29 presents graphs of $C_{p_{LE}}$ versus $C_{T_{loc}}$ at the six spanwise pressure stations of the research model. Local separation is shown to have been delayed by 5^{o}, to $\alpha = 16^{o}$, at the station just outboard of the fence, with a delay of approximately 3^{o}, to $\alpha = 14^{o}$, at the station nearest the tip. Inboard effects are minor. The extension of the outboard curves along their initial slope again indicates flow modification without alteration of the local angle of attack. As discussed previously, the fence flow mechanism is rather one of isobar unsweeping and leading-edge compartmentation.

Recall that thrust data in figure 27 indicated an early loss of effectiveness just inboard of the fence. This was believed to be partially the result of an accumulation of viscous fluid on the inboard side of the device from the spanwise boundary layer flow. It was, consequently, thought that by opening an adjacent slot inboard of the fence, this viscous accumulation could be "blown off" by the slot jet stream (see sketch in BACKGROUND section). The concept was tested on the F-3 fence with the inboard slot contoured with SC-1. Results of force and moment measurements are shown in figure 24. Although there is an additional low-α drag penalty as expected, definite axial force improvements are indicated beyond 13^{o} α. For instance, at $\alpha = 14.3^{o}$, an 8.6 percent reduction in axial force is realized with addition of the slot. The general nature of the pitching moment curve is

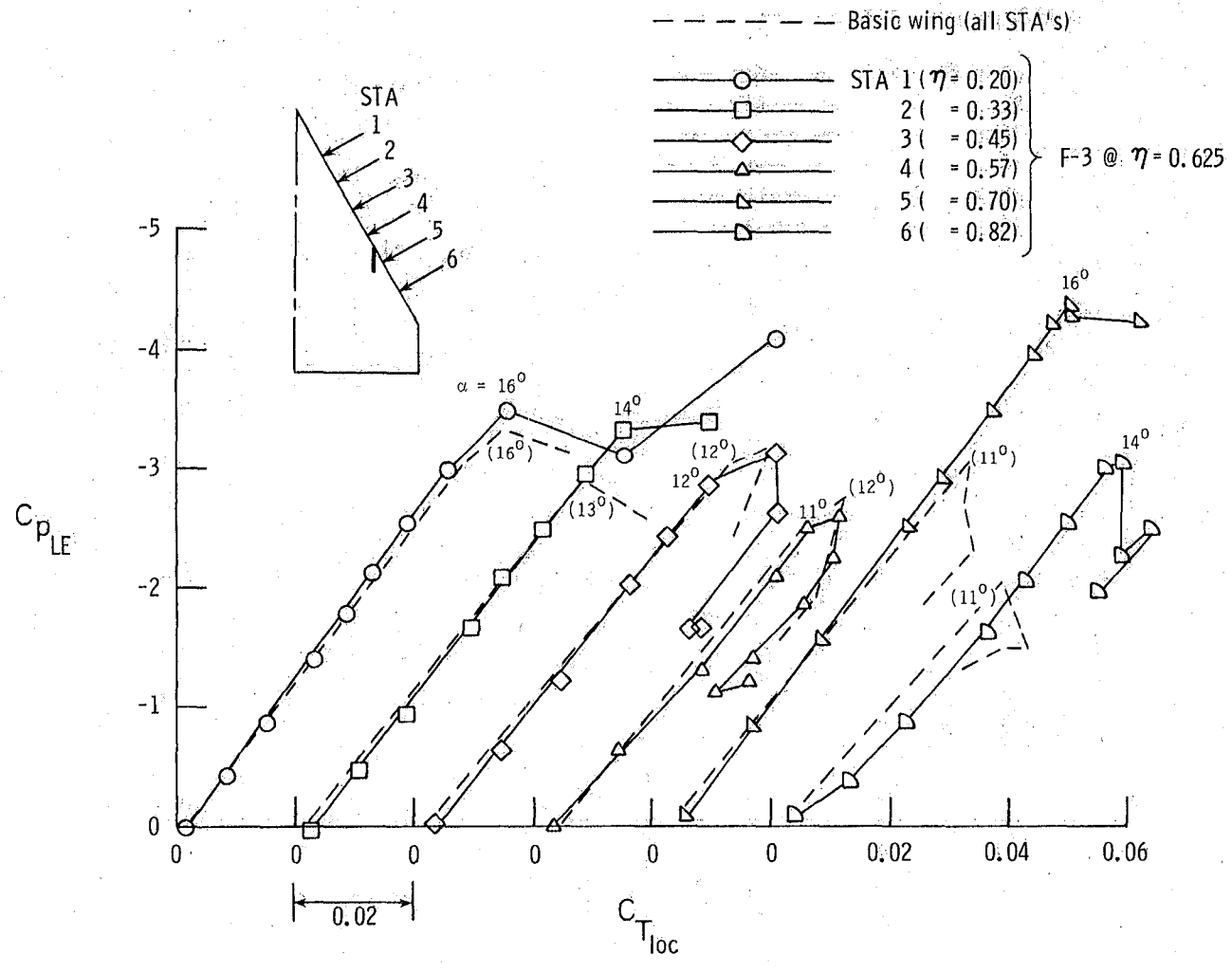

Figure 29.- Effect of the fence on leading-edge static pressure-thrust relationship. Selected high-α data points have been omitted for clarity. Angles in parentheses refer to basic wing data (see fig. 16).

unaffected, but the configuration appears to be slightly more stable beyond $\alpha \simeq 11^{o}$. No significant effects are evident in normal force and rolling moment. Figure 28 shows that a slight improvement in induced drag also results from addition of the adjacent inboard slot. This advantage, however, dissipates by 19^{o} α as the fence and slot-fence data converge.

The reduction in drag with an adjacent slot inboard of the fence is shown in figure 30 to result from thrust improvements outboard of the device, rather than inboard as was expected. In fact, no influence is evident inboard. The spanwise leading-edge pressure variation at $\alpha = 16^{o}$, in figure 31, shows the same trend. This leads to the conclusion that the inboard loss of fence effectiveness at high α is not hastened by a viscous fluid accumulation, but rather is totally a result of inviscid effects. As noted earlier, the unsweeping of the upper surface isobars leads to increased suction peaks occurring closer to the leading edge on the inboard side of the device. This results in a steeper upper surface pressure recovery behind the suction peak and. consequently, earlier separation. Comparison with a single slot at $\eta = 0.625$, in figure 31, indicates that the additional improvement outboard is primarily a fence effect. It is believed that the spanwise flow being lifted over the fence by the slot airstream results in the formation of a vortex off the upper edge of the fence. This vortex lies on the outboard side of the device and rotates in a sense so as to induce a downwash velocity outboard. The resulting outboard reduction

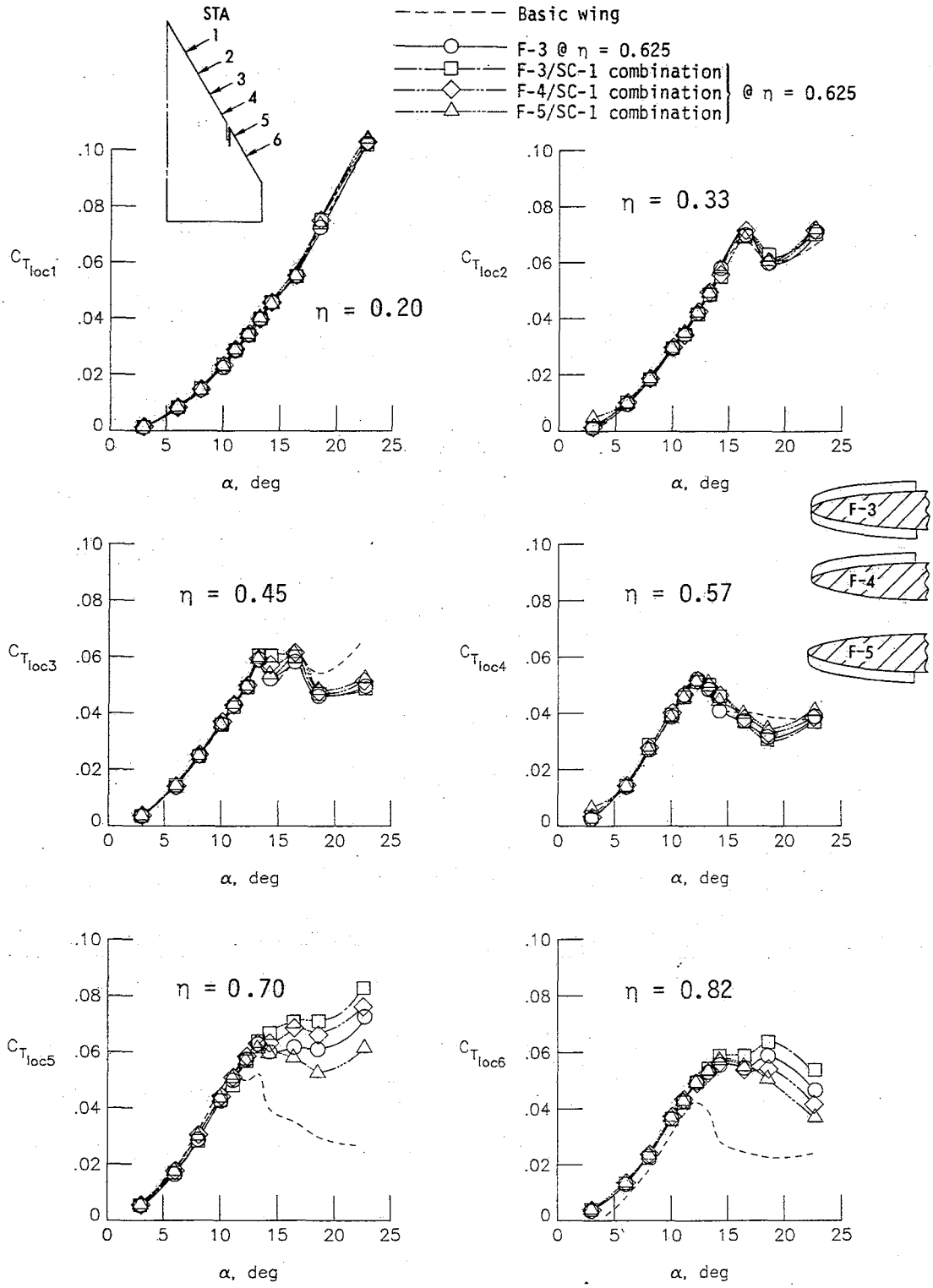

Figure 30.- Effects of slot-fence combinations on leading-edge thrust.

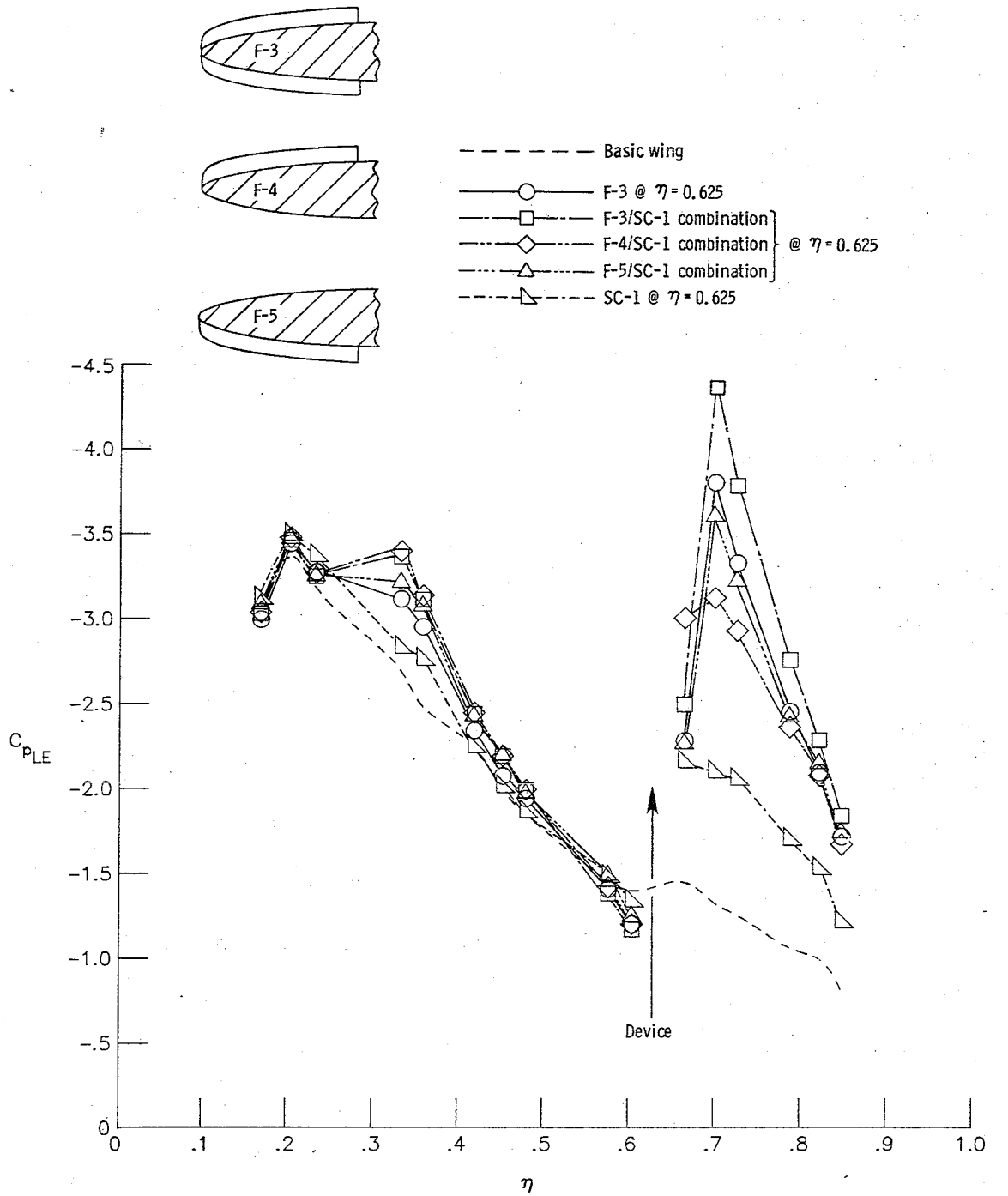

Figure 31.- Effects of slot-fence combinations on spanwise leading-edge static pressure distribution at $\alpha = 16^0$.

in local effective angle of attack delays separation (see fig. 26), with accompanying improvements in leading-edge suction and thrust.

In order to determine the role that the upper and lower edges of the fence play in the flow mechanism of the slot-fence combination, tests were run with each edge alternately removed. Results of pressure measurements and thrust integrations appear in figures 31 and 30, respectively. Removal of the lower edge of the fence (F-4) results in little effect inboard but substantial high-α losses of leading-edge suction outboard. The lower edge of the fence, therefore, may have been helpful in guiding the lower surface flow through the slot (see BACKGROUND section). Removal of the upper portion of the fence (F-5) also results in outboard losses of leading-edge suction and thrust. This is most likely attributed to elimination of the upper surface vortex tripped by the upper edge of the fence, along with its accompanying downwash velocity outboard. The upper surface flow characteristics, therefore, revert back to those of a single slot, with the characteristic high-α loss of leading-edge suction and thrust.

In summary, the fence possesses significant drag-reduction potential, in addition to its ability to improve the longitudinal stability characteristics of the delta planform. The high-α loss of leading-edge thrust occurring inboard of the device was found to be an inviscid effect (viz., isobar unsweeping), rather than due to viscous accumulation inboard as originally thought. Finally, addition of an adjacent inboard slot resulted in a slight performance improvement, possibly through the formation of a favorably rotating vortex outboard of the fence.

Pylon Vortex Generators

The function of the pylon vortex generator relies on the formation of a streamwise vortex at the sharp upper edge of a vertical blade extending ahead of and below the wing leading edge (see BACKGROUND section). Figure 32 summarizes the capabilities of this device (VG-1) in single and multiple configurations. The VG-1 had a leading-edge sweepback angle of 30^{o} and toe-in angle of 10^{o} (see fig. 5). These values were found in previous research (ref. 5) to produce the best compromise between low- and high-α performance. The axial force and percent drag reduction (PD) curves show the expected low-α drag penalty with a single VG-1 at $\eta = 0.50$. This penalty continues to $\alpha \simeq 8^{o}$ (which is the angle for separation onset on the basic wing), at which point the device begins to show a favorable effect. Beyond 10^{o} α, a single VG-1 provides substantial drag reduction, with a maximum improvement of approximately 15 percent (PD curve) at $\alpha = 14^{o}$. In addition, the mid-α C_A reversal characteristic of the basic wing is eliminated. A constant C_A increment at higher α accounts for the tapering off of the relative drag improvement seen in the PD curve.

The longitudinal stability effects of a single VG-1 located at $\eta = 0.50$ are reflected by improved linearity of the pitching moment curve in figure 32. Alleviation of the initial pitch-down and a 2^{o} delay in pitch-up, to $\alpha = 13^{o}$, are indicated. The pitch-up with the VG is also very mild in comparison with the basic wing. The normal force curve shows a loss of lift beyond 10^{o} α, implying a reduction of vortex lift contribution due to delayed separation. In addition,

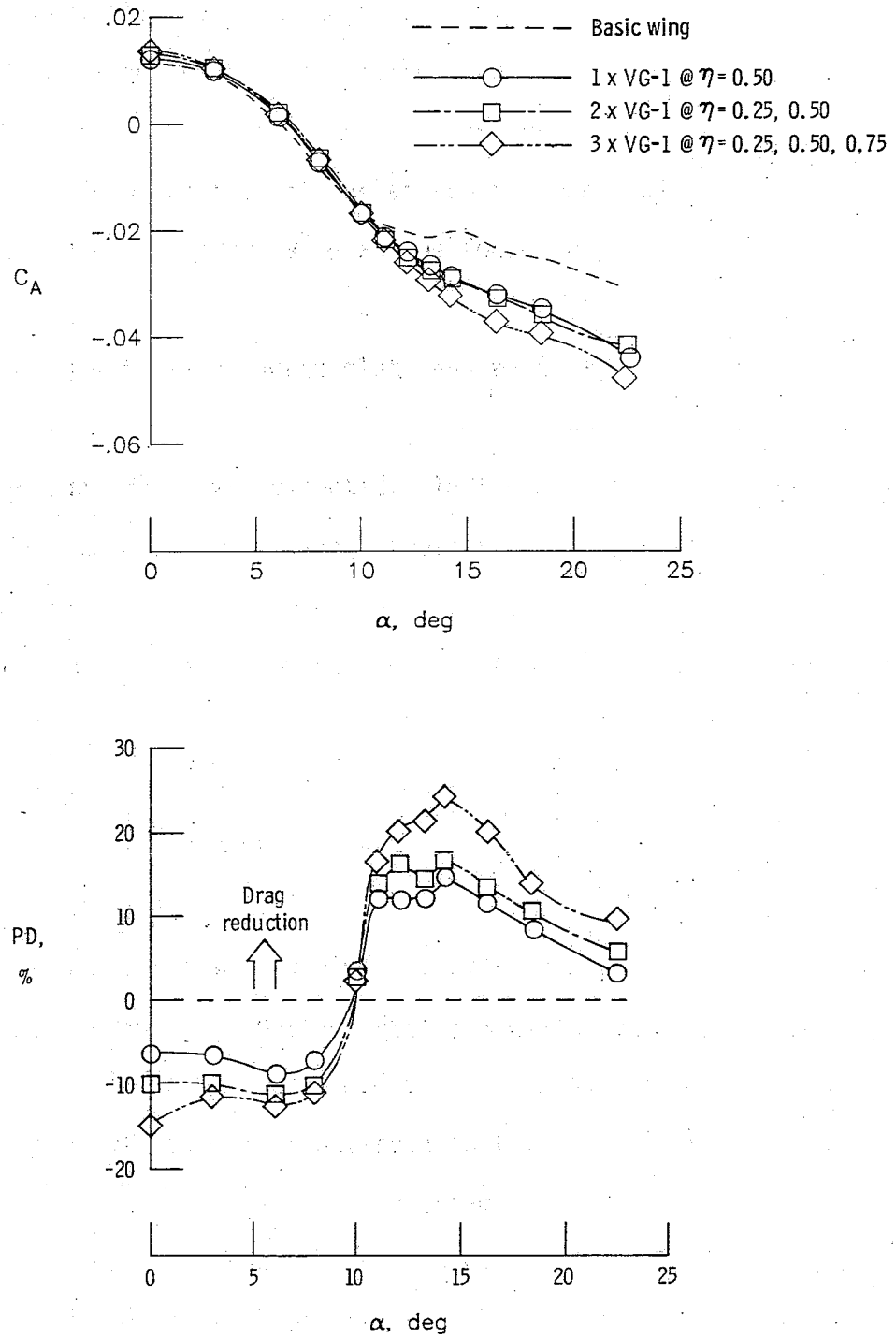

Figure 32.- Force and moment characteristics of single and multiple pylon vortex generator configurations.

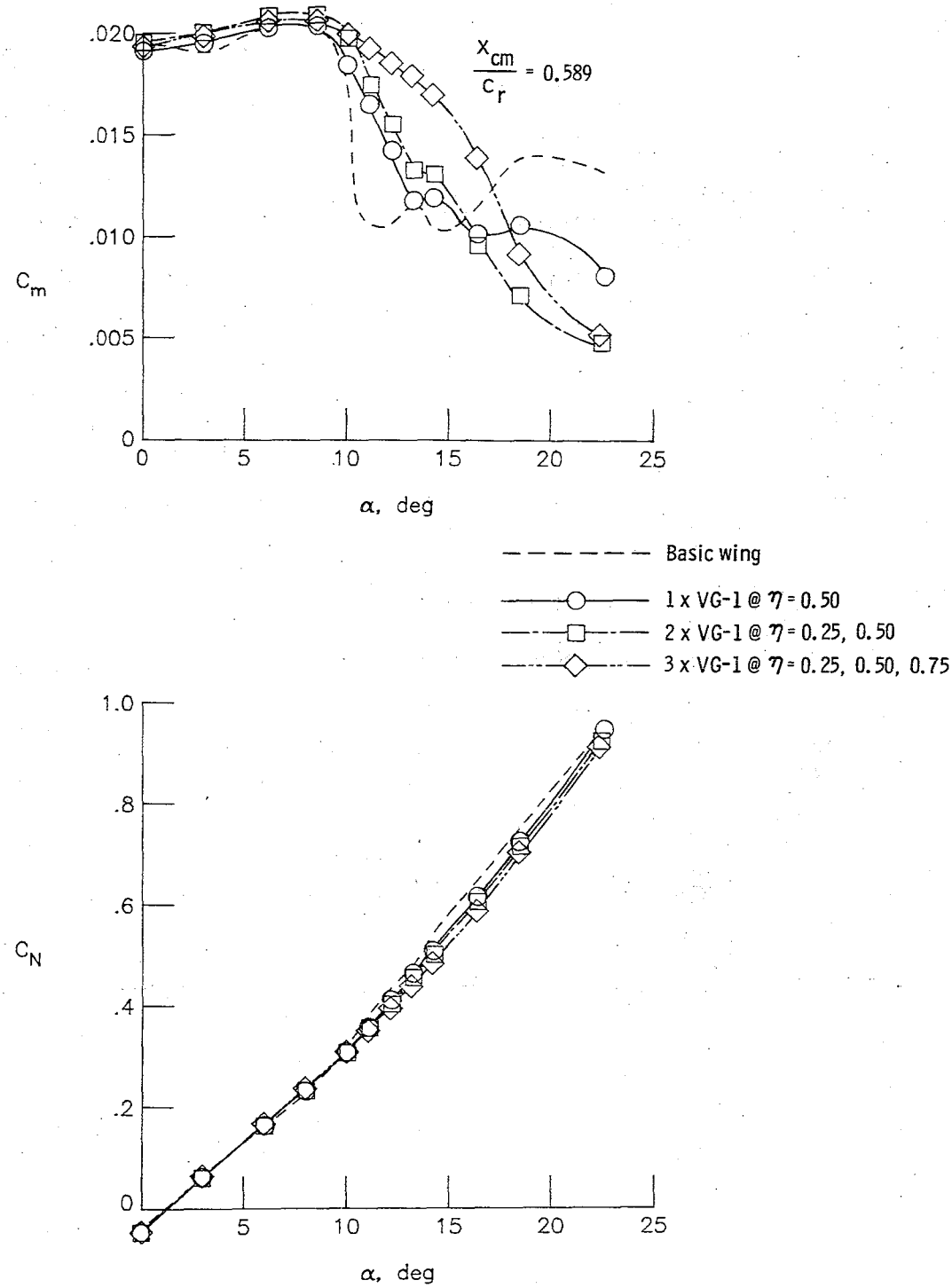

Figure 32.- Continued.

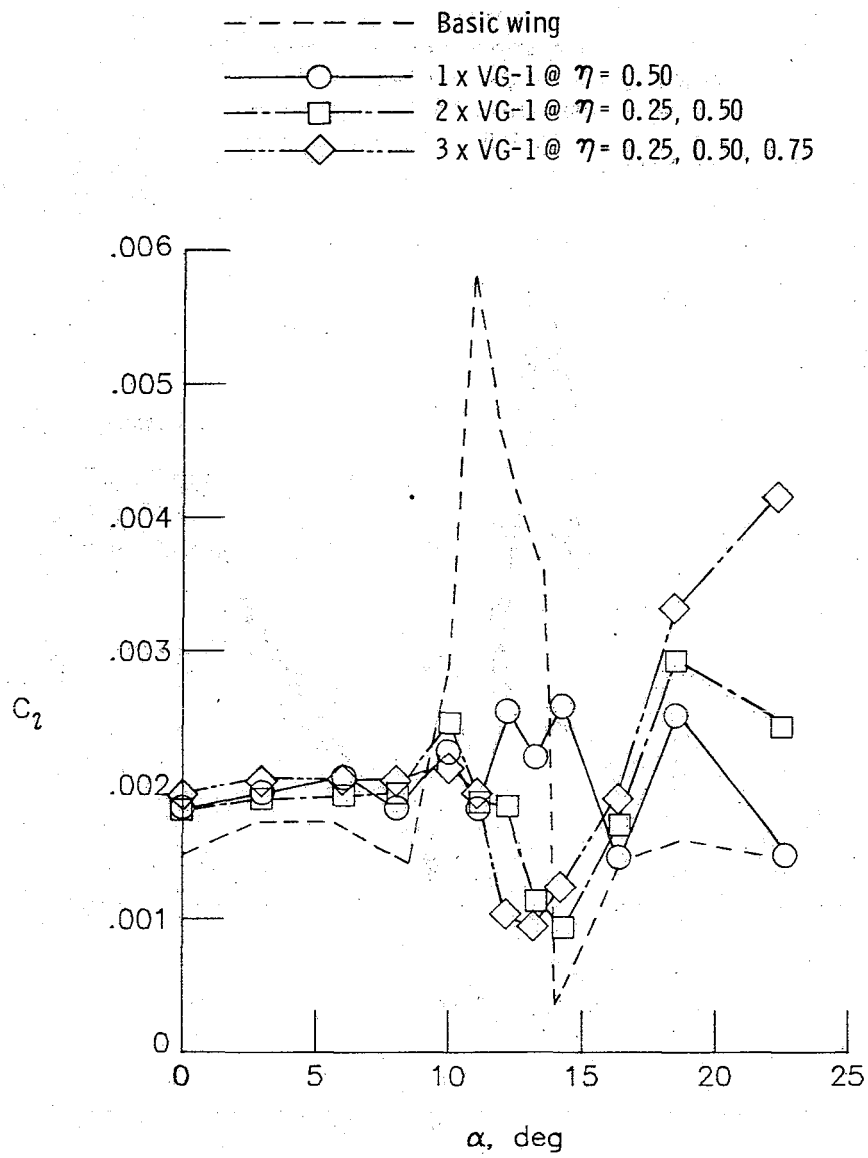

Figure 32.- Concluded.

the magnitude of the fluctuations in the C_l curve of the basic wing are significantly reduced, indicating a more gradual and symmetric growth of separation.

The performance of the vortex generator can be further enhanced through its use in multiple arrangements. Results of balance measurements on double (η = 0.25, 0.50) and triple (η = 0.25, 0.50, 0.75) VG-1 configurations are presented in figure 32. Generally, an increasing number of VG's results in progressively higher low-α drag penalty (PD and C_A curves and Table III) but improved high-α performance. Drag reductions of 17 percent with two and 24 percent with three VG-1's (relative to the basic wing) are obtained at $\alpha \simeq 14^o$. However, further losses of normal force are found, as expected, due to improved suppression of flow separation and vortex lift. The longitudinal stability is similarly improved progressively with increasing number of VG's, as shown by the improved linearity of the C_m curve. Two VG-1's have no further influence on the pitch-up at $\alpha = 13^o$ but produce a more stable configuration at higher α than a single VG-1. Three VG-1's result in a more gradual initial pitch-down together with complete elimination of instability. This is significant since the point of maximum percent drag reduction now lies in a longitudinally stable α range. In general, all VG arrangements eliminate the wing rock of the basic wing in the intermediate α range.

As briefly noted in the BACKGROUND section, the formation of a vortex at the swept-forward leading edge of the vortex generator is a result of the prevailing sidewash velocity ahead of the wing leading

TABLE III.- VORTEX GENERATOR ZERO-α DRAG CHARACTERISTICS

	Device	Percent increase in wetted area over BW	C_{D_o}	Percent increase in C_{D_o} over BW
	Basic wing	-	0.01261	-
Baseline	1 x VG-1	0.5	.01344	6.58
	2 x VG-1	.9	.01391	10.31
	3 x VG-1	1.4	.01448	14.83
L.E. length reduction	1 x VG-2	.3	.01323	4.92
	1 x VG-3	.1	.01312	4.04
Chord reduction	1 x VG-4	.2	.01315	4.28
	1 x VG-5	.2	.01327	5.23
Diagonal cut	1 x VG-6	.3	.01338	6.11
	1 x VG-7	.1	.01314	4.20
With missile	1 x VG-8	2.6	.01368	8.48
Without missile	1 x VG-9	1.3	.01330	5.47

edge. At low α, this sidewash velocity is not of sufficient magnitude to cause vortex formation due to the toe-in angle of the device (see fig. 5). When the sidewash is less than the toe-in angle of the VG, a pressure drag is produced in addition to the skin friction drag of the device. This accounts for the low-α drag penalty noted in the PD and C_A curves. Increasing α, accompanied by increasing sidewash velocity, eventually leads to vortex formation at the VG leading edge. This vortex travels over the wing upper surface and rotates in a sense so as to induce a downwash velocity on its outboard side. Due to the prevailing sidewash velocity, the upper surface path followed by this vortex is angled toward the wing tip. Therefore, it should be noted that any reference to inboard or outboard effects of the VG applies to either side of this vortex rather than the device itself.

As shown by the separation boundary in figure 33, the vortex action of a single VG-1 at $\eta = 0.50$ results in substantial delays in local separation on the outboard side. The extensive delay adjacent to the VG is attributed to the exponential variation of the vortex tangential velocity and, thus, the induced downwash. Slight delays of separation inboard are attributed to the compartmentation effect of the device. The sense of rotation of the VG vortex is opposite that of the primary vortex, thereby reducing its strength and obstructing its inboard movement. Static pressure variations around the wing leading edge, in figure 34, indicate that once inboard separation does occur (between 14° and 16° α at STA 3), the upper surface flow eventually stagnates at a

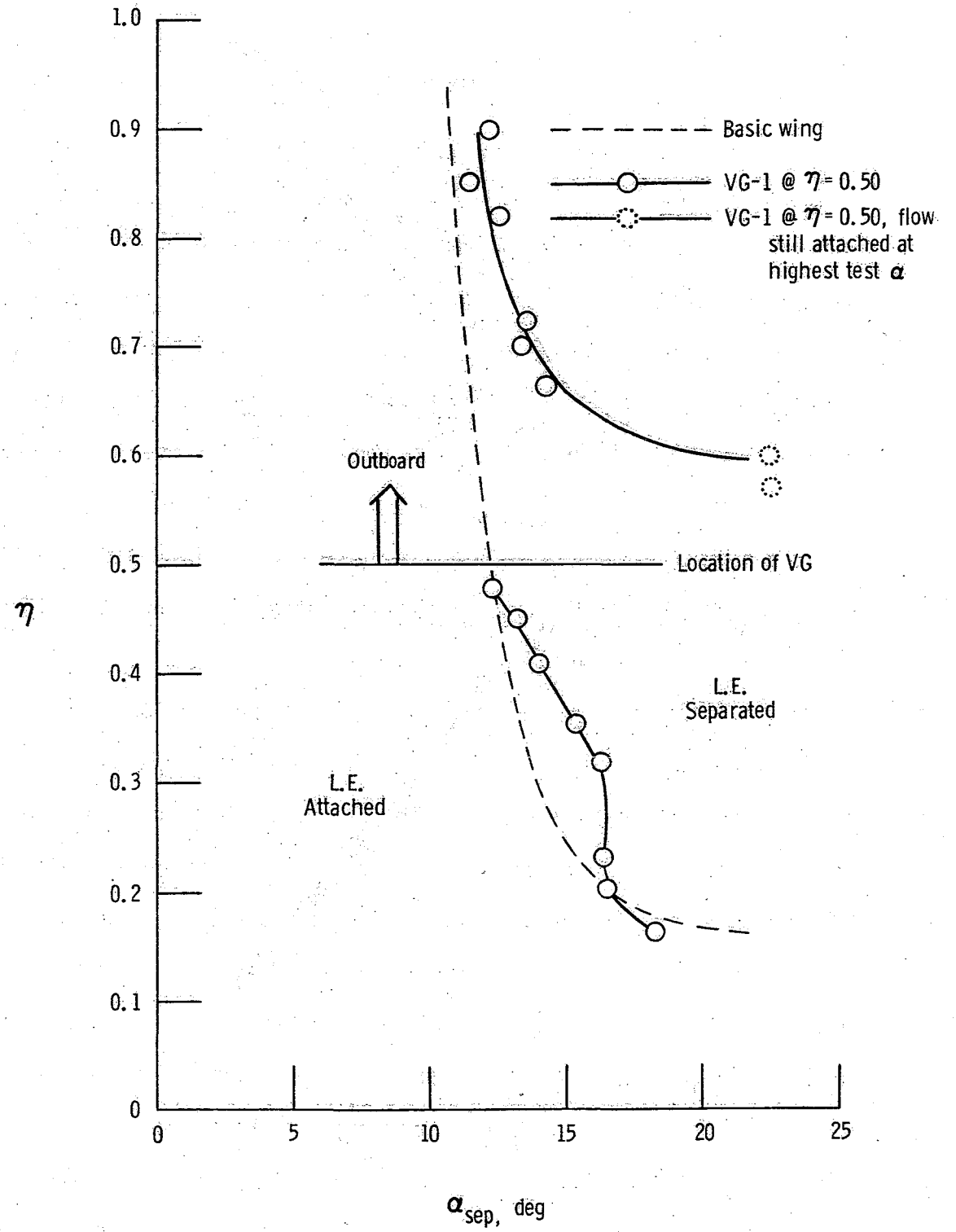

Figure 33.- Effect of the pylon vortex generator on leading-edge separation ($C_{p_{LE}}$ derived).

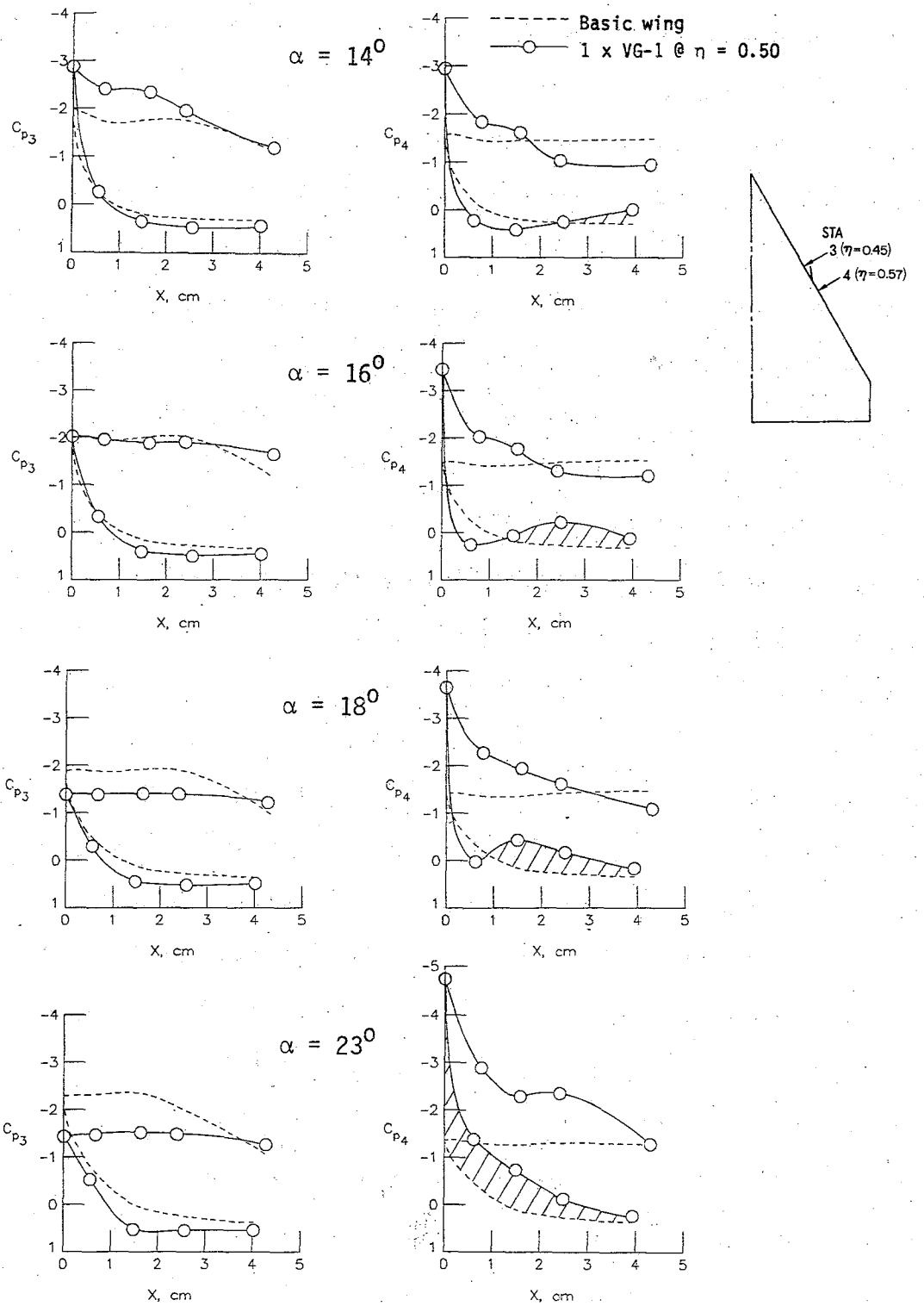

Figure 34.- Local static pressure effects of the pylon vortex generator. Shaded regions indicate lower vortex contribution.

higher constant pressure than on the basic wing (see $\alpha = 18^{o}$ and 23^{o} plots). This results in a smaller contribution to leading-edge suction.

An aspect of the VG flow mechanism not yet discussed is the formation of a vortex at the lower edge of the device, as shown in sketch D of the BACKGROUND section. At the lowest angles of attack, this vortex passes beneath the wing, undetected by the leading edge. At higher α, however, the vortex begins to impinge on the lower surface of the wing, as indicated by the minor suction peak in the lower surface pressures at STA 4 at $\alpha = 14^{o}$ (fig. 34). This suction peak moves progressively closer to the leading edge with increasing α, suggesting that at angles higher than those considered here, this lower-edge vortex would pass completely over the wing. Once this occurs, its own contribution to the wing leading-edge thrust (cross-hatched in fig. 34) is lost. In addition, this vortex may act to degrade the upper VG vortex.

Local thrust variations for single and multiple VG-1 configurations appear in figure 35. The high-α C_A improvements noted in figure 32 are shown to result from thrust enhancement outboard of each VG. The figure also demonstrates the ability of multiple VG's to effectively eliminate the adverse inboard effect of the single device. Note that at low α (attached flow on the basic wing), local thrust values just outboard of each VG (for all VG-1 configurations) fall below those of the basic wing. This is attributed to the induced downwash in these regions, which effectively reduces the local angle of attack and, thus, the suction forces around the leading edge. At higher α, however, this

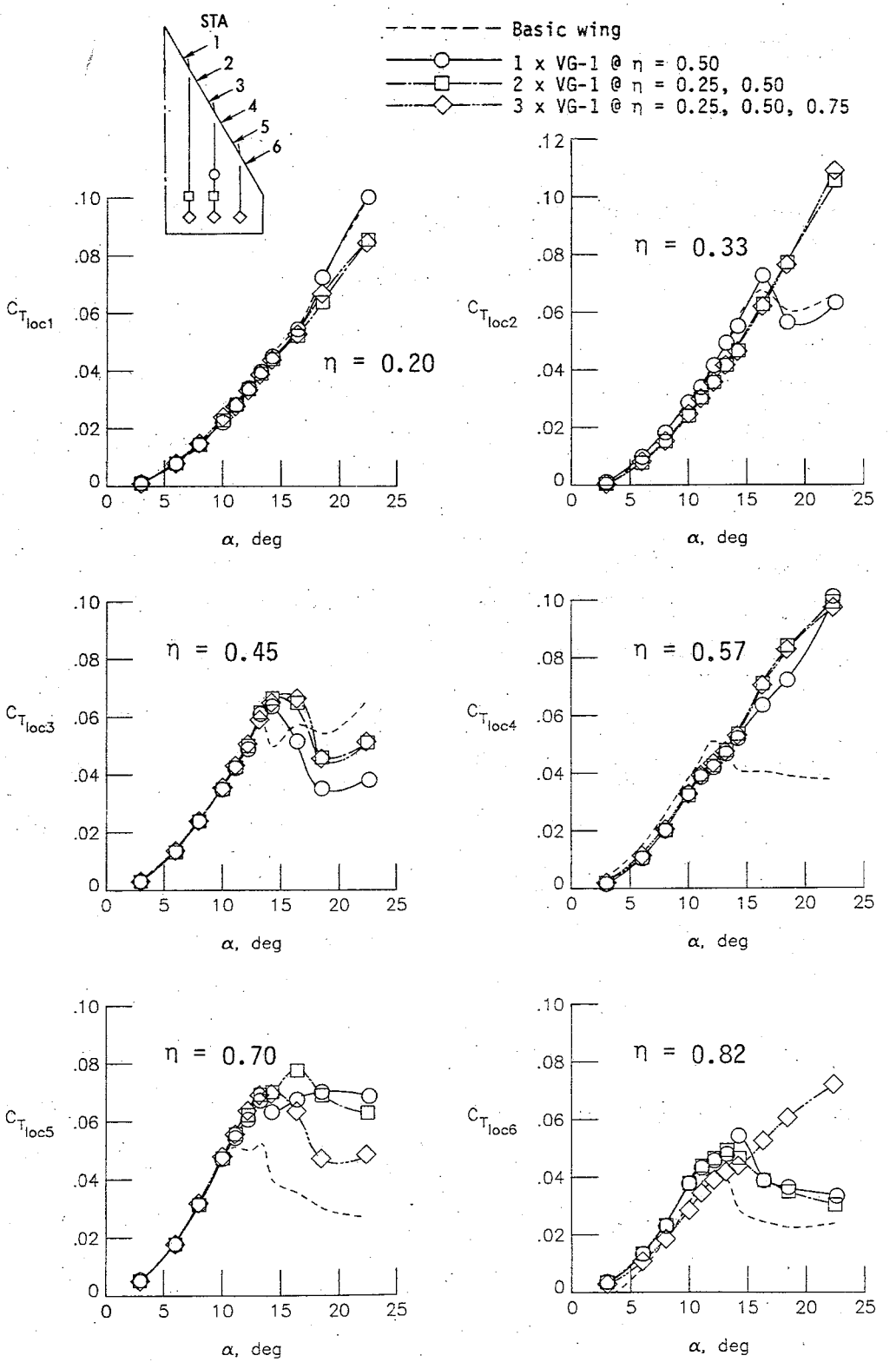

Figure 35.- Effects of single and multiple pylon vortex generators on leading-edge thrust.

effect acts to delay separation and, thus, retain leading-edge suction to the highest angles tested.

The spanwise leading-edge pressure distributions at $\alpha = 14^{o}$ (where the maximum percent drag reduction occurs) for single and multiple VG-1 configurations are presented in figure 36. The single VG-1 curve shows only a localized ineffectiveness on the inboard side of the device. In addition, the plots show how the mutual interaction of multiple VG's acts to enhance the leading-edge suction along the span. The wavelike shape of the curves just outboard of each device is attributed to the outboard drift of the VG vortex, discussed previously. Comparison of the curves indicates that the VG has a more pronounced effect near the tip, where the flow has a tendency toward early separation. This accounts for the substantial drag and longitudinal stability improvements with the addition of a VG-1 at $\eta = 0.75$ (triple VG-1 configuration). It is believed that two VG-1's located at $\eta = 0.50$ and 0.75 would provide almost the same leading-edge thrust enhancement of the triple VG-1 configuration tested here.

Plots of $C_{P_{LE}}$ versus $C_{T_{loc}}$ at various spanwise positions for the single VG-1 configuration are presented in figure 37(a). The linearity of the STA 4 curve at high α is consistent with an attached flow condition. The reduction in slope of the curve from its initial value is attributed to the suction peak produced by the lower VG vortex, which additionally contributes to the leading-edge thrust but is not detected in the $C_{P_{LE}}$ measurements until it has passed over the leading edge at higher α. Without the suction contribution of this lower VG

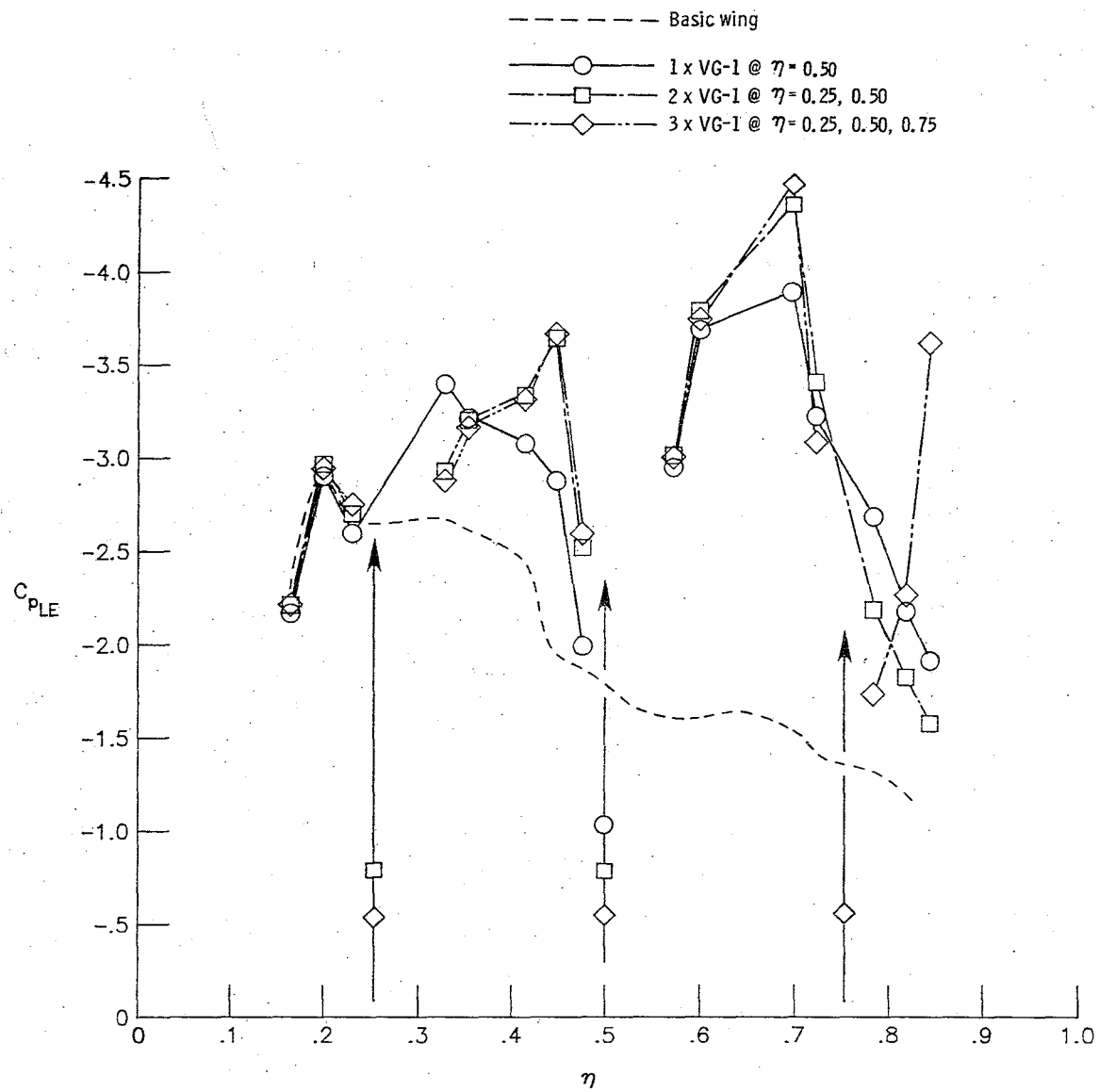

Figure 36.- Spanwise leading-edge static pressure distributions for single and multiple pylon vortex generator configurations at $\alpha = 14^{0}$.

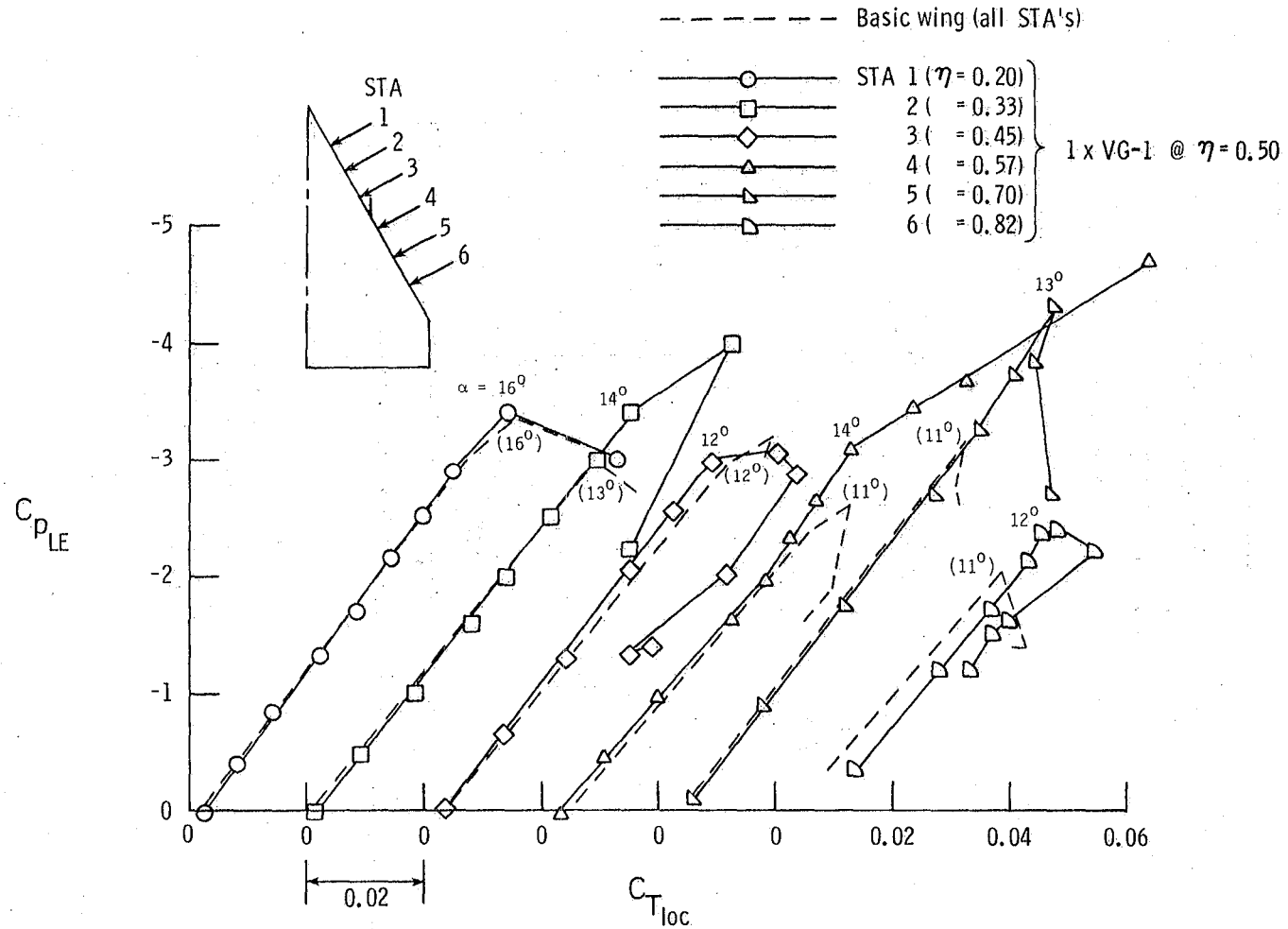

(a) Overall spanwise effect.

Figure 37.- Effect of the pylon vortex generator on leading-edge static pressure-thrust relationship. Selected high-α data points have been omitted for clarity. Angles in parentheses refer to basic wing data (see fig. 16).

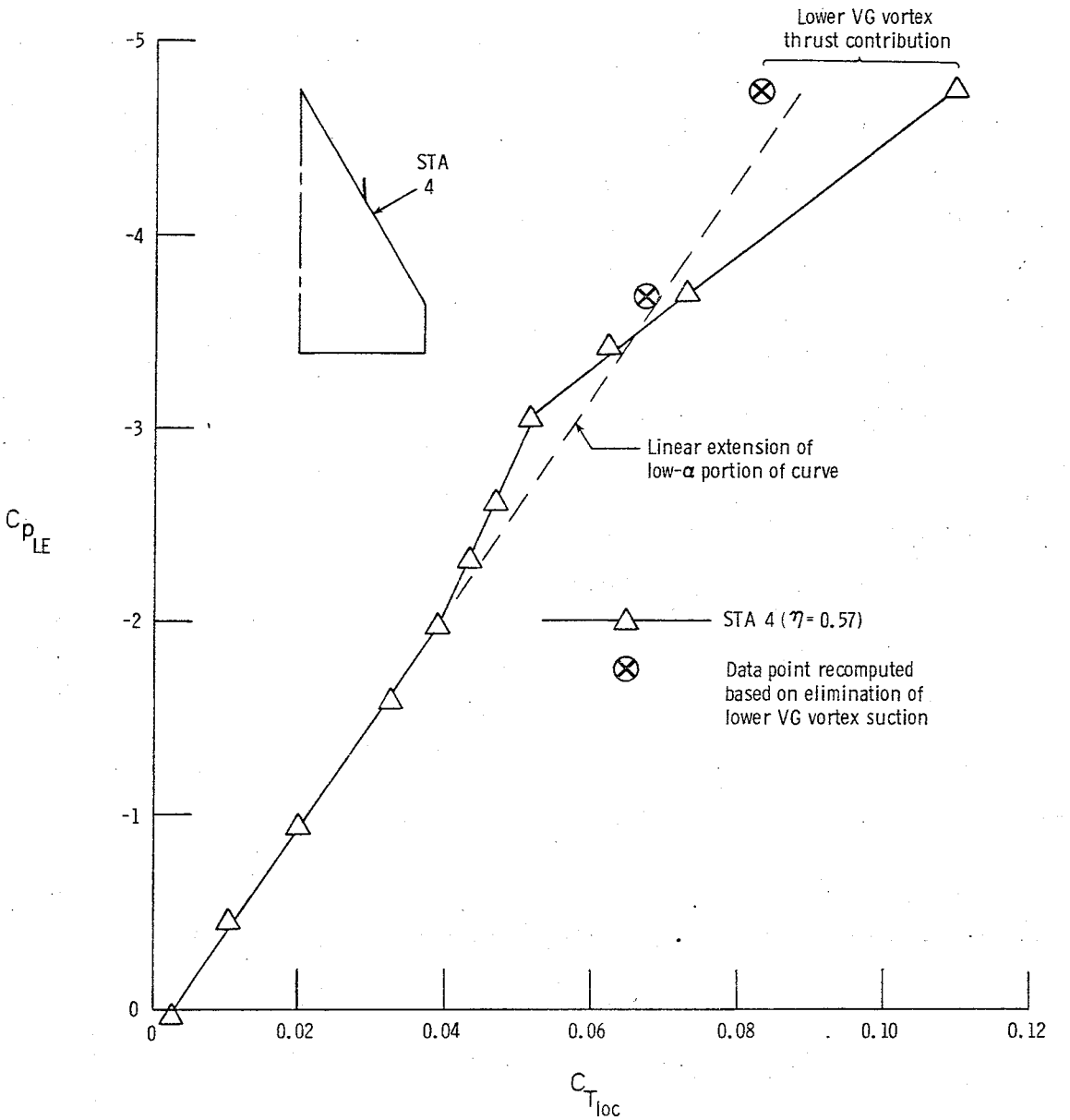

(b) Local outboard effect of lower VG vortex.

Figure 37.- Concluded.

vortex, therefore, the $C_{P_{LE}}$ versus $C_{T_{loc}}$ curve would continue along its initial slope. To check this hypothesis, the influence of the lower surface suction was removed by reintegrating to obtain leading-edge thrust using lower surface pressures measured on the basic wing at STA 4 for $\alpha = 18^{o}$ and 23^{o}. The resulting data points are plotted in figure 37(b), along with a replotting of the STA 4 data from part (a). Indeed, these recomputed points are found to shift much closer to the linear extension of the low-α portion of the curve, reflecting the significant thrust contribution from the lower-edge vortex.

In an attempt to alleviate the low-α drag penalty associated with vortex generators, possible reduction of the VG size without adversely affecting high-α performance was investigated. The size reductions were in the form of progressive lower-edge cut-off, which effectively reduced the leading-edge length of the VG, and back-edge cut-off, which reduced the chord of the device. In addition, a diagonal cutback (in effect removing the chordwise tip) was included as another means of VG size reduction. Geometric details of these size modifications are presented in figure 5.

Zero-α drag data for single VG configurations utilizing the various geometries tested appear in Table III. As expected, lower-edge (VG-1 to VG-2, 3) and diagonal cutbacks (VG-1 to VG-6, 7) resulted in substantial zero-α drag reductions. The initial chord reduction (VG-2 to VG-4) also produced a low-α drag improvement; however, further cutback (to VG-5) resulted in a drag increase. This anomalous result may be due to the construction method used. As previously noted, an additional

thickness was used on the outboard side of the VG for added stiffness to avoid excessive deflection. As sketched below, cutback to VG-5, thus, resulted in a thick base, with the additional pressure (base) drag appearing in the overall zero-α drag of the configuration.

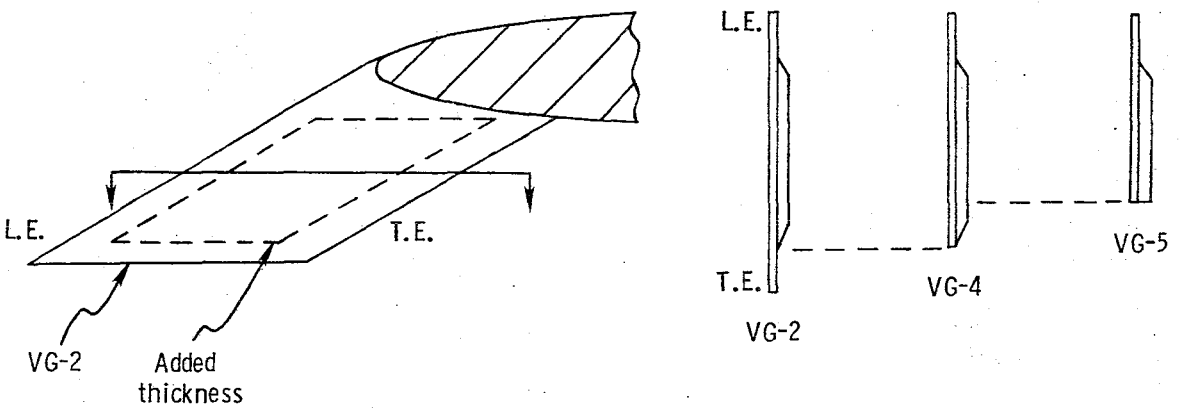

Sketch J

Figure 38 shows the overall drag and longitudinal stability effects of variations in VG leading-edge length (lower-edge cutback). A 30 percent reduction from VG-1 (to VG-2) results in the appearance of a C_A reversal at $\alpha \approx 13^o$. In addition, substantial drag increase and severe pitch-up are indicated at high α. Further reduction in leading-edge length (to VG-3; 60 percent reduction from VG-1) results in little further effect on drag up to 16^o α but a loss of effectiveness at higher α. This is also reflected by increased severity of pitch-up at $\alpha \approx 19^o$.

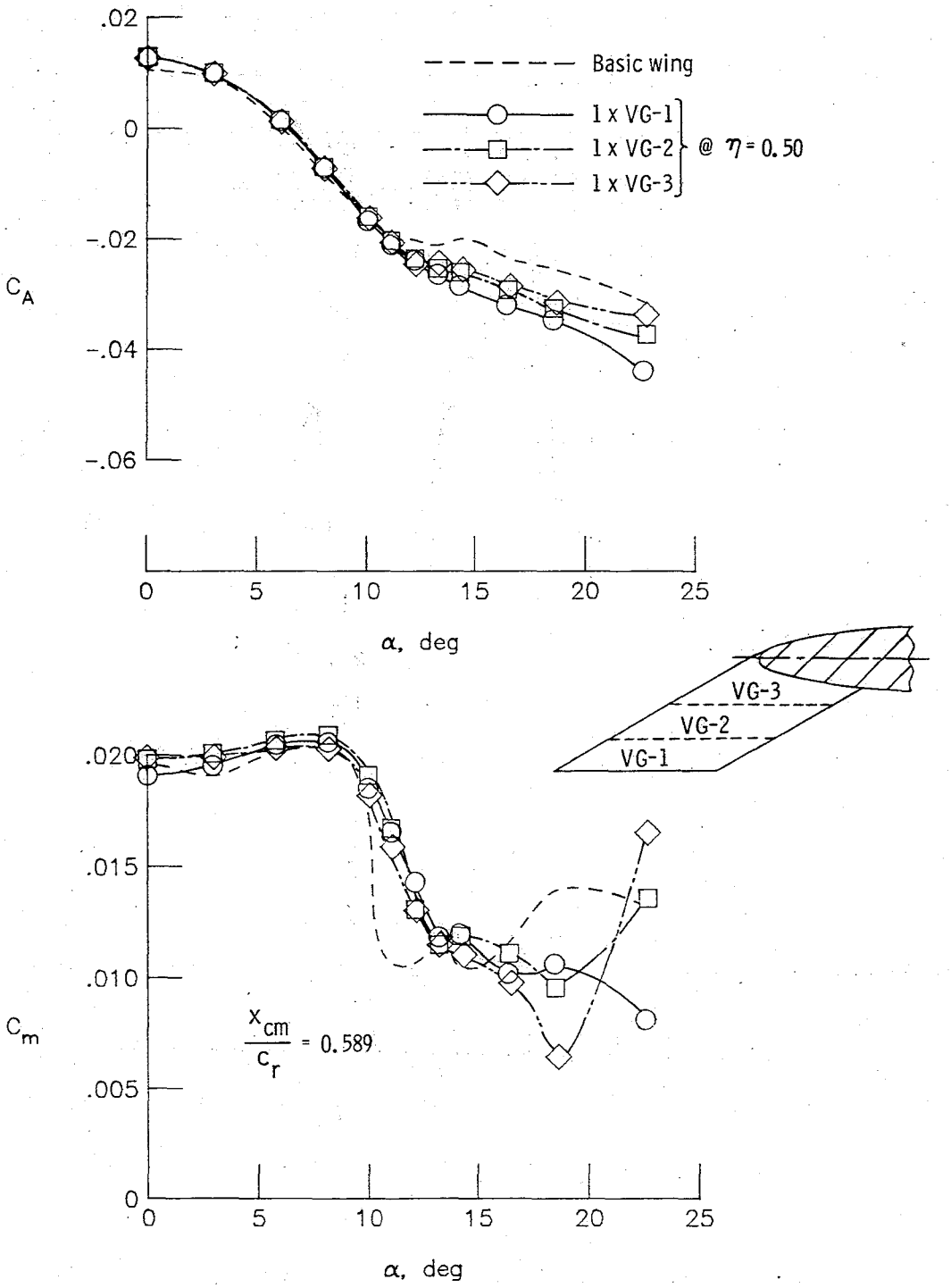

Figure 38.- Performance effects of pylon vortex generator leading-edge length reduction.

The primary function of the VG leading edge is to provide a sharp edge along which the VG vortex may form and build in strength before passing over the wing. A decrease in the length of this edge, therefore, would be expected to reduce the vortex strength. The accompanying reduction in downwash on the outboard side then results in earlier separation. This effect is evident in the static pressure distributions around the wing leading edge at $\alpha = 14^{o}$ (STA's 5 and 6), in figure 39(a). Figure 39(b) presents pressure distributions just outboard of the VG (STA 4) at $\alpha = 16^{o}$ and 19^{o}. With VG-3, there is no evidence of the lower-edge vortex suction on the lower surface pressures as was the case with VG-1. The lower vortex may, thus, be passing over the wing leading edge at a lower α. The opposite sense of rotation of this lower vortex would induce an upwash velocity outboard, leading to earlier separation; in addition, the associated suction peak on the lower surface and its contribution to the leading-edge thrust (shaded in fig. 39(b)) is lost. A second advantage of a long VG leading-edge length may, thus, be its ability to keep the lower VG vortex below the wing and acting near the leading edge to higher α.

The effects of VG chord reduction on drag and longitudinal stability are shown in figure 40. For structural reasons, VG-2 (30 percent leading-edge length reduction from VG-1) was used as the baseline geometry for analyzing this parameter. Axial force indicates that a 25 percent reduction in VG-2 chord (to VG-4) produces a drag improvement beyond 12^{o} α, in addition to the low-α drag reduction noted earlier. In addition, the severe pitch-up at $\alpha \simeq 19^{o}$ of the VG-2 has been

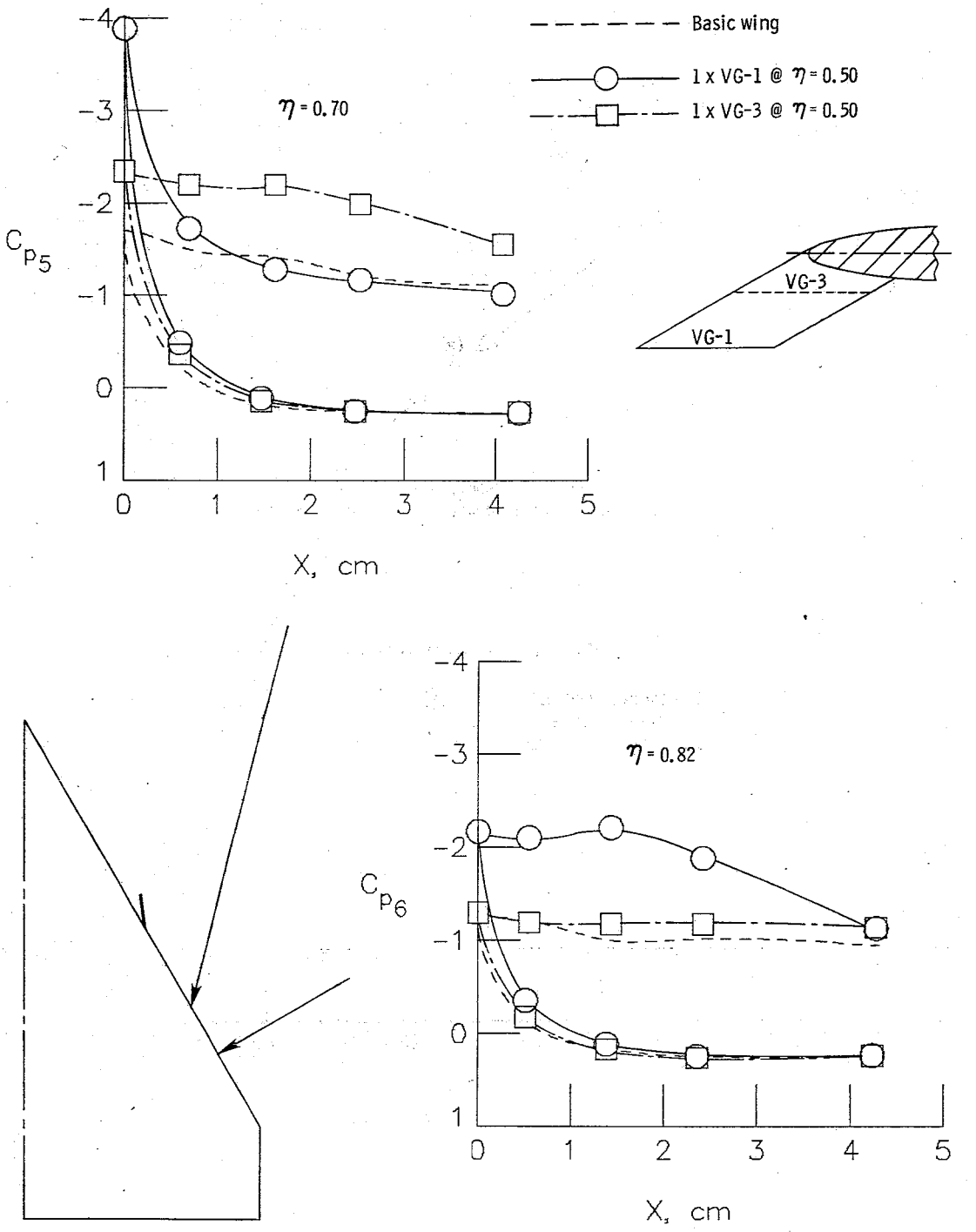

(a) $\alpha = 14^{o}$.

Figure 39.- Outboard static pressure effects of pylon vortex generator leading-edge length reduction.

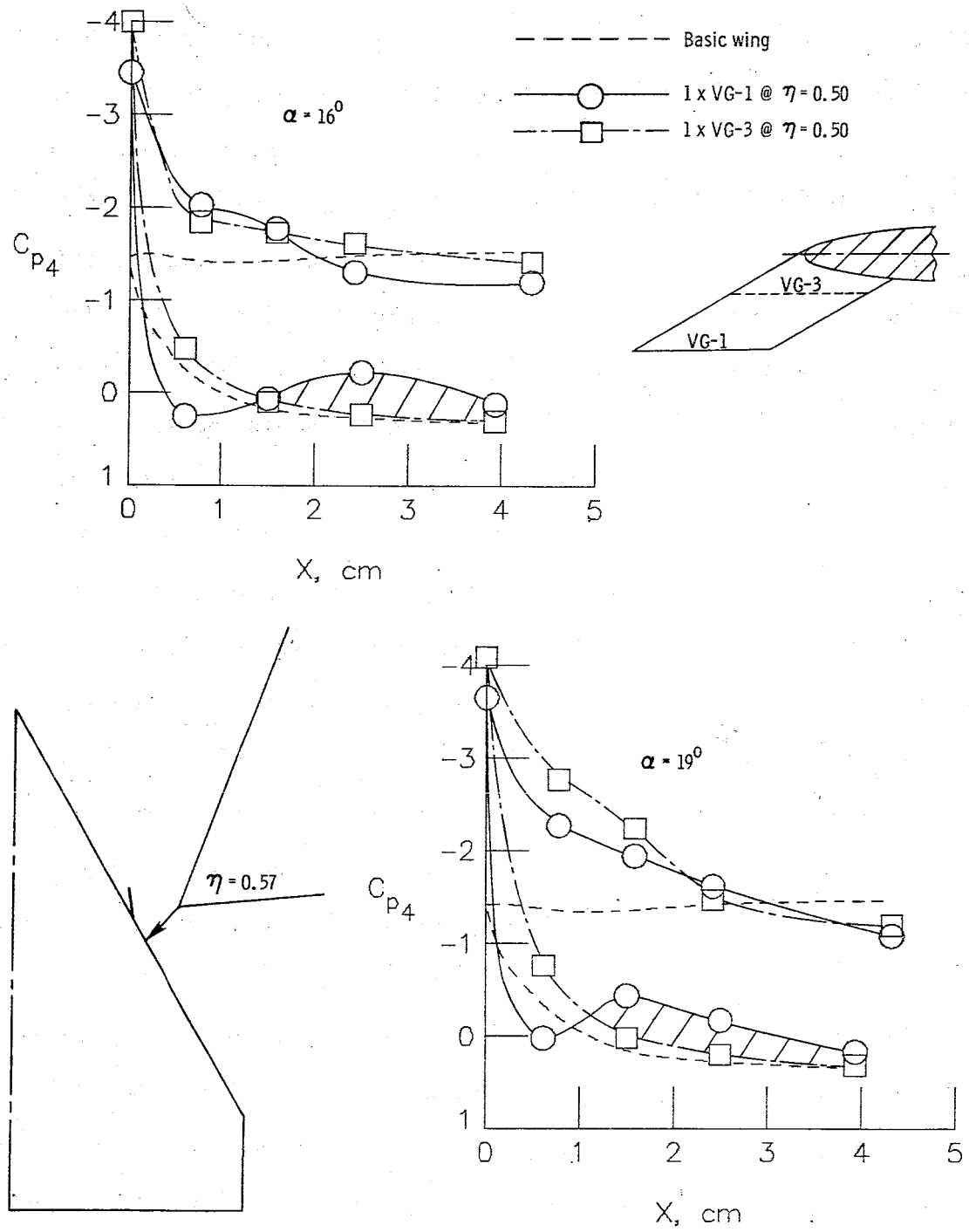

(b) $\alpha = 16^{\circ}$ and 19°.

Figure 39.- Concluded.

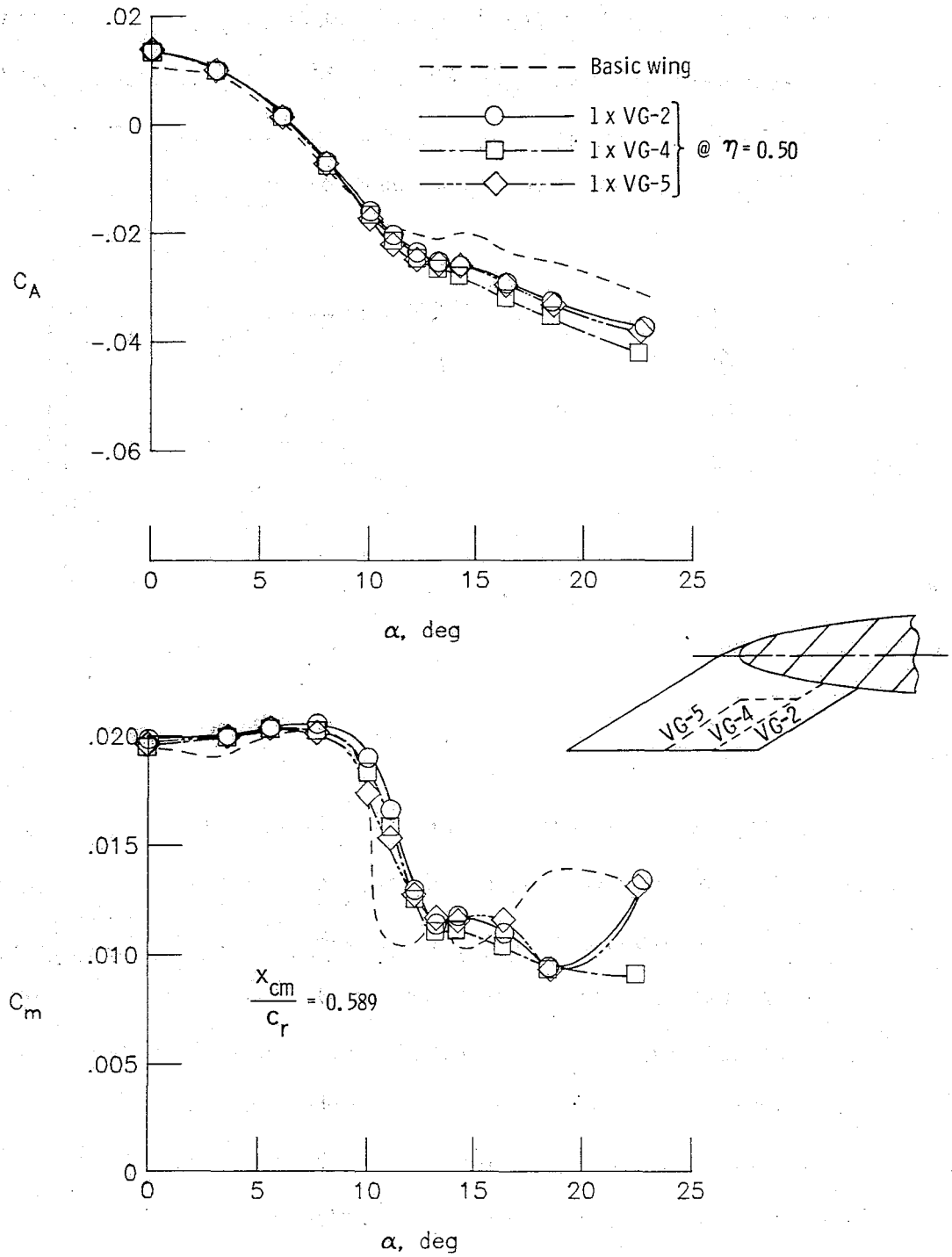

Figure 40.- Performance effects of pylon vortex generator chord reduction.

eliminated. Further chord reduction (to VG-5; 50 percent reduction from VG-2), however, results in increased high-α drag and reappearance of pitch-up at $\alpha \simeq 19^{o}$. Local thrust variations in figure 41 indicate that these trends result primarily from flow modifications outboard of the device. Substantial high-α thrust enhancement is indicated at STA's 5 and 6 with the initial chord reduction (VG-2 to VG-4), but this improvement is lost with further cutback (to VG-5). Therefore, there is a specific VG chord within the range tested which will produce the optimum combination of low- and high-α performance.

The original design of the vortex generator presumed that the flow mechanism depended totally on the vortex formed at its leading edge and passing over the wing upper surface. However, it now appears that the vortices formed at the lower and back edges of the device may be of importance. As the VG chord is reduced, the proximity of these edges to the VG leading edge eventually becomes such so as to cause interference between corresponding vortices. In addition, at a high enough α, these lower- and back-edge vortices may pass completely over the wing leading edge and interfere with the upper surface flow. Specific effects on performance would seemingly depend on the strength of these vortices, which depends partially on the length of the corresponding edges. However, at this stage there are insufficient data to provide definite conclusions on the VG flow mechanisms producing the trends observed with VG chord reduction. The geometries tested, however, did provide a general idea of the VG proportions required for optimum performance.

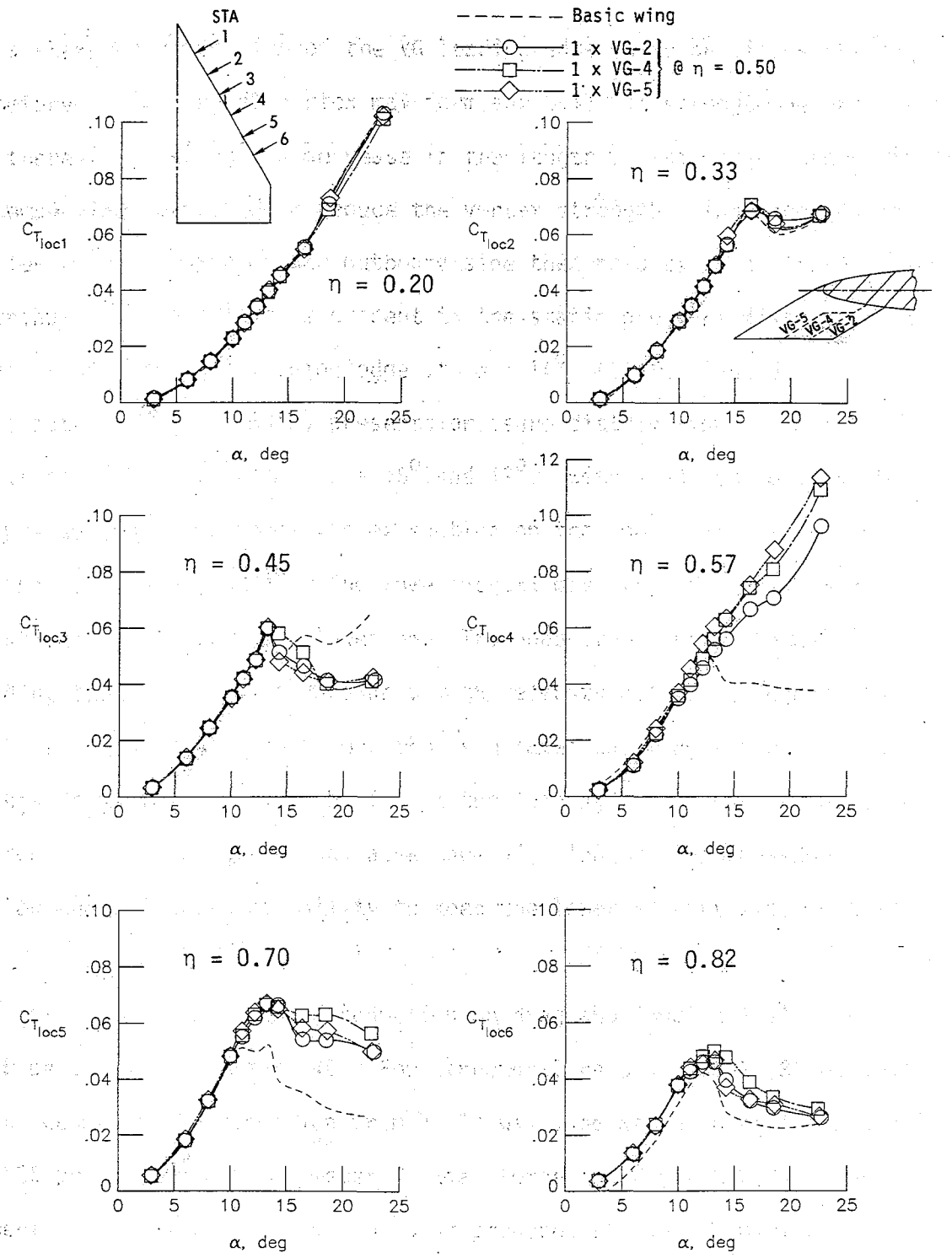

Figure 41.- Effects of pylon vortex generator chord reduction on leading-edge thrust.

Performance effects of simultaneous cutbacks of the lower and back edges of the VG, in the form of diagonal cuts (see fig. 5), will now be considered. Figure 42 presents force and moment data for single VG-1, 6, and 7 configurations. Axial force indicates a reduction in suction effectiveness beyond 13^{o} α with increasing cutback. In addition, the initial cutback (VG-1 to VG-6) results in pitch-up at $\alpha \simeq 19^{o}$, which becomes more severe with further reduction (to VG-7). Inspection of local thrust variations, in figure 43, reveals that these effects on high-α performance are again attributed to outboard flow modifications.

The losses resulting from cutback to VG-6 are most likely attributed to an effective elimination of the lower edge of the VG. This eliminates the lower surface suction peak produced by the lower-edge vortex and, thus, its contribution to the leading-edge thrust. Another possibility is that the proximity of the leading and back edges near the tip of the VG-6 may cause a weakening of the VG leading-edge vortex as a result of interference with the counter-rotating back-edge vortex. The additional loss of effectiveness with cutback to VG-7 is believed to be primarily the result of leading-edge length reduction. As previously noted, this reduces the strength of the VG leading-edge vortex by reducing the distance over which it forms.

The possible use of pylon vortex generators also as carriers of slender external stores (such as air-to-air missiles) will now be considered. The VG tested was similar to VG-1 but had an extended chord in order to provide a mounting position for the wooden dowel simulating the external store (see fig. 6). This device was tested with (VG-8)

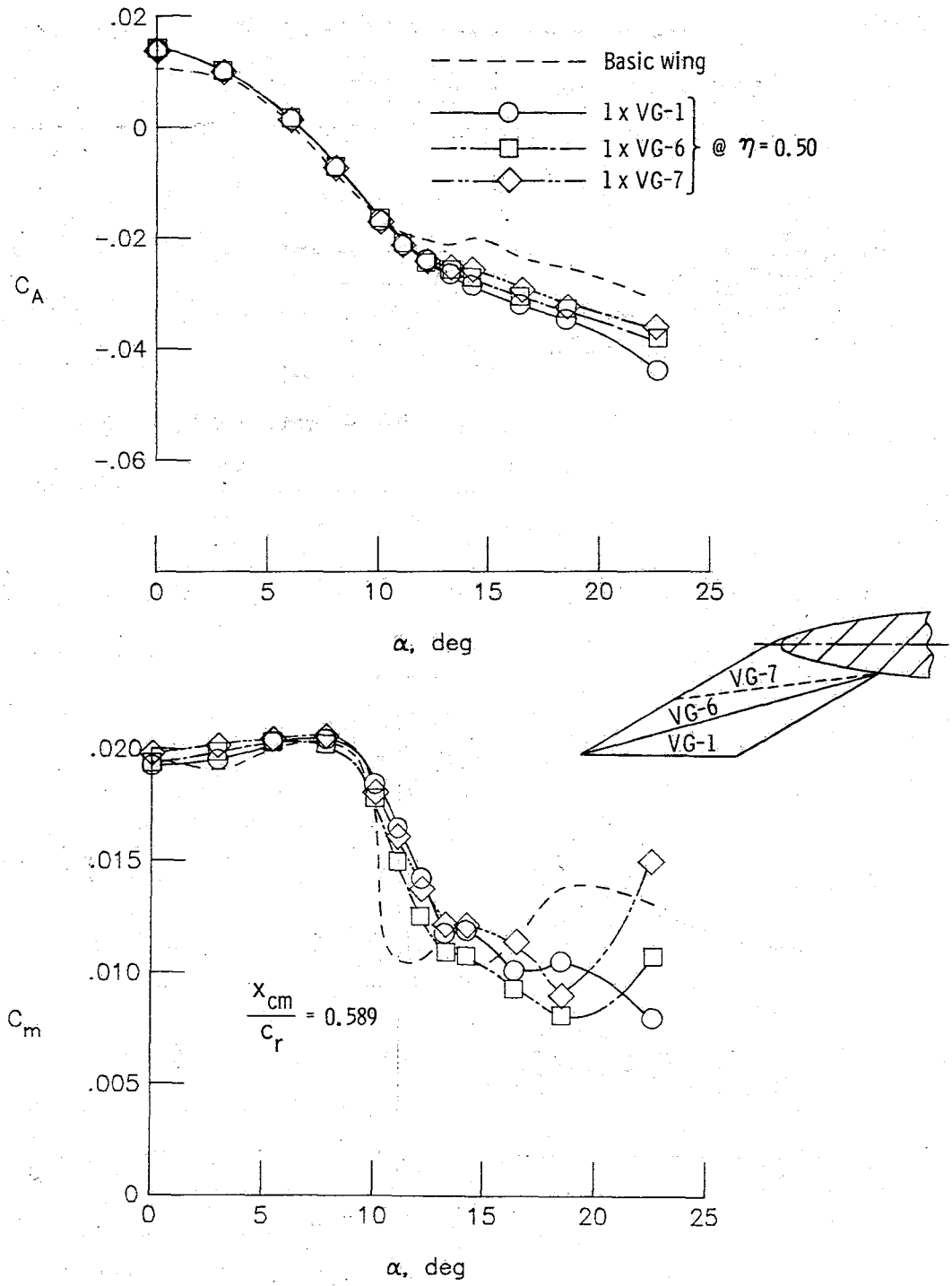

Figure 42.- Performance effects of pylon vortex generator diagonal cutback.

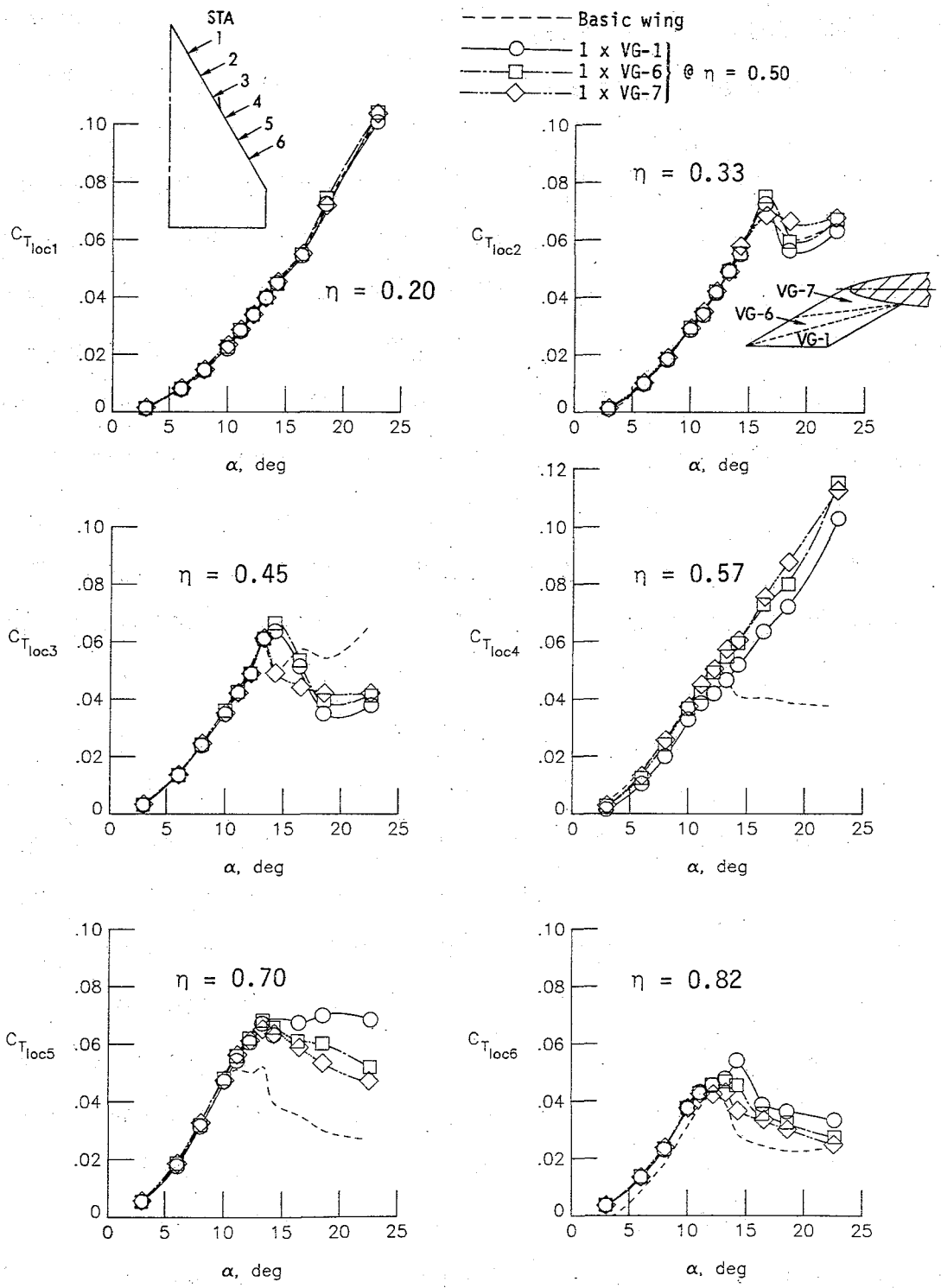

Figure 43.- Effects of pylon vortex generator diagonal cutback on leading-edge thrust.

and without (VG-9) the store in single VG configurations (at $\eta = 0.50$). Table III indicates a low-α drag penalty due to the chord extension and store addition; however, this is not of concern since a drag increase would in any case be obtained with a pylon. Selected results of force and moment measurements on VG-8 and VG-9 configurations are presented and compared with the baseline VG-1 configuration (at $\eta = 0.50$) in figure 44. The C_A curve indicates a loss of drag performance beyond 12^o α with VG-8 as compared with VG-1. Static pressure data, not presented, indicate that the external store prevents the formation of a vortex at the lower edge of the VG, thereby reducing the lower surface contribution to the wing leading-edge thrust. However, a significant high-α drag advantage over the basic wing is still realized. In addition, VG-8 delays the pitch-up of the basic wing by approximately 2^o, to $\alpha \simeq 13^o$.

Figure 44 shows that once the slender external store has been released, the extended chord VG-9 continues to perform as a drag reducer. However, the drag reduction effectiveness of the device appears to have been hampered by the chord extension (from VG-1). Surface pressure data indicate that this may be a result of the persistence of the lower-edge vortex along the extended edge, eliminating its suction effect on the wing leading-edge region. However, the resulting drag reduction would still be an improvement over a conventional pylon configuration, which would continue to produce a drag penalty even at higher α. Further research should be performed on modifications that will allow for the realization of a greater portion

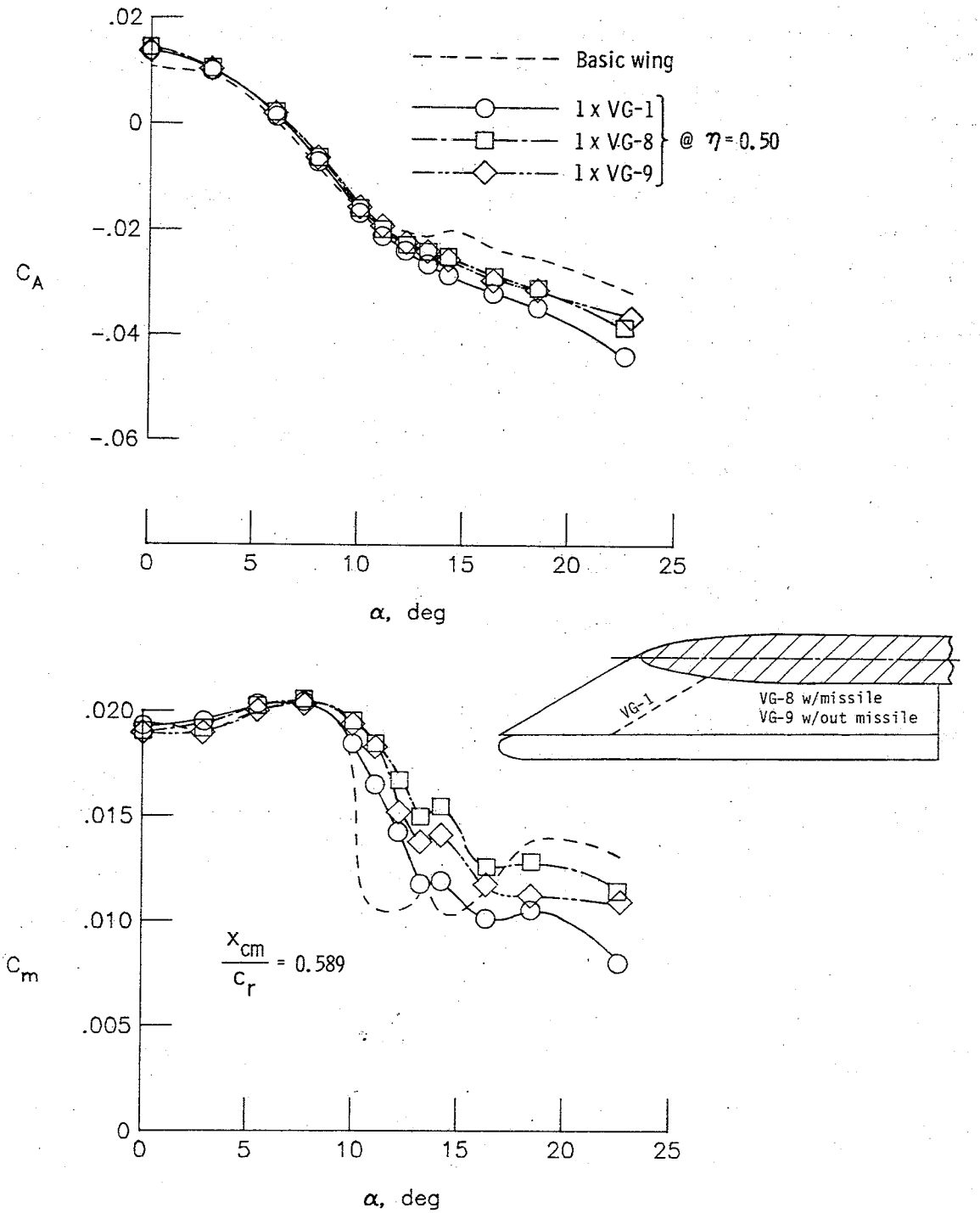

Figure 44.- Performance of an extended chord pylon vortex generator utilized as a carrier of slender external stores.

of the VG drag-reduction potential, both with and without the external store. Variations in VG chord length and chordwise location of the store along the lower edge of the VG may be initial steps.

In summary, the pylon vortex generator produces substantial improvements in high-α drag and longitudinal stability when utilized on highly swept leading edges. The lower VG vortex apparently plays an important role through its own contribution to the leading-edge thrust and, thus, should be considered in the design of the VG shape. The mutual interaction of multiple VG's acts to further enhance the leading-edge suction along the span. However, a low-α drag penalty is characteristic of the vortex generator. VG size reductions in the form of leading-edge length and diagonal cutbacks reduce the low-α drag penalty but also result in a loss of performance at high α. Reduction in VG chord to a certain degree produces performance improvements at both low and high α. The vortex generator has potential also as a carrier of slender external stores. Although the performance of the extended chord VG is not as efficient as that of the baseline VG-1, substantial drag and longitudinal stability improvements over the basic wing are produced both with and without the external store.

Sharp Leading-Edge Extension

The common basis of the devices discussed thus far has been that of maintaining attached flow at the wing leading edge in order to retain leading-edge suction to higher α. An alternative to this conventional approach of drag reduction is provided by the sharp leading-edge extension (SLEE), or vortex plate, which manipulates the natural tendency toward flow separation and vortex formation at a swept leading edge. A sharp-edged plate lying in the plane of the wing lower surface and projecting ahead of the wing leading edge forces separation along its leading edge and subsequent vortex formation. Ideally, this vortex is maintained just ahead of the wing leading edge along the entire span, with its associated suction acting on the leading-edge thickness to generate a thrust force. Flow reattachment just aft of the leading-edge curvature helps to maintain attached chordwise flow on the wing upper surface (see sketch A in INTRODUCTION).

Balance data for a SLEE configuration utilizing an 0.71 cm extension (see fig. 8) is presented in figure 45. This device had a spanwise coverage of η = 0.25 to 0.93 and was tested with an F-2 fence at its inboard edge (η = 0.25). The fence was intended to obstruct the spanwise boundary layer flow originating between the wing apex and the inboard edge of the SLEE, to allow the formation of a clean SLEE vortex. This fence was shown in previous testing (ref. 5) to delay a mid-α longitudinal instability produced by the SLEE and to maintain C_A improvement to significantly higher α. At low α, the vortex suction is insufficient to offset the additional drag of the SLEE, accounting

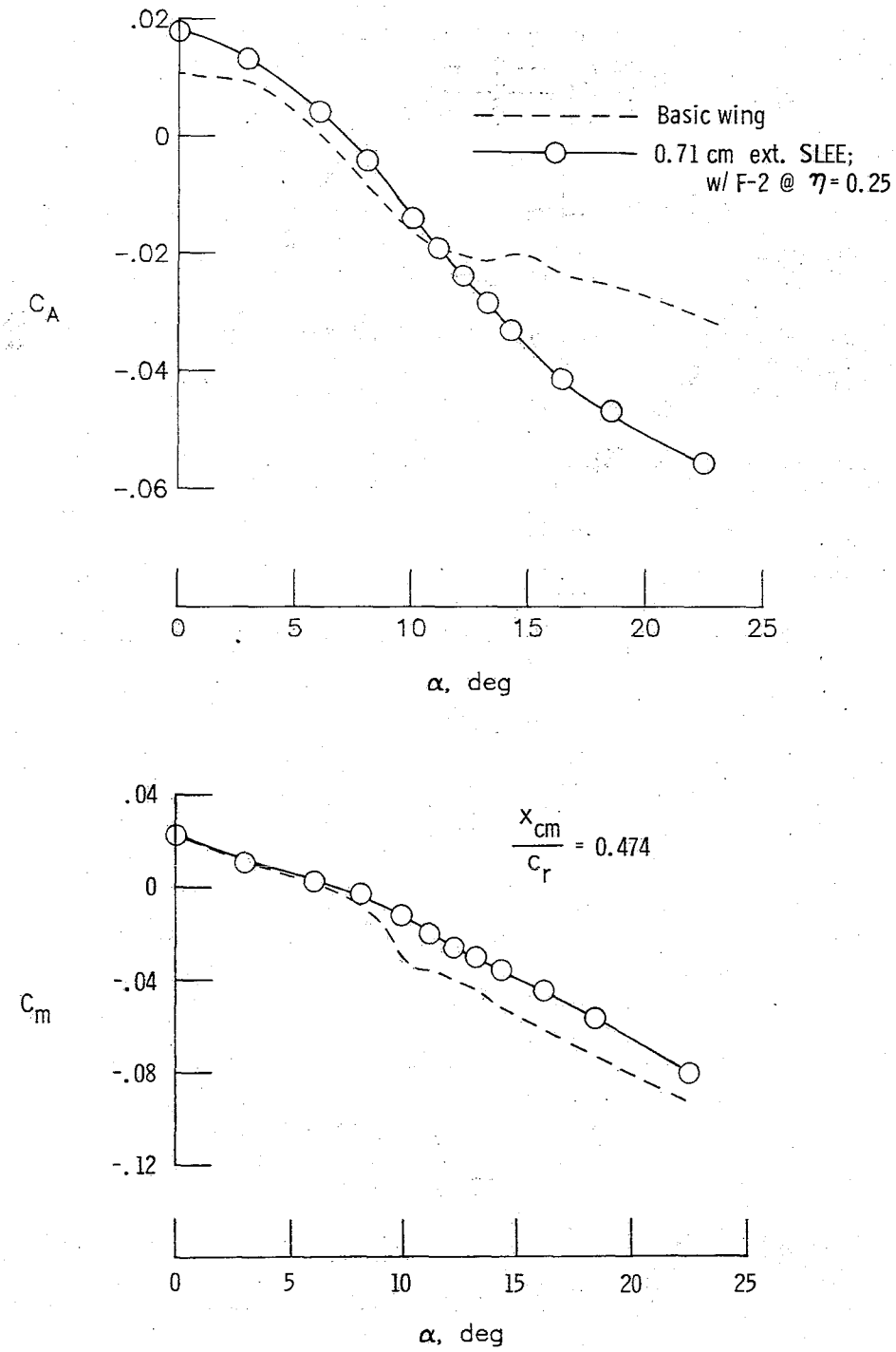

Figure 45.- Force and moment characteristics of a sharp leading-edge extension configuration.

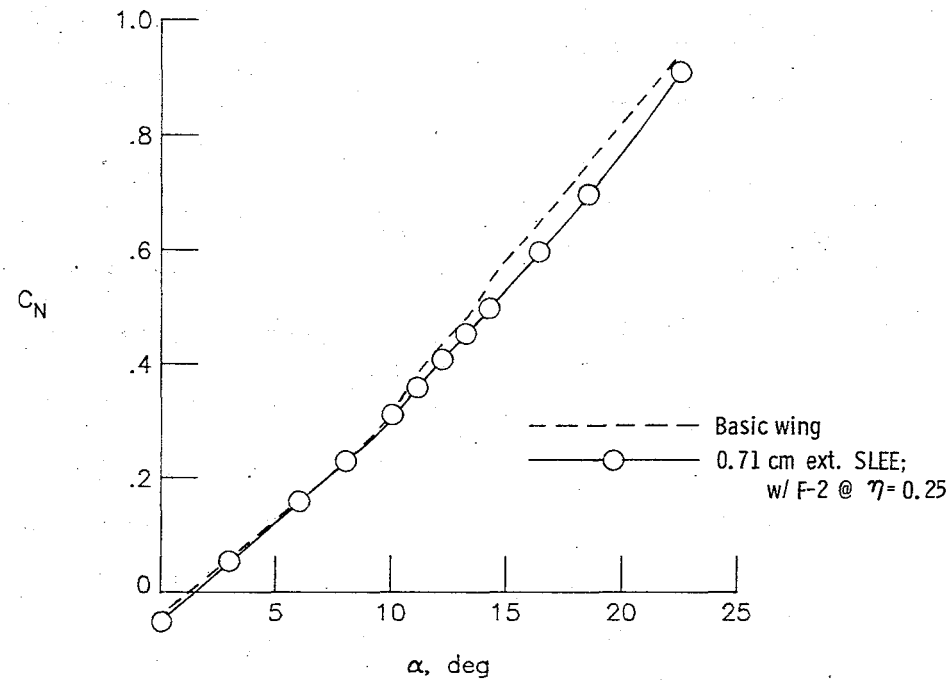

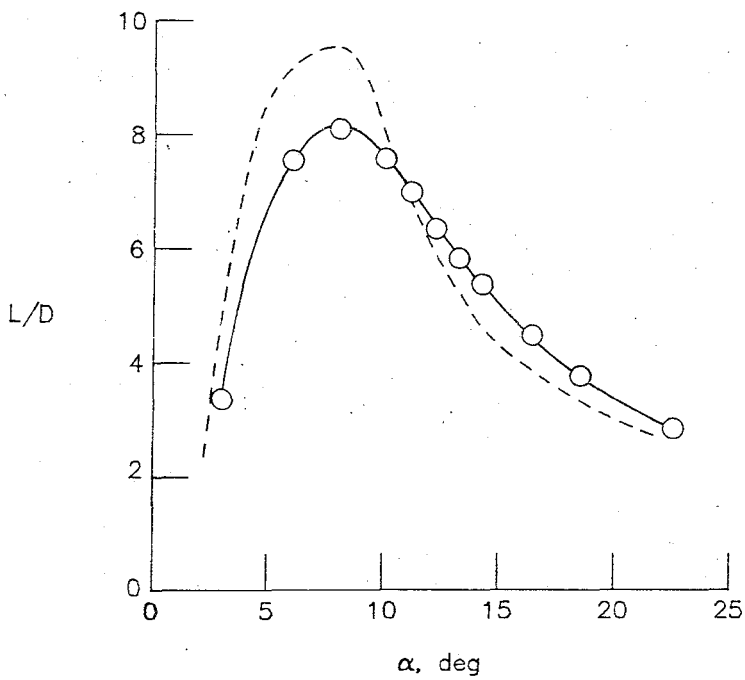

Figure 45.- Continued.

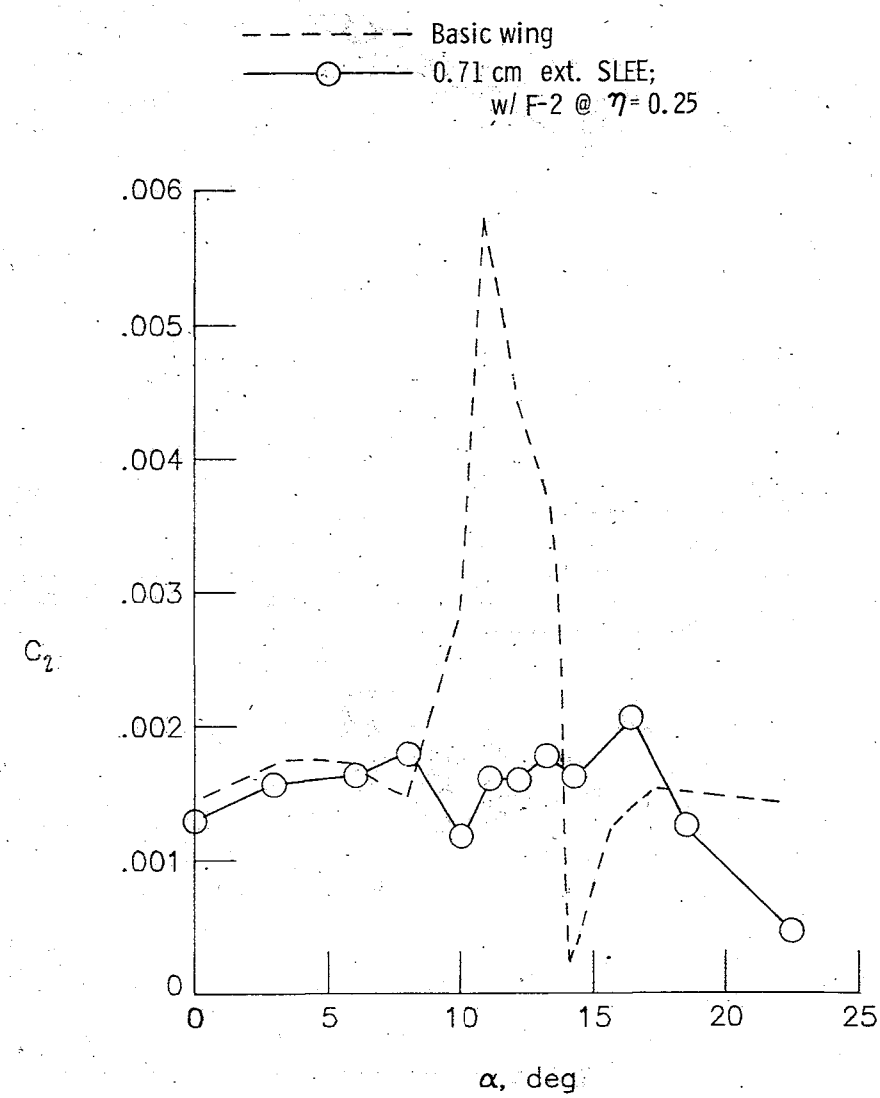

Figure 45.- Concluded.

for the net C_A increase. Therefore, to avoid a cruise drag penalty, the SLEE should be designed as a retractable device. Beyond $\alpha \simeq 12^o$, the vortex strength and its optimum position produce substantial C_A improvements over the basic wing. The ability of the SLEE to maintain its vortex ahead of the leading edge is also reflected in delayed onset of vortex lift, reducing the C_N beyond $\alpha \simeq 10^o$. From a performance standpoint, the low-α drag increase results in severe losses in L/D. Beyond 12^o α, however, substantial improvements are noted, with the L/D increment tapering off gradually with increasing α. In addition, the rolling moment instability of the basic wing between 8^o and 14^o α is eliminated. The longitudinal stability of the configuration is slightly reduced from that of the basic wing, but the linearity of the C_m curve is significantly improved. Here, the moment reference center has once again been selected to better show up the effects of the device. The new location (see DATA REDUCTION) is 3.82 cm (5 percent of root chord) aft of the original moment reference center given in figure 2.

Static pressure distributions around the wing leading edge for the 0.71 cm ext. SLEE configuration at $\alpha = 12^o$ are presented in figure 46. Attached leading-edge flow inboard of STA 6 on the basic wing results in high suction peaks near the leading edge with subsequent pressure recovery on the upper surface. However, the vortex-induced reattachment due to the SLEE produces a stagnated flow condition, with elimination of the peak negative pressures near the leading edge, but with high negative pressures over a greater portion of the leading-edge curvature. Note, especially, the high negative C_p on the lower

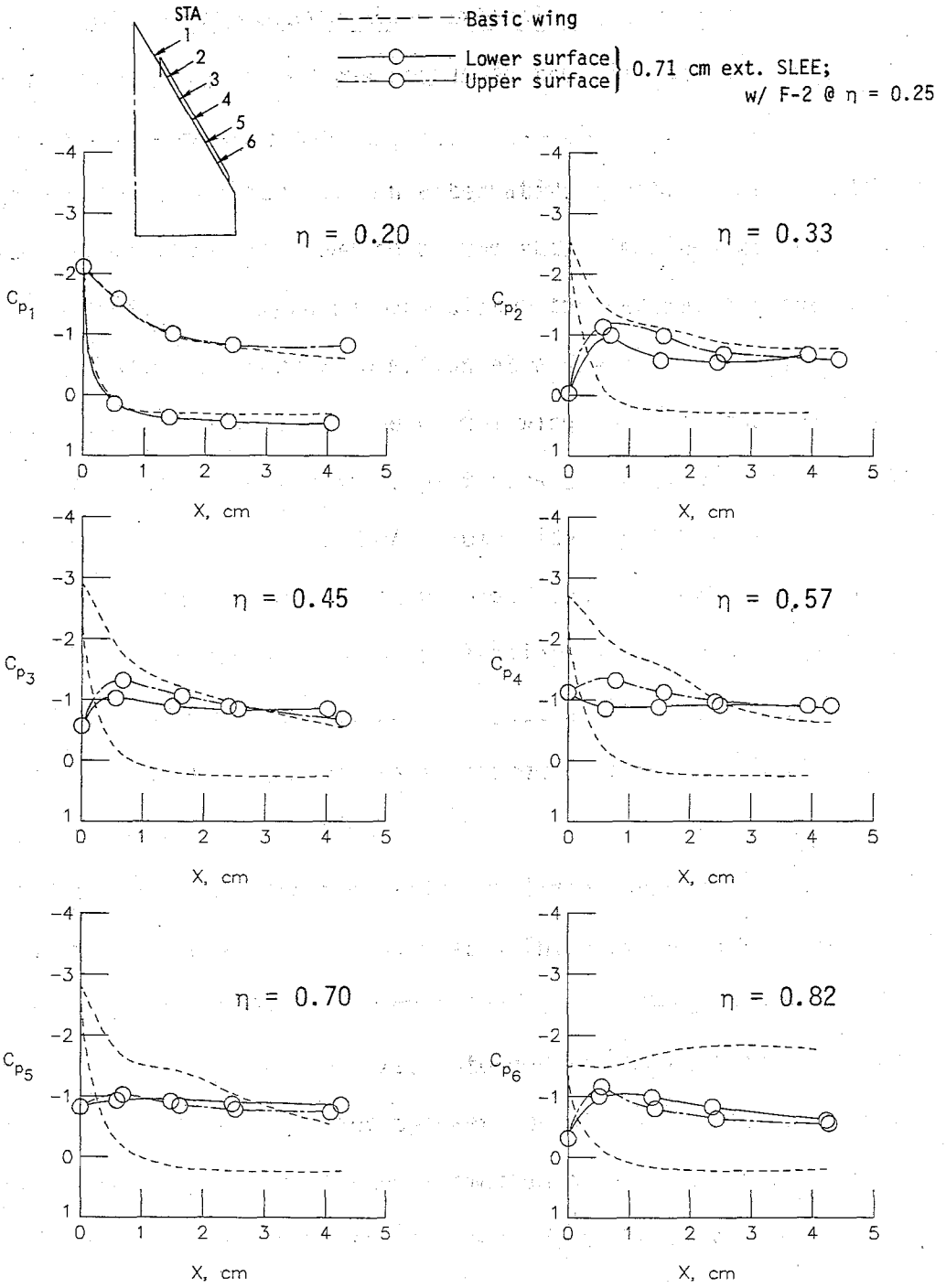

Figure 46.- Effects of the sharp leading-edge extension on static pressure distributions around the leading edge at $\alpha = 12^{o}$.

surface in contrast with the positive values measured on the basic wing. With the basic wing at a lifting condition, the stagnation point occurs just below the leading-edge curvature. The associated positive pressure acting on the forward sloping surface (see sketch K, below) contributes a positive axial force and, therefore, drag. On the other hand, when the stagnation point lies on the lower surface of the SLEE, the positive pressure produces no axial force (sketch K). In addition, the high flow velocity at the SLEE edge develops a high suction level to generate a thrust force.

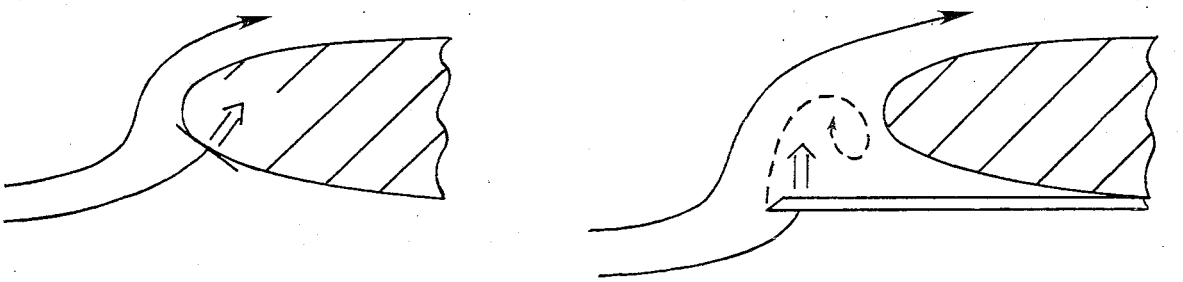

Basic wing w/ SLEE

Sketch K

Leading-edge pressure variations, in figure 47, indicate that at low α the leading-edge suction produced by the SLEE vortex is substantially less than the potential flow suction of the basic wing. However, once potential flow is lost, the SLEE eventually provides an improvement over the basic wing (beyond $\alpha \simeq 15^{o}$ at $\eta = 0.724$, $\alpha \simeq 19^{o}$ at $\eta = 0.416$). Static pressure distributions around the wing

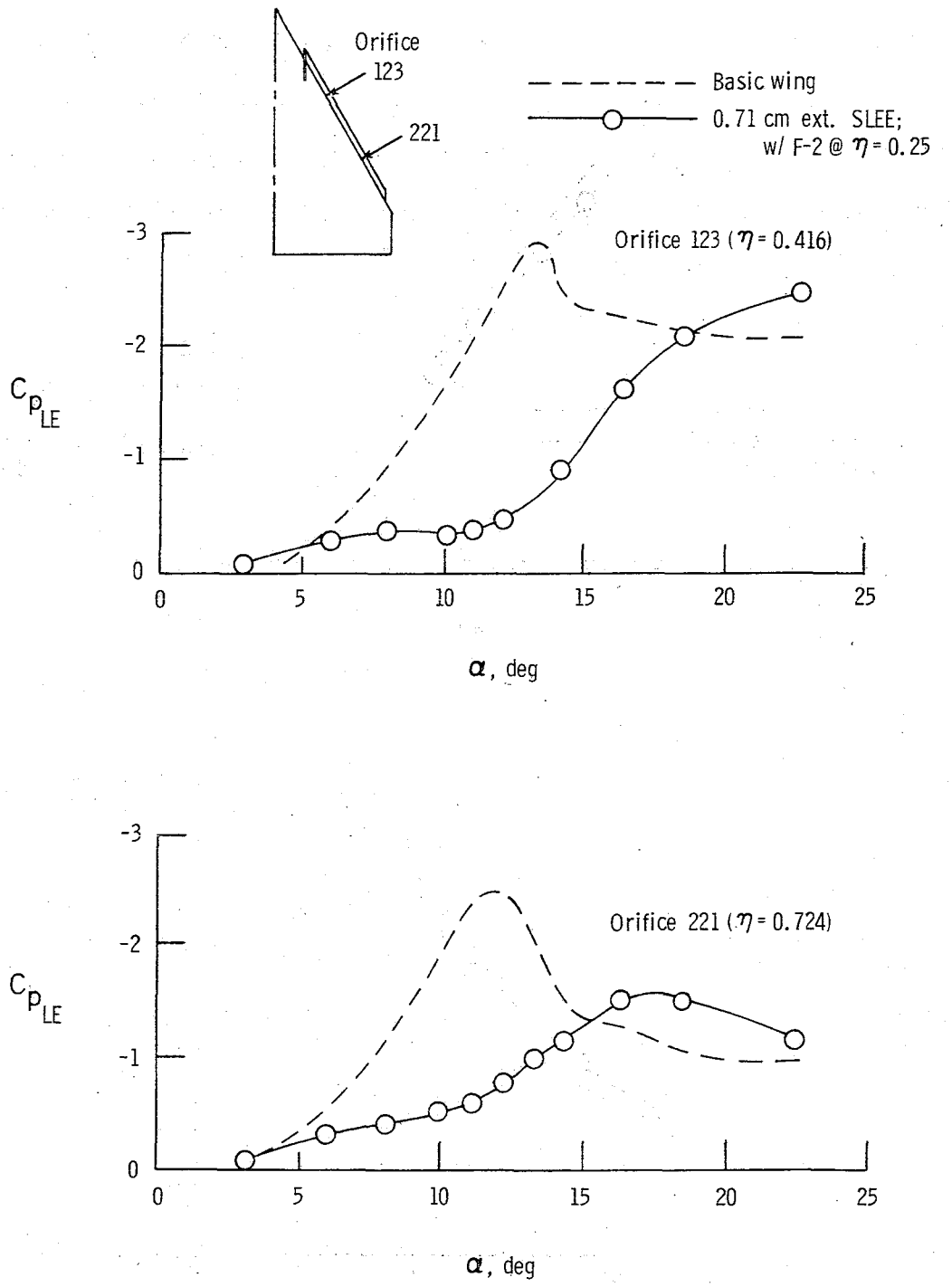

Figure 47.- Leading-edge suction effects of the sharp leading-edge extension.

leading edge at $\alpha = 22^{o}$ (fig. 48) indicate that the greatest contribution to the leading-edge thrust improvement comes from the low pressures induced on the lower surface. The accelerated loss of thrust at STA 1 may be attributed to the unsweeping of the upper surface isobars by the fence (see Fence section). The spanwise $C_{T_{loc}}$ distributions, in figure 49, are consistent with the $C_{p_{LE}}$ data just presented. At $\alpha = 12^{o}$, the leading-edge thrust produced along the SLEE falls below that of the basic wing; however, by 23^{o} α, substantial improvements are noted along the entire length of the device. Decreasing thrust increment toward the tip suggests an expansion or diffusion of the SLEE vortex core due to increasing upwash and entrainment effects. Means to alleviate the loss of SLEE effectiveness due to vortex diffusion will be discussed later.

Optimizing the SLEE extension will now be considered as a possible means of further performance improvements. The possibility of such improvements is suggested by the fact that over-extension of the SLEE would result in reattachment on the device itself, with local suction peaks and the possibility of separation near the wing leading edge. In addition, the vortex suction would mainly act in the normal direction, with little effect on axial force. This condition is depicted in sketch L, below:

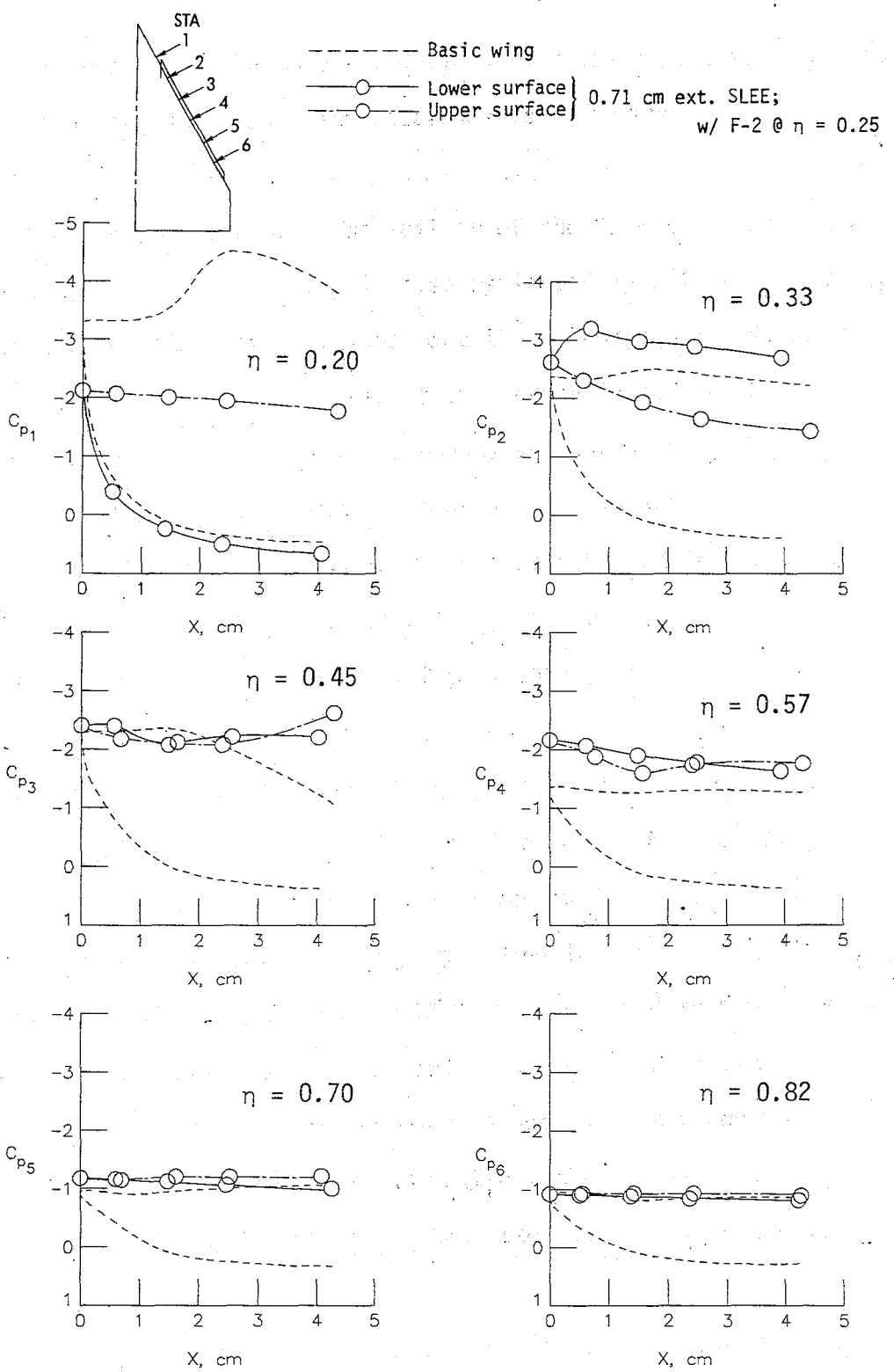

Figure 48.- Effects of the sharp leading-edge extension on static pressure distributions around the leading edge at $\alpha = 22^{o}$.

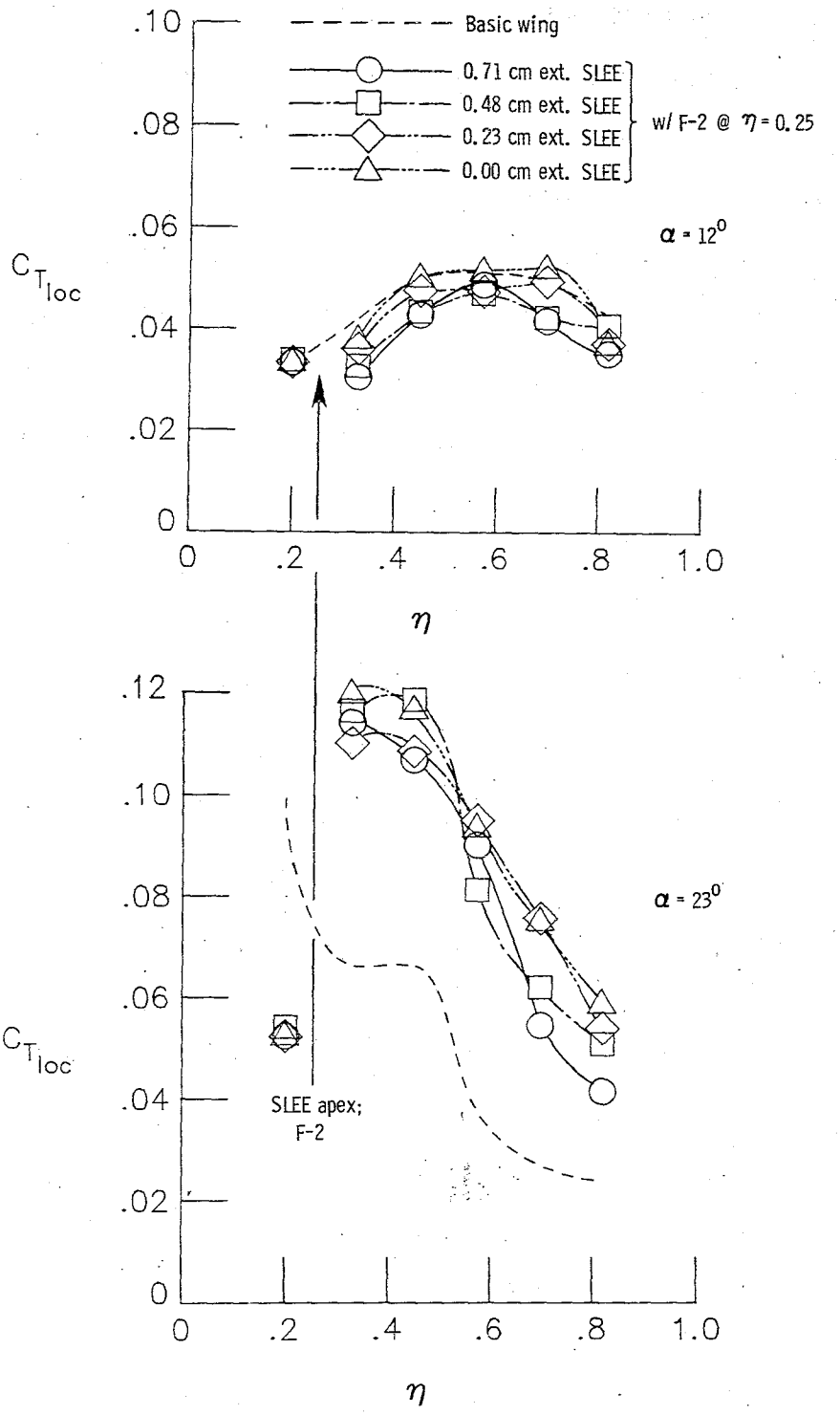

Figure 49.- Effects of SLEE extension on spanwise distribution of leading-edge thrust.

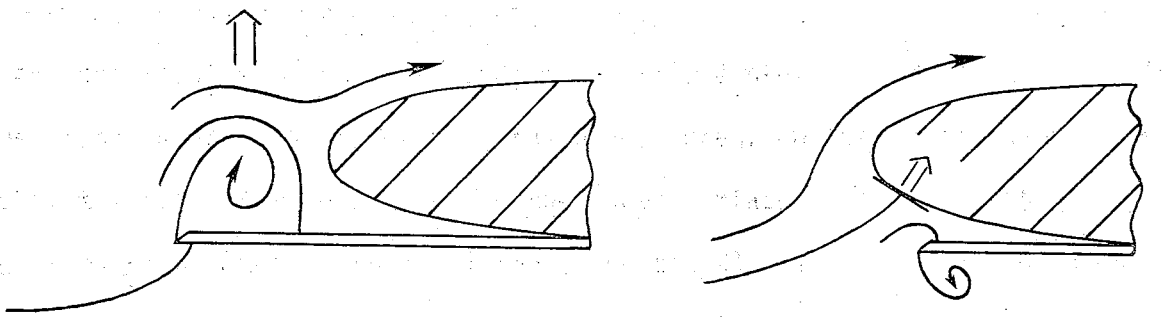

Sketch L

However, considering the range of extensions tested here, the over-extended condition is unlikely to be a factor except in a very narrow α range. Nevertheless, this condition does provide a conceptual upper bound for the SLEE extension. On the other hand, under-extension of the SLEE may not allow the stagnation point to move to the SLEE even at high α, leading to a large drag contribution, as discussed previously (see sketch L). Therefore, the minimum requirement for the SLEE extension would appear to be that it project ahead of the stagnation point at the highest α of interest.

Selected balance data for configurations utilizing SLEE extensions ranging from 0.71 to 0 cm (with an adjacent F-2 fence at the SLEE apex) are presented in figure 50. Little effect from SLEE extension is evident in C_A up to $\alpha \simeq 16^o$. At higher α, however, decreasing extension results in progressively improved axial force characteristics, with the

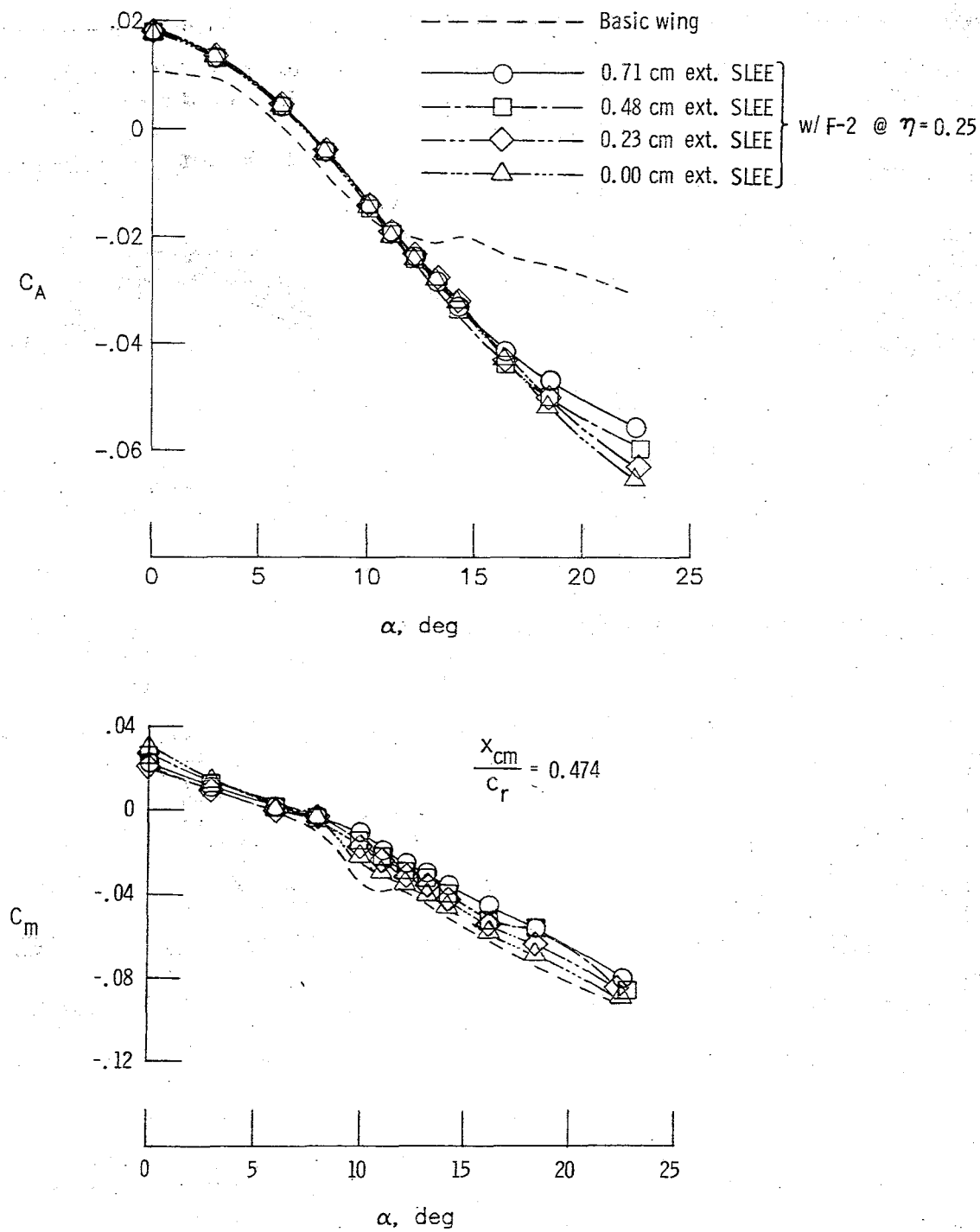

Figure 50.- Effects of SLEE extension on performance.

improvements continuing down to zero extension. In addition, the longitudinal stability of the configuration is slightly improved. Although not presented here, effects on normal force and lift-to-drag are minor.

Comparison of static pressure distributions around the wing leading edge for the 0.71 and 0 cm SLEE extensions (fig. 51) indicates a delay in onset of vortex suction on the leading edge as the SLEE extension is reduced. At $\alpha = 12^{o}$, the 0.71 cm ext. SLEE configuration is characterized by stagnated leading-edge flow; whereas with the 0 cm extension, attached flow still persists on the upper surface. Apparently, the vortex size with zero extension is such so as to produce a stagnated condition only on the lower portion of the leading-edge region (see STA 5 inset sketches). This delay is shown in figure 52 to pay off in improved leading-edge thrust at higher α. At the highest angles tested, a distinct advantage with reduced SLEE extension appears only at STA's 5 and 6. However, at higher angles, thrust improvements would also be expected at the remaining spanwise stations, as the SLEE vortex moves inboard. While the adverse inboard effect of the fence is again seen at STA 1, the favorable outboard effect at STA 2 allows for continued thrust improvement to the highest angles tested.

As already noted, the purpose of locating a fence inboard of the SLEE was to aid in the formation of a clean SLEE vortex. The possibility of substituting a chordwise slot (w/SC-1) for the fence was investigated on the 0.48 cm ext. SLEE configuration. Selected results appear in figure 53. Axial force is slightly improved in the mid-α range with the use of the slot; however, early loss of slot

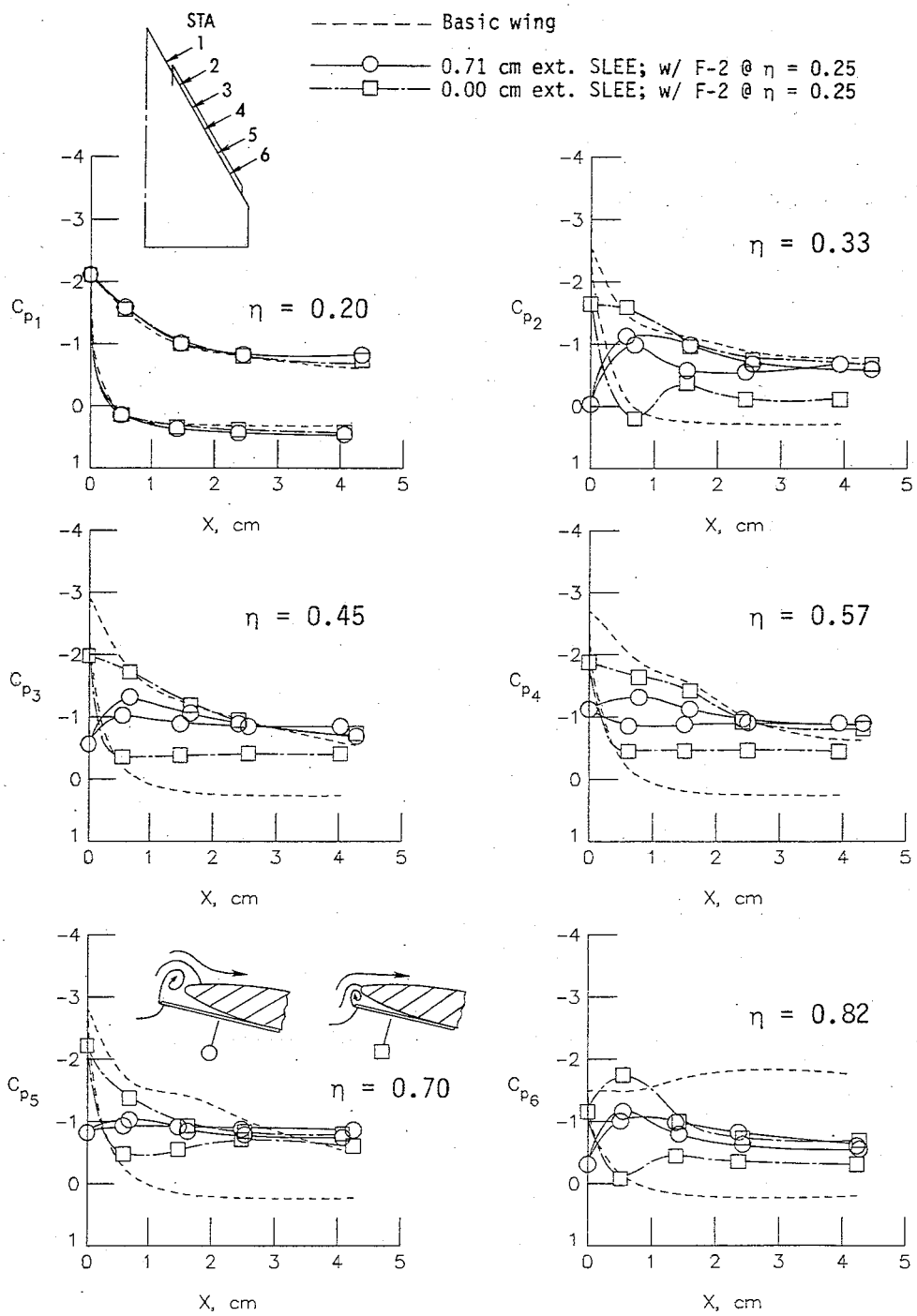

Figure 51.- Effects of SLEE extension on static pressure distributions around the leading edge at $\alpha = 12^{0}$.

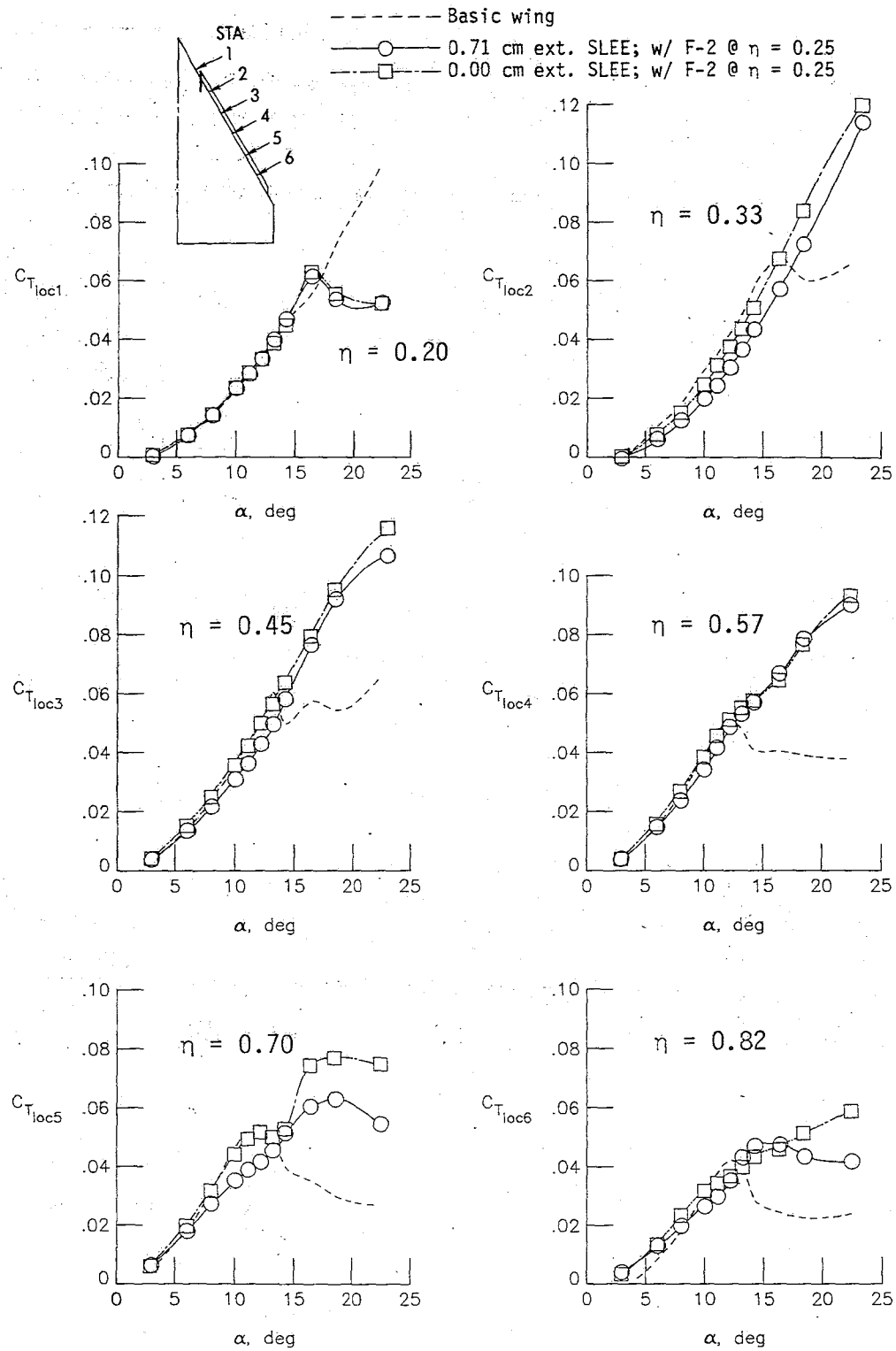

Figure 52.- Effects of SLEE extension on leading-edge thrust.

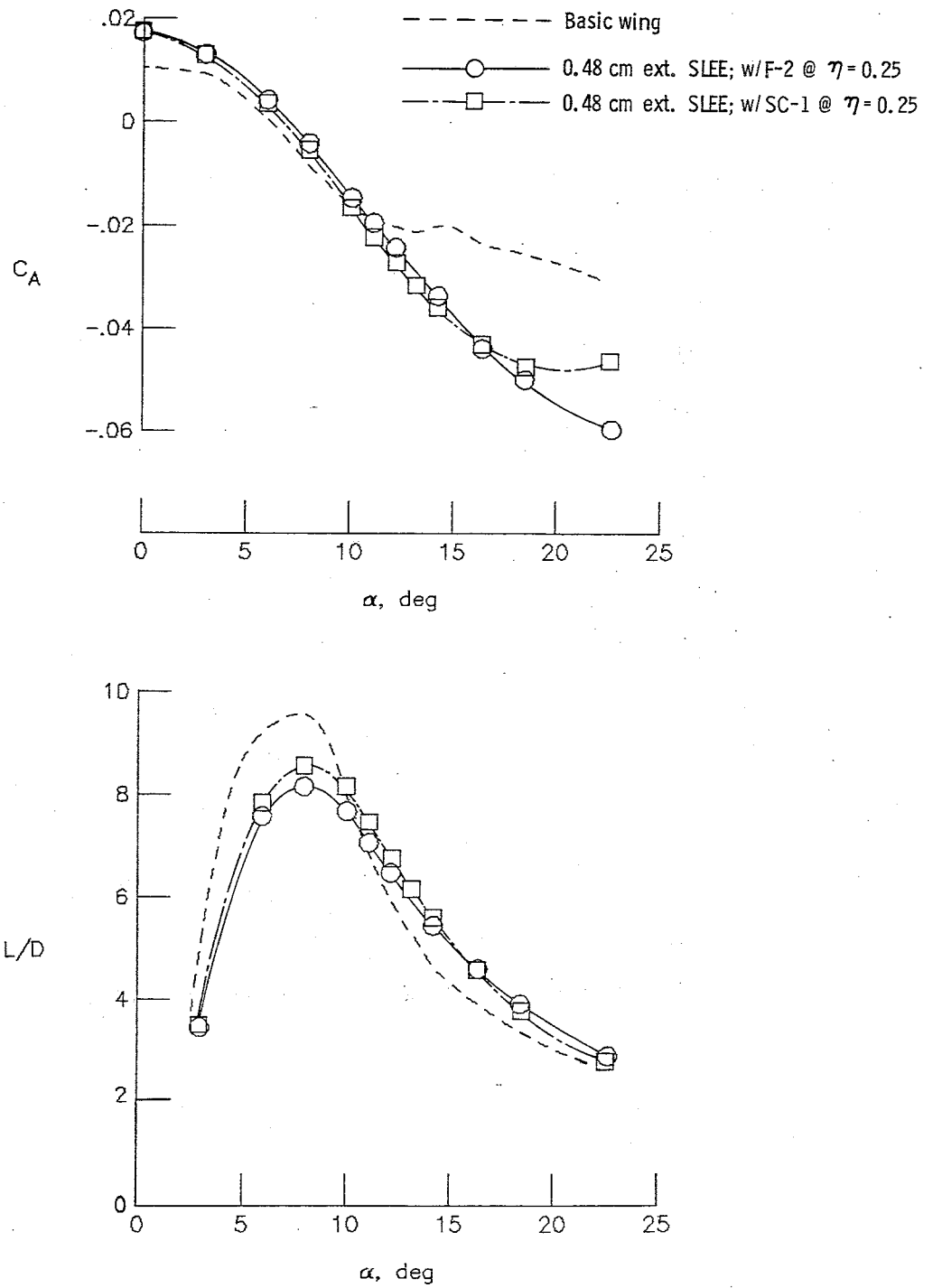

Figure 53.- Performance comparison of the fence and chordwise slot at the SLEE apex.

effectiveness (see Chordwise Slots section) results in a sudden loss of SLEE performance beyond $\alpha \simeq 16^{o}$. The same trends are evident in lift-to-drag. Although not presented, no significant effects are noted in pitching moment. The chordwise slot, therefore, seems to be slightly more effective than the fence in obstructing the spanwise flow near the wing apex up to approximately 16^{o} α. However, highly maneuverable aircraft encounter a wide range of angles of attack and, thus, the high-α performance capability with the fence may be well worth the small penalty at mid α.

As noted previously, the tendency of the SLEE vortex to expand and migrate onto the wing surface will ultimately limit the drag-reduction effectiveness of the device. The previous success of fences and chordwise slots in compartmentation of the wing leading edge suggested that their use along the SLEE would limit the growth of the SLEE vortex and, thus, improve its outboard effectiveness. Each device (F-2 and slot w/SC-1) was, thus, alternately tested at $\eta = 0.625$ (midpoint of SLEE) on a 0.48 cm ext. SLEE configuration also utilizing an F-2 fence at $\eta = 0.25$. Selected force and moment data appear in figure 54. While the additional F-2 fence at $\eta = 0.625$ produces the expected low-α drag (or C_A) penalty, substantial improvement in SLEE suction effectiveness is indicated beyond $\alpha \simeq 16^{o}$, with no adverse effects on longitudinal stability. Tuft photographs in figure 55 support the view that this improvement is due to a compartmentation of the SLEE. In interpretation of these photographs, a herringbone tuft pattern represents a vortex core (shown as a dashed line), whereas a divergence of

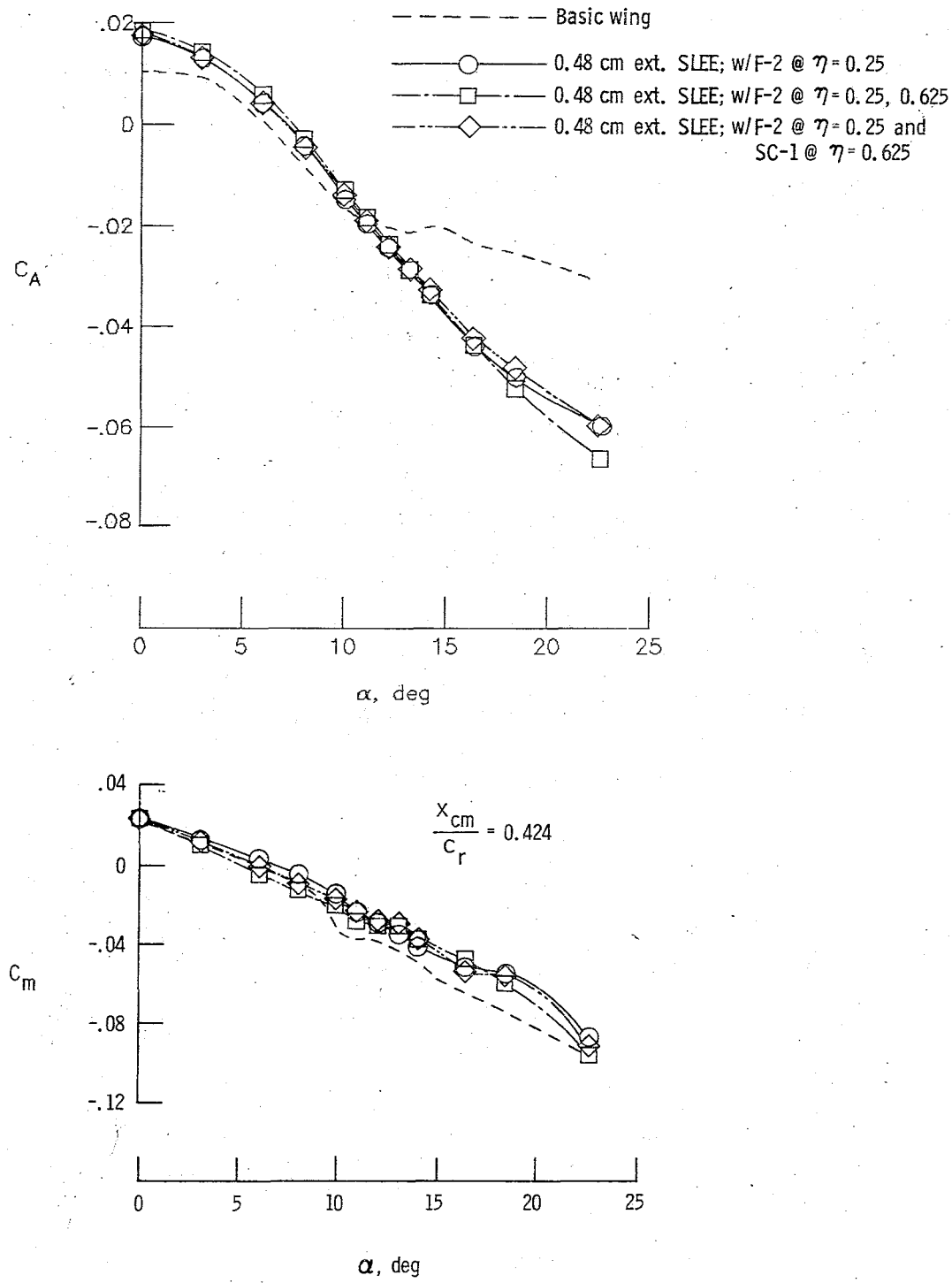

Figure 54.- Performance effects of the fence and chordwise slot in combination with the SLEE.

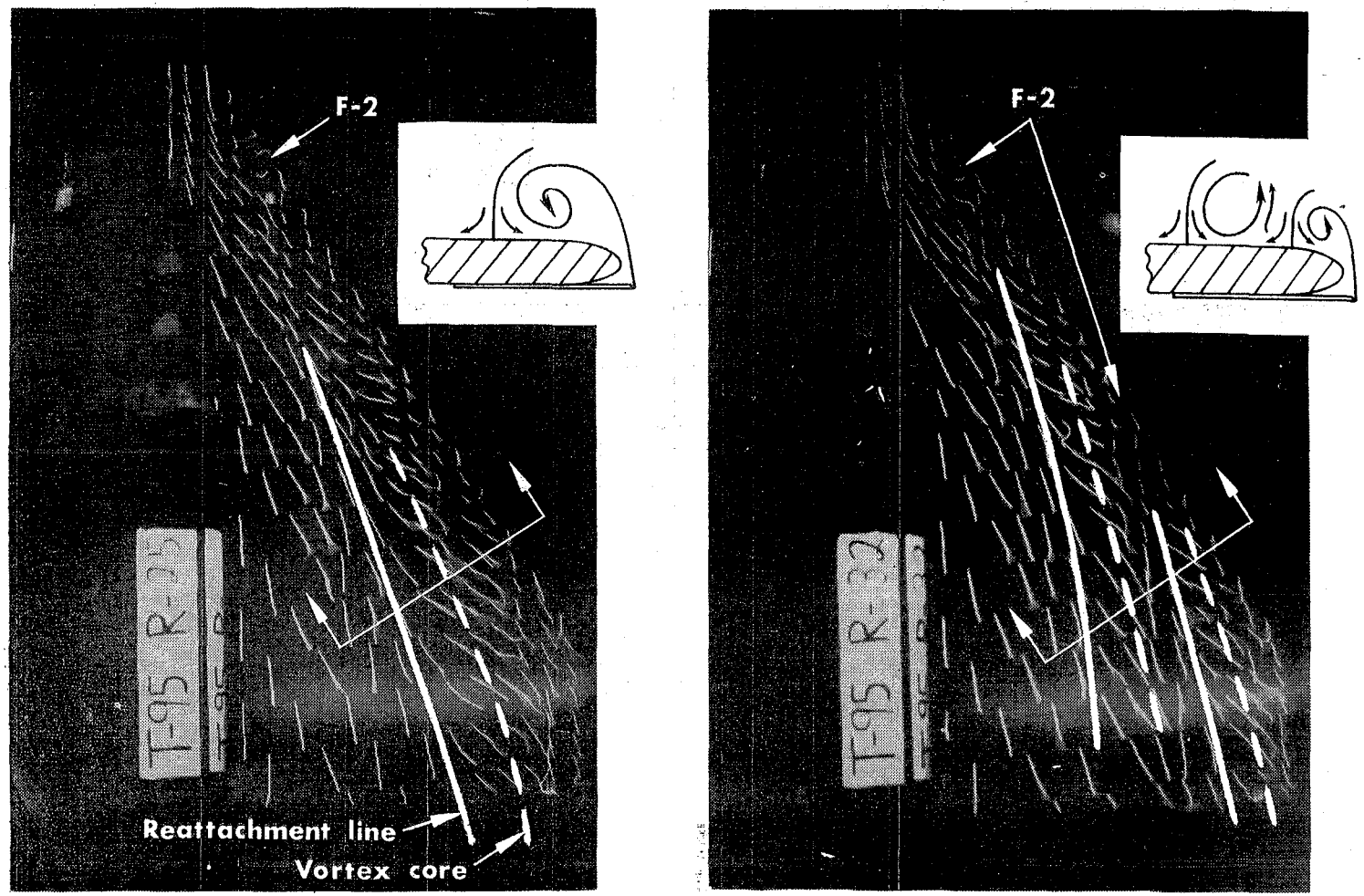

Figure 55.- Upper surface tuft photographs of 0.48 cm ext. SLEE with F-2 at η = 0.25 configuration with and without an F-2 fence at η = 0.625 (α = 14°).

adjacent tufts indicates a flow reattachment line (solid line). In the absence of the outboard fence, the SLEE vortex is free to expand, having migrated completely onto the wing surface at $\alpha = 14^{o}$. A fence at $\eta = 0.625$, however, splits the SLEE vortex into two smaller vortices; one emanating just outboard of the fence and the other near the wing apex. This limits the growth of the outboard vortex and keeps the leading-edge region near the tip under the influence of vortex suction to higher α. The inboard vortex is, subsequently, forced onto the wing surface by the fence and acts as a barrier to the streamwise migration of the outboard vortex.

The effect of this additional F-2 fence at $\eta = 0.625$ on the leading-edge suction is depicted in figure 56. At $\alpha = 16^{o}$, a slight suction improvement outboard of the fence roughly balances the characteristic loss of suction on the inboard side. However, at $\alpha = 23^{o}$, a substantial increase in the outboard thrust increment accounts for the net improvement noted in the C_A curve.

The chordwise slot, on the other hand, is shown in figure 54 to be ineffective in the role of SLEE compartmentation. The spanwise local thrust distribution at $\alpha = 16^{o}$, in figure 56, shows signs of compartmentation through a slight thrust increment just outboard of the slot. However, by 23^{o} α, this improvement has vanished due to loss of slot effectiveness. This slot at $\eta = 0.625$ was also tested in combination with a slot (as opposed to F-2) at $\eta = 0.25$ on the 0.48 cm ext. SLEE configuration, but with the same results (not presented).

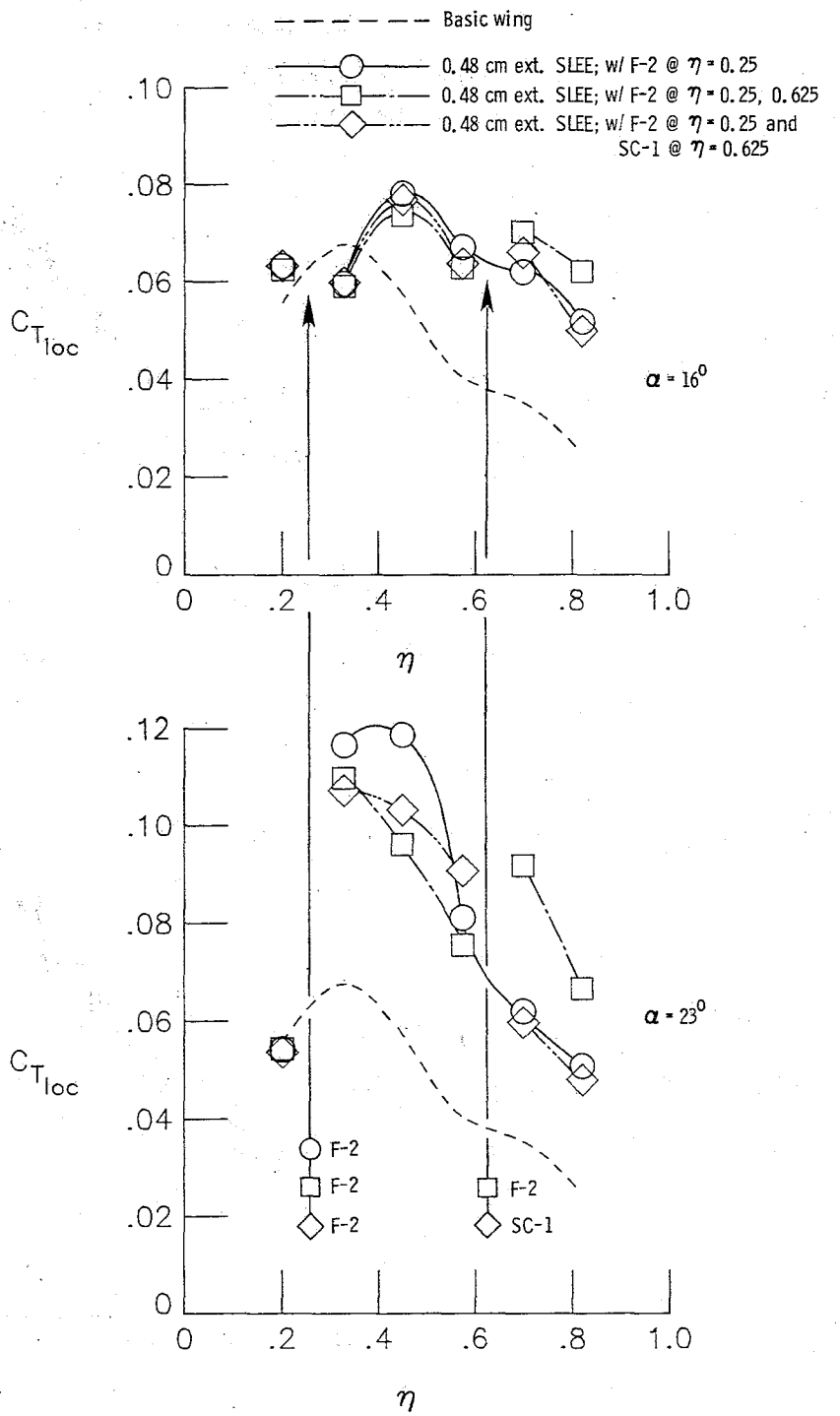

Figure 56.- Effects of the fence and chordwise slot on leading-edge thrust distribution along the SLEE.

In summary, the sharp leading-edge extension is effective in drag reduction and rolling moment stabilization at high α, with no adverse effects on longitudinal stability. The drag reduction is insensitive to SLEE extension at low and mid α; however, there is a distinct advantage to having a shorter extension at high α, assuming the extension is beyond the stagnation point. When utilized at the apex of the SLEE, the chordwise slot is slightly more effective than the fence in obstructing the spanwise flow near the wing apex at mid α. However, far better performance at high α makes the fence more desirable for use on highly maneuverable aircraft. Unlike the chordwise slot, the fence also possesses the ability to compartment the SLEE when used along its length, thereby retaining leading-edge suction to higher α.

Leading-Edge Vortex Flaps

As an extension of the SLEE concept, leading-edge vortex flaps were tested as a possible means of obtaining further improvements in leading-edge thrust at high α. This device is similar in appearance to a conventional leading-edge flap which is deflected to align it with the local upwash in order to provide a smooth onflow at the wing leading edge and, thus, avoid separation. The vortex flap, however, relies upon a separation vortex forced by underdeflection relative to the oncoming flow to generate a suction force on the flap and, thus, provide a thrust component. Ideally, this vortex induces reattachment just aft of the leading-edge curvature, thereby allowing attached flow on the upper surface. The thrust component generated on the vortex flap, thus, leads to alleviation of the lift-dependent drag (see sketch A in INTRODUCTION).

The flow mechanism of the vortex flap will now be discussed in detail with respect to the 30° downward-deflected ($\downarrow$) VF-3. This was a constant chord flap (flap chord 7.3 percent of mean geometric chord) beginning at $\eta = 0.25$ and extending out to the wing tip (see fig. 7). Elimination of the first 25 percent of the flap near the wing apex (η = 0 to 0.25) was based on its relative ineffectiveness due to low prevailing upwash in that region (ref. 3). Figure 57 presents wing leading-edge static pressure variations at selected spanwise positions for a configuration utilizing a 30° $\downarrow$ VF-3. As an aid in the discussion, a qualitative summary of the various stages of leading-edge flow development with increasing α, at constant deflection angle, is also

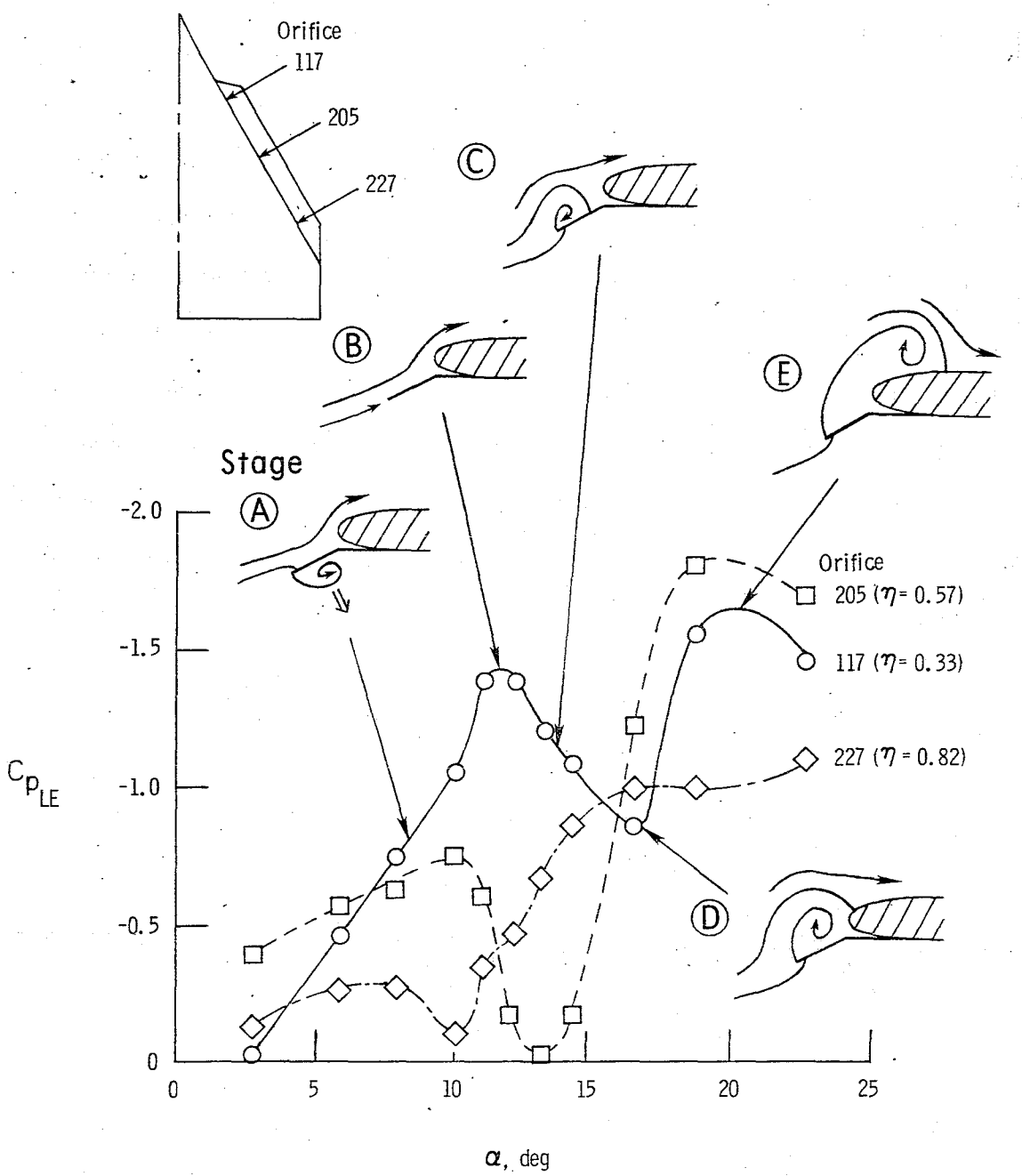

Figure 57.- Leading-edge static pressure variation and flow development on a 30° ↓ VF-3 configuration. Stages of flow development are arbitrarily indicated on the orifice 117 curve.

included. Due to entrainment effects and the spanwise upwash distribution ahead of the leading edge, these successive stages of flow development will also be found with increasing outboard distance for constant flap deflection and angle of attack. At low α (stage A), the vortex flap is effectively overdeflected relative to the small upwash and, thus, induces vortex formation on its lower side. The resulting orientation of the flap normal force vector produces a drag increase and loss of lift. Eventually, a smooth onflow at the flap edge (stage B) occurs, as the flap angle matches the upwash. Note that to this stage, $C_{P_{LE}}$ has become more negative with increasing α due to the rapid development of potential flow suction around the leading edge. Therefore, separation at the knee is likely due to the high degree of leading-edge curvature. At stage C, the upwash angle nominally exceeds the flap angle, resulting in vortex formation and reattachment on the flap upper surface. Tuft photographs (fig. 58) indicate that the transition of the flow pattern from over- to under-deflection occurs between $\alpha = 6^{o}$ and 10^{o} for the 30^{o} ↓ VF-3. At $\alpha = 6^{o}$, tufts near the flap leading edge are hidden, indicating separation on the lower side. At $\alpha = 10^{o}$, however, these tufts lie on the face of the flap, indicating favorable separation. With further increases in α, or outboard distance, reattachment moves toward the leading edge, eventually coinciding with the leading edge at stage D. The relatively high pressure at the reattachment position corresponds to the low point on the $-C_{P_{LE}}$ dip in figure 57. This may be regarded as the "design" point since the full chord of the flap is under vortex suction. The locus of the minimum

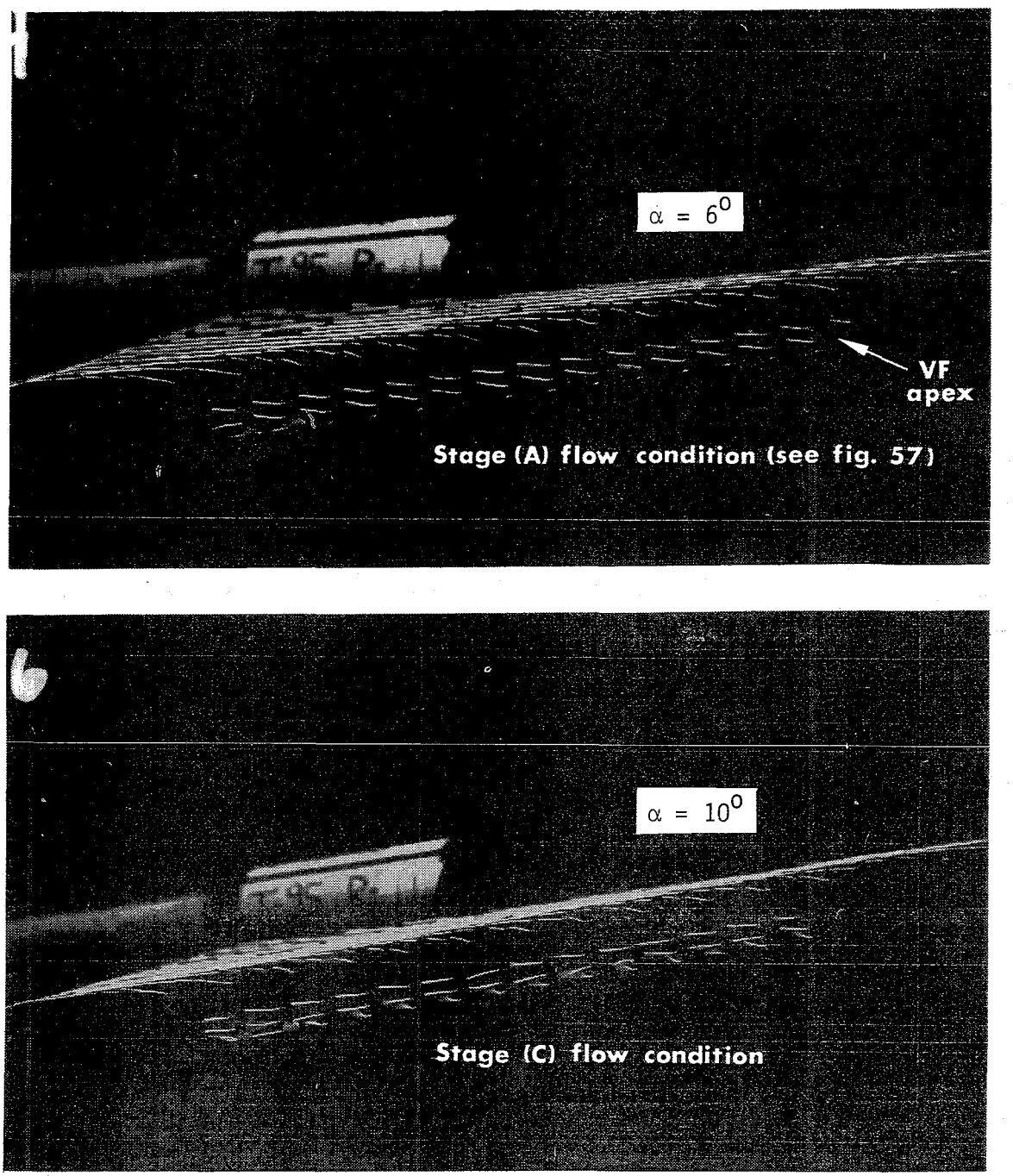

Figure 58.- Side tuft photographs of 30° ↓ VF-3 configuration at $\alpha = 6^{\circ}$ and 10°.

$-C_{p_{LE}}$ points along the span may, thus, be used as a guide to design an optimum twisted flap for a given average deflection angle (see next paragraph). As the flow reattachment position and, subsequently, the flap vortex move onto the wing upper surface (stage E), the flap thrust effectiveness diminishes.

The locus of $C_{p_{LE}}$ derived design points along the 30^{o} ↓ VF-3 is plotted in figure 59. As previously noted, the ideal flow condition is first met near the wing tip and moves inboard with increasing α. This curve also provides a general idea of the relative flap twist necessary to produce the ideal flow condition simultaneously along the entire flap. However, this twisted flap, apart from being impractical, may not be desirable since loss of effectiveness would also occur at once along the entire span.

Figure 59 also presents the locus of the initial relative maximum $-C_{p_{LE}}$ points (see fig. 57) along the 30^{o} ↓ VF-3. This curve may be thought of as a boundary between over- and under-deflection of the flap relative to the oncoming flow. Again, due to the spanwise upwash distribution, vortex formation initially occurs near the tip and spreads inboard with increasing α. This is also evident in the tuft photographs in figure 60. Although these were taken of the 60^{o} ↓ VF-3, the same basic trends would be expected with a 30^{o} ↓ deflection but at lower angles of attack. The chordwise orientation of the tufts on the flap at $\alpha = 14^{o}$ is indicative of attached flow. By 16^{o} α, however, the flap vortex has formed and advanced to approximately the midpoint of the flap (position 'b'). Due to expansion of the vortex core

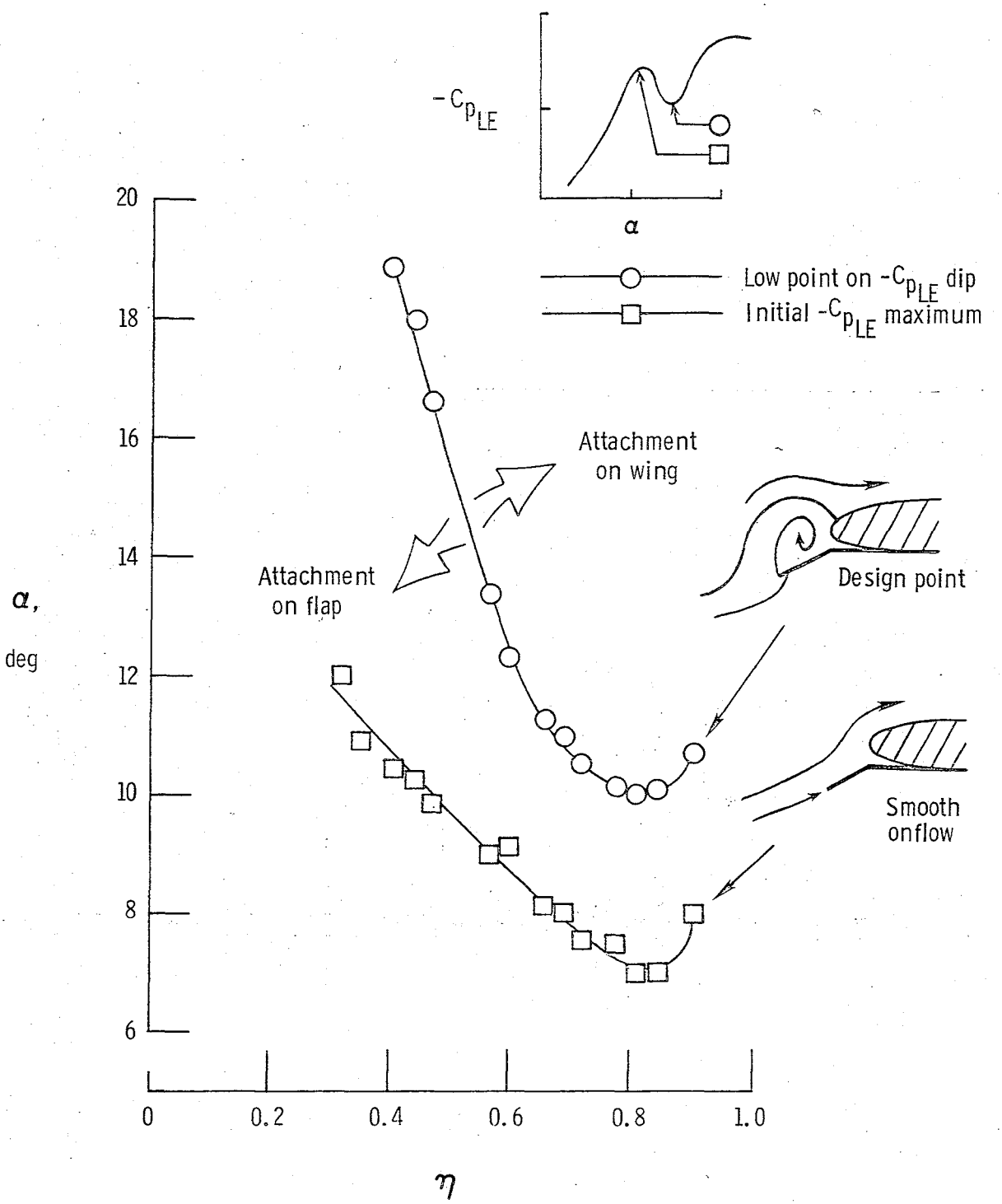

Figure 59.- Local design point distribution ($C_{p_{LE}}$ derived) along 30^{o} ↓ VF-3 (see fig. 57).

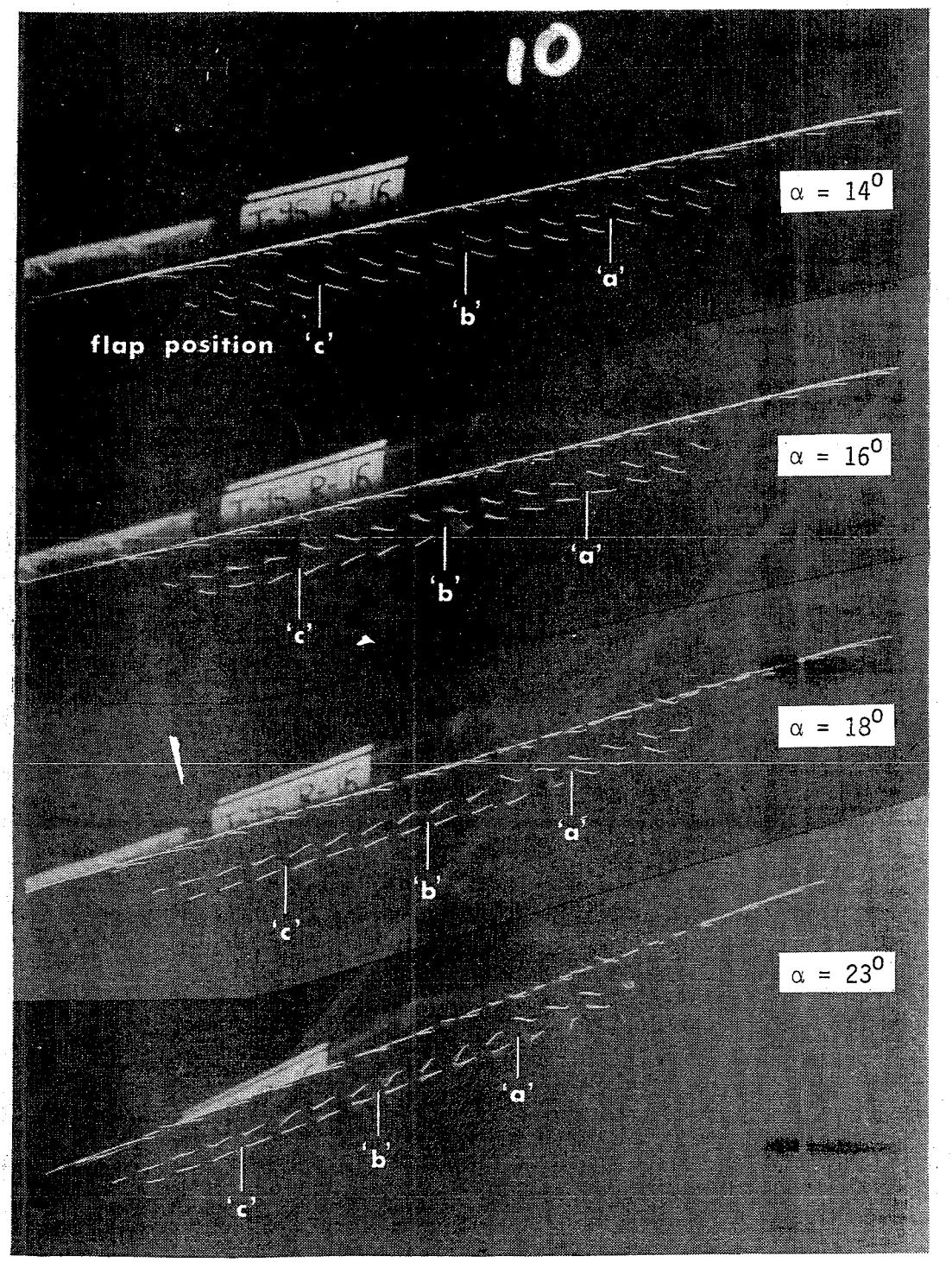

Figure 60.- Side tuft photographs of 60° ↓ VF-3 configuration at $\alpha = 14^{\circ}$, 16°, 18°, and 23°.

toward the tip, reattachment between positions 'b' and 'c' occurs on the flap face (indicated by the diverging tufts on the flap), with nearly an ideal flow condition aft of position 'c'. Further increases in α are accompanied by continued inboard movement of the vortex, with its apex lying near the flap apex at $\alpha = 23^{o}$. At this stage, reattachment aft of position 'c' occurs on the wing upper surface, as evidenced by the realignment of the tufts along the length of the flap.

Leading-edge thrust variations for the 30^{o} ↓ VF-3 configuration are presented in figure 61. No effect is evident on the leading-edge thrust at low α since separation occurs on the lower side of the flap. At mid α, however, the flap induces a thrust loss outboard of STA 1, corresponding to the leading-edge suction loss noted in figure 57. However, as the ideal flow condition is reached near the tip, the flap effectiveness begins to appear as a substantial thrust improvement. At angles of attack higher than those considered here, further inboard movement of the ideal flow condition would result in thrust improvements also at the inboard stations.

The effects of the 30^{o} ↓ VF-3 on the overall performance characteristics of the configuration are given in figure 62. A large axial force improvement over the basic wing is found at high α and is sustained to the highest angles tested. The severe low-α drag penalty is not of concern since at cruise the flap would be undeflected or retracted; as is the loss of normal force at low α, which is attributed to the effective negative camber induced by the downward flap deflection. The migration of the primary vortex onto the wing upper surface leads to onset of

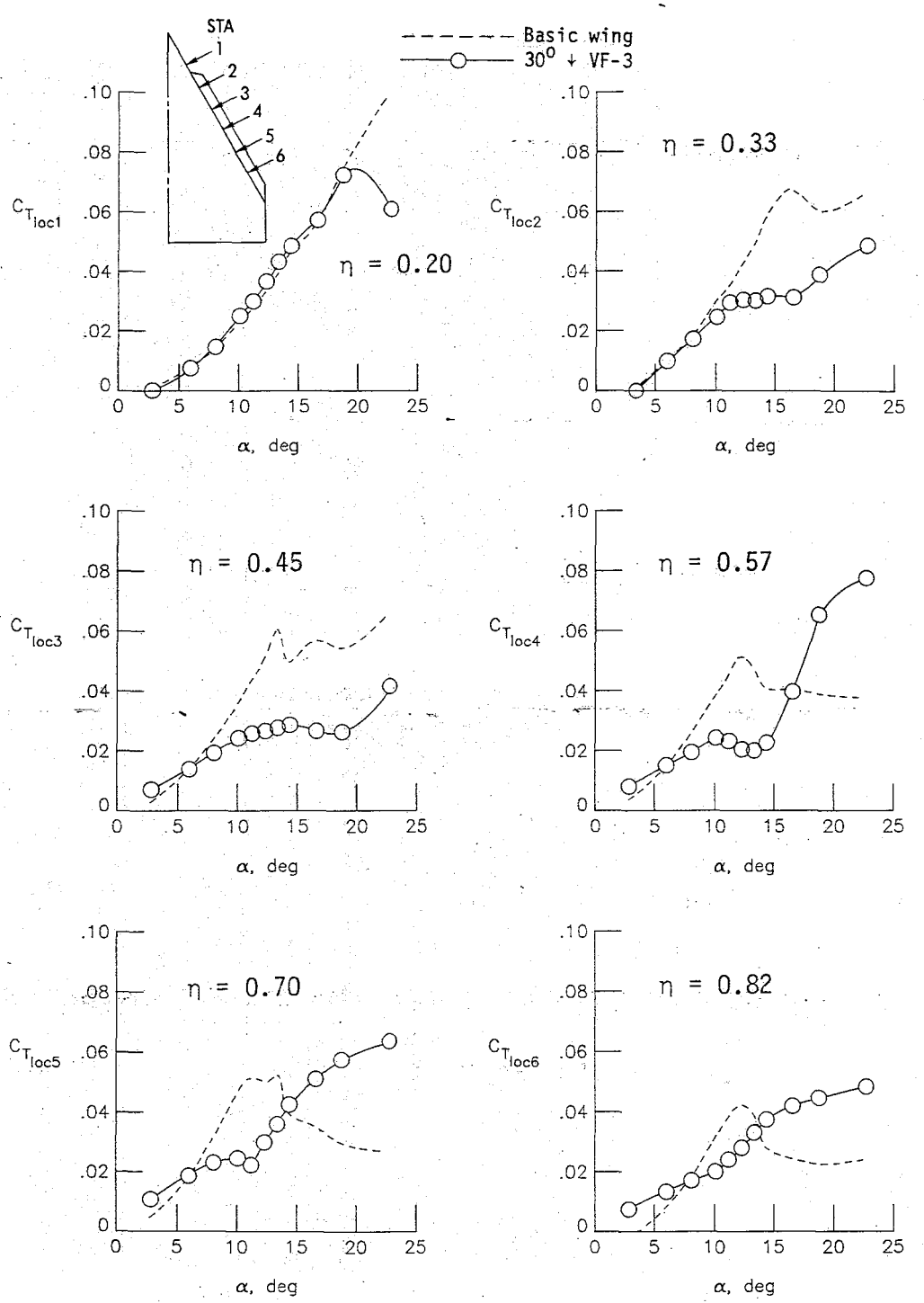

Figure 61.- Effects of 30° ↓ VF-3 on wing leading-edge thrust.

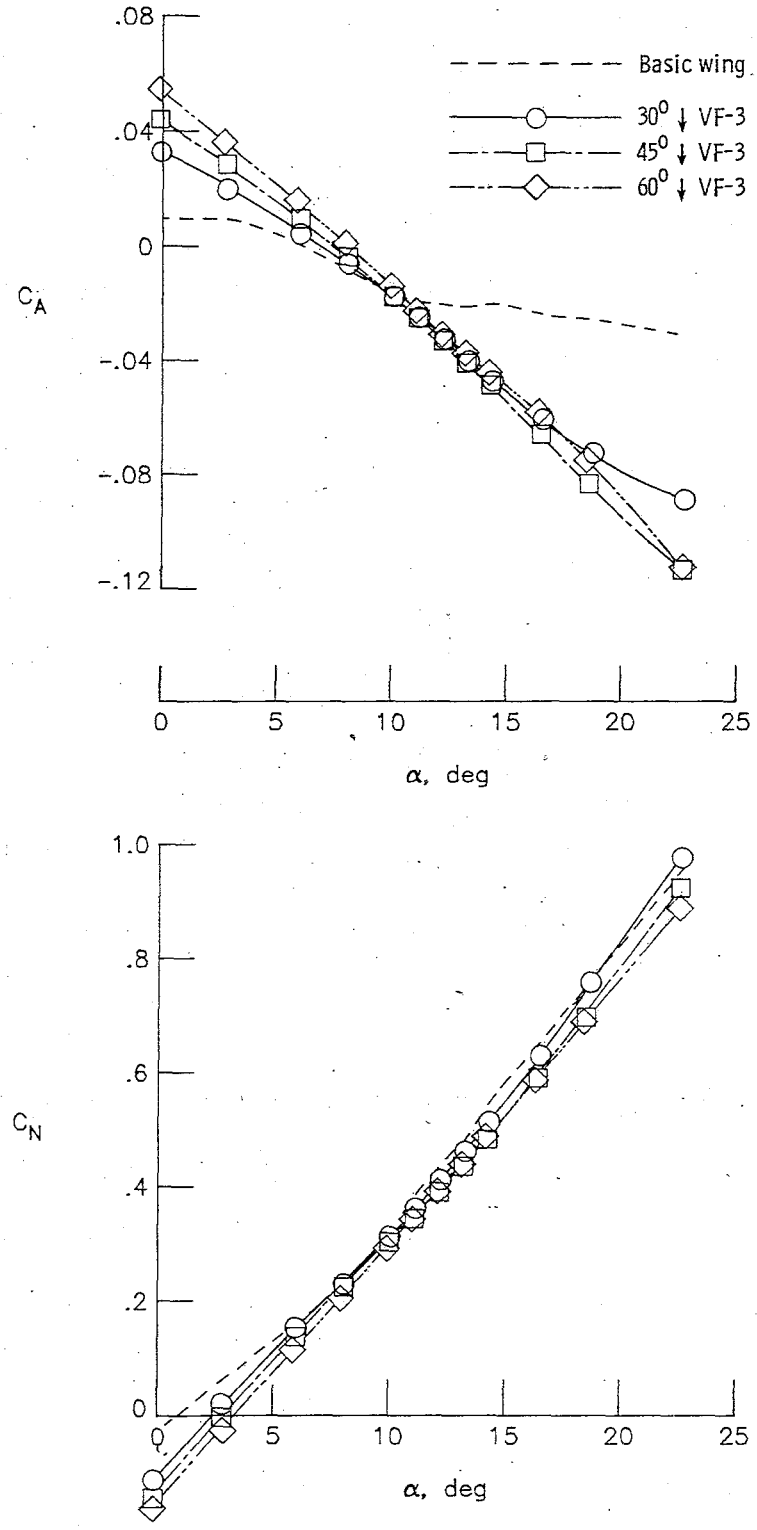

Figure 62.- Effects of vortex flap deflection angle on force and moment characteristics.

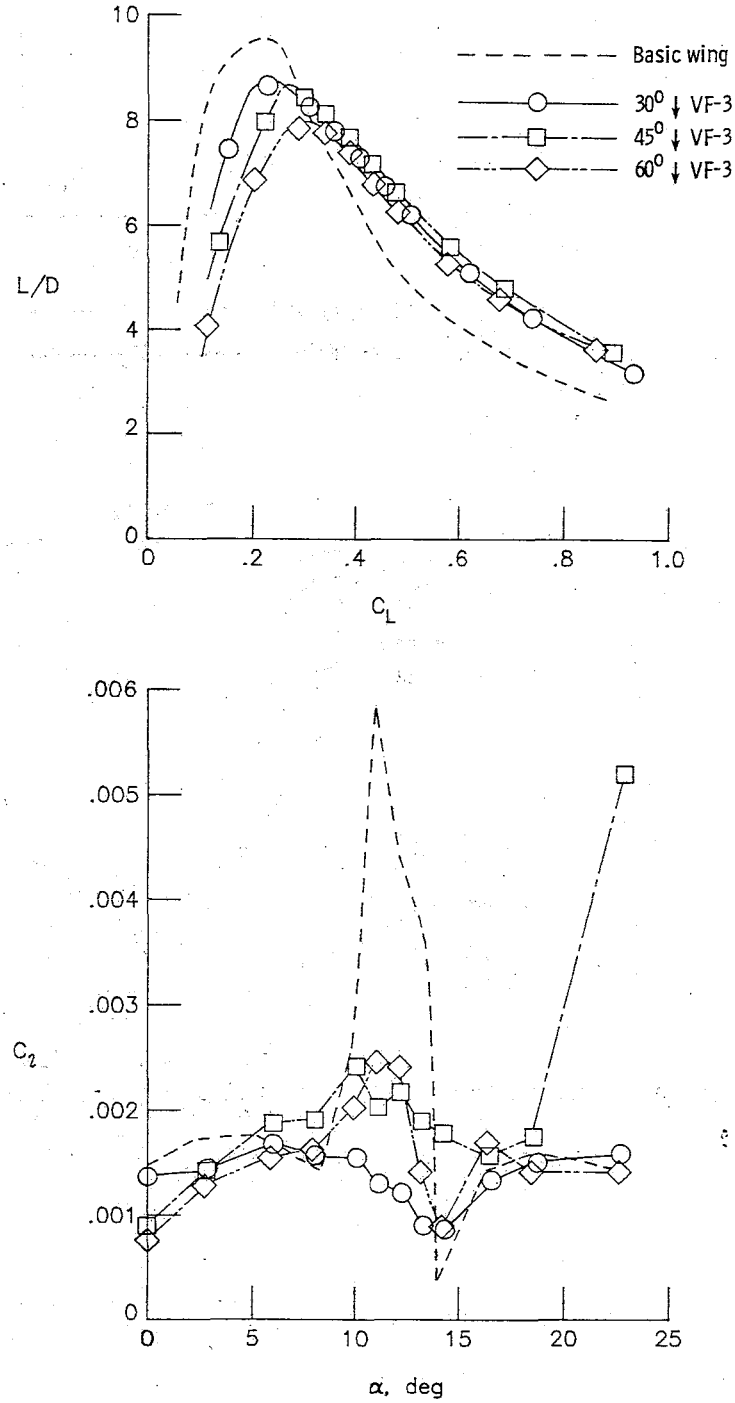

Figure 62.- Concluded.

vortex lift at approximately $\alpha = 14^{o}$, accounting for the convergence of the C_N curve toward the basic wing data at higher α. The resulting effect on L/D is a loss of performance at low α but substantial improvement beyond $C_L \simeq 0.3$. The C_l data indicate that the vortex flap also eliminates the severe mid-α rolling moment instability of the basic wing.

Longitudinal stability effects of the 30^{o} ↓ VF-3 are depicted in figure 63. The moment reference center has once again been moved to the same position used with the SLEE data (3.82 cm aft of the original reference center indicated in fig. 2) to better show up the effects of the device. The 30^{o} ↓ VF-3 produces a slight reduction in longitudinal stability at mid and high α but eliminates the nonlinearities of the basic wing at $\alpha \simeq 8^{o}$. The chordwise location of the center of pressure for this same configuration (derived from C_m and C_N data) is plotted as a function of α in figure 63. The forward movement of x_{cp} relative to the basic wing beyond $\alpha \simeq 6^{o}$ (the angle at which vortex formation is initiated on the flap face) is attributed to a forward movement of the center of pressure along the flap. Whereas attached flow on the basic wing positions the suction peak near the leading edge, the vortex suction effect on the flap moves this suction peak forward onto the flap surface (sketch M). Since pitch-up is the result of a forward movement of the center of pressure, those flap configurations producing the most aft center of pressure will be considered the most desirable as far as longitudinal stability is concerned.

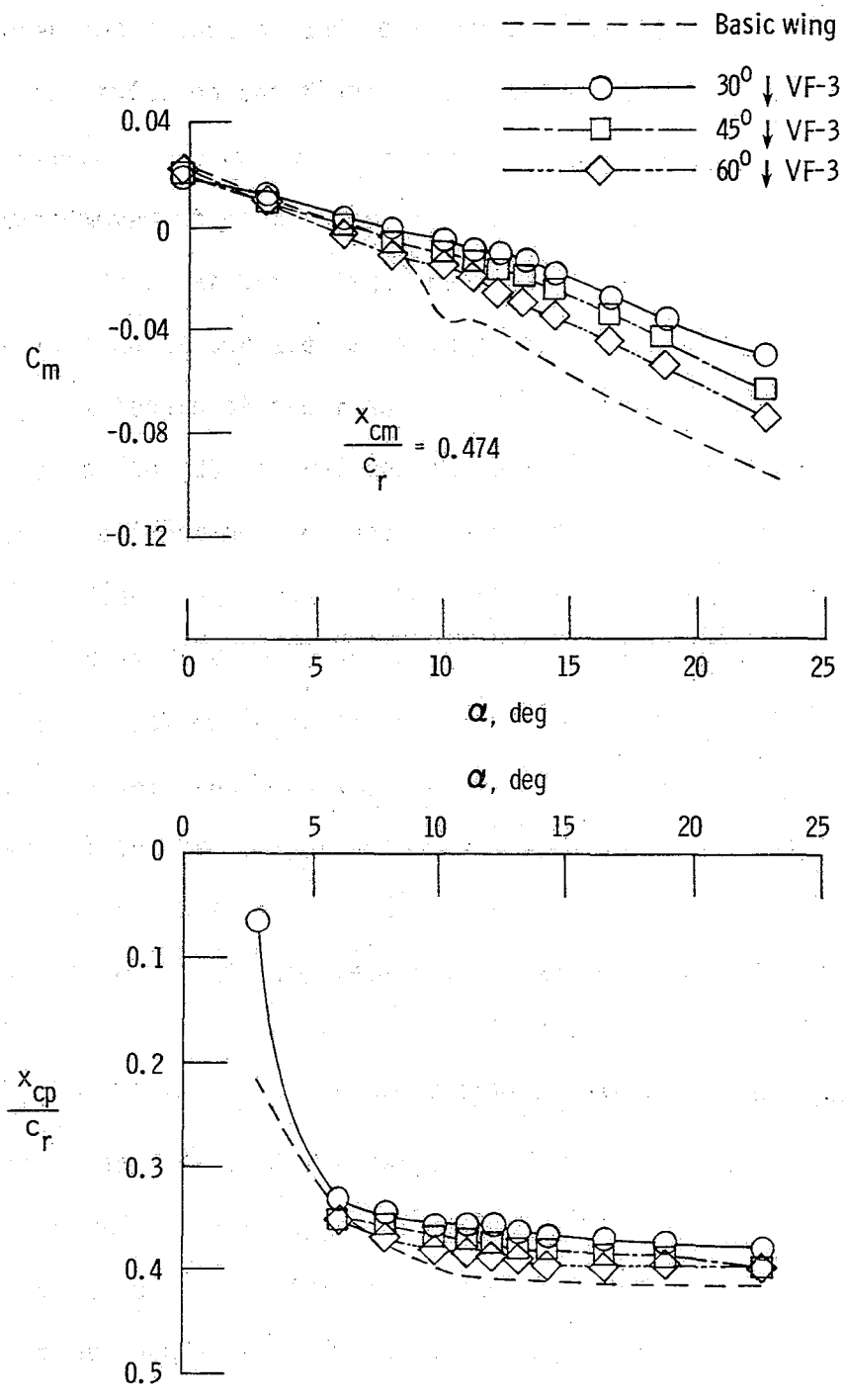

Figure 63.- Effects of vortex flap deflection angle on longitudinal stability characteristics.

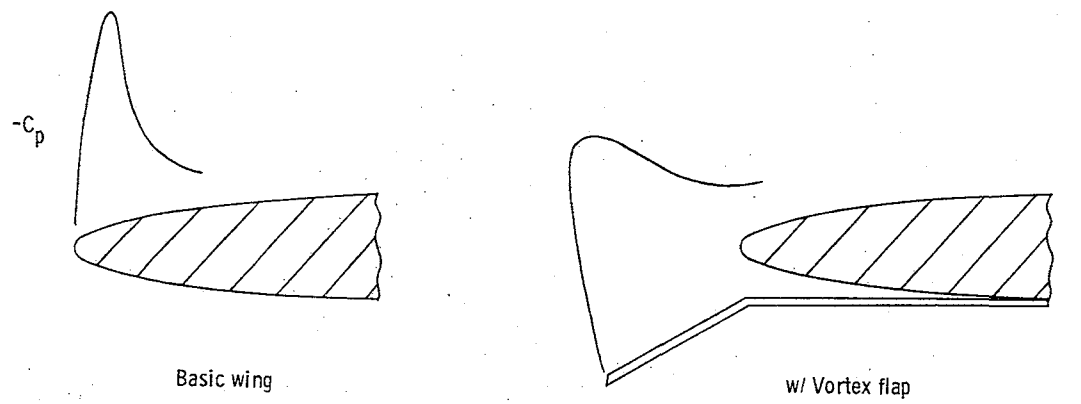

Sketch M

Comparison of experimental results with theory (ref. 15) for the 30^{o} ↓ VF-3 configuration appears in figure 64. The downward shift in the experimental lift data as compared with theory is attributed to the effective negative camber induced by the asymmetric trailing-edge region (see fig. 2). Otherwise, the experimental lift and drag data show relatively good agreement with theory throughout the angle-of-attack range.

For a more basic assessment of the aerodynamic effectiveness of the various flap configurations tested, an analysis on a per unit flap area basis will also be used. This will provide an indication of the efficiency with which the surface area of a particular flap configuration is being utilized for drag reduction. Figure 65 presents balance and leading-edge pressure-integrated thrust data for the 30^{o} ↓ VF-3 configuration. The axial force curve has been shifted downward to zero to

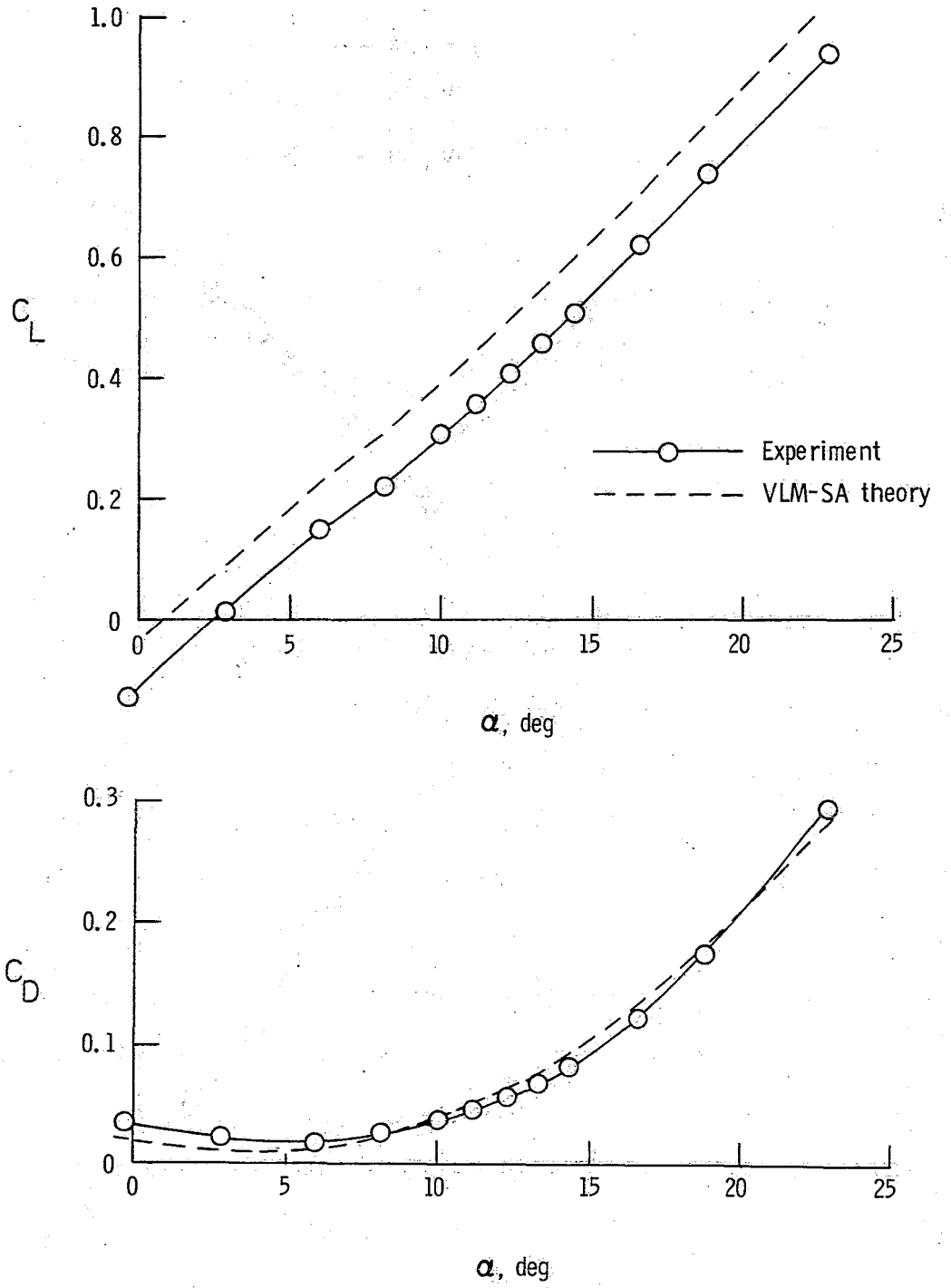

Figure 64.- Comparison of 30^0 ↓ VF-3 experimental data with VLM-SA theory.

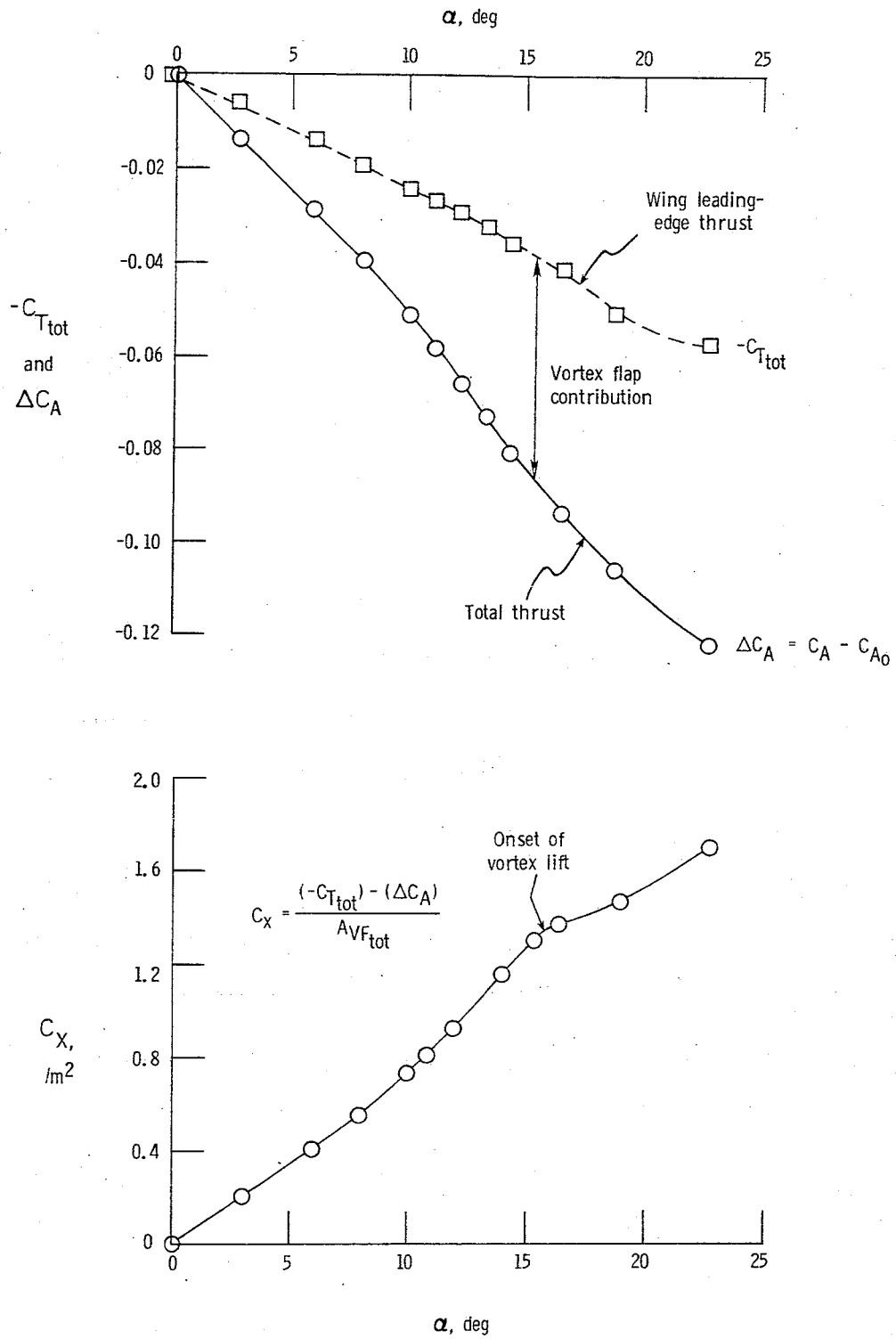

Figure 65.- Thrust contribution from 30° ↓ VF-3 flap surface.

eliminate the profile drag component. $C_{T_{tot}}$ represents the contribution of the wing leading-edge suction to the axial force obtained by a spanwise summation of $C_{T_{loc}}$. The difference in the two curves, therefore, represents directly the thrust contribution of the flap. This difference is divided by the total flap surface area and plotted in figure 65. The curve indicates an improvement in flap efficiency with increasing α. The sudden reduction in slope at $\alpha \simeq 16^{o}$ indicates the onset of loss of flap thrust effectiveness due to vortex migration onto the wing upper surface. This is consistent with the onset of vortex lift noted in the C_N curve (fig. 62) at approximately the same α. Additional evidence is provided by the photographs in figure 66. At $\alpha = 14^{o}$, the mini-tufts near the wing leading edge are generally chordwise, implying reattachment either on the flap or at the knee, with attached flow prevailing on the wing upper surface. At $\alpha = 17^{o}$, however, these same tufts are angled toward the wing tip, suggesting vortex action and reattachment on the upper surface.

The effects of flap deflection on overall performance are shown in figures 62 and 63. Axial force shows an improvement at high α with an increase in downward deflection of VF-3 from 30^{o} to 45^{o}, but a loss of performance with further deflection to 60^{o}. The effective increase in negative camber with increasing flap deflection results in a reduction of normal force at low α. The same trends are evident at higher α due to a delay in vortex migration onto the wing upper surface. Lift-to-drag appears relatively insensitive to flap deflection beyond $C_L \simeq 0.4$. This is attributed to the self-compensating for thrust effect

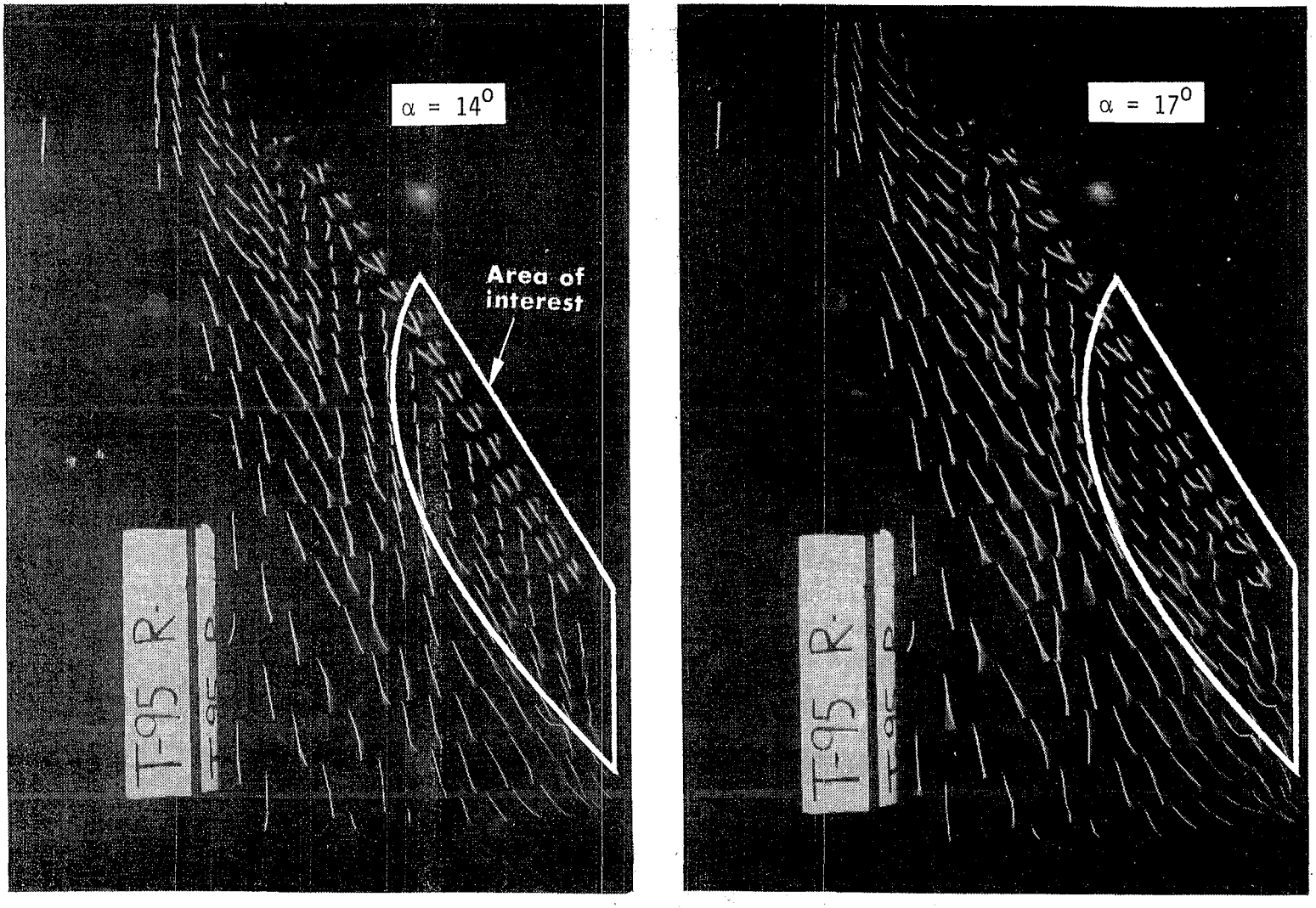

Figure 66.- Upper surface tuft photographs of 30° ↓ VF-3 configuration at α = 14° and 17°.

A major concern of the aircraft design engineer is that of producing adequate lift to reduce the landing speed. In addition, deceleration of the aircraft from cruise to landing speed has been a problem requiring the use of speed brakes and high approach angles of attack. An up-deflected (↑) vortex flap was tested in the present investigation as a possible aid in alleviation of these problems (ref. 17). It was believed that the suction effect of a vortex formed on the lee side of the flap (see sketch F in BACKGROUND) would produce both lift and drag increments ideal for the landing approach. The vortex flow induced on the wing upper surface would provide additional lift.

Results of balance measurements on a 30^{o} ↑ VF-7 configuration (see fig. 7) are presented in figure 67. Normal force indicates onset of vortex lift almost simultaneously with departure from $\alpha = 0^{o}$. The strong spanwise inclination of the tufts near the wing leading edge at $\alpha = 6^{o}$, in figure 68, is indicative of this upper surface vortex flow. Note the well-defined reattachment line with chordwise flow downstream. The resulting improvement in C_N implies that the required lift at landing may be obtained at a lower flight speed. The rolling distance after touch-down, which is proportional to the square of the landing speed, can thereby be significantly reduced. At $\alpha = 0^{o}$, the 30^{o} ↑ VF-7 produces a relatively small increase in axial force since there is no addition of frontal area (see fig. 7). However, at mid and high α, large increases in drag are available for deceleration of the aircraft during the landing approach. In addition, the linearity of the pitching moment curve is significantly improved over that of the basic wing. The

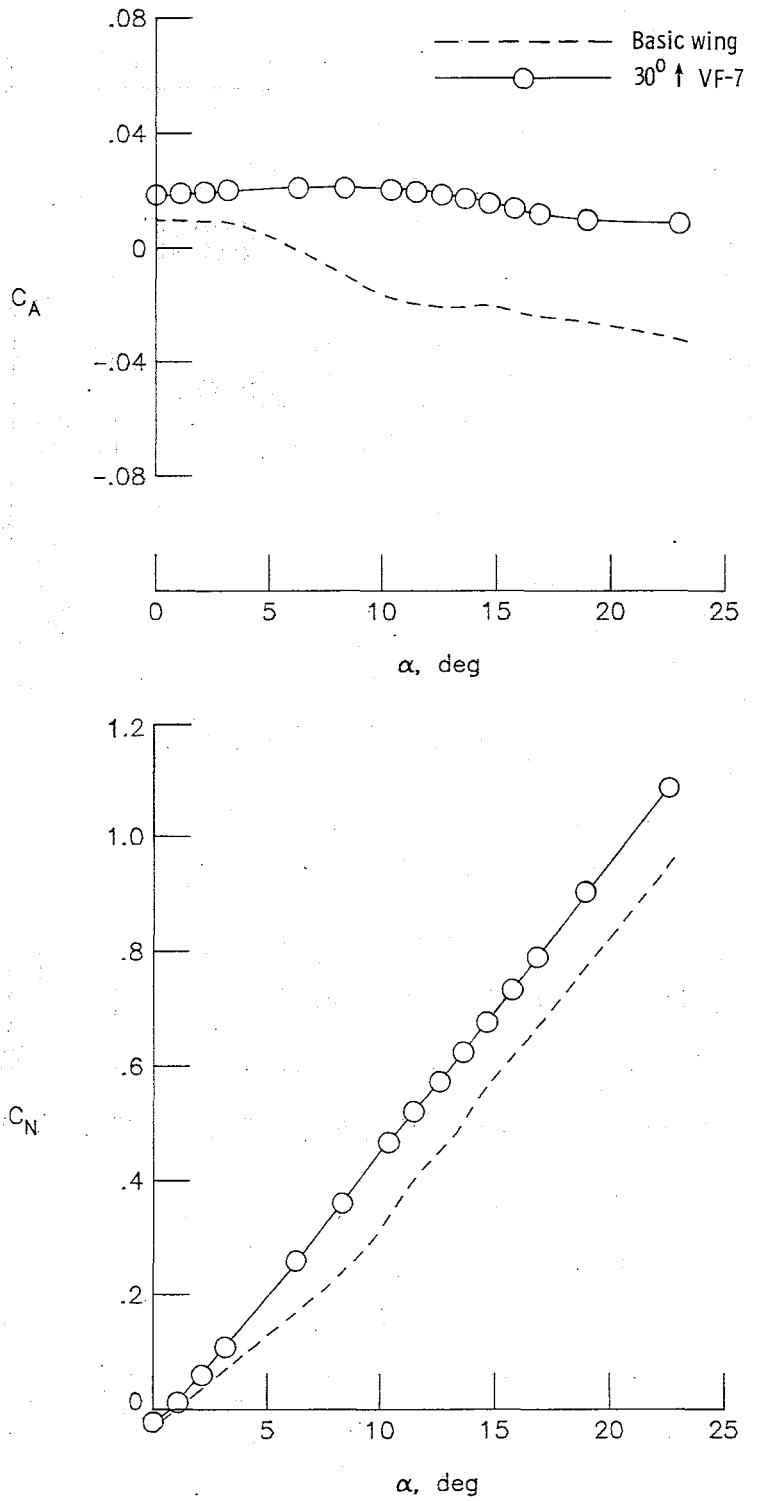

Figure 67.- Effects of upward vortex flap deflection on force and moment characteristics.

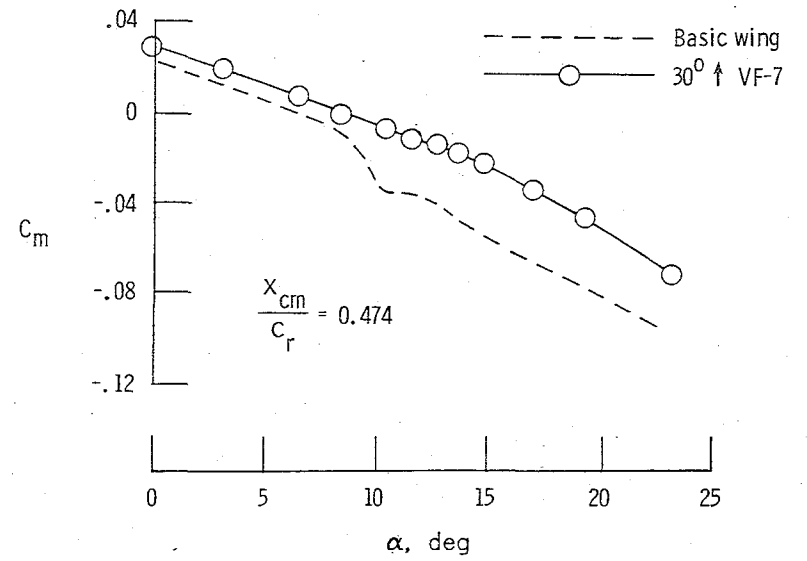

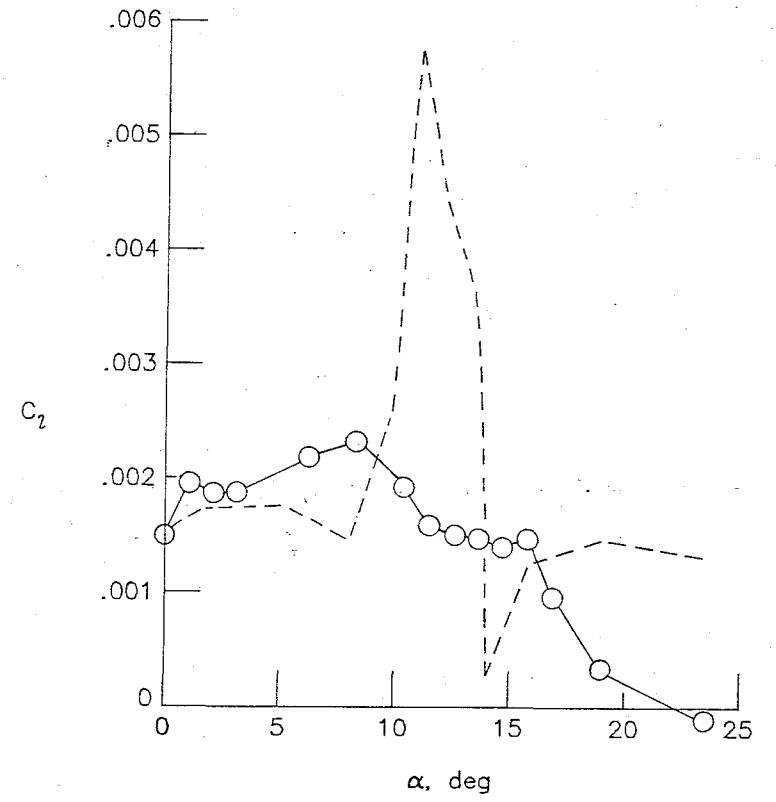

Figure 67.- Concluded.

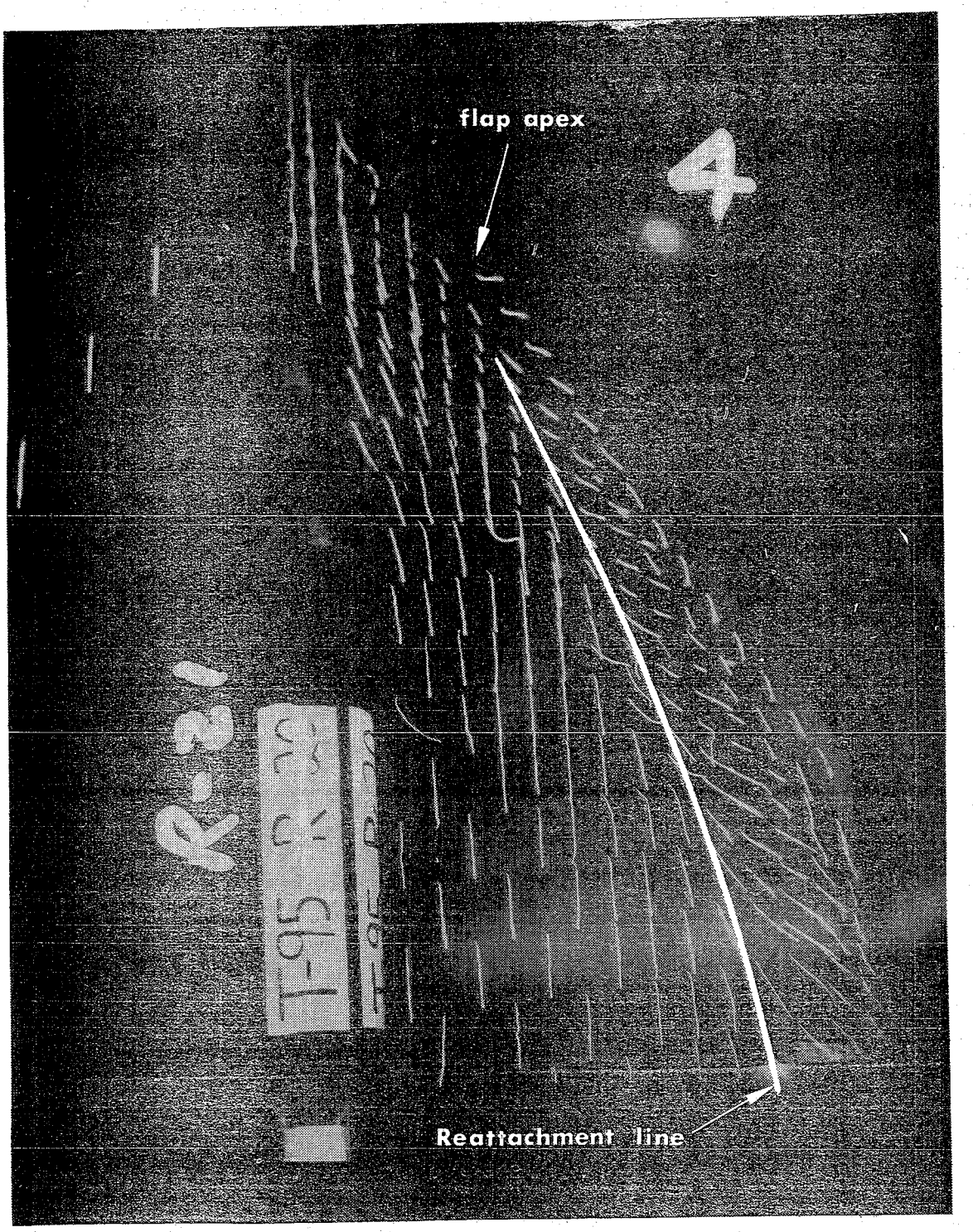

Figure 68.- Upper surface tuft photograph of 30^{o} ↑ VF-7 configuration at $\alpha = 6^{o}$.

rolling moment characteristics are excellent up to approximately $\alpha = 16^{o}$, at which point a minor instability appears. However, the severe wing rock of the basic wing between 8^{o} and 14^{o} α is eliminated. These characteristics are significant since any unstable behavior at near-stall landing conditions may be critical.

An inverse tapered vortex flap was also tested in the present investigation to take advantage of certain flow phenomena characteristic of the device. It was reasoned that increasing the flap chord toward the wing tip would better accommodate the expanding vortex core and, accordingly, produce a more efficient drag reducer. This inverse tapered flap (VF-2) was designed with approximately the same surface area as the constant chord VF-3 (see fig. 7), allowing for direct performance comparison. Balance data for the 30^{o} ↓ VF-2 and VF-3 configurations are presented in figure 69. The axial force data indicate a slight improvement in drag-reduction effectiveness beyond $\alpha \simeq 16^{o}$ with the inverse tapered VF-2. However, there is a slight loss of normal force within this same α range. The longitudinal stability characteristics (not presented) are not significantly different from those of the constant chord flap.

Static pressure distributions around the wing leading edge (fig. 70) confirm that drag performance improvements with the inverse tapered VF-2 are indeed attributable to its ability to better maintain the vortex on the flap and delay its migration onto the upper surface in the outboard region. Stagnated pressures at $\eta = 0.70$ and 0.82 with the constant chord VF-3 at $\alpha = 12^{o}$ suggest that reattachment has moved

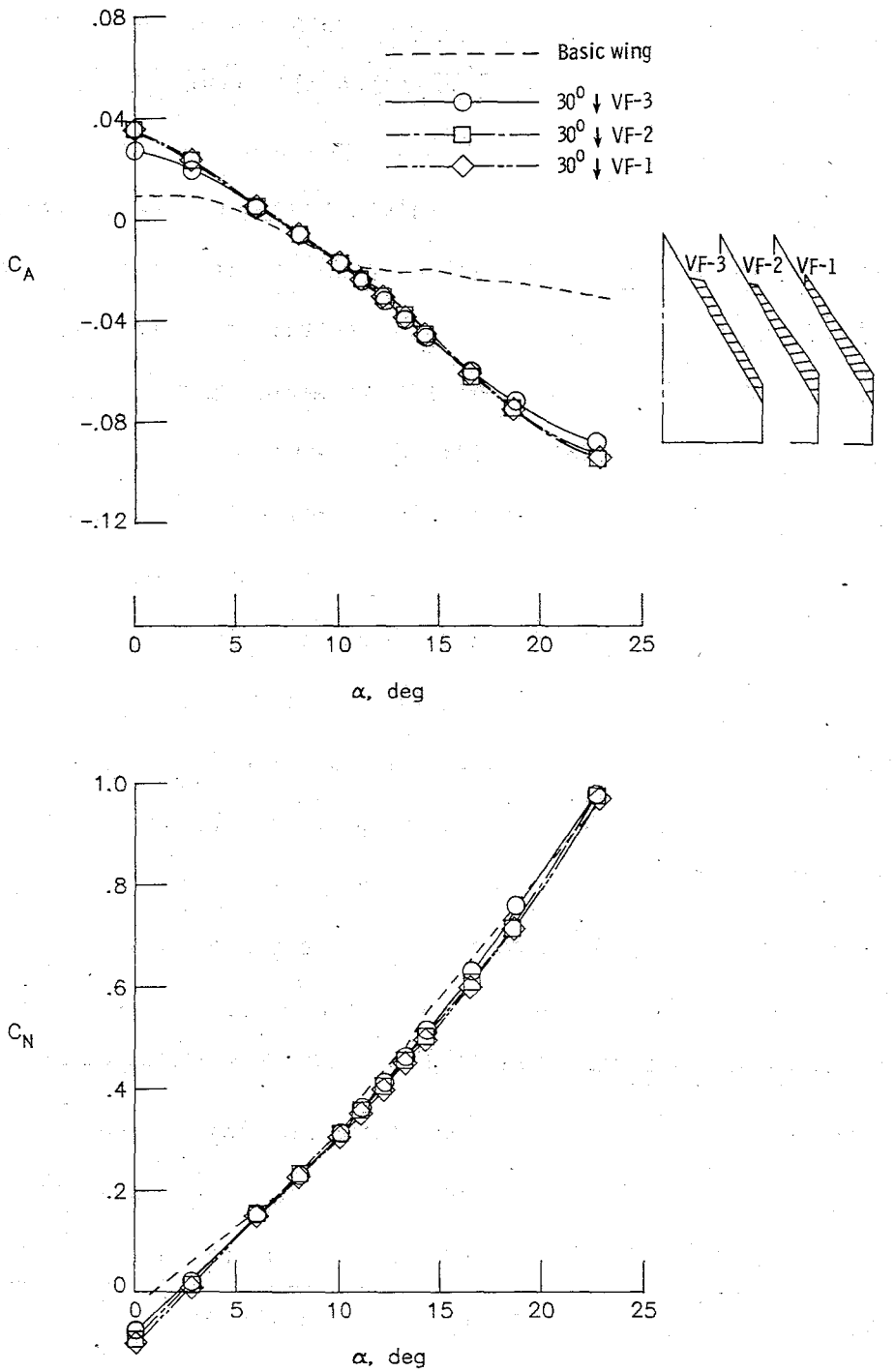

Figure 69.- Effects of inverse tapered flap chord distribution and apex shape on vortex flap performance.

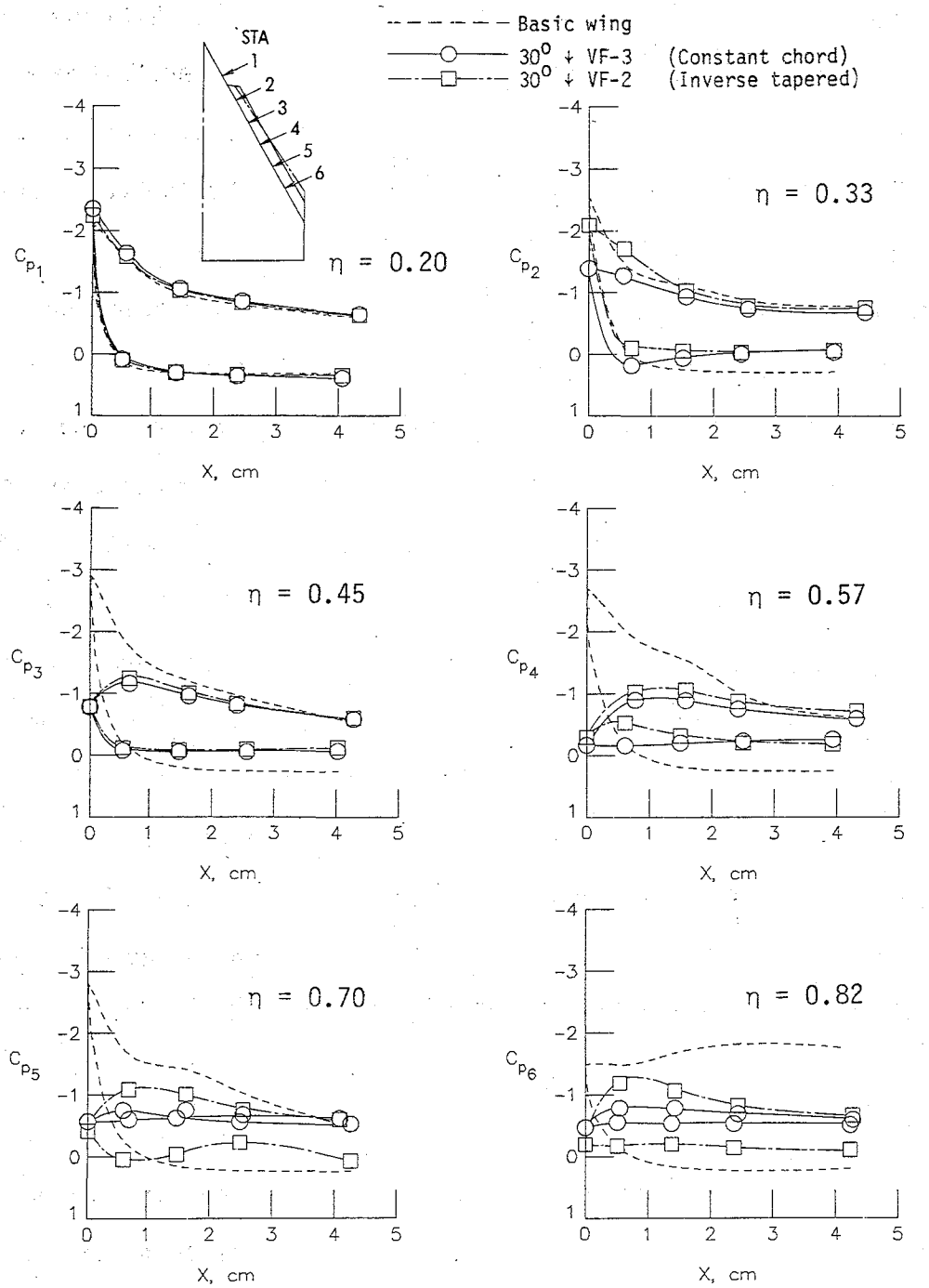

Figure 70.- Effects of inverse tapered vortex flap chord distribution on static pressure distributions around the leading edge at $\alpha = 12^{o}$.

to the wing surface. The inverse tapered VF-2, however, has retained attached flow at the leading edge, with reattachment still on the flap. Tuft photographs taken at $\alpha = 16^{0}$ (fig. 71) indicate the same trends. The chordwise orientation of the tufts near the wing leading edge with the VF-2 indicates attached upper surface flow, whereas the spanwise inclined tufts with the VF-3 configuration are the result of vortex spillover. The delay in onset of vortex lift with the VF-2 accounts for the reduced normal force noted in figure 69.

A comparison of the $C_{p_{LE}}$ derived locus of design points along the 30^{0} ↓ VF-2 and VF-3 appears in figure 72. The relatively smaller flap chord near the apex of the VF-2, as compared with the VF-3, reduces the α at which the design point is met. The opposite effect is evident outboard of $\eta \simeq 0.60$. Delays in vortex spillover of up to 3^{0} α at these outboard stations with the VF-2 account for the high-α improvements noted in the C_A characteristics.

Comparison on a per unit flap area basis, in figure 73, indicates that the inverse tapered flap area distribution is somewhat more efficient than the constant chord variation up to $\alpha \simeq 16^{0}$. More pronounced improvements are indicated at higher α, as the VF-3 begins to lose outboard suction effectiveness. An implication of this result is that savings in system weight are possible through appropriate geometric design of the vortex flap.

An additional inverse tapered vortex flap (VF-1), characterized by a chordwise-cut apex, as opposed to the sweptback apex of the VF-2, was tested to determine the importance of flap apex shape. It was thought

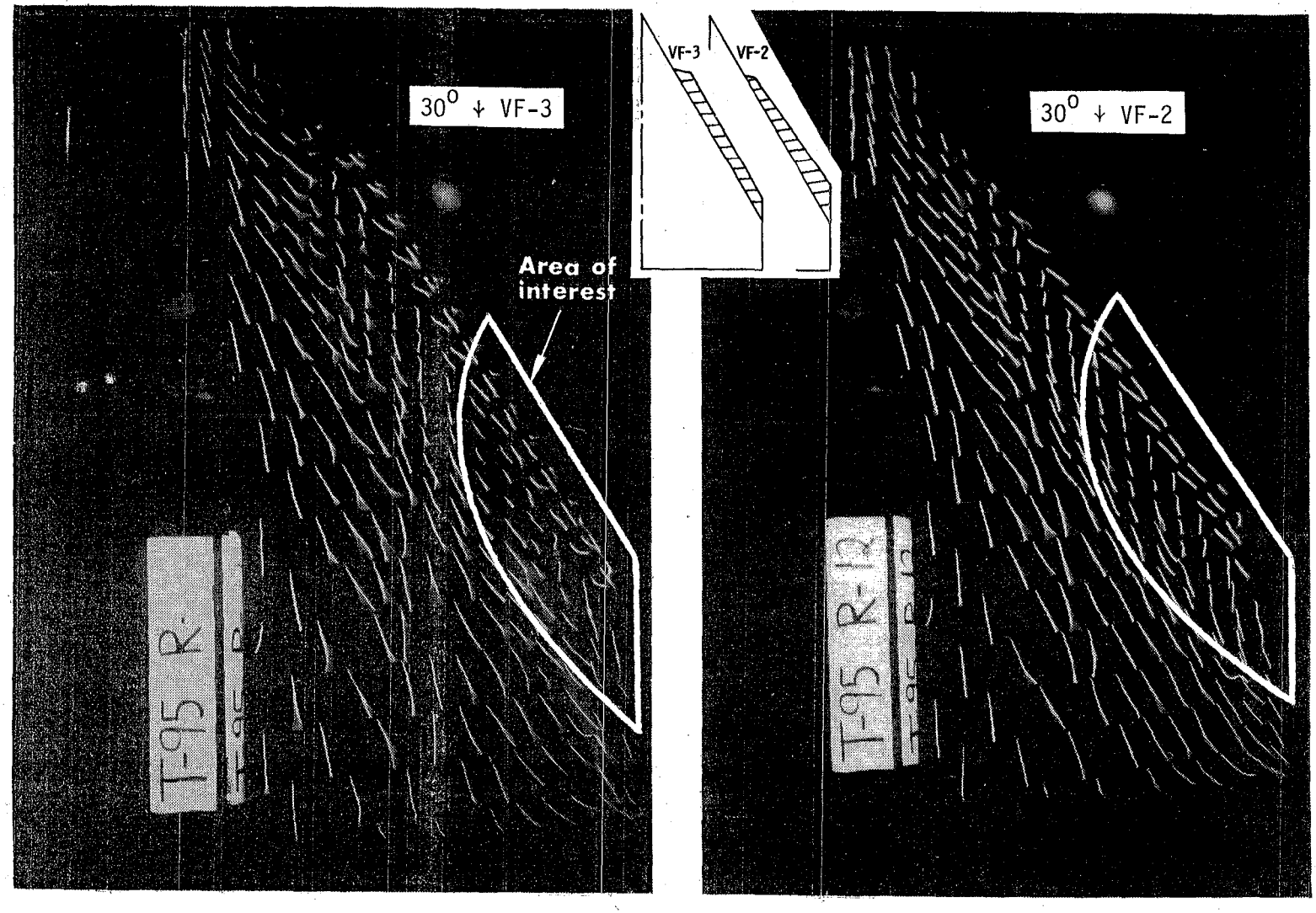

Figure 71.- Upper surface tuft photographs of 30° ↓ VF-2 and VF-3 configurations at $\alpha = 16^{\circ}$.

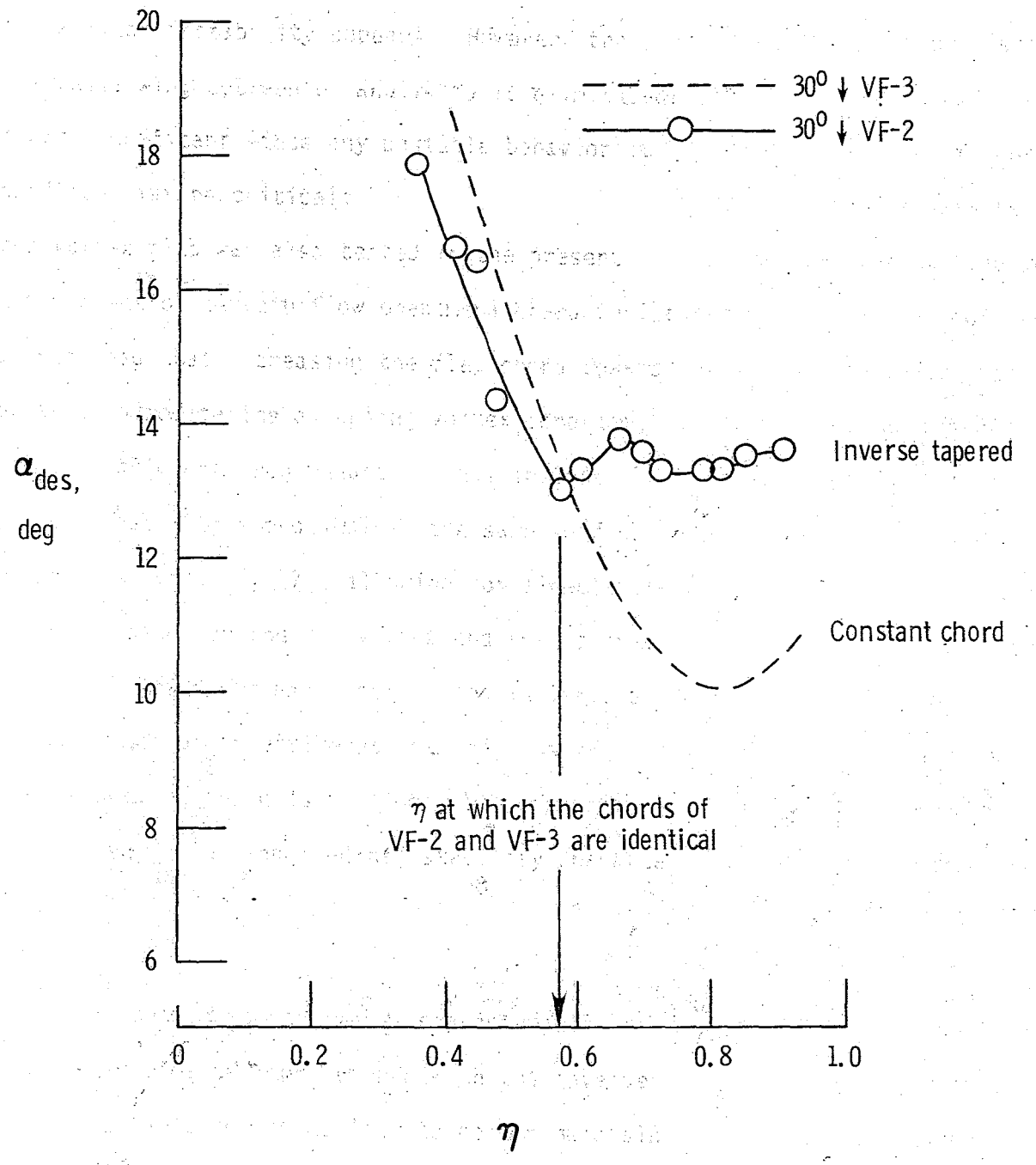

Figure 72.- Effects of inverse tapered flap chord distribution on local design point distribution ($C_{p_{LE}}$ derived) along the vortex flap.

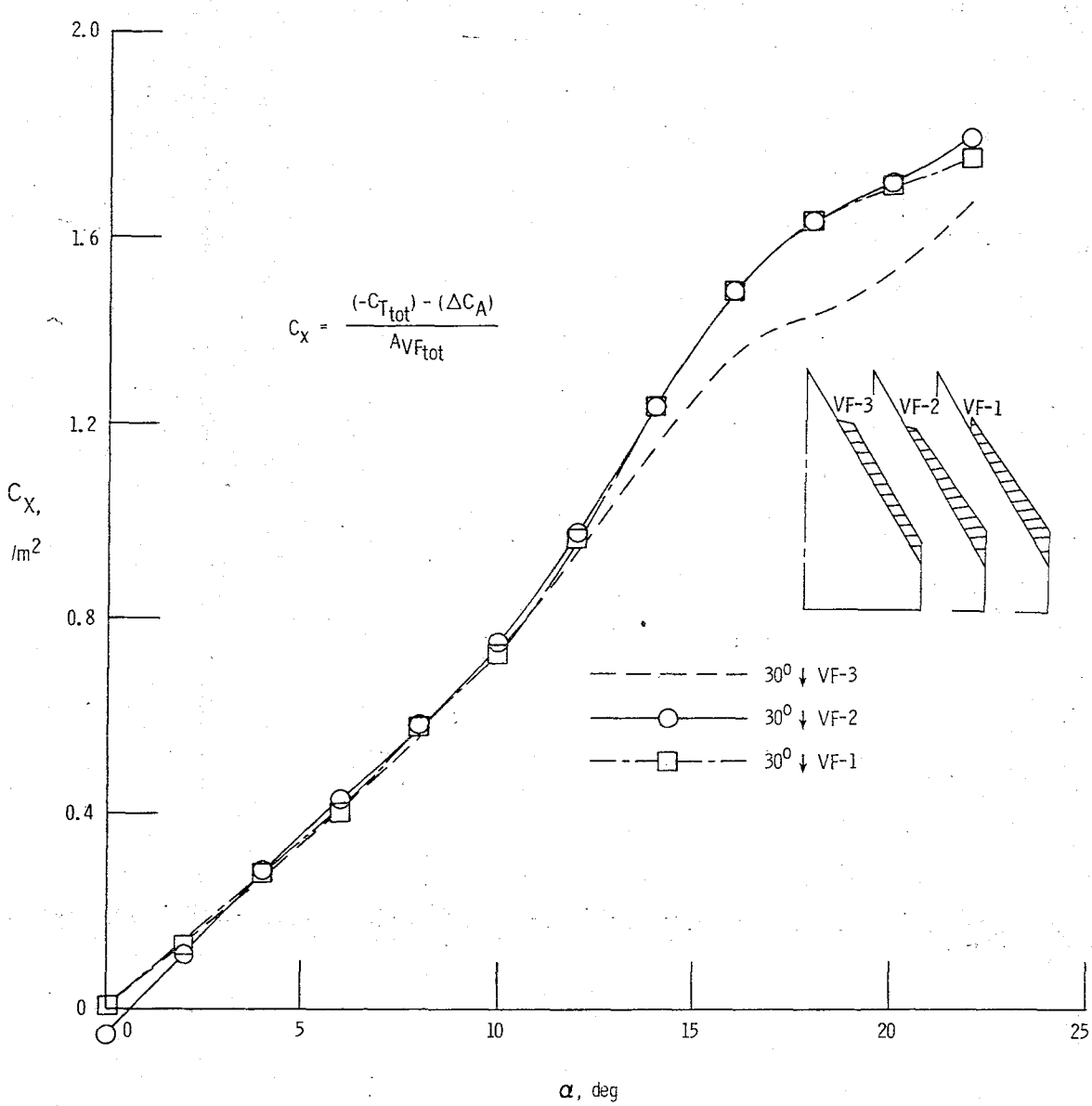

Figure 73.- Effects of inverse tapered vortex flap chord distribution and apex shape on flap thrust parameter.

that a counter-rotating vortex formed at this chordwise edge would interfere with the formation of the primary flap vortex. Balance data in figure 69, however, indicate that this particular apex modification has insignificant effects on overall performance. The close agreement of the flap thrust coefficient data in figure 73 provides added support.

As evidenced by the vortex flap data presented thus far, streamwise migration of the flap vortex with increasing outboard distance is the primary limitation to efficient flap performance at high α. Segmentation of the flap was suggested as one method of alleviating this problem through the formation of an independent vortex on the outboard segment, thereby delaying thrust loss near the tip. The geometries of the segmented flaps tested appear in figure 7. VF-4 was derived from VF-3 simply by segmenting the flap at its midpoint and, thus, afforded the opportunity to isolate the performance effects attributed solely to segmentation. VF-5 and VF-6 were included to investigate the possibility of further performance improvements through variations in flap chord distribution.

Results of balance measurements on configurations utilizing the segmented vortex flaps at 30^{o} downward deflections are presented in figure 74. Comparison of VF-3 and VF-4 axial force data indicates little overall effect from segmentation. However, slight reductions in normal force and longitudinal stability result at high α. Comparison with VF-5 and VF-6 data suggests that a substantial amount of flap area may be eliminated with little sacrifice of C_A performance up to $\alpha \simeq 18^{o}$. Beyond $\alpha \simeq 18^{o}$, the inverse tapered VF-6, with 42 percent less surface

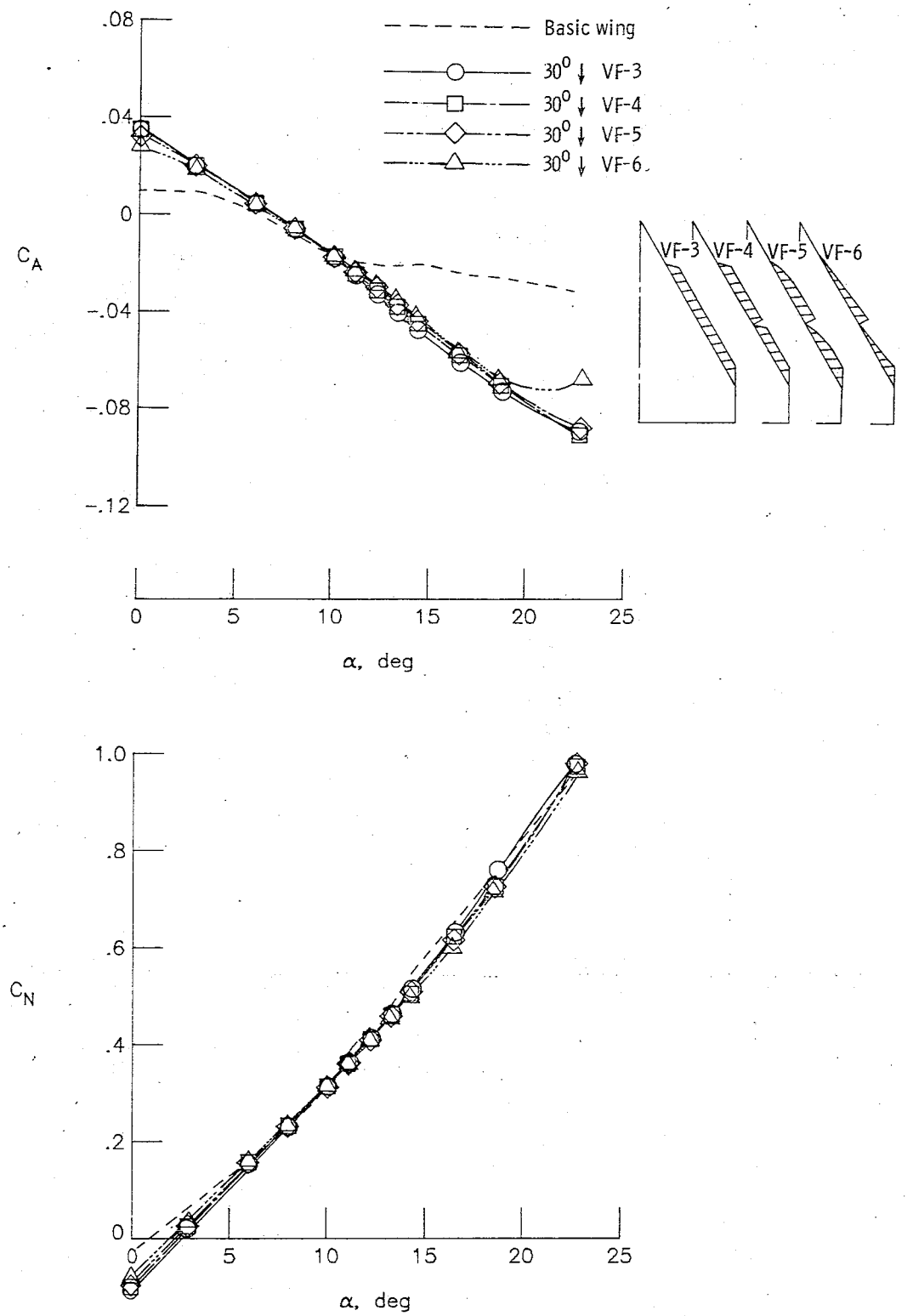

Figure 74.- Effects of segmentation and flap geometry on vortex flap performance ($\delta = 30^{o}$).

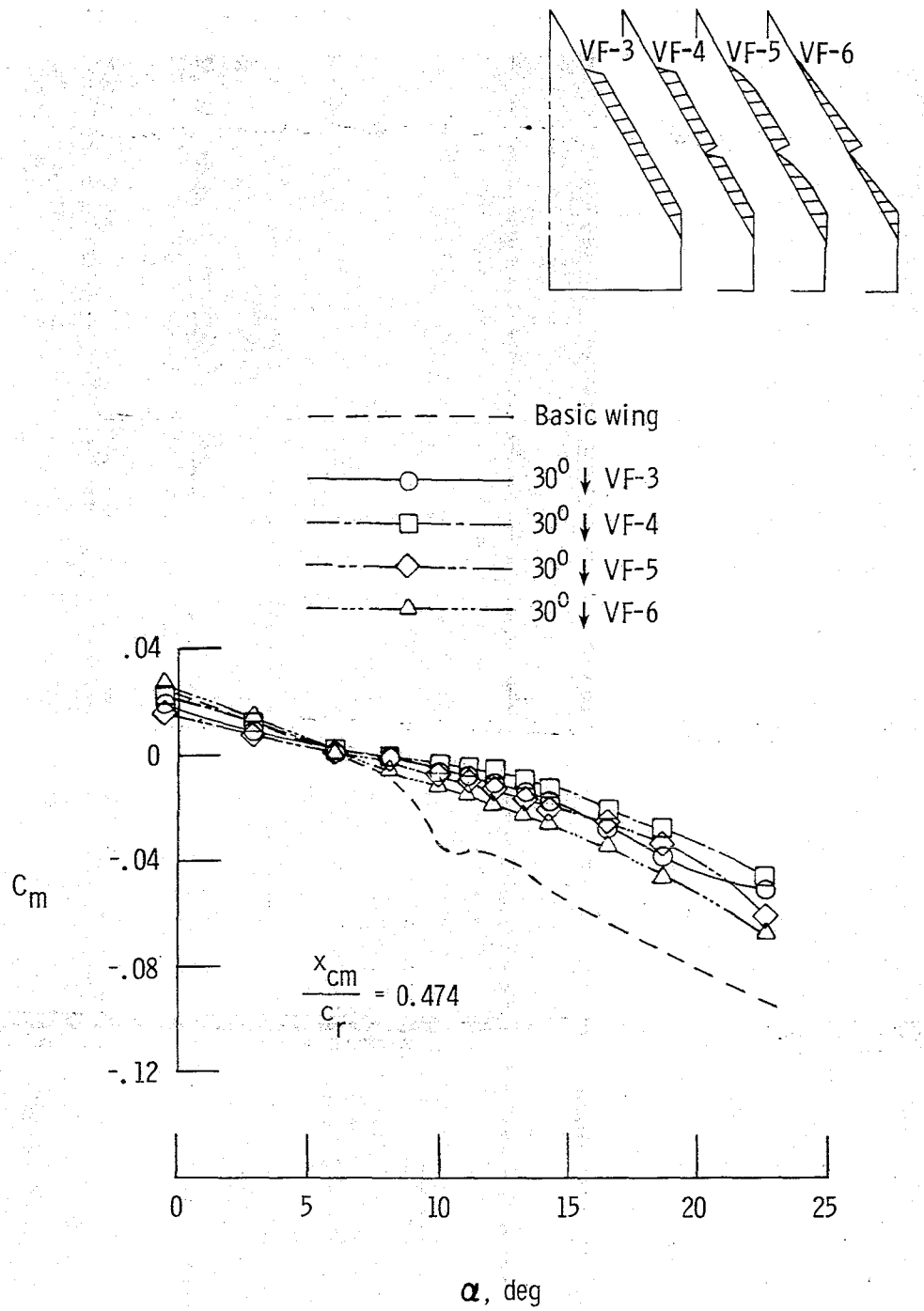

Figure 74.- Concluded.

area than the constant chord VF-4, loses effectiveness, while the parabolic VF-5 (13 percent reduction in area) continues to perform on par with the VF-4. Reduction in flap area actually results in an improvement in longitudinal stability beyond $\alpha \simeq 8^{o}$, with little effect on normal force. Balance data for 45^{o} downward deflections of these segmented flaps (fig. 75) indicates the same trends. However, the 30^{o} deflections will be used for description of the underlying flow mechanisms.

The performance of the various segmented vortex flaps on a per unit flap area basis is summarized in figure 76. As previously noted, the flap thrust coefficient, C_X, provides an indication of C_A effects attributed solely to vortex suction on the flap surface. Segmentation of the full length VF-3 into VF-4 results in substantial improvement in flap area efficiency beyond $\alpha \simeq 16^{o}$, as loss of flap suction has apparently been delayed. The parabolic (VF-5) and inverse tapered (VF-6) segmented flaps provide further improvements at lower α, but with earlier loss of effectiveness with decreasing flap area. Each particular segmented flap geometry seems to be the most efficient of those considered within a specific α range, implying that the actual geometry selected would depend on the design angle of attack.

Tuft photographs in figure 77 confirm that C_X improvements resulting from segmentation are indeed attributed to retention of vortex suction on the outboard flap segment. The mini-tuft pattern and static pressure distribution at STA 6 with the full length VF-3 suggest flow reattachment on the upper surface. However, the aft portion of the

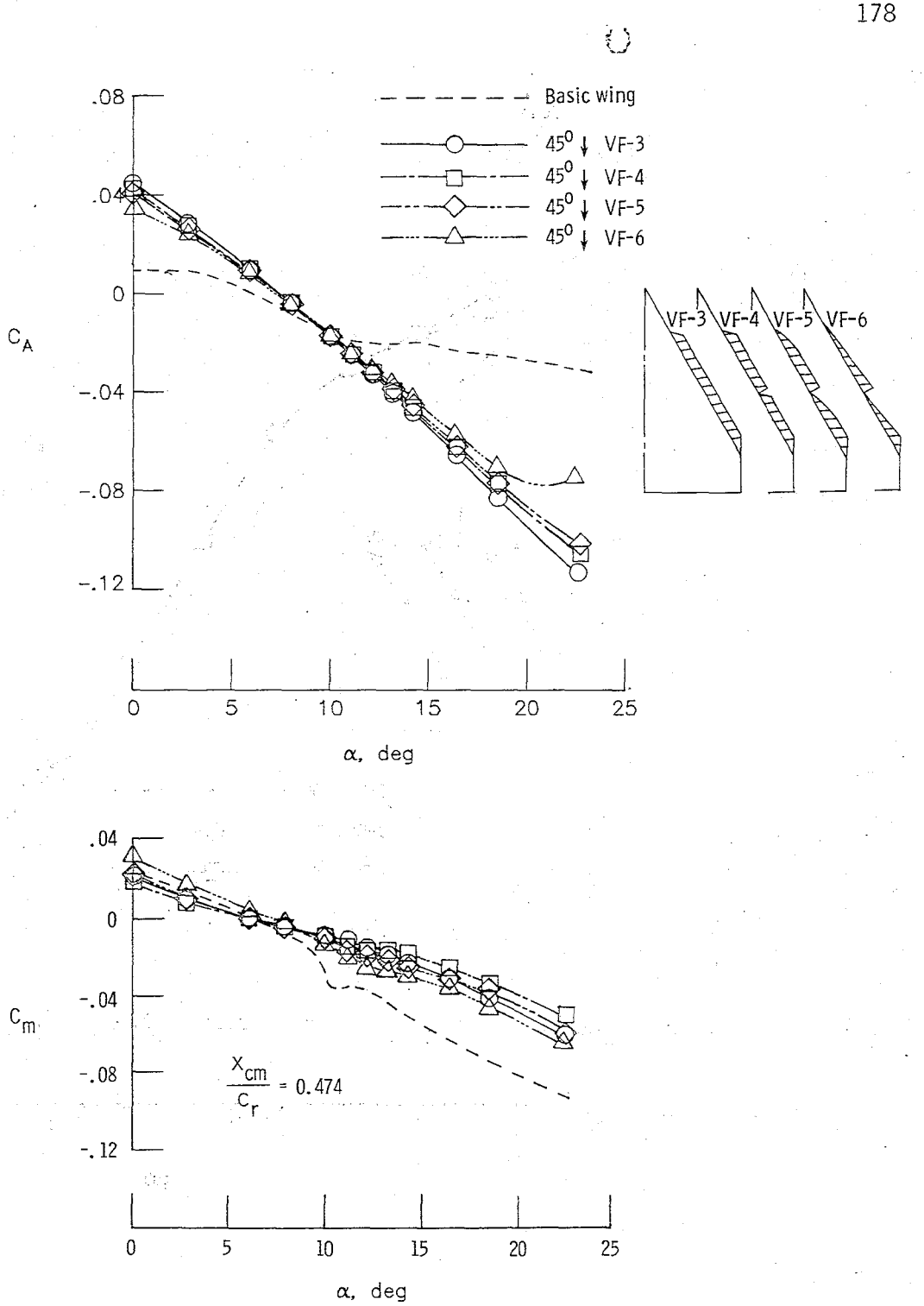

Figure 75.- Effects of segmentation and flap geometry on vortex flap performance ($\delta = 45^{o}$).

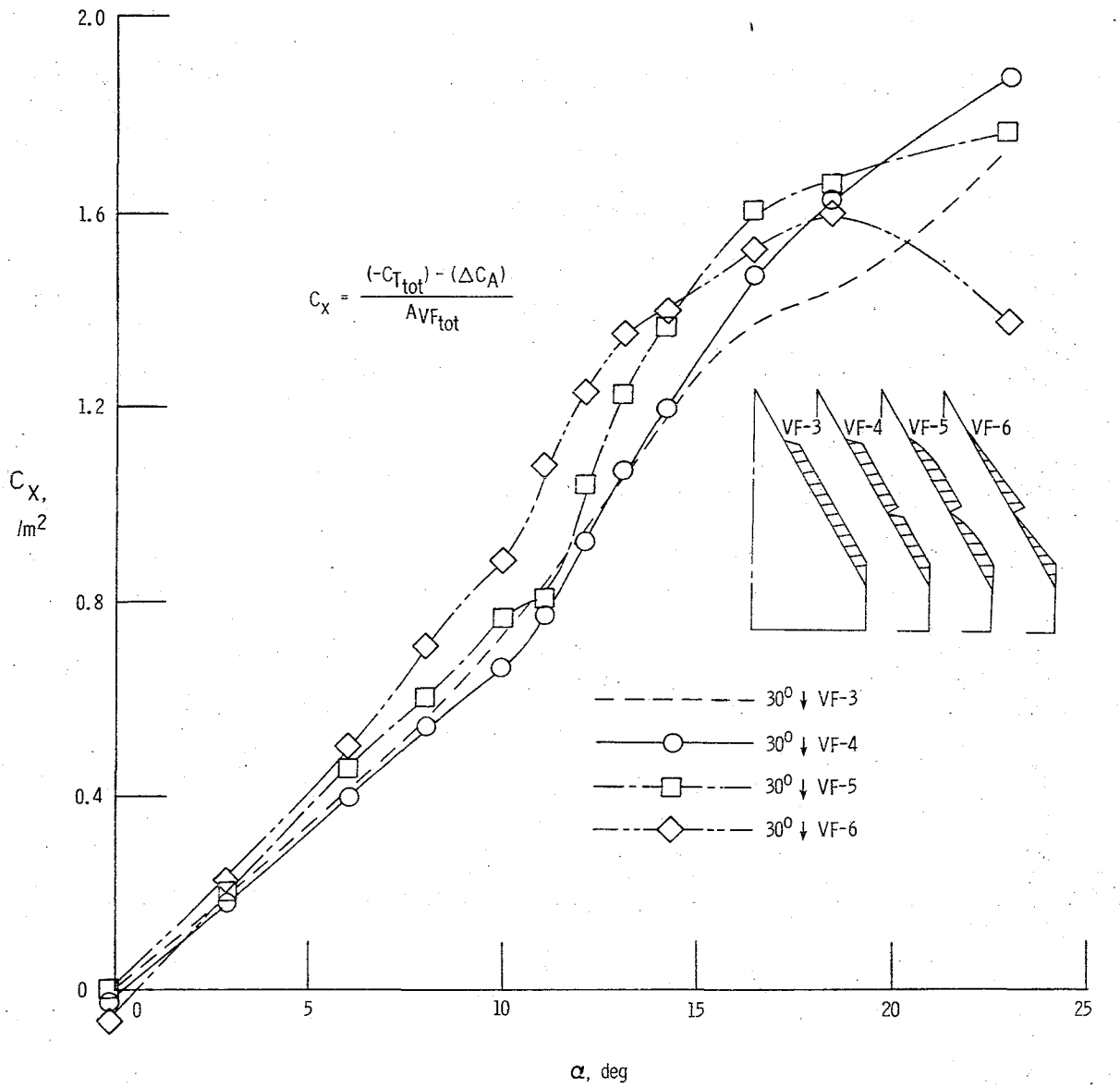

Figure 76.- Effects of segmentation and vortex flap geometry on flap thrust parameter.

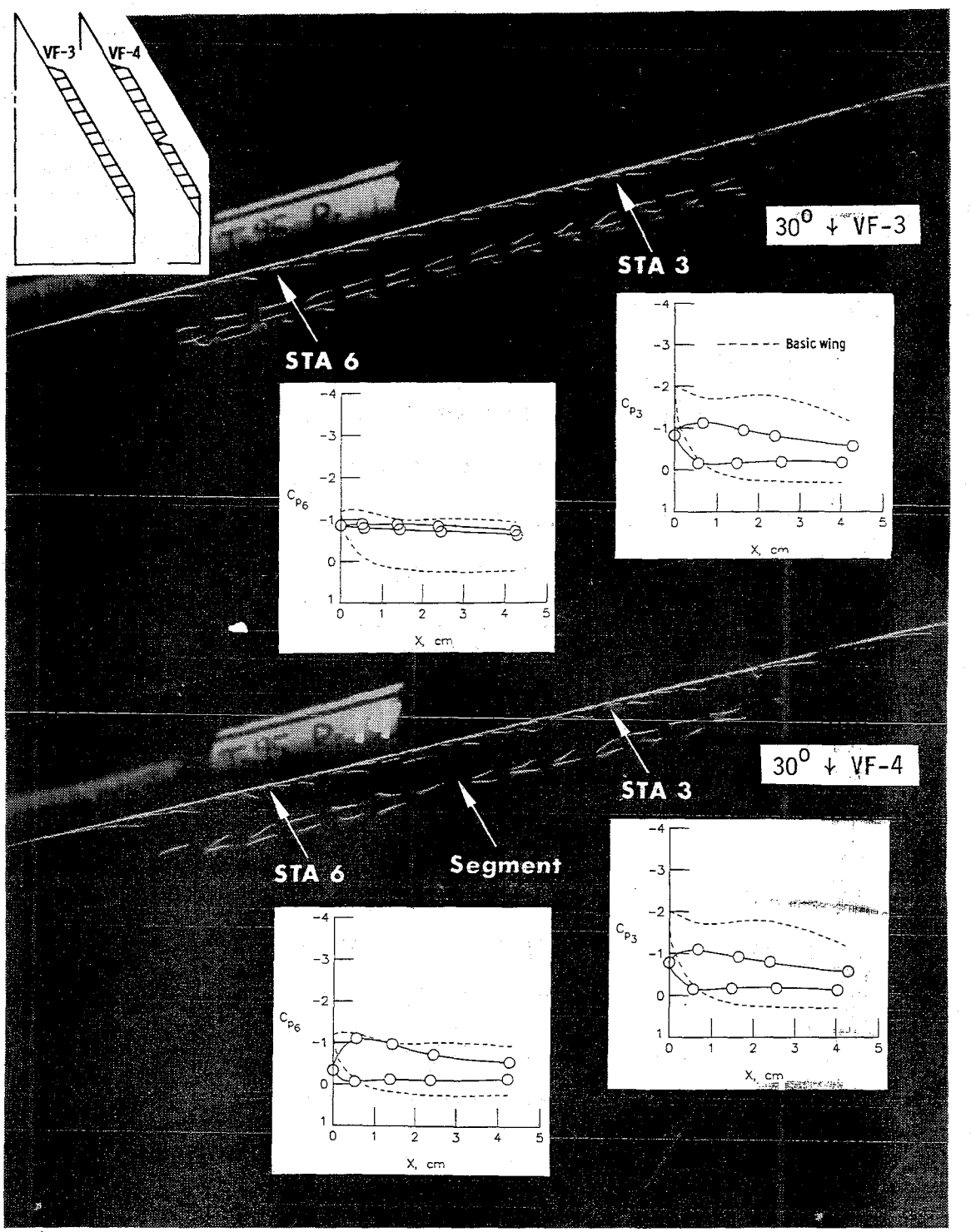

Figure 77.- Side tuft photographs of 30° ↓ VF-3, VF-4, VF-5, and VF-6 configurations at α = 14°.

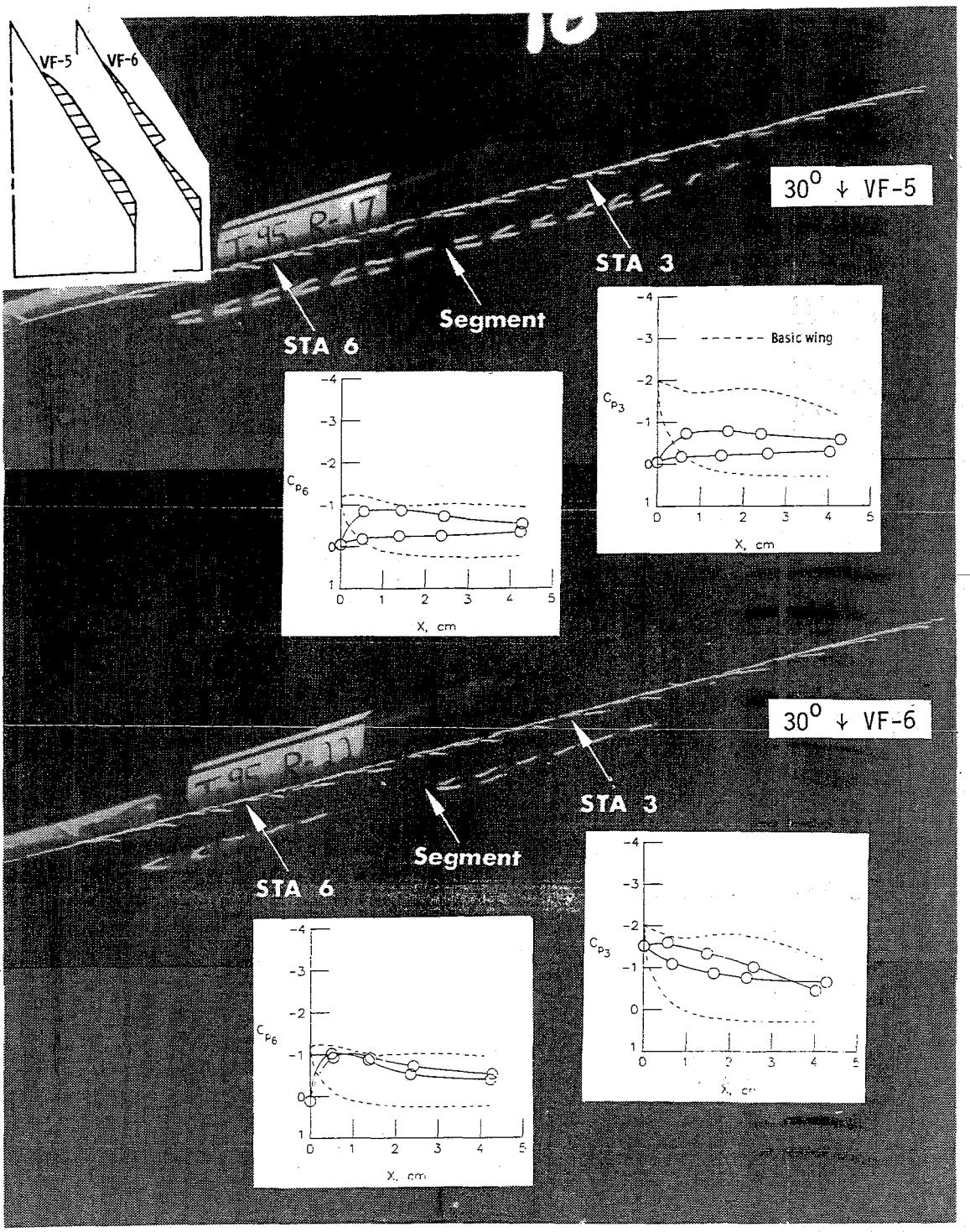

Figure 77.- Concluded.

segmented VF-4 appears to still be fully under the influence of vortex suction (as shown by the mini-tufts on the flap slanting away from the wing leading edge) with reattachment in the vicinity of the knee (attached flow indicated on the wing leading edge). The flow through the break has apparently forced the vortex on the forward flap segment to peel off and, most likely, travel over the upper wing surface. The parabolic VF-5 and inverse tapered VF-6 show the same basic trends but with accelerated forward movement of the outboard vortex. Comparison with static pressure distributions at STA 3, where segmentation would appear to have little influence, suggests that this is purely a geometric effect. As a result, the tuft photographs in figure 78 indicate a reduction in upper surface vortex flow in the outboard region upon segmentation of VF-3 (to VF-4), but with the opposite effect with cutback from VF-4 to VF-5 and, subsequently, VF-6. As noted in previous sections, an increase in upper surface vortex flow tends to increase the overall lift of the wing but also the severity of the lift-dependent drag.

Figure 79 presents the $C_{p_{LE}}$ derived locus of design points along each of the 30^{0} down-deflected segmented flaps. Although the data points are scattered, certain trends are consistent with those observed in the tuft photographs. Since effects inboard of $\eta = 0.625$ are purely geometric, the VF-3 and VF-4 data points approximately coincide. Reduction in flap chord with VF-5 and VF-6 results in satisfaction of the design condition at progressively lower α along this forward segment. The convergence of the data in the vicinity of the break

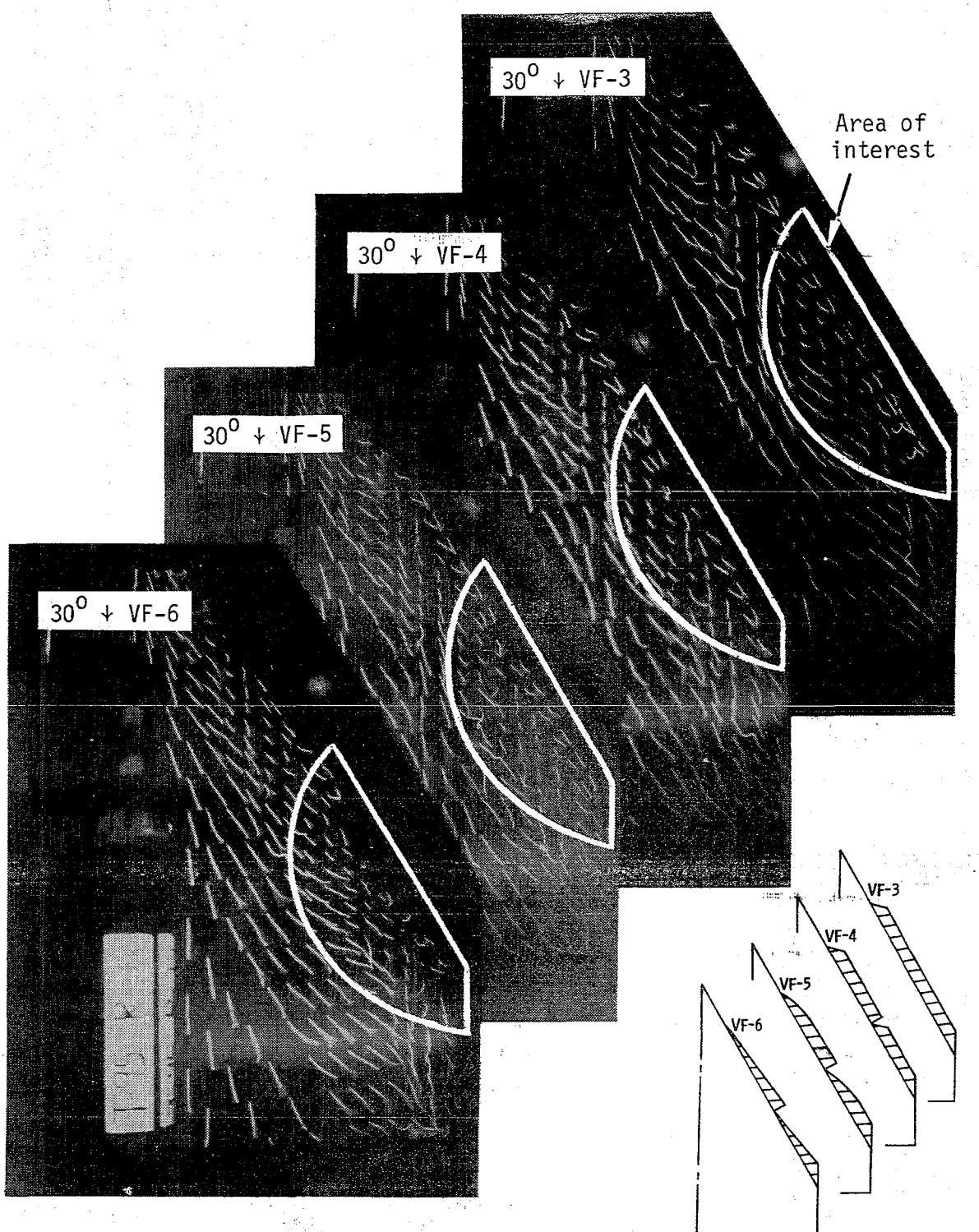

Figure 78.- Upper surface tuft photographs of 30° ↓ VF-3, VF-4, VF-5, and VF-6 configurations at $\alpha = 18^{\circ}$.

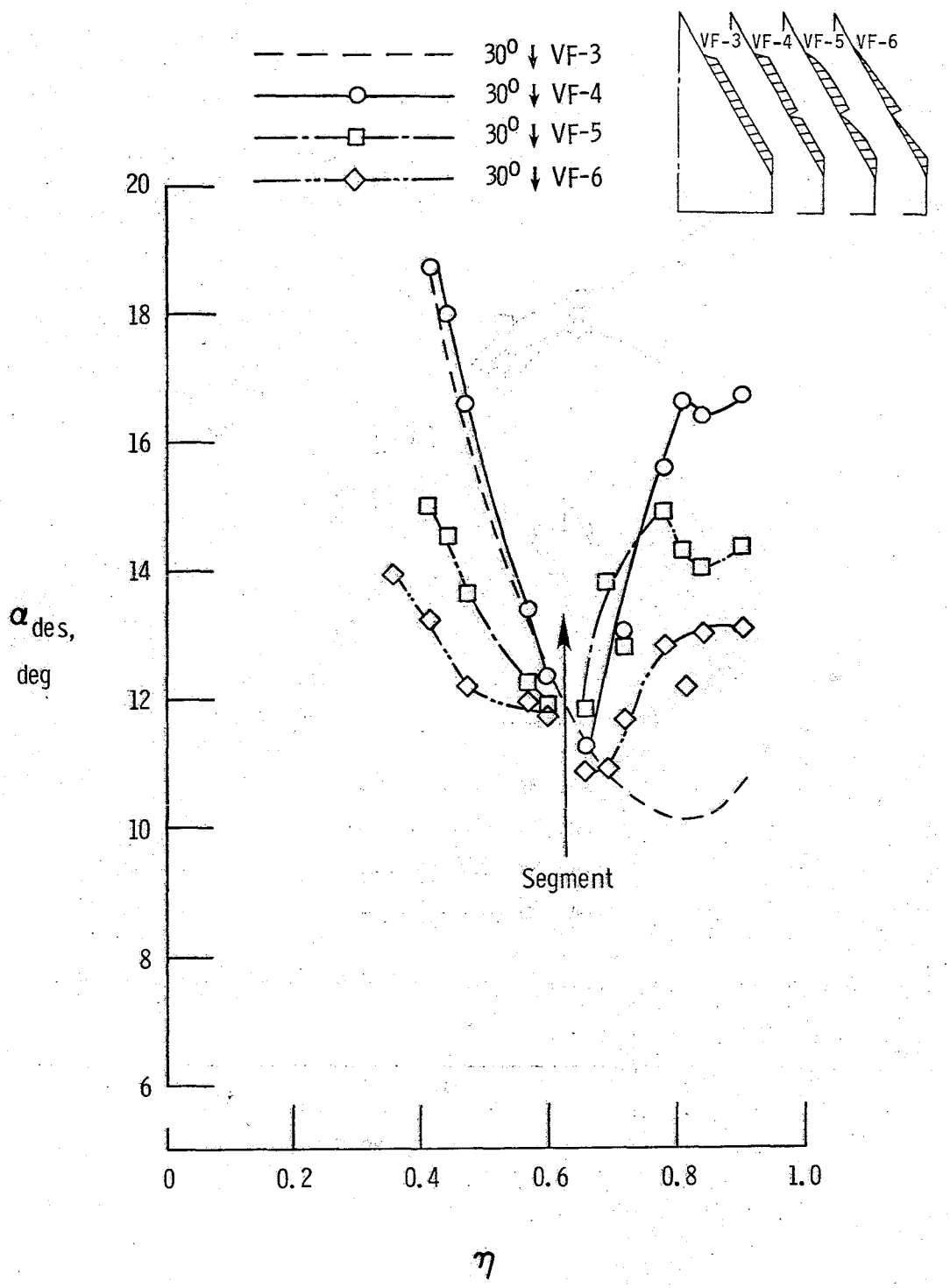

Figure 79.- Effects of segmentation and flap geometry on local design point distribution ($C_{p_{LE}}$ derived) along the vortex flap.

(η = 0.625) is attributed to the equality of the respective flap chords (see fig. 7). The effect of segmentation (VF-3 to VF-4) is evident along the outboard segment in the form of a delay of several degrees in vortex migration onto the upper surface. The effects of chord reduction noted on the inboard flap segment are also evident here.

The utilization of vortex flaps for roll augmentation was briefly investigated using the inverse tapered segmented VF-6. It was anticipated that asymmetric flap deflections would alter the spanwise lift distribution so as to produce adequate rolling moments at high lift, when conventional control surfaces, such as ailerons, are degraded by flow separation. Rolling moment data for a configuration utilizing a 30^{o} ↓ VF-6 on the left-hand and 45^{o} ↓ VF-6 on the right-hand wing panel are presented in figure 80. The positive shift in the C_{ℓ} curve as compared with the basic wing is purely a planform effect. The imbalance of planform area addition produces an additional lift increment on the left, with a resulting right-wing-down rolling moment. Beyond $\alpha \simeq 16^{o}$, the flap deflection effect becomes evident. The strong positive rolling moment initiated at this α is due to the earlier migration of the 30^{o} ↓ flap vortex onto the left wing panel as compared with the vortex emanating from the 45^{o} ↓ VF-6 on the right. The additional vortex lift on the left produces a maximum positive rolling moment of 0.0041 at $\alpha \simeq 18^{o}$. The subsequent migration of the 45^{o} ↓ VF-6 vortex onto the right wing panel, with its lift acting at an η value greater than that of the left-hand vortex, produces a reversal in the rolling moment at higher α. The fact that strong positive and negative rolling moments

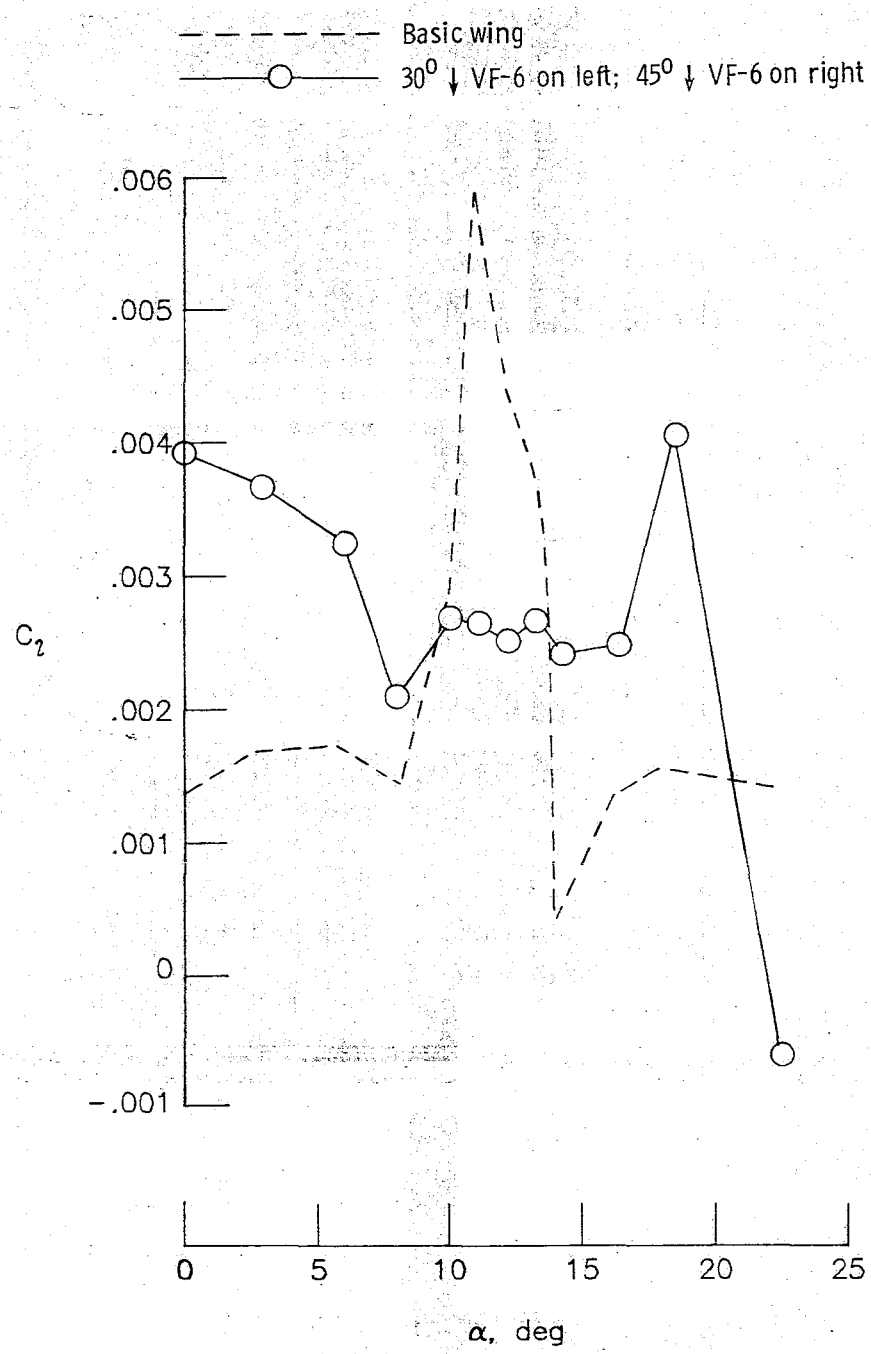

Figure 80.- Effect of differential vortex flap deflection on rolling moment characteristics.

are separated by only 4^{o} or 5^{o} α may produce undesirable handling qualities at high lift. In addition, the magnitudes of the rolling moments produced by the configuration tested here are inadequate to be of practical value on an actual aircraft. However, a greater differential in flap deflections may provide the required rolling moments.

Based on the previous performance of fences and chordwise slots, individually and in combination with the SLEE, their potential for improving the performance of the vortex flaps was also investigated. The 30^{o} ↓ VF-3 was tested with a single slot (w/SC-1) and then with a single F-3 fence at its apex (η = 0.25), again in an attempt to aid in the formation of an undisturbed flap vortex by blocking the leading-edge cross-flow near the wing apex. An additional test run was made with a single chordwise slot cut into the flap itself (S') at η = 0.625, with the slot in the wing leading edge remaining sealed (see fig. 7). As with segmentation, the flow through the slot was expected to aerodynamically compartment the flap and, thus, induce the formation of an independent primary vortex on its outboard side. Ideally, the entire flap surface would thereby remain under the influence of vortex suction to higher α.

Axial and normal force data for the vortex flap-slot/fence configurations just described are presented in figure 81. Both graphs indicate the overall ineffectiveness of each concept. Effects on pitching and rolling moment, not presented, are also negligible. Static pressure data for the configurations with either a slot or fence at η = 0.25 show no evidence of a local effect from the additional device.

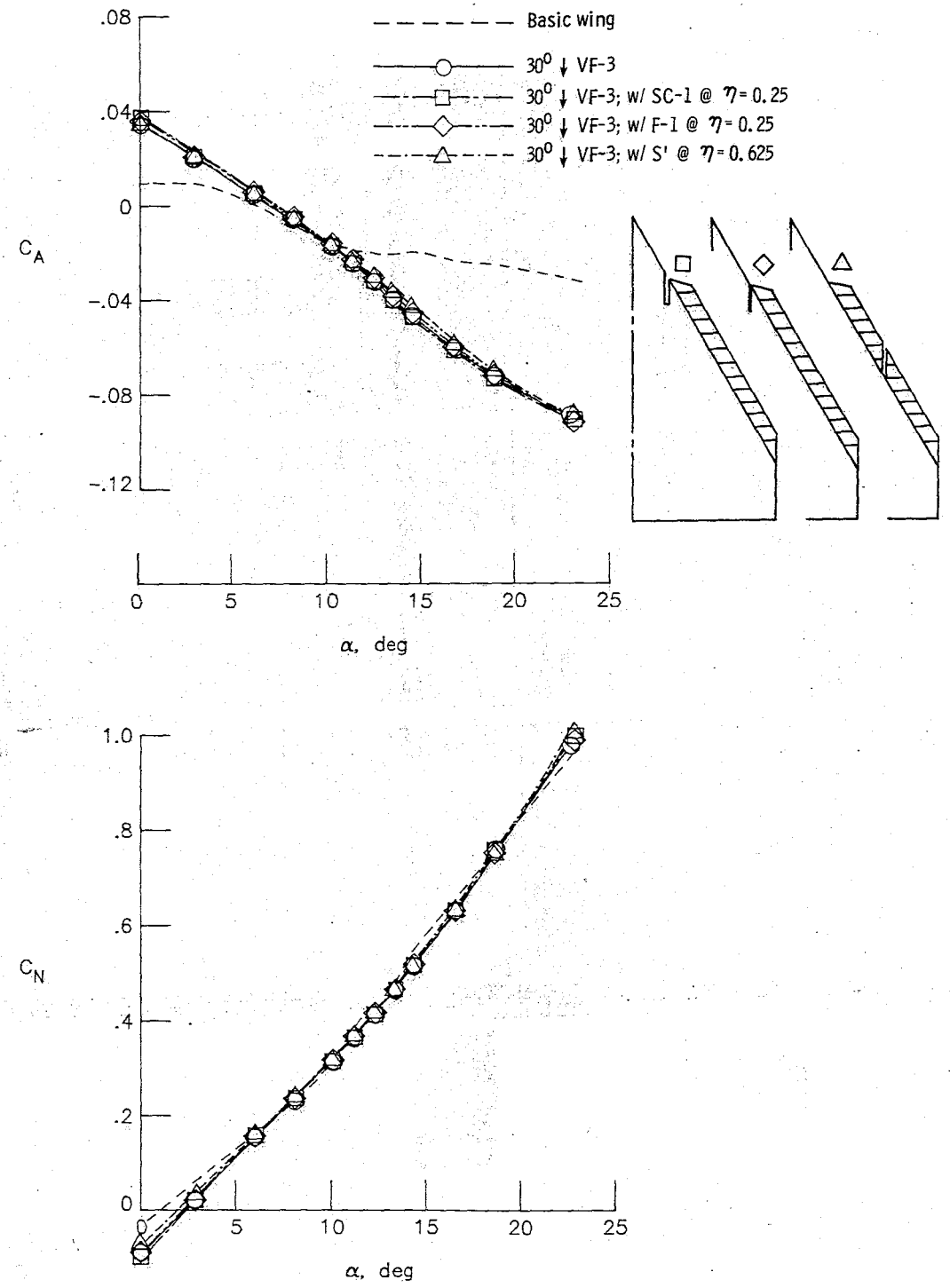

Figure 81.- Performance effects of the fence and chordwise slot in combination with the vortex flap.

The fact that these devices did not extend out ahead of the wing leading edge, where the formation of the flap vortex occurs, may be responsible. In that case, the chordwise slot cut into the flap at $\eta = 0.625$ would be expected to perform effectively, assuming the flow through the slot is sufficient for compartmentation. Indeed, the tuft photographs in figure 82 show evidence of a second flap vortex outboard of the slot. As depicted by the static pressure distributions in the same figure, the wing leading-edge flow at STA 5 ($\eta = 0.70$) in the case of the VF-3 without a slot has already reached a stagnated condition, implying reattachment on the upper wing surface. The additional vortex formed as a result of the slot at $\eta = 0.625$, however, retains attached flow at the wing leading edge, with the ideal flow condition to be met at higher α, as indicated in figure 83. Apparently, however, the sum of the suction effects from the two smaller flap vortices (with a slot at $\eta = 0.625$) is approximately equal to the suction produced by the single expanded vortex (without a slot), since no C_A effect is evident. Additional support is provided in figure 84, which shows that on a per unit flap area basis, the suction effectiveness of the flap surfaces are equivalent.

Finally, since the SLEE and vortex flap make use of basically the same flow mechanism, a brief comparison of their suction effectiveness is appropriate. Comparison of axial force data for the 45^{o} ↓ VF-3 and 0 cm ext. SLEE (each found as the most effective in its respective class), in figure 85, shows a significant advantage beyond $\alpha \simeq 10^{o}$ with the vortex flap. However, on a ΔC_A (relative to the basic wing)

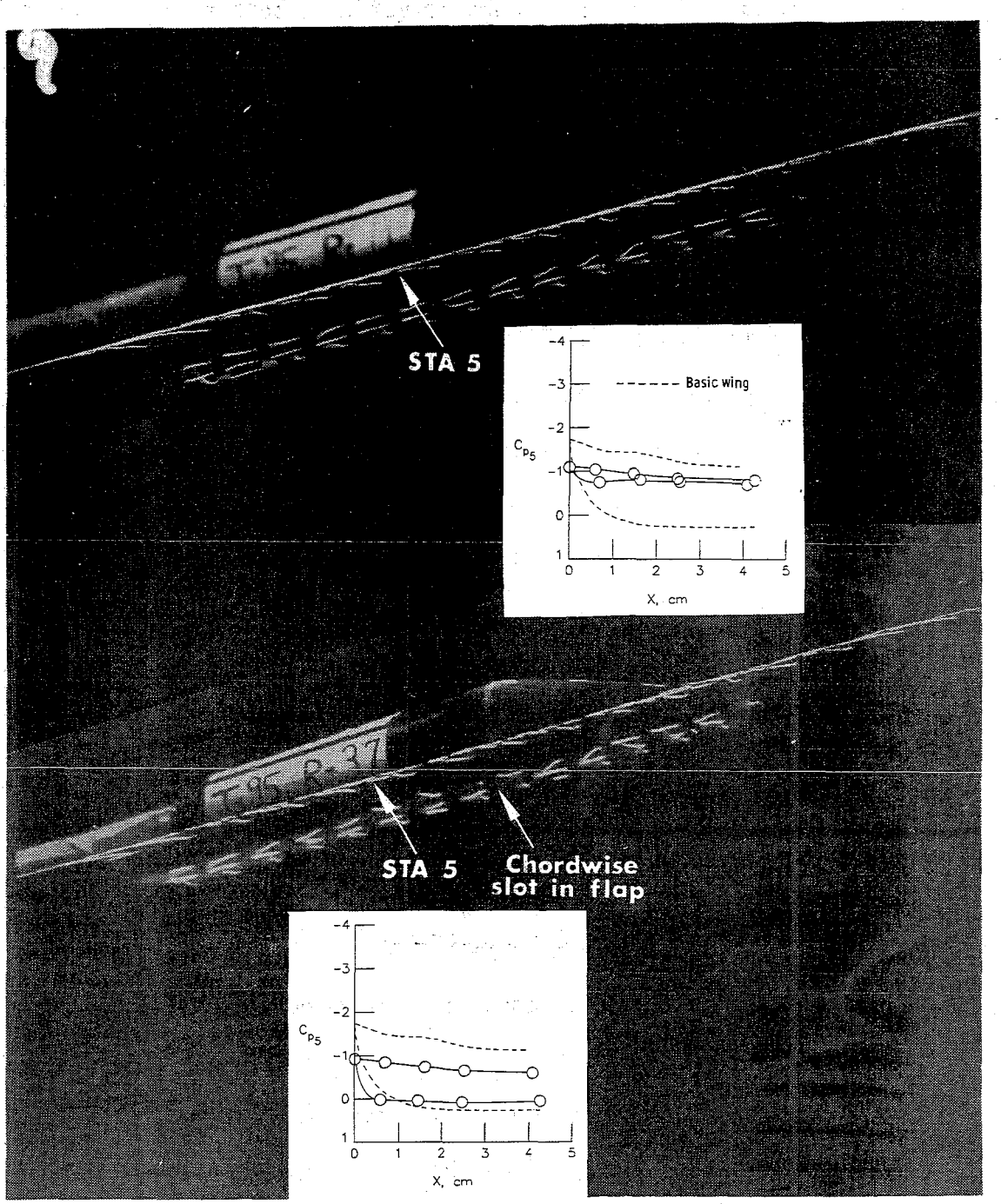

Figure 82.- Side tuft photographs of 30^{o} + VF-3 configuration with and without a slot in the flap at $\eta = 0.625$ ($\alpha = 14^{o}$).

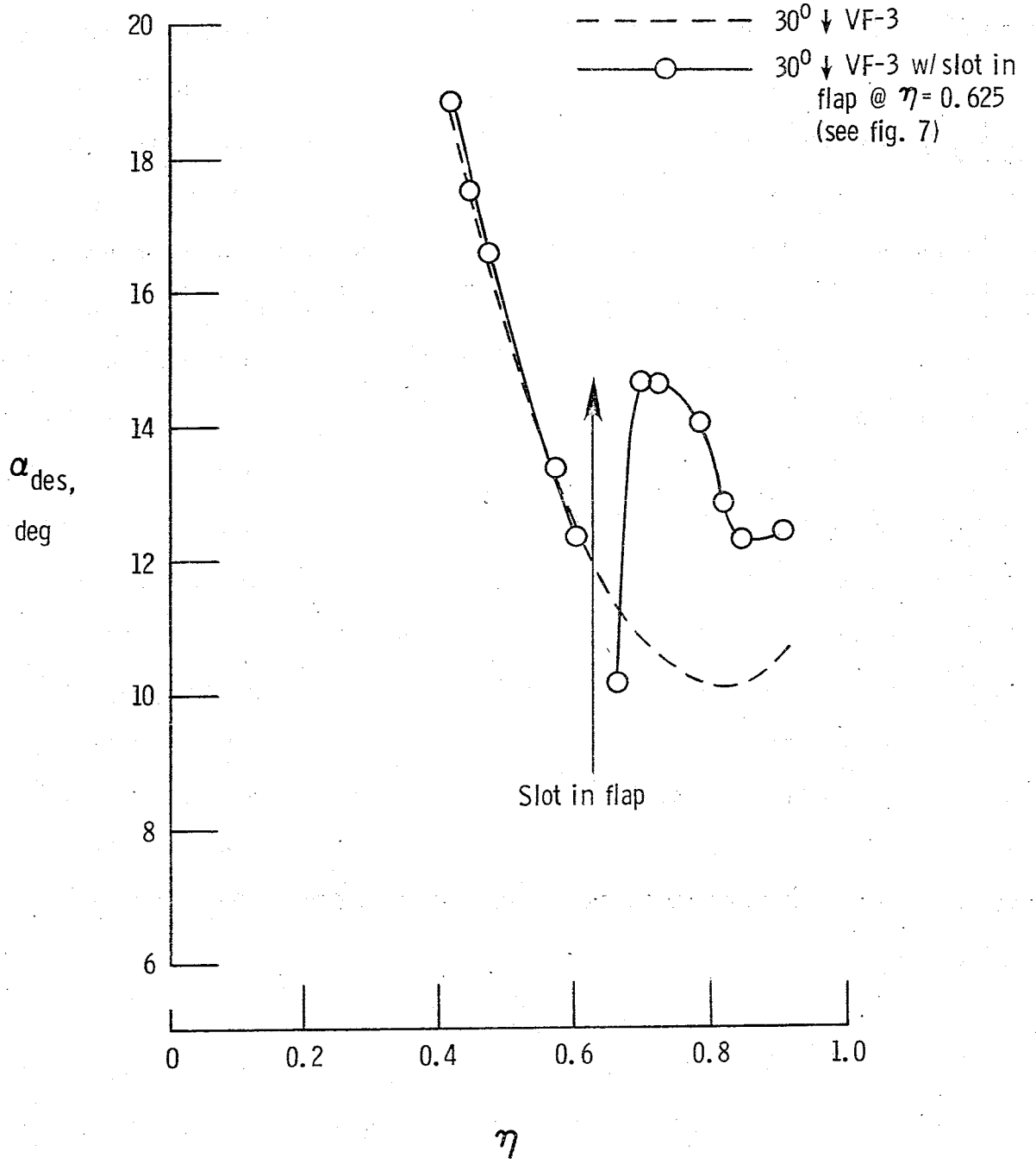

Figure 83.- Effect of a chordwise slot in the vortex flap on spanwise local design point distribution ($C_{p_{LE}}$ derived).

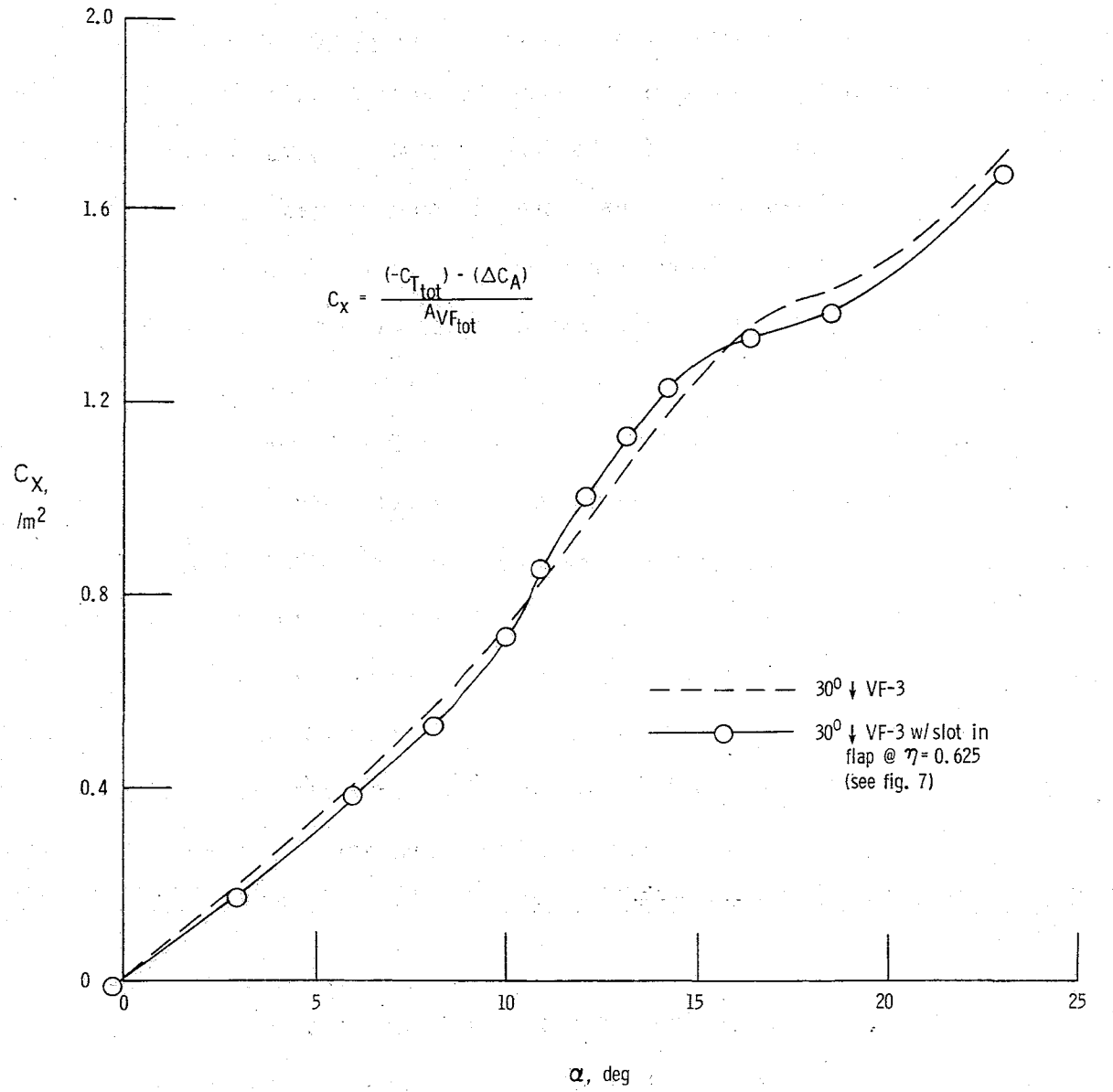

Figure 84.- Effect of a chordwise slot in the vortex flap on flap thrust parameter.

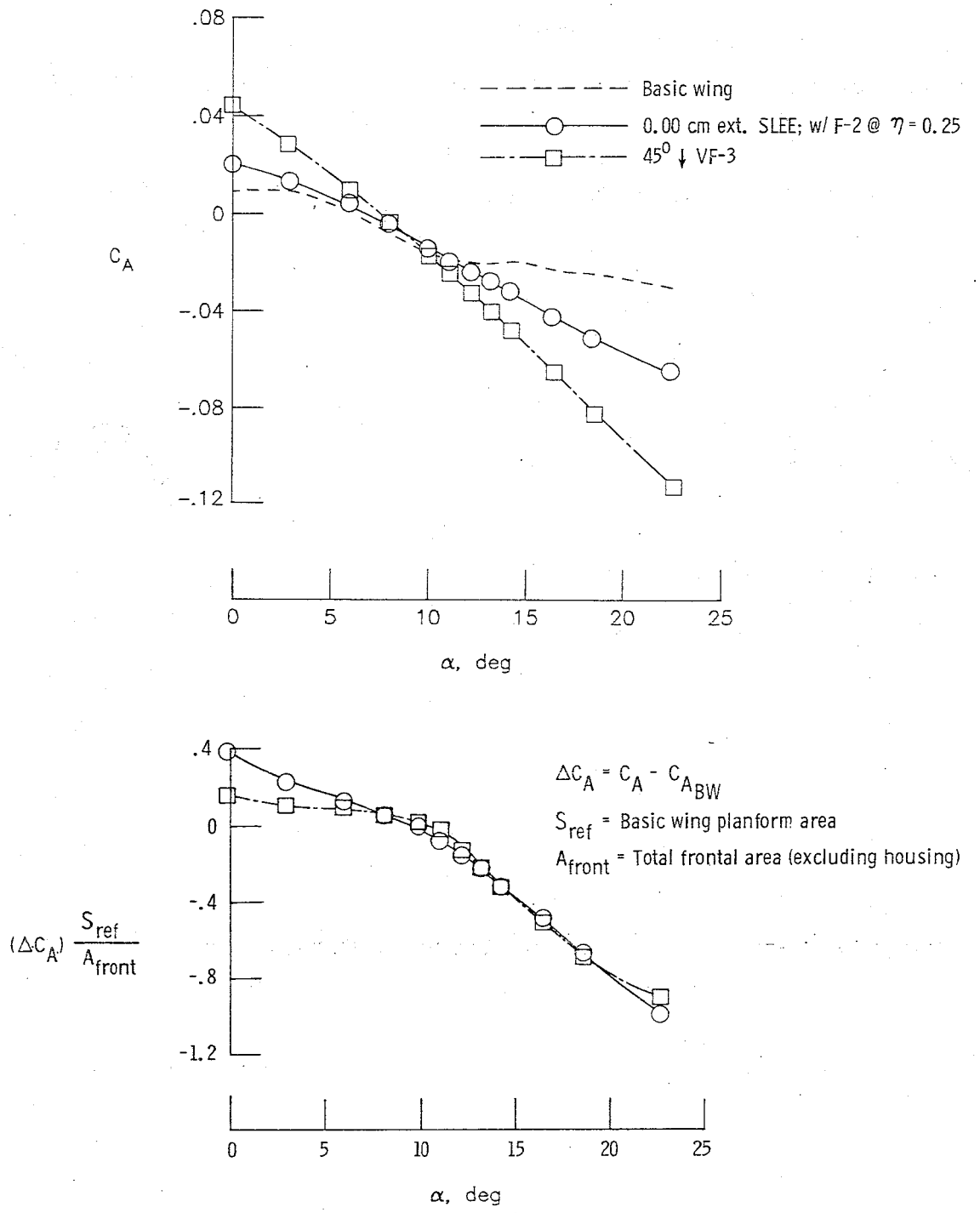

Figure 85.- Comparison of sharp leading-edge extension and vortex flap performance.

and frontal area basis, the two devices perform identically. Therefore, although the high-α drag performance of the vortex flap is significantly better than that of the SLEE, the additional weight of the vortex flap and the fact that the SLEE may be rapidly deployed must be considered.

In summary, the vortex flap provides substantial leading-edge thrust improvements, resulting in sizable axial force and lift-to-drag increments at high α and elimination of the severe mid-α rolling moment instability of the basic wing. In order to eliminate the characteristic low-α drag penalty, however, the vortex flap would have to be retracted or undeflected at cruise. Forty-five degrees appears to be the optimum flap deflection angle based strictly on drag-reduction performance; however, lift-to-drag is relatively insensitive to flap deflection in the range C_L = 0.4 to 0.9. An upward deflected vortex flap, by producing aerodynamic drag and vortex lift increments, is also effective as a deceleration and high-lift device for approach and landing. A large downward deflection of the vortex flap upon touch-down can provide continued aerodynamic braking, with the added advantage of increased downpressure on the wheels. High-α performance may be improved through the use of an inverse tapered, as opposed to a constant, flap chord distribution, which is better able to accommodate the expanding vortex core and, thus, delay vortex spillover in the outboard region. A two-segment constant chord flap improves the flap thrust efficiency at high α through the formation of a separate vortex on the outboard segment, which delays the outboard loss of leading-edge suction. Elimination of the relatively ineffective portions of the

constant chord flap, leading to the parabolic (13 percent area reduction) and inverse tapered (42 percent reduction) segmented flap configurations, results in little or no loss of drag-reduction performance except at the highest test α. Therefore, on a per unit area basis, these segmented flap geometries are more efficient than the constant chord flap. Differential deployment of the vortex flap appears to also have roll augmentation potential at high lift. The use of a chordwise slot cut into a full length flap at its midpoint generates an aerodynamic segmentation effect by splitting the primary vortex into two smaller vortices but with no significant influence on the total leading-edge thrust.

CONCLUSIONS

This report has presented the results of a wind-tunnel investigation undertaken to examine the potential for further drag reduction through refined versions of leading-edge devices such as chordwise slots, fences, pylon vortex generators, sharp leading-edge extensions, and leading-edge vortex flaps. The results were based on low-speed balance and static pressure measurements taken on a 60-deg cropped delta wing model in the NASA-Langley Research Center 7- by 10-foot high-speed tunnel. The intended use of the devices tested would be to reduce the severe lift-dependent drag penalties associated with highly swept wings at high lift. This section highlights what are believed to be the most significant findings of the investigation.

The chordwise slot, fence, and vortex generator devices produce substantial high-α drag and longitudinal stability improvements when utilized on highly swept leading edges. The use of these devices in multiple arrangements further enhances the leading-edge suction along the span by alleviating the adverse inboard effect of each particular device. However, each device is characterized by a low-α drag penalty. In the case of the chordwise slot, the main contribution to this drag increase is from friction acting on the internal side surfaces, with the pressure drag acting on the vertical face at the end of the slot of secondary importance. Sealing the slot at cruise would be one method of avoiding this drag penalty. Likewise, high-α performance is improved with increasing slot depth, but with no effect from the contour of the back face.

In the case of the fence, the characteristic high-α loss of leading-edge thrust on the inboard side of the device is attributed to its unsweeping of the upper surface isobars, rather than to any viscous accumulation on the inboard side.

Vortex generator size reduction in the form of leading-edge length and diagonal cutbacks reduce the low-α drag of the device but also adversely affect high-α performance. Reduction in VG chord to a certain extent results in performance improvements throughout the α range; however, further reduction actually produces an increase in low-α drag. The utilization of variable VG toe-in along the span to match the prevailing sidewash ahead of the leading edge may be one method of simultaneously reducing the low-α drag and improving high-α performance. The lower VG vortex apparently plays an important role through its own contribution to the leading-edge thrust and, thus, should also be considered in the design of the VG shape. An extended chord VG provides the added advantage of possible use also as a carrier of slender external stores, providing substantial drag and longitudinal stability improvements both with and without the external store.

The vortex suction effect of the sharp leading-edge extension and leading-edge vortex flap devices produces substantial lift-to-drag increments at high α, in addition to improving the linearity of the pitching and rolling moment curves. The drag-reduction effectiveness of the SLEE is insensitive to extension at low and mid α; however, there is a distinct advantage to having a shorter extention at high α, as long as the device extends at least beyond the stagnation point.

The performance of the SLEE is enhanced by the utilization of either a fence or chordwise slot at its apex to obstruct the spanwise flow originating near the wing apex and allow for the formation of an undisturbed primary vortex. The fence also possesses the ability to compartment the SLEE when used along its length, delaying outboard loss of effectiveness.

In the case of the vortex flap, the lift-to-drag is insensitive to deflection angle in the range $C_L \simeq 0.4$ to 0.9. High-α drag-reduction effectiveness is improved through the utilization of an inverse tapered, as opposed to a constant, flap chord distribution to better accommodate the expanding vortex core. In addition, segmentation of the vortex flap improves the high-α performance of the device on a per unit flap area basis through the formation of a separate vortex on the outboard segment. A chordwise slot in the vortex flap has the same aerodynamic effect but has no influence on the total leading-edge thrust. Parabolic and inverse tapered segmented flap chord distributions provide further improvements in flap area efficiency. The performance of these flaps suggest that similar variations in SLEE extension may improve the device's ability to hold the primary vortex ahead of the leading edge. Twisting the SLEE and vortex flap in future tests may also aid in that respect.

By means of an upward deflection, the vortex flap is also effective as a deceleration and high-lift device for approach and landing. Large downward deflection upon touch-down provides continued aerodynamic braking, along with the added advantage of downpressure on the wheels.

In addition, differential deployment of the vortex flap appears to provide roll augmentation at high α.

Finally, it should be noted that the devices tested here are still in the early stages of development and, therefore, future tests must be performed on scale models of actual aircraft to determine the effects of parameters such as camber, sweep, twist, and fuselage interference prior to making any final decisions on their effectiveness. In addition, it is recommended that future research include testing of the lateral/directional characteristics of the devices to complete a data base to be used in the final design.

REFERENCES

1. Rao, D. M.: Leading-Edge "Vortex Flaps" for Enhanced Subsonic Aerodynamics of Slender Wings. ICAS-80-13.5, 12th Congress of the International Council of the Aeronautical Sciences (Munich), 1980.

2. Rao, D. M. and Johnson, T. D., Jr.: Subsonic Wind-Tunnel Investigation of Leading-Edge Devices on Delta Wings (Data Report). NASA CR 159120, 1979.

3. Rao, D. M.: Leading Edge Vortex-Flap Experiments on a 74-Deg. Delta Wing. NASA CR 159161, 1979.

4. Bobbitt, P. J.: Modern Fluid Dynamics of Subsonic and Transonic Flight. AIAA Paper 80-0861, 1980.

5. Johnson, T. D., Jr. and Rao, D. M.: Experimental Study of Delta Wing Leading-Edge Devices for Drag Reduction at High Lift. NASA CR 165846, 1982.

6. Küchemann, D., FRS: Types of Flow on Swept Wings. J. Royal Aero. Soc., Vol. 57, pp. 683-699, November 1953.

7. Harris, C. D. and Bartlett, D. W.: Wind Tunnel Investigation of Effects of Underwing Leading-Edge Vortex Generators on a Supercritical-Wing Research Airplane Configuration. NASA TM X-2471, 1972.

8. Rao, D. M. and Johnson, T. D., Jr.: An Investigation of Delta Wing Leading-Edge Devices. J. Aircraft, Vol. 18, No. 3, pp. 161-167, 1981.

9. Fox, C. H., Jr. and Huffman, J. K.: Calibration and Test Capabilities of the Langley 7- by 10-Foot High Speed Tunnel. NASA TM X-74027, 1977.

10. Fox, C. H., Jr.: Real Time Data Reduction Capabilities at the Langley 7- by 10-Foot High Speed Tunnel. NASA TM 78801, 1980.

11. Rao, D. M. and Tingas, S. A.: Subsonic Balance and Pressure Investigation of a 60-Deg. Delta Wing with Leading-Edge Devices (Data Report). NASA CR 165806, 1981.

12. Gillis, C. L., Polhamus, E. C., and Gray, J. L., Jr.: Charts for Determining Jet-Boundary Corrections for Complete Models in 7- by 10-Foot Closed Rectangular Wind Tunnels. NACA NR L-123, 1945.

13. Herriot, J. G.: Blockage Corrections for Three-Dimensional-Flow Closed-Throat Wind Tunnels, with Consideration of the Effect of Compressibility. NACA Rep. 995, 1950.

14. Ridder, S.: On the Induced Drag of Thin Plane Delta Wings. An Experimental Study of the Spanwise Distribution of the Leading Edge Forces at Low Speeds. KTH AERO TN 57, Royal Institute of Technology (Stockholm), 1971.

15. Margason, R. J. and Lamar, J. E.: Vortex-Lattice Fortran Program for Estimating Subsonic Aerodynamic Characteristics of Complex Planforms. NASA TN D-6142, 1971.

16. Stadler, E. L. and Trammler, S. J.: F-4C Performance Data and Substantiation. McDonnel Aircraft Corporation Report G 853, Vol. I, 1968.

17. Marchman, J. F.: The Aerodynamics of Inverted Leading Edge Flaps on Delta Wings. AIAA Paper 81-0356, 1981.

1. Report No.	2. Government Accession No.	3. Recipient's Catalog No.
NASA CR- 165923		

4. Title and Subtitle	5. Report Date
Subsonic Balance and Pressure Investigation of a 60-Deg Delta Wing with Leading-Edge Devices	May 1982
	6. Performing Organization Code 505-31-43-03

7. Author(s)	8. Performing Organization Report No.
Stephen A. Tingas* and Dhanvada M. Rao**	
	10. Work Unit No.

9. Performing Organization Name and Address	11. Contract or Grant No.
North Carolina State University Mechanical and Aerospace Engineering Department Raleigh, NC 27650	NCCI-46
	13. Type of Report and Period Covered Contractor Report
12. Sponsoring Agency Name and Address National Aeronautics and Space Administration Washington, DC 20546	14. Sponsoring Agency Code 505-31-43-03

15. Supplementary Notes

*North Carolina State University, Raleigh, NC 27607

**Vigyan Research Associates, Inc., 28 Research Drive, Hampton, VA 23666

16. Abstract

Low supersonic wave drag makes the thin highly swept delta wing the logical choice for use on aircraft designed for supersonic cruise. However, the high-lift maneuver capability of the aircraft is limited by severe induced-drag penalties attributed to loss of potential flow leading-edge suction. This drag increase may be alleviated through leading-edge flow control to recover lost aerodynamic thrust through either retention of attached leading-edge flow to higher angles of attack or exploitation of the increased suction potential of separation-induced vortex flow. A low-speed wind-tunnel investigation was undertaken to examine the high-lift devices such as fences, chordwise slots, pylon vortex generators, leading-edge vortex flaps, and sharp leading-edge extensions. The devices were tested individually and in combinations in an attempt to improve high-alpha drag performance with a minimum of low-alpha drag penalty. This report presents an analysis of the force, moment, and static pressure data obtained in angles of attack up to 23^{0}, at Mach and Reynolds numbers of 0.16 and 3.85×10^{6} per meter, respectively. The results indicate that all the devices produced drag and longitudinal/lateral stability improvements at high lift with, in most cases, minor drag penalties at low angles of attack.

17. Key Words (Suggested by Author(s))	18. Distribution Statement
Leading-edge devices Delta Wing Subsonic wind-tunnel test Balance and pressure data High-lift drag reduction	Unclassified - Unlimited Subject Category - 02

19. Security Classif. (of this report)	20. Security Classif. (of this page)	21. No. of Pages	22. Price
Unclassified	Unclassified	216	A10

For sale by the National Technical Information Service, Springfield, Virginia 22161

End of Document